

*TARGETED IMAGING AGENTS FOR  
DETECTING TUMOUR CELL DEATH  
FOLLOWING THERAPY*



FLAVIU BULAT

CHURCHILL COLLEGE

SUPERVISORS: DR FINIAN J. LEEPER

PROF. KEVIN M. BRINDLE

OCTOBER 2019

THIS DISSERTATION IS SUBMITTED FOR THE DEGREE OF

DOCTOR OF PHILOSOPHY







## DECLARATION

This thesis is submitted for the requirements of the degree of Doctor of Philosophy. It describes work carried out in the Department of Chemistry, Cambridge Institute for Cancer Research and the Department of Clinical Neurosciences (Wolfson Brain Imaging Centre and Molecular Imaging Chemistry Laboratory) from October 2014 to September 2018.

This thesis is the result of my own work and includes nothing which is the outcome of work done in collaboration except as declared in the Preface and specified in the text. It is not substantially the same as any that I have submitted, or, is being concurrently submitted for a degree or diploma or other qualification at the University of Cambridge or any other University or similar institution except as declared in the Preface and specified in the text. I further state that no substantial part of my thesis has already been submitted, or, is being concurrently submitted for any such degree, diploma or other qualification at the University of Cambridge or any other University or similar institution except as declared in the Preface and specified in the text.

This thesis does not exceed the word limit of 60,000 words as set by the Physics and Chemistry Degree Committee.

Flaviu Bulat MChem  
Cambridge, October 2019



## ABSTRACT

Cell death is an important target for imaging the early response of tumours to treatment. In this study a phosphatidylserine-binding protein (C2Am) has been derivatised with a fluorine-18 containing maleimide for imaging tumour cell death in a xenograft murine advanced colorectal cancer.

A one-pot, two-step automated synthesis of *N*-(5-[<sup>18</sup>F]fluoropentyl)maleimide using a GE TRACERlab FX<sub>FN</sub> automated module (within 58±5.8 min (n = 12), >98% radiochemical purity and 12±3% decay corrected yield) has been developed. This was used to label the single cysteine present on C2Am within 30 min in PBS ( $A_m=212000\pm30000$  MBq/μmol (n = 3)). Using xenograft models of breast and colorectal cancer, and a TRAIL-R2 agonist for inducing cell death, the binding of [<sup>18</sup>F]FPenM-C2Am was tested *in vitro* and *in vivo* using biodistribution and dynamic PET imaging studies. Cell death detection was validated by cell death histology assays CC3 and TUNEL. For colorectal cancer, there was a positive correlation between [<sup>18</sup>F]FPenM-C2Am signal in tumours post treatment and the corresponding histologic markers of cell death CC3 (Pearson  $r = 0.82$ ) and TUNEL (Pearson  $r = 0.95$ ).

[<sup>18</sup>F]FPenM-C2Am showed a favourable biodistribution profile, with predominantly renal clearance and minimal retention in spleen (0.79±0.05 %ID/g), liver (1.18±0.13 %ID/g), small intestine (0.97±0.25 %ID/g) and kidney (6.90±0.56 %ID/g) at 2 h after probe administration. In a xenograft model of colorectal cancer treated with a TRAIL-R2 agonist, for 24h, at 0.2-0.4 mg/kg, i.v. [<sup>18</sup>F]FPenM-C2Am generated tumour-to-muscle and tumour-to-blood ratios following treatment of 6.7±0.8-fold and 1.89±0.23-fold, respectively, at 2 h after administration. A statistically significant pairwise difference was obtained between the tumour-to-muscle contrast prior to and following therapy (P=0.0137, unpaired two-tailed t-test).

Given the favourable biodistribution profile of [<sup>18</sup>F]FPenM-C2Am, and its ability to produce rapid and cell death-specific image contrast, this agent has potential for clinical translation. We have initiated cGMP manufacture and toxicology studies required for a Phase 1 trial.

Aberrant cell surface glycosylation has been described as one of the key hallmarks of cancer. Monitoring glycosylation could provide an insight into tumour progression, proliferation and ultimately could potentially be used for monitoring treatment response.

Aberrant glycosylation can be observed by harnessing the cell's metabolism to incorporate into its glycome unnatural sugars bearing bioorthogonal chemical reporters. These reporters are targeted subsequently by fluorescent, magnetic or optoacoustic probes that allow imaging.

As part of this work, we have demonstrated *in vitro* that a peracetylated cyclopropene mannosamine (Ac<sub>4</sub>ManNCCp)-modified sugar can be used as a tool for imaging hypersialylation in an advanced colorectal cancer model. Further optimisation of the probe to improve solubility is required to facilitate transitioning from *in vitro* to *in vivo* imaging. Nevertheless, overcoming this solubility issue would allow for facile labelling of surface glycans using PET radionuclides.

## DEDICATION

*This work is dedicated to my parents and grandparents, who went above and beyond to offer me the best opportunities in life and raised me to become a better person.*



## ACKNOWLEDGEMENTS

First and foremost, I would like to thank my supervisors: Dr Finian J. Leeper and Prof. Kevin M. Brindle. They've not only offered me the unique opportunity to undertake this fantastic project but also guided, encouraged and motivated me along the way. Finian taught me the value of critical thinking and attention to detail, allowing me sufficient independence to attempt my own ideas. Kevin has been a patient guide offering me exceptional mentorship during challenging times and kept me motivated through stimulating conversations. Without his help and visionary research, this work would have not been possible. I would like to thank both for allowing me enough freedom to develop as an independent scientist.

Secondly, I owe thanks to Dr André Neves for helping me at every step to become a better scientist. Throughout the last 4 years we have developed an efficient and effortless collaboration, that was not only enjoyable but also incredibly successful.

I was fortunate enough to work alongside a team of inspiring scientists and I would like to thank them for their direct contribution to the success of this project: Dmitry Soloviev for teaching me the basics of radiochemistry, Susana Ros for developing the mutated cell lines, De-en Hu and Matthew Clayton for skilfully cannulating mice for all the experiments, Friederike Hesse for her help with mice tumour implantations and cannulations, Kelly Homes for her project management skills, Robert Wilkinson and MedImmune for providing the TRAIL-R2 agonist (MEDI3039) used in this study and Robert Bielik for sharing his practical knowledge of radiochemistry. I owe special thanks to Sarah McGuire and Marion Karniely for their patience and endless moral support they've provided me with during the past years.

Further thanks go to the Leeper group members who made my PhD journey more enjoyable: Emma Durham, Maxime Couturier, Annabel Murphy and Daniel Parle. I would also like to thank Connor Wilmington-Holmes for his contributions to this project.

Much appreciated was also the constant help of the Dept of Chemistry's technical staff Nic Davies and Naomi Hobbs regarding safe quenching and disposal of dangerous

chemical waste. Moreover, I am extremely grateful for all the hard work the Core Facilities has done to facilitate my work at Cancer Research UK Cambridge Institute.

Furthermore, I would like to thank Prof. Franklin Aigbirhio for providing me with access to the radiochemistry facilities required for accomplishing this project. I would also like to thank his research group: Abigail Hancock-Scott, Dave Williamson, Emily Fisher, Matt Hird, Nisha Kuzhuppilly-Ramakrishnan, Selena Milicevic-Sephton, Stephen Thompson, Steven Kealy, and Yanyan Zhao for their stimulating conversations regarding radiochemistry and PET imaging. Thanks to the Radio Pharmacy Unit team: Istvan Boros, Tunde Miklovicz, Stefan Hader, Roberto Canales-Candela and Paul Burke for facilitating access to the cyclotron and fluorine-18.

I also owe thanks to my examiners, Prof. Franklin Aigbirhio and Dr Adam McMahon, for their constructive feedback and interest in my thesis.

I am eternally grateful to my grandparents and parents, Ruxanda and Iulian, for the sacrifices they made on my behalf. Thank you for your love, support and for always having faith in me.

Finally, I would like to thank my wife Luana for being my trustworthy reflection and confiding partner. Her selfless support has been invaluable to the success of this work, as was her devotion to our relationship through the wonderful and challenging times of both our PhDs.



# CONTENTS

<b>1 INTRODUCTION .....</b>	<b>1</b>
1.1 CANCER – A WORLDWIDE DISEASE .....	1
1.2 MONITORING OF TREATMENT RESPONSE IN CANCER .....	4
1.3 TARGETED CELL DEATH IMAGING AS A MARKER OF EARLY TREATMENT RESPONSE IN CANCER .....	10
1.3.1 <i>Phosphatidylserine, an early stage cell death biomarker</i> .....	10
1.3.2 <i>Imaging cell death – a clinical challenge</i> .....	13
1.3.3 <i>C2A protein, the subunit of Synaptotagmin I</i> .....	16
1.4 POSITRON EMISSION TOMOGRAPHY (PET) .....	17
1.4.1 <i>Latest PET equipment development</i> .....	22
1.4.2 <i>Single-photon emission computed tomography (SPECT)</i> .....	24
<b>2 LABELLING OF C2AM FOR PET IMAGING .....</b>	<b>28</b>
2.1 PROTEIN BIOCONJUGATION FOR MOLECULAR IMAGING .....	28
2.1.1 <i>Protein bioconjugation via thiol labelling</i> .....	30
2.1.2 <i>Radioisotope of choice, radiotracer properties and radiosynthesis</i> ...	34
2.1.3 <i>Radioactive maleimides used for protein labelling</i> .....	37
2.1.4 <i>Microfluidic (Advion NanoTek) vs batch (GE TRACERlab FX<sub>FN</sub>) radiochemistry</i> .....	40
2.2 SYNTHESIS OF PRECURSORS TO PROSTHETIC GROUPS .....	41
2.2.1 <i>Precursors synthesis</i> .....	42

2.2.2	<i>Synthesis of precursors for [<sup>18</sup>F]FPenM</i> .....	45
2.2.3	<i>Kinetics of N-(5-fluoropentyl)maleimide conjugation with L-glutathione</i> .....	48
2.3	RADIOSYNTHESIS OF PROSTHETIC GROUPS.....	51
2.3.1	<i><sup>18</sup>F-Fluorination of iodonium salts to yield [<sup>18</sup>F]SFB</i> .....	51
2.3.2	<i>Production of [<sup>18</sup>F]SFB by <sup>18</sup>F-fluorination of ethyl 4-(trimethylammonio)benzoate</i> .....	54
2.3.3	<i>2-[<sup>18</sup>F]Fluoroethylazide</i> .....	58
2.3.4	<i>Manual production of N-(5-[<sup>18</sup>F]fluoropentyl)maleimide ([<sup>18</sup>F]FPenM)</i> .....	61
2.3.5	<i>Automated radiosynthesis of [<sup>18</sup>F]FPenM for pre-clinical imaging</i> ..	63
2.3.6	<i>Solid phase extraction (SPE) cartridge and optimisation of [<sup>18</sup>F]FPenM purification</i> .....	67
2.3.7	<i>Radiolysis of water and effects on [<sup>18</sup>F]FPenM</i> .....	73
2.4	LABELLING C2AM WITH [ <sup>18</sup> F]FPENM .....	76
2.4.1	<i>[<sup>18</sup>F]FPenM-C2Am radiotracer synthesis</i> .....	76
2.4.2	<i>[<sup>18</sup>F]FPenM-C2Am radiotracer stability test</i> .....	83
2.5	CONCLUSION.....	86
2.6	EXPERIMENTAL.....	88
2.6.1	<i>General synthetic chemistry (Department of Chemistry)</i> .....	88
2.6.2	<i>Radiochemistry (in the Wolfson Brain Imaging Centre - Cambridge)</i> .....	103
2.6.3	<i>Protein reduction and storage (CRUK – Cambridge Institute)</i> .....	113

<b>3 IN VITRO STUDIES USING [<sup>18</sup>F]FPENM-C2AM IN BREAST AND COLORECTAL CANCER CELL LINES .....</b>	<b>115</b>
3.1 INTRODUCTION .....	115
3.2 MONITORING CELL DEATH FOLLOWING TREATMENT USING FLUORESCENCE IMAGING.....	118
3.2.1 <i>Assessment of MDA-MB-231-D cell viability using SYTOX<sup>®</sup> green following incubation of the cells with MEDI3039 (10 pM) .....</i>	<i>118</i>
3.2.2 <i>Assessment of MDA-MB-231-D cell viability using SYTOX<sup>®</sup> green in cells incubated with MEDI3039 (5 pM).....</i>	<i>121</i>
3.2.3 <i>Assessment of Colo205-D cell viability using SYTOX<sup>®</sup> green in cells incubated with MEDI3039 (5 pM) .....</i>	<i>121</i>
3.3 LABELLING DYING TUMOUR CELLS USING [ <sup>18</sup> F]FPENM-C2AM.....	125
3.3.1 <i>Labelling MDA-MB-231-D cells with [<sup>18</sup>F]FPenM-C2Am.....</i>	<i>127</i>
3.3.2 <i>Labelling Colo205-D cells with [<sup>18</sup>F]FPenM-C2Am .....</i>	<i>129</i>
3.4 CONCLUSION.....	130
3.5 EXPERIMENTAL.....	130
3.5.1 <i>Detection of cell death using flow cytometry: .....</i>	<i>131</i>
3.5.2 <i>Detection of cell death using [<sup>18</sup>F]FPenM-C2Am:.....</i>	<i>131</i>
3.5.3 <i>General cell culture protocols for Colo205-D and MDA-MB-231-D cancer cell lines: .....</i>	<i>132</i>
<b>4 IN VIVO DETECTION OF CELL DEATH USING [<sup>18</sup>F]FPENM-C2AM IN A MURINE XENOGRAFT MODEL OF COLORECTAL CANCER.....</b>	<b>133</b>
4.1 INTRODUCTION .....	133
4.2 BIODISTRIBUTION ANALYSIS OF [ <sup>18</sup> F]FPENM-C2AM IN BALB/C NU/NU MICE BEARING COLO205-D TUMOURS .....	134

4.3 PET/CT IMAGING AND BIODISTRIBUTION ANALYSIS OF [ <sup>18</sup> F]FPenM-C2AM IN BALB/C NU/NU MICE BEARING COLO205-D TUMOURS .....	137
4.4 CONCLUSION.....	145
4.5 EXPERIMENTAL.....	146
4.5.1 Colo205-D implantation and tumour formation in mice.....	146
4.5.2 [ <sup>18</sup> F]FPenM-C2Am synthesis for biodistribution experiment.....	147
4.5.3 [ <sup>18</sup> F]FPenM-C2Am synthesis for PET imaging experiment.....	150
<b>5 IMAGING TUMOUR GLYCANS.....</b>	<b>154</b>
5.1 INTRODUCTION TO GLYCANS AND THEIR RELEVANCE IN CANCER .....	154
5.1.1 Aberrant glycosylation in cancer .....	156
5.1.2 Imaging of glycans.....	159
5.1.3 Bioorthogonal reporter and metabolic labelling strategies.....	161
5.2 SYNTHESIS OF N-CYCLOPROPENYL CARBAMATE MANNOSAMINE (Ac <sub>4</sub> MANNCCp).....	166
5.3 <i>IN VITRO</i> METABOLIC LABELLING OF COLO205-D CELLS .....	167
5.4 <i>IN VIVO</i> METABOLIC LABELLING OF COLO205-D TUMOURS.....	173
5.5 CONCLUSION.....	176
5.6 EXPERIMENTAL.....	177
5.6.1 Synthesis of Ac <sub>4</sub> ManNCCp .....	177
5.6.2 Metabolic labelling of Colo205-D with Ac <sub>4</sub> ManNCCp and Tz-PEG <sub>11</sub> -DyLight 649 derivatization for flow cytometry analysis.....	180
<b>6 CONTRIBUTIONS AND FUTURE WORK.....</b>	<b>183</b>
6.1 IMAGING CELL DEATH USING C2A PROTEIN .....	183

6.2 IMAGING TUMOUR GLYCANS IN AN ADVANCED COLORECTAL CANCER USING AC <sub>4</sub> MANNCCP .....	184
<b>7 REFERENCES.....</b>	<b>186</b>
<b>8 APPENDICES.....</b>	<b>224</b>
8.1 GE TRACERLAB FX <sub>FN</sub> PROGRAMMING SEQUENCE FOR 2-[ <sup>18</sup> F]FLUOROETHYL AZIDE .....	224
8.2 GE TRACERLAB FX <sub>FN</sub> PROGRAMMING SEQUENCE FOR <i>N</i> -(5-[ <sup>18</sup> F]FLUOROPENTYL)MALEIMIDE PREPARATION .....	225
8.3 GE TRACERLAB FX <sub>FN</sub> ACTIVITY REPORT FOR <i>N</i> -(5-[ <sup>18</sup> F]FLUOROPENTYL)MALEIMIDE RADIOSYNTHESIS AND SEMI-PREP PURIFICATION CHROMATOGRAM .....	228
8.4 ADVION NANOTEK ACTIVITY BALANCE SHEET FOR [ <sup>18</sup> F]SFB RADIOSYNTHESIS .....	230
8.5 PROTOCOL FOR CULTURING COLO205D CANCER CELLS .....	231
8.6 PROTOCOL FOR CULTURING MDA-MB-231-D CANCER CELLS .....	232
8.7 LIQUID CHROMATOGRAPHY MASS SPECTROMETRY SPECTRUM OF REDUCED C2AM (DECONVOLUTED) .....	233
8.8 LIQUID CHROMATOGRAPHY MASS SPECTROMETRY SPECTRUM OF <i>N</i> -(5-FLUOROPENTYL)MALEIMIDE-C2AM (CECONVOLUTED).....	233
8.9 HPLC CHROMATOGRAMS OF FPENM-C2AM STANDARD AND [ <sup>18</sup> F]FPENM-C2AM .....	234
8.10 <sup>1</sup> H, <sup>13</sup> C AND <sup>19</sup> F NMR SPECTRA FOR <i>N</i> -SUCCINIMIDYL-4-FLUOROBENZOATE STANDARD.....	235
8.11 <sup>1</sup> H AND <sup>19</sup> F NMR SPECTRA FOR <i>N</i> -(2-(2,5-DIOXO-2,5-DIHYDRO-1H-PYRROL-1-YL)ETHYL)-4-FLUOROBENZAMIDE .....	236

8.12 <sup>1</sup> H AND <sup>13</sup> C NMR SPECTRA FOR ETHYL 4-(TRIMETHYLAMMONIUM TRIFLATE) BENZOATE PRECURSOR.....	237
8.13 <sup>1</sup> H AND <sup>13</sup> C NMR SPECTRA FOR 2-AZIDOETHYL METHYLSULFONATE PRECURSOR .....	238
8.14 <sup>19</sup> F NMR SPECTRUM FOR 2-FLUOROETHYL AZIDE (HPLC STANDARD) ....	239
8.15 7-OXANORBORN-5-ENE-2,3-DICARBOXYLIC ANHYDRIDE .....	240
8.16 2-(5-HYDROXPENTYL)-3A,4,7,7A-TETRAHYDRO-1H-4,7-EPOXYISOINDOLE-1,3(2H)-DIONE .....	241
8.17 5-(1,3-DIOXO-1,3,3A,4,7,7A-HEXAHYDRO-2H-4,7-EPOXYISOINDOL-2-YL)PENTYL METHANESULFONATE .....	243
8.18 2-(5-FLUOROPENTYL)-3A,4,7,7A-TETRAHYDRO-1H-4,7-EPOXYISOINDOLE-1,3(2H)-DIONE .....	245
8.19 1-(5-FLUOROPENTYL)-1H-PYRROLE-2,5-DIONE .....	247
8.20 <sup>1</sup> H AND <sup>13</sup> C NMR SPECTRA OF 5-(1,3-DIOXO-1,3,3A,4,7,7A-HEXAHYDRO-2H-4,7-EPOXYISOINDOL-2-YL) PENTYL 4-NITROBENZENESULFONATE.....	251
8.21 <sup>19</sup> F NMR AND ACCURATE MASS SPECTRA OF N <sup>5</sup> -(1-((CARBOXYMETHYL)AMINO)-3-((1-(5-FLUOROPENTYL)-2,5-DIOXOPYRROLIDIN-3-YL)THIO)-1-OXOPROPAN-2-YL)GLUTAMINE .....	252
8.22 <sup>1</sup> H NMR SPECTRA OF 5-(1,3-DIOXO-1,3,3A,4,7,7A-HEXAHYDRO-2H-4,7-EPOXYISOINDOL-2-YL) PENTYL 4-METHYL-BENZENESULFONATE .....	254
8.23 <sup>1</sup> H AND <sup>13</sup> C NMR SPECTRA OF (2-METHYL-3-(TRIMETHYLSILYL)CYCLOPROP-2-EN-1-YL)METHANOL ( <b>31</b> ).....	255
8.24 <sup>1</sup> H AND <sup>13</sup> C NMR SPECTRA OF 2-(METHYLCYCLOPROP-2-EN-1-YL)METHYL (4-NITROPHENYL) CARBONATE ( <b>33</b> ).....	256
8.25 <sup>1</sup> H NMR SPECTRA OF N-(((2-METHYLCYCLOPROP-2-EN-1-YL)METHOXY)CARBONYL)MANNOSAMINE TETRAACETATE ( <b>36</b> ) AC <sub>4</sub> MANCCP .....	257

## LIST OF FIGURES

- FIGURE 1. PET TRACERS ROUTINELY USED FOR DETECTION AND MONITORING TREATMENT RESPONSE OF CANCER. .... 6
- FIGURE 2. THE STRUCTURE OF PHOSPHATIDYLETHANOLAMINE (LEFT) AND THE NEGATIVELY CHARGED PHOSPHATIDYLSERINE (RIGHT). ONE OF THE FATTY ACIDS REPRESENTED BY THE R SUBSTITUENT GROUPS IS OFTEN STEARIC ACID AND THE OTHER IS OFTEN AN UNSATURATED FATTY ACIDS: OLEIC ACID (C<sub>18</sub> MONOUNSATURATED), ARACHIDONIC ACID (C<sub>20</sub> TETRAUNSATURATED) OR DOCOSAHEXAENOIC ACID (C<sub>22</sub> HEXAUNSATURATED).<sup>107,108</sup> ..... 11
- FIGURE 3. FOUR REPRESENTATIVE TRACERS FOR IMAGING CELL DEATH. FROM LEFT TO RIGHT: (A) [<sup>99m</sup>Tc]ANNEXIN-HYNIC- V, A GOLD STANDARD IN PRE-CLINICAL STUDIES THAT FAILED CLINICAL TRIALS; (B) [<sup>18</sup>F]ICMT-11, WHICH FAILED TO SHOW A CORRELATION BETWEEN UPTAKE AND POSITIVE TREATMENT RESPONSE; (C) [<sup>18</sup>F]ML-10 AND (D) [<sup>18</sup>F]C-SNAT, BOTH SHOWED GUT UPTAKE, HEPATOBILIARY AND RENAL EXCRETION THUS LIMITING THEIR APPLICATION TO UPPER BODY CANCERS (E.G. BREAST, NECK, BRAIN); ..... 13
- FIGURE 4. (A) C2AM PROTEIN NMR SOLUTION STRUCTURE. THE BLUE ARROW INDICATES THE MUTATED SITE AT POSITION 78, OPPOSITE TO THE BINDING SITE IN ORDER TO MINIMISE EFFECTS ON AFFINITY FOR PS, WHERE SERINE HAS BEEN REPLACED BY A CYSTEINE RESIDUE TO ENABLE CONJUGATION WITH MALEIMIDE PROSTHETIC GROUPS. (B) AMINO ACID REPRESENTATION OF THE BINDING SITE. THE THREE GREEN SPHERES REPRESENT Ca<sup>2+</sup> IONS COORDINATED BY ASPARTATE RESIDUES. <sup>142</sup> ..... 16
- FIGURE 5. SCHEMATIC OF THE MEDISO NANOSCAN PET DETECTOR: A POSITRON-EMITTING ISOTOPE (RADIATION WARNING TREFOIL) GENERATES A POSITRON (B<sup>+</sup>) PARTICLE WHICH UPON ANNIHILATION WITH AN ELECTRON SITUATED IN THE NEAR PROXIMITY PRODUCES TWO 511 KEV GAMMA PHOTONS (WAVY BLACK ARROWS) AT 180° WITH RESPECT TO EACH OTHER. A STATIC CIRCULAR ARRAY OF DETECTORS (BLACK RECTANGLE = CRYSTAL ARRAYS, NUMBERED BOXES = PMT), DETECTS THE TWO OPPOSING  $\gamma$  PHOTONS AS A COINCIDENCE EVENT (RED RECTANGLES). THIS IS THEN

PROCESSED BY THE COINCIDENCE UNIT WHICH WILL RECONSTRUCT THE TRAJECTORY OF THESE PHOTONS THUS DETERMINING THE SPATIAL POSITION OF THE SOURCE..... 18

FIGURE 6. DIFFERENT TYPES OF COINCIDENCES. TRUE COINCIDENCE OCCURS WHEN THE TWO GAMMA PHOTONS FOLLOWING AN ANNIHILATION PROCESS END UP EXCITING TWO DETECTORS OPPOSITE EACH OTHER ( $180^\circ$ ). SCATTERED COINCIDENCE OCCURS DUE TO CHANGE OF TRAVEL DIRECTION OF ONE OF THE GAMMA PHOTONS DUE TO INTERACTION WITH SURROUNDING ELECTRONS (COMPTON EFFECT). AS A RESULT, THE GENERATED LOR IS MISLEADING AS IT DOES NOT CONTAIN THE SITE OF ANNIHILATION. A RANDOM COINCIDENCE OCCURS WHEN TWO DIFFERENT ANNIHILATION SITES EMIT GAMMA PHOTONS THAT REACH DETECTORS WITHIN THE COINCIDENCE TIME LEADING TO THE FORMATION OF AN ERRONEOUS LOR BETWEEN THEM. THE STATIC CIRCULAR ARRAY OF DETECTORS (BLACK RECTANGLE = CRYSTAL ARRAYS, NUMBERED BOXES = PMT), DETECTS THE TWO OPPOSING  $\gamma$  PHOTONS AS COINCIDENCE EVENTS (RED RECTANGLES).<sup>149</sup> ..... 18

FIGURE 7. ELECTRON-POSITRON ANNIHILATION DIAGRAM. POSITRON (RED) TRAVELS  $\sim 1$  MM AND ANNIHILATES WITH AN ELECTRON (BLUE) TO GENERATE TWO 511 KEV GAMMA PHOTONS AT  $\sim 180^\circ$  TO EACH OTHER. GAMMA PHOTONS ARE DETECTED BY OPPOSING DETECTORS COMPOSED OF A CRYSTAL ARRAY (BLACK RECTANGLES) AND A PHOTOMULTIPLIER TUBE (WHITE BOX). LINE OF RESPONSE VOLUME IS HIGHLIGHTED IN YELLOW. .... 19

FIGURE 8. ACQUISITION USING 2D (A) AND 3D (B). IN 2D MODE, COLLIMATORS LIMIT GAMMA PHOTONS ACCESS TO SCINTILLATORS REDUCING THE LOR TO ADJACENT RINGS. IN THE 3D MODE, DETECTORS CAN BE REACHED BY ANY GAMMA PHOTON. DETECTORS ARE COMPOSED OF COLLIMATORS (BLUE LINES; A) A CRYSTAL ARRAY (BLACK RECTANGLES; A&B) AND A PHOTOMULTIPLIER TUBE (WHITE BOX A&B).<sup>150</sup> ..... 19

FIGURE 9. PET ACQUISITION AND RECONSTRUCTION DETECTOR MODES. 1-1 MODE MEANS THAT 1 DETECTOR IS ACCEPTING COINCIDENCE EVENTS FROM JUST 1 OPPOSING DETECTOR. A 1-3 MODE MEANS 1 DETECTOR ACCEPTS COINCIDENCES FROM 3 ADJACENT AND OPPOSING DETECTORS. FOR EXAMPLE DETECTOR 0 ACCEPTS COINCIDENCES FROM 5,6 AND 7. 1-5 MODE MEANS THAT 1 DETECTOR ACCEPTS COINCIDENCES FROM 5 OPPOSING DETECTORS. ACQUISITION AND RECONSTRUCTION



CAN BE DONE IN THREE DIFFERENT MODES: 1-1, 1-3 AND 1-5. THIS DIRECTLY AFFECTS SENSITIVITY, THE HIGHER THE MODE THE HIGHER THE SENSITIVITY. NOTABLY, RAW DATA INCREASES SIGNIFICANTLY UPON USING A HIGH DETECTOR MODE. PICTURE TAKEN FROM THE MEDISO NANOSCAN PET MANUAL. ....20

FIGURE 10. COMPARISON BETWEEN PET AND TIME-OF-FLIGHT PET IMAGING. THE STATIC CIRCULAR ARRAY OF DETECTORS (BLACK RECTANGLE = CRYSTAL ARRAYS, NUMBERED BOXES = PMT), DETECTS THE TWO OPPOSING  $\gamma$  PHOTONS AS COINCIDENCE EVENTS (RED RECTANGLES), LOR (YELLOW BACKGROUND), GREY BARS REPRESENT THE PROBABILITY OF CONTAINING THE INITIAL ANNIHILATION EVENT AND ITS LOCATION WITHIN THE LOR. IN THE CASE OF TOF-PET, THE HIGHER THE GREY BAR THE HIGHER THE PROBABILITY. ADAPTED FROM VANDENBERGHE ET AL.<sup>152</sup> .....22

FIGURE 11. SCHEMATIC OF THE LATEST MEDISO ANYSCAN TRIO GAMMA CAMERA SPECT SCANNER. GAMMA PHOTONS (WAVY BLACK LINES) ARE COLLIMATED TO A NAI(TL) THALIIUM DOPED SODIUM IODIDE CRYSTAL, SIGNAL BEING PICKED-UP AND AMPLIFIED BY PHOTOMULTIPLIER TUBES AND CONVERTED TO AN ELECTRICAL SIGNAL. THE IMAGE IS THEN RECONSTRUCTED FOR ANALYSIS. THE SCANNER HAS THE CAPABILITY TO USE MULTI MODAL IMAGING BY COMBINING THREE DIFFERENT MODALITIES IN ONE SCANNER. IT HAS THE POSSIBILITY TO COMBINE SPECT, CT AND PET ALL IN ONE SCANNER.<sup>158</sup> .....25

FIGURE 12. EXAMPLES OF  $^{18}\text{F}$ -LABELLED MALEIMIDES FOR PROTEIN THIOL LABELLING AND ALSO THE STRUCTURE OF  $^{18}\text{F}$ SFB INTERMEDIATE FOR THE SYNTHESIS OF  $^{18}\text{F}$ FBEM. ....37

FIGURE 13. PRECURSORS ARRANGED IN THE ORDER THAT WERE CONSIDERED FOR  $^{18}\text{F}$ -FLUORINATION IN THIS STUDY. COMPOUNDS **1** AND **3** ARE PRECURSORS FOR  $^{18}\text{F}$ FBEM, **2** FOR  $^{18}\text{F}$ FPPD, **4** FOR 2- $^{18}\text{F}$ FLUOROETHYLAZIDE AND **5** FOR  $^{18}\text{F}$ FPENM. ....42

FIGURE 14. SYNTHESIS OF ETHYL 4-FLUOROBENZOATE HPLC STANDARD **28** .....44

FIGURE 15. AZIDO SULFONATE PRECURSORS SYNTHESIS.....44

FIGURE 16. THREE PROTECTED MALEIMIDE PRECURSORS SYNTHESISED IN THIS STUDY...45

FIGURE 17. SUPERIMPOSED UV-VIS (200 TO 400 NM) SPECTRA OF <b>16</b> (1 mM AND 0.5 mM) AND GSH (1 mM). <b>16</b> ABSORBS LIGHT AT 300 NM WHILE GSH DOES NOT. ....	48
FIGURE 18. PLOT SHOWING 1/ <b>16</b> CONCENTRATION WITH TIME FOLLOWING CONJUGATION WITH GSH AT PH 7.27 AND 24.8 °C. INITIAL CONCENTRATION OF <b>16</b> = GSH = 0.625 MM .....	49
FIGURE 19. PLOT SHOWING 1/ <b>16</b> CONCENTRATION WITH TIME FOLLOWING CONJUGATION WITH GSH AT PH 7.19 AND 24.8 °C. INITIAL CONCENTRATION OF <b>16</b> = GSH = 1.25 MM .....	50
FIGURE 20. PLOT SHOWING 1/ <b>16</b> CONCENTRATION WITH TIME FOLLOWING CONJUGATION WITH GSH AT PH 6.58 AND 24.7 °C INITIAL CONCENTRATION OF <b>16</b> = GSH = 2.5 MM .....	50
FIGURE 21. RADIO-CHROMATOGRAMS OF 4 SAMPLES POST ADVION SYNTHESIS OF [ <sup>18</sup> F]SFB STARTING FROM IODONIUM PRECURSOR <b>1</b> . THE RADIO-CHROMATOGRAMS SHOW: <sup>18</sup> F-FLUORIDE ONLY ( <b>A</b> ); THEN REACTION MIXTURES HEATED AT 180 °C ( <b>B</b> ), 190 °C ( <b>C</b> ) AND 160 °C ( <b>D</b> ).....	53
FIGURE 22. <sup>18</sup> F-FLUORINATION OF PRECURSOR <b>3</b> . RADIO-CHROMATOGRAM ( <b>A</b> ) SHOWING ESTER <b>20</b> ELUTING AT 12.1MIN (PEAK 4). UV CHROMATOGRAM ( <b>B</b> ) SHOWING UV ABSORBANCE (254 NM) OF THE CRUDE <sup>18</sup> F-FLUORINATION REACTION TO YIELD <b>20</b> (PEAK 8 AT 11.8 MIN). UV CHROMATOGRAM ( <b>C</b> ) SHOWING UV ABSORBANCE (254 NM) OF THE CRUDE <sup>18</sup> F-FLUORINATION REACTION TO YIELD <b>20</b> CO-INJECTED WITH ETHYL 4-FLUOROBENZOATE STANDARD <b>28</b> (PEAK 9 AT 11.8 MIN).....	56
FIGURE 23. GE TRACERLAB FX <sub>FN</sub> MODIFIED TO MIMIC A GE TRACERLAB FX <sub>N</sub> PRO (DUAL REACTOR) AUTOMATED SYNTHESIZER. PICTURE SHOWING REACTOR 1 (BLUE ARROW – LEFT) AND REACTOR 2 (RED ARROW - RIGHT) .....	57
FIGURE 24. GE HEALTHCARE TRACERLAB FX <sub>FN</sub> CONTROL SCREEN SHOWING THE DEFAULT LINE CONNECTIONS. THESE WERE MODIFIED TO ACCOMMODATE AN EXTERNAL REACTOR AS DESCRIBED IN THE TEXT. ....	58
FIGURE 25. HPLC ANALYSIS OF DISTILLED 2- <sup>18</sup> F]FLUOROETHYLAZIDE. ....	60

- FIGURE 26. RADIO-HPLC CHROMATOGRAM OF THE CRUDE CLICK REACTION BETWEEN 2-<sup>[18F]</sup>FLUOROETHYL AZIDE AND C2AM-PEG<sub>4</sub>-DBCO. THE PEAK AT 11.8 MIN IN THE RADIOCHROMATOGRAM **A** IS THE <sup>18</sup>F-LABELLED C2AM. CHROMATOGRAM **B** (UV 280NM) SHOWS C2AM-PEG<sub>4</sub>-DBCO AS A MIX OF STEREOISOMERS **26** AND **27** AT 11.4 MIN..... 60
- FIGURE 27. THREE RADIO-CHROMATOGRAMS SHOWING <sup>18</sup>F-LABELLING OF PRECURSORS: TOSYLATE **14** (**A**), MESYLATE **5** (**B**), **25** (**C**) TO YIELD THE FURAN PROTECTED MALEIMIDE **23**. PEAK AT 2.3 MIN REPRESENTS UNREACTED K<sup>[18F]</sup>F AND PEAK AT 9.5 MIN REPRESENTS <sup>18</sup>F-FLUORINATED MALEIMIDE **23**. ..... 62
- FIGURE 28. VALIDATION OF <sup>[18F]</sup>FPENM RADIOSYNTHESIS. RADIOCHROMATOGRAM **A** SHOWS <sup>[18F]</sup>FPENM ELUTING AT AT 10.2 MIN. CHROMATOGRAM **B** REPRESENTS THE UV TRACE OF RADIOTRACER <sup>[18F]</sup>FPENM AND PEAK 2 AT 9.7 MIN DISPLAYING THE FPENM RESIDUAL PEAK. CHROMATOGRAM **C** DISPLAYS THE SPIKED SAMPLE (SHOWN IN **B**) WITH FPENM HPLC STANDARD (PEAK 2 AT 9.7 MIN). ..... 66
- FIGURE 29. RADICAL FORMATION AND POLYMERISATION OF *N*-ALKYL MALEIMIDES AS DESCRIBED BY ZOTT AND HEUSINGER<sup>240</sup> AND KAGIYA *ET AL.*<sup>242</sup> ..... 67
- FIGURE 30. RADIO-HPLC CHROMATOGRAM OF THE CRUDE <sup>[18F]</sup>FPENM AS ELUTED FROM THE AUTOMATED TRACERLAB FX<sub>FN</sub> SYNTHESIS RIG. THE CHROMATOGRAM SHOWS **24** AT 7.3 MIN WITH 81% RADIOCHEMICAL PURITY. .... 68
- FIGURE 31. RADIO-HPLC CHROMATOGRAM OF THE C18 SEP-PAK CARTRIDGE-PURIFIED <sup>[18F]</sup>FPENM. THE CHROMATOGRAM SHOWS **24** (7.3 MIN, > 95% RADIOCHEMICAL PURITY) AS IT WAS READY TO BE CONJUGATED TO C2AM. .... 69
- FIGURE 32. UV-HPLC (210NM) CHROMATOGRAM OF PRODUCTS ELUTED FROM THE FIRST THREE METHODS USING C18 SEP-PAK LIGHT CARTRIDGES (**A**, **B**, **C** CORRESPOND TO METHODS 1, 2, 3 - SEE TABLE 6). PEAK AT 5.5 MIN IS AN IMPURITY, POTENTIALLY 5-(*N*-MALEIMIDO)PENTANOL. METHOD 3 SHOWN IN CHROMATOGRAM **C** DID NOT SHOW THE PRESENCE OF THIS PARTICULAR IMPURITY HENCE IT WAS SELECTED AS THE OPTIMUM CARTRIDGE PURIFICATION METHOD..... 70
- FIGURE 33. IONISING RADIATION CAUSING WATER RADIOLYSIS YIELDING HIGHLY REACTIVE RADICALS, IONS AND HYDROGEN PEROXIDE. (ADAPTED FROM LOUSADA *ET AL.*)<sup>247</sup> .. 74

FIGURE 34. RADIOCHROMATOGRAMS OF [<sup>18</sup>F]FPENM. **B** (NO ASCORBIC ACID ADDED) SHOWS MULTIPLE PEAKS HAVE APPEARED (15 MINS POST FORMULATION) DESPITE HPLC PURIFICATION AND FORMULATION. **A** (ADDITION OF 1 MG/M<sub>L</sub> ASCORBIC ACID) SHOWS SIGNIFICANTLY LESS SIDE-PRODUCT FORMATION (15 MINS POST FORMULATION). ..... 75

FIGURE 35. HPLC CHROMATOGRAM OF REDUCED C2AM-SH. CHROMATOGRAM SHOWS THE UV ABSORBANCE AT 280 NM OF C2AM PEAK 2 AT 11.6 MIN. PEAK 1 AT 3.7 MIN ARE PRESUMABLY AGGREGATES OF C2AM. PEAK 3 (37.9 MIN) IS DUE TO THE HPLC SOLVENT SYSTEM CHANGE AT 20 MIN. .... 77

FIGURE 36. HPLC CHROMATOGRAM OF THE CRUDE MICHAEL-ADDITION REACTION BETWEEN **24** AND C2AM-SH YIELDING [<sup>18</sup>F]FPENM-C2AM. RADIOCHROMATOGRAM **A**: [<sup>18</sup>F]FPENM-C2AM IS THE FIRST PEAK (12.7 MIN), PEAK 5 (38.7 MIN) IS UNREACTED **24**. CHROMATOGRAM **B** SHOWS THE UV ABSORBANCE AT 280 NM: THE FIRST PEAK IS [<sup>18</sup>F]FPENM-C2AM (11.8 MIN), PEAK 2 REPRESENTS TRACES OF ASCORBIC ACID (14.8 MIN), THE FINAL PEAK (37.9 MIN) IS DUE TO THE HPLC SOLVENT SYSTEM CHANGE AT 20 MIN. CHROMATOGRAMS **C** AND **D** ARE EXPANDED CHROMATOGRAMS **A** AND **B** RESPECTIVELY FOCUSED ON THE [<sup>18</sup>F]FPENM-C2AM PEAK. .... 78

FIGURE 37. QC CHROMATOGRAM OF PURE [<sup>18</sup>F]FPENM-C2AM. RADIOCHROMATOGRAM (**A**) REPRESENTS THE RADIODETECTOR TRACE AND SHOWED [<sup>18</sup>F]FPENM-C2AM ELUTION AT 12.8 MIN. CHROMATOGRAM **B** REPRESENTS THE UV (280 NM) TRACE AND SHOWED ABSORBANCE OF REDUCED C2AM PROTEIN AT 11.9 MIN AND 12.1 MIN (FPENM-C2AM). THE PEAK AT 36 MIN IS THE SOLVENT FRONT DUE TO THE SOLVENT SYSTEM CHANGE AT 20 MIN. PEAKS 1, 2 AND 3 ARE PROBABLY CAUSED BY DIMERIZATION OF UNLABELLED C2AM (DISULPHIDE BOND FORMATION) AND HYDROPHOBIC INTERACTIONS PROMOTED AGGREGATION HENCE THE MULTIPLE PEAKS..... 79

FIGURE 38. QC CHROMATOGRAM OF PURE [<sup>18</sup>F]FPENM-C2AM WITH ADDED (SPIKED) FPENM-C2AM HPLC STANDARD. CHROMATOGRAM **A** REPRESENTS THE RADIODETECTOR TRACE AND SHOWED [<sup>18</sup>F]FPENM-C2AM ELUTION AT 12.8 MIN. CHROMATOGRAM **B** REPRESENTS THE UV (280 NM) TRACE AND SHOWED ABSORBANCE OF REDUCED C2AM PROTEIN AT 11.9 MIN AND 12.2 MIN (FPENM-

C2AM). CHROMATOGRAM **C** REPRESENTS THE UV (280 NM) TRACE AND SHOWED ABSORBANCE OF REDUCED C2AM PROTEIN AT 11.8 MIN AND 12.1 MIN (FPENM-C2AM SPIKED WITH FPENM-C2AM HPLC STANDARD HENCE THE INCREASED PEAK). THE PEAK AT 36 MIN IS THE SOLVENT FRONT DUE TO THE SOLVENT SYSTEM CHANGE AT 20 MINUTES..... 79

FIGURE 39. [<sup>18</sup>F]FPENM-C2AM ANALYSED ON A UPLC ULTIMATE 3000 USING A GE SUPERDEX 75 (300 MM) ANALYTICAL COLUMN. TOP CHROMATOGRAM (UV 280 NM CHANNEL) SHOWS 2 PEAKS SEPARATING OXIDISED C2AM FROM C2AM AND [<sup>18</sup>F]FPENM-C2AM. THE FIRST SMALL PEAK INCREASES WITH TIME, CONFIRMING OXIDATION AND DIMERIZATION OF C2AM WITH TIME SHOWN IN FIGURE 40..... 80

FIGURE 40. SAME [<sup>18</sup>F]FPENM-C2AM SAMPLE AS SHOWN IN FIGURE 39 INJECTED AGAIN AFTER 24 HOURS AT ROOM TEMPERATURE. ANALYSED ON A UPLC ULTIMATE 3000 USING A GE SUPERDEX 75 (300 MM) ANALYTICAL COLUMN. UV CHROMATOGRAM (280 NM CHANNEL) SHOWS MULTIPLE PEAKS SEPARATING AGGREGATES (PEAK 1, 20% AREA), OXIDISED C2AM (PEAK 2, 40% AREA) FROM CONJUGATED C2AM (FPENM-C2AM, 40% AREA) SEEN AS PEAK 3. CHROMATOGRAMS COURTESY OF DR ANDRÉ NEVES..... 81

FIGURE 41. UV CHROMATOGRAMS SHOWING OXIDATION OF FRESHLY REDUCED C2AM AND THEN SUBSEQUENT REDUCTION USING DTT. CHROMATOGRAM **A**: DIMERIZATION OF C2AM WAS ACCELERATED BY THE ADDITION OF CuCl<sub>2</sub> (50 mM) TO CONFIRMING THAT PEAK 1 AT 3.2 MIN IS THE OXIDISED C2AM. CHROMATOGRAM **B**: REDUCTION OF OXIDISED C2AM FROM CHROMATOGRAM **A** USING DTT (20 mM, 4 MIN) SHOWED COMPLETE REDUCTION OF PROTEIN. CHROMATOGRAM **C**: EXPANSION OF CHROMATOGRAM **B** TO ALLOW OBSERVATION OF THE REDUCED PROTEIN PEAK 1 AT 4 MIN, THE LARGE PEAK AT 8.2 MIN REPRESENTS DTT. CHROMATOGRAMS COURTESY OF DR ANDRÉ NEVES..... 82

FIGURE 42. PET/CT SCAN OF A NAP-5 CARTRIDGE (COLUMN VOLUME 8.3 mL) USED FOR [<sup>18</sup>F]FPENM-C2AM PURIFICATION, WITH 2.71 MBQ ACTIVITY LEFT ON THE CARTRIDGE. THE TRANSVERSE PLANE (BOTTOM RIGHT PICTURE) CLEARLY SHOWS SIGNIFICANT ACTIVITY (IN RED) ON THE LOADING AND ELUTING FRITS. MAXIMUM-INTENSITY-PROJECTION (TOP LEFT), CORONAL (TOP RIGHT) AND SAGITTAL (BOTTOM

LEFT) PLANES ALSO CONFIRM THE PRESENCE OF ACTIVITY MAINLY IN THE PLASTIC FRITS. PET IMAGES PALETTE SHOWN: SOKOLOV..... 83

FIGURE 43. [<sup>18</sup>F]FPENM-C2AM RADIOTRACER STABILITY TEST IN PBS AT 37 °C (BLACK 5 MIN, PINK 1 H AFTER INCUBATION AT 37 °C). PEAK AT 13.1 MIN IS [<sup>18</sup>F]FPENM-C2AM RADIOTRACER. C2AM CONCENTRATION WAS 1 mM. SENSITIVITY OF THE RADIODETECTOR WAS INCREASED BEFORE ANALYSING THE 1-HOUR SAMPLE TO COMPENSATE FOR DECAY AND TO ENABLE PEAK OBSERVATION ALONG WITH OTHER POTENTIAL DECOMPOSITION PRODUCTS. .... 84

FIGURE 44. [<sup>18</sup>F]FPENM-C2AM RADIOTRACER STABILITY IN PBS AT 37 °C: BLACK 2 H, BLUE 3 H AFTER INCUBATION IN PBS AT 37 °C. PEAK AT 13.2 MIN IS [<sup>18</sup>F]FPENM-C2AM RADIOTRACER. C2AM CONCENTRATION WAS 1 mM. .... 84

FIGURE 45. STABILITY OF [<sup>18</sup>F]FPENM-C2AM IN A SOLUTION OF BOVINE SERUM ALBUMIN (BSA). RADIO HPLC CHROMATOGRAM (A) SHOWING [<sup>18</sup>F]FPENM-C2AM AT 13.1 MIN FOLLOWING INCUBATION IN BSA AT 37 °C FOR 1 H. UV TRACE (B) RECORDED AT 280 NM SHOWS BSA PEAK 1 AT 7.5 AND PEAK 2 AT 8.4 MIN FOR THE 2 H INCUBATION. C2AM CONCENTRATION WAS 1 mM..... 85

FIGURE 46. STABILITY OF [<sup>18</sup>F]FPENM-C2AM IN A SOLUTION OF BOVINE SERUM ALBUMIN (BSA). RADIO HPLC CHROMATOGRAM (A) SHOWING [<sup>18</sup>F]FPENM-C2AM FOLLOWING INCUBATION IN BSA AT 37 °C (BLACK 2 H, BLUE 3 H). UV TRACE (B) RECORDED AT 280 NM SHOWS BSA PEAK 1 AT 7.5 AND PEAK 2 AT 8.4 MIN FOR THE 3 H INCUBATION. IN THE RADIOCHROMATOGRAM (A) A PEAK APPEARS AT 8.9 MIN (14% AREA) SUGGESTING A PRODUCT OF AGGREGATION OF BSA AND [<sup>18</sup>F]FPENM-C2AM OR A METABOLITE. C2AM CONCENTRATION WAS 1 mM. .... 86

FIGURE 47. ADVION NANOTEK MODULAR AUTOMATED SYNTHESISER IN A LEAD SHIELDED HOT CELL. .... 105

FIGURE 48. SCHEMATIC OF THE ARRANGEMENT OF PUMPS, LINES AND VALVES ON AN ADVION NANOTEK..... 106

FIGURE 49. GE HEALTHCARE TRACERLAB FX<sub>FN</sub> WINDOWS XP CONTROL SCREEN. IT ALLOWS MANUAL CONTROL OVER EACH VALVE AND AUTOMATED CONTROL THROUGH PRE-PROGRAMMED MACROS CONTROLLING VALVES, HPLC AND GAS FLOW. .... 108

FIGURE 50. HPLC OF [<sup>18</sup>F]FPENM SHOWING THE RADIOCHROMATOGRAM. PEAK 4 AT 10.1 MINUTES REPRESENTS [<sup>18</sup>F]FPENM..... 112

FIGURE 51. SCHEMATIC DIAGRAM OF A FLOW CYTOMETER. CELLS FLOW IN A SINGLE FILE THROUGH A FLOW CHAMBER WHERE A SET OF PERPENDICULAR LASER LIGHT BEAMS PASSES THROUGH. THE OPTICAL PROPERTIES OF CELLS ARE DETECTED BY ANALYSING SCATTERED INCIDENT LIGHT. DETECTORS SUCH AS FORWARD-, SIDE-SCATTER AND OTHER FLUORESCENT OPTICAL DETECTORS (OPTICAL MIRRORS AND FILTERS SELECTIVELY ALLOW THE PASSAGE OF LIGHT OF DIFFERENT WAVELENGTHS) CONVERT THE LIGHT INTO ELECTRICAL SIGNALS WHICH ARE THEN INTERPRETED BY DEDICATED SOFTWARE (E.G. BD FACSDIVA). SCHEMATIC ADAPTED FROM CREATIVE DIAGNOSTICS – FLOW CYTOMETRY GUIDE.<sup>259</sup>..... 116

FIGURE 52. HISTOGRAMS A (CONTROL) AND B (TREATED WITH MEDI3039 10 pM) SHOW SIGNIFICANTLY INCREASED SYTOX<sup>®</sup> GREEN NUCLEAR STAIN EMISSION (530 NM) UPON TREATMENT (OVERLAY OF 3 REPLICATES). HISTOGRAMS C (CONTROL) AND D (TREATED) SHOW SIGNIFICANT REDUCTION OF NADH AUTOFLUORESCENCE (450NM) UPON TREATMENT (OVERLAY OF 3 REPLICATES). SCATTER PLOTS E (CONTROL) AND F (TREATED) SHOWING RECTANGULAR GATES WHICH SPLIT THE CELL POPULATION INTO VIABLE CELLS, APOPTOTIC CELLS AND NECROTIC CELLS BY PLOTTING NADH AUTOFLUORESCENCE AGAINST SYTOX<sup>®</sup> GREEN FLUORESCENCE..... 120

FIGURE 53. SCATTER PLOTS SHOWING SYTOX<sup>®</sup> GREEN (50 nM) STAINED MDA-MB-231-D CONTROL CELLS (LEFT) AND TREATED CELLS (RIGHT) WITH MEDI3039 (5 pM). RECTANGULAR GATES SPLIT THE CELL POPULATION INTO VIABLE CELLS, APOPTOTIC CELLS AND NECROTIC CELLS BY PLOTTING NADH AUTOFLUORESCENCE (EMISSION AT 450 NM) AGAINST SYTOX<sup>®</sup> GREEN FLUORESCENCE (EMISSION AT 530 NM)..... 121

FIGURE 54. SCATTER PLOTS SHOWING COLO205-D CELL VIABILITY (BY NADH UV AUTOFLUORESCENCE AT 450 NM) AND CELL MEMBRANE INTEGRITY (SYTOX<sup>®</sup> GREEN EMISSION AT 530 NM) OF CONTROL (LEFT PLOT) AND CELLS TREATED WITH 5 pM MEDI3039 (RIGHT PLOT)..... 122

FIGURE 55. PLOTS SHOWING EXTENT OF CELL DEATH UPON MEDI3039 TREATMENT OF THE TWO CANCER CELL TYPES. PLOT **A** SHOWS THE AVERAGE % OF EVENTS IDENTIFIED AS CELLS; **B** SHOWS THE AVERAGE % OF VIABLE CELLS. **C** THE AVERAGE % OF APOPTOTIC CELLS; **D** THE AVERAGE % OF NECROTIC CELLS. DATA ARE MEAN ± SEM (N = 3, PER

GROUP AND THE ERROR BARS LIE WITHIN THE SYMBOLS WHEN NOT VISIBLE). STATISTICAL ANALYSIS WAS PERFORMED USING UNPAIRED TWO-TAILED T TEST WITH WELCH'S CORRECTION. (\*P<0.05, \*\*P<0.005, \*\*\*P<0.0005, \*\*\*\*P<0.0001); TT = TREATED CELLS..... 123

FIGURE 56. BINDING OF [<sup>18</sup>F]FPENM-C2AM TO CONTROL AND MEDI3039-TREATED (10 pM) OF MDA-MB-231-D CELLS. THE AVERAGE % OF TOTAL ACTIVITY RETAINED BY THE CELL PELLET IS SHOWN. STATISTICAL ANALYSIS WAS PERFORMED USING A PAIRED TWO-TAILED T TEST (\*\*P<0.005). AVERAGE RATIO BETWEEN CONTROL AND TREATED, SIGNAL TO BASELINE RATIO (SBR) WAS 4.3±0.6. DATA ARE MEAN ± SEM (N = 3, PER GROUP)..... 128

FIGURE 57. LABELLING OF MEDI3039-TREATED AND CONTROL MDA-MB-231-D CELLS WITH DIFFERENT CONCENTRATIONS OF [<sup>18</sup>F]FPENM-C2AM. PLOTS SHOW THE % OF TOTAL ACTIVITY RETAINED PER MILLION CELLS FOR EACH OF THE FIVE [<sup>18</sup>F]FPENM-C2AM CONCENTRATIONS..... 128

FIGURE 58. LABELLING OF MEDI3039-TREATED (5 pM) AND CONTROL COLO205-D CELLS WITH DIFFERENT CONCENTRATIONS OF [<sup>18</sup>F]FPENM-C2AM. PLOTS SHOWING THE % OF ACTIVITY RETAINED PER MILLION CELLS OUT OF THE TOTAL ACTIVITY ADDED FOR EACH OF THE FIVE [<sup>18</sup>F]FPENM-C2AM CONCENTRATIONS. THE PLOT ALSO SHOWS THE BINDING RATIO FOR TREATED AND UNTREATED CELLS FOR EACH [<sup>18</sup>F]FPENM-C2AM CONCENTRATION. DATA ARE MEAN ± SEM (N = 2, PER GROUP)..... 129

FIGURE 59. BIODISTRIBUTION PROFILE OF [<sup>18</sup>F]FPENM-C2AM IN CONTROL AND (MEDI3039, 0.4 MG/KG) TREATED BALB/C NU/NU MICE BEARING COLO205-D TUMOURS. AN UNPAIRED ONE-TAILED T-TEST SHOWED A SIGNIFICANT DIFFERENCE BETWEEN CONTROL AND TREATED TUMOUR (P=0.0006); CONTROL AND TREATED STOMACH (P=0.0022). DATA ARE MEAN ± SEM (N = 3, PER GROUP; THE ERROR BARS LIE WITHIN THE SYMBOLS WHEN NOT VISIBLE); (NS >0.05, \*P<0.05, \*\*P<0.005, \*\*\*P<0.0005)..... 136

FIGURE 60. TUMOUR-TO-MUSCLE AND TUMOUR-TO-BLOOD RATIOS IN CONTROL AND TREATED (MEDI3039, 0.4 MG/KG, I.V.) COLO205-D XENOGRAFT TUMOUR BEARING BALB/C NU/NU MICE. UNPAIRED TWO-TAILED T-TESTS WITH WELCH'S CORRECTION SHOWED SIGNIFICANT DIFFERENCES (\*\*P<0.01) BETWEEN TUMOUR-TO-MUSCLE AND



TUMOUR-TO-BLOOD RATIOS BETWEEN CONTROL AND TREATED. DATA ARE MEAN  $\pm$  SEM (N = 3, PER GROUP)..... 137

FIGURE 61. PET/CT IMAGING PROTOCOL PIPELINE AND THE TIMES ASSOCIATED WITH EACH PROCESS. END-OF-BOMBARDMENT TO SCANNER TIME WAS LESS THAN TWO HOURS (APPROXIMATELY THE FLUORINE-18 HALF-LIFE OF 109.7 MINUTES)..... 138

FIGURE 62. CELL DEATH IMAGING USING [<sup>18</sup>F]FPENM-C2AM. SAGITTAL PET/CT IMAGES OF A REPRESENTATIVE TUMOUR-BEARING MOUSE (FIRST COHORT N = 3), BEFORE (**AT**) AND 24 HOURS AFTER MEDI3039 TREATMENT (0.4 MG/KG, I.V.) (**BT**). IMAGING WAS PERFORMED 2 HOURS AFTER THE ADMINISTRATION OF [<sup>18</sup>F]FPENM-C2AM (0.23 UG/G, 4.9–6 MBQ, I.V.). TUMOUR (T), LIVER (LI) AND KIDNEY (K) ARE SHOWN. PET IMAGE PALETTE USED: NIH FIRE. (IMAGE COURTESY OF DR ANDRÉ NEVES) ..... 139

FIGURE 63. AVERAGE %ID/G OF [<sup>18</sup>F]FPENM-C2AM (**A**: 4.6 MG AND **B**: 9.2 MG) INJECTED I.V. IN A COHORT OF (**A**: N=3 AND **B**: N=2) NU/NU MICE BEARING COLO205-D TUMOURS THAT WERE TREATED WITH MEDI3039 (**A**: 0.4 MG/KG AND **B**: 0.2 MG/KG, I.V.) AND IMAGED USING THE PET/CT PROTOCOL OVER A 3-DAY PERIOD. ORGANS WERE COLLECTED FOR BIODISTRIBUTION, WEIGHED AND COUNTED ON DAY THREE AFTER 2 HOURS OF DYNAMIC PET IMAGING. KIDNEY UPTAKE DEMONSTRATED A GOOD CLEARANCE WITH LOW RETENTION (**A**: 6.2 $\pm$ 0.5 AND **B**: 7.9 $\pm$ 0.1 %ID/G). DATA ARE MEAN  $\pm$  SEM (ERROR BARS LIE WITHIN THE SYMBOLS WHEN NOT VISIBLE)..... 141

FIGURE 64. TIME ACTIVITY CURVES FOR [<sup>18</sup>F]FPENM-C2AM POST-TREATMENT, SHOWN AS TUMOUR-TO-MUSCLE RATIO (LEFT) AND KIDNEY AND LIVER CLEARANCE (RIGHT). THE TUMOUR UPTAKE PEAKED AT 20 MINUTES FOLLOWING INJECTION, WITH SUBSEQUENT CLEARANCE. AFTER ONE HOUR OF ADMINISTRATION, THE TUMOUR-TO-MUSCLE RATIO INCREASED THUS GENERATING TUMOUR-MUSCLE CONTRAST (GREY LINE, LEFT PLOT) IN THE RANGE OF 4 TO 6-FOLD (N = 5). KIDNEY UPTAKE PEAKED AT 20 MINUTES POST INJECTION, WITH SUBSEQUENT CLEARANCE OF >90% WITHIN 2 HOURS. LIVER UPTAKE PEAKED AT 10 MINUTES POST INJECTION, WITH EFFICIENT CLEARANCE AFTERWARDS. ALL DATA HAS BEEN DECAY-CORRECTED. (FIGURES COURTESY OF DR ANDRÉ NEVES) ..... 142

FIGURE 65. HISTOLOGY SAMPLES STAINED WITH CLEAVED CASPASE-3 (CC3). GALLBLADDER (GB)/LIVER (LI) LEFT AND SMALL INTESTINE (SI) ON THE RIGHT. MINIMAL CC3 STAINING PRESENT WAS PROBABLY DUE TO SLOW PREPARATION OF

HISTOLOGICAL SPECIMENS AND THE FACT THAT THE SMALL INTESTINE EPITHELIAL CELLS HAVE A HIGH PROLIFERATION AND CELL DEATH RATE.<sup>279</sup> ..... 143

FIGURE 66. SAGITTAL PET/CT IMAGES OF [<sup>18</sup>F]FPENM-C2AM IN THE SAME MOUSE BEARING A COLO205D TUMOUR (WHITE ARROW) 24 HOURS BEFORE (TOP ROW) AND 24 HOURS AFTER TREATMENT (LOWER ROW) WITH MEDI3039 (0.4 MG/KG). TUMOUR UPTAKE 24 HOURS AFTER MEDI3039 DRUG ADMINISTRATION (LOWER ROW) STARTS TO INCREASE 1-HOUR POST INJECTION. PET PALETTE USED: NIH FIRE. IMAGES COURTESY OF DR ANDRÉ NEVES. .... 143

FIGURE 67. MAXIMUM INTENSITY PROJECTION PET/CT IMAGES 2 HOURS POST [<sup>18</sup>F]FPENM-C2AM INJECTION IN A COLO205D TUMOUR-BEARING MOUSE THE TUMOUR (WHITE ARROW) AND GALLBLADDER (WHITE CHEVRON) ARE INDICATED. IMAGES WERE ACQUIRED 24 HOURS BEFORE (LEFT IMAGE) AND 24 HOURS AFTER TREATMENT WITH MEDI3039 (0.4 MG/KG) (RIGHT IMAGE). IMAGES COURTESY OF DR ANDRÉ NEVES. .... 144

FIGURE 68. HISTOLOGY STAINING OF TUMOURS WITH HEMATOXYLIN AND EOSIN (HE), CLEAVED CASPASE-3 (CC3) AND TERMINAL DEOXYNUCLEOTIDYL TRANSFERASE dUTP NICK END LABELLING (TUNEL). IMAGES COURTESY OF DR ANDRÉ NEVES. .... 145

FIGURE 69. RADIOCHROMATOGRAM (A) AND UV CHROMATOGRAM (B) OF THE PROSTHETIC GROUP [<sup>18</sup>F]FPENM PRIOR TO C2AM CONJUGATION. THE ABSORBANCE OF THE PROSTHETIC GROUP IN THE UV (AT 210 NM) IS MINIMAL DUE TO THE LACK OF AROMATICITY OF THE *N*-ALKYLMALEIMIDE (<sup>18</sup>F]FPENM) MOLECULE. .... 147

FIGURE 70. RADIOCHROMATOGRAM (A) OF CRUDE [<sup>18</sup>F]FPENM-C2AM SOLUTION PRIOR TO DESALTING (USING A NAP-5 CARTRIDGE). PEAK #1 WAS THE [<sup>18</sup>F]FPENM-C2AM CONJUGATE, WHICH ELUTES AT 12.6 MIN; PEAK #2 WAS A DEGRADATION BY-PRODUCT OF [<sup>18</sup>F]FPENM AT 22.4 MIN AND PEAK #3 WAS UNREACTED [<sup>18</sup>F]FPENM AT 38.5 MIN. UV 280 NM CHROMATOGRAM (B) SHOWING THE [<sup>18</sup>F]FPENM-C2AM CONJUGATE PEAK #1 AT 11.7 MIN, PEAK #2 REPRESENTING ASCORBIC ACID ADDITIVE AT 14.8 MIN, PEAKS #3 AND #4 CAUSED BY THE SOLVENT SYSTEM CHANGING FROM 100% PBS TO 10% MECN IN PBS AND THE NEW SOLVENT FRONT REACHING THE DETECTOR. THE ESTIMATED CONVERSION YIELD OF THE CONJUGATION REACTION WAS >91%. NOTE THAT THE UV DETECTOR IS LOCATED UPSTREAM OF THE RADIODETECTOR IN THE

HPLC SYSTEM, GENERATING A DIFFERENCE IN MEASURED RETENTION TIMES OF CA.  
0.8 MIN..... 148

FIGURE 71. UV AND RADIOCHROMATOGRAM OF >99% PURE [<sup>18</sup>F]FPENM-C2AM CONJUGATE. PEAK #1 ELUTING AT 12.8 MIN RADIOCHROMATOGRAM (TOP) REPRESENTS [<sup>18</sup>F]FPENM-C2AM AFTER NAP-5 COLUMN PURIFICATION AND WAS USED FOR *IN VIVO* BIODISTRIBUTION STUDIES. PEAK #1 IN THE UV 280 NM CHROMATOGRAM (BOTTOM) ELUTING AT 11.9 MIN REPRESENTS THE CONJUGATED C2AM. PEAK #2 AT 36 MINUTES AND PEAK #3 AT 37.9 MIN ARE CAUSED BY THE SOLVENT SYSTEM CHANGING FROM 100% PBS TO 10% ME CN IN PBS THUS THE NEW SOLVENT FRONT REACHING THE DETECTOR AS PEAK #2 AND #3..... 149

FIGURE 72. RADIOCHROMATOGRAM (A) AND UV (B) OF FRACTION 3 ELUTED FROM NAP-5 SIZE EXCLUSION COLUMN. PEAK #1 ELUTING AT 16.5 MIN IN THE UV 280 NM CHROMATOGRAM (B) REPRESENTS ASCORBIC ACID, PEAK #2 AT 37.9 MIN WAS CAUSED BY THE SOLVENT SYSTEM CHANGING FROM 100% PBS TO 10% ME CN IN PBS THUS THE NEW SOLVENT FRONT REACHING THE DETECTOR..... 149

FIGURE 73. QC CHROMATOGRAM OF PURE [<sup>18</sup>F]FPENM-C2AM WITH ADDED (SPIKED) FPENM-C2AM HPLC STANDARD. CHROMATOGRAM A REPRESENTS THE RADIODETECTOR TRACE AND SHOWED [<sup>18</sup>F]FPENM-C2AM ELUTION AT 12.8 MIN. CHROMATOGRAM B REPRESENTS THE UV (280 NM) TRACE AND SHOWED ABSORBANCE OF REDUCED C2AM PROTEIN AT 11.9 MIN AND 12.2 MIN (FPENM-C2AM). CHROMATOGRAM C REPRESENTS THE UV (280 NM) TRACE AND SHOWED ABSORBANCE OF REDUCED C2AM PROTEIN AT 11.8 MIN AND 12.1 MIN (FPENM-C2AM SPIKED WITH FPENM-C2AM HPLC STANDARD HENCE THE INCREASED PEAK). THE PEAK AT 36 MIN IS THE SOLVENT FRONT DUE TO THE SOLVENT SYSTEM CHANGE AT 20 MINUTES..... 151

FIGURE 74. RADIOCHROMATOGRAM OF >99% PURE [<sup>18</sup>F]FPENM-C2AM CONJUGATE (TOP) AND UV 280 NM CHROMATOGRAM OF [<sup>18</sup>F]FPENM-C2AM CONJUGATE (BOTTOM). PEAK #1 SHOWN AT 12.7 MIN IN RADIOCHROMATOGRAM (A) REPRESENTS [<sup>18</sup>F]FPENM-C2AM AFTER NAP-5 COLUMN PURIFICATION AND USED FOR *IN VIVO* PET IMAGING. PEAK #1 ON THE UV 280 NM CHROMATOGRAM (B) AT 12.2 MIN REPRESENTS THE REDUCED C2AM. PEAKS ELUTING BETWEEN 6 AND 8 MINUTES ARE PROBABLY AGGREGATION OF DIMERIC C2AM. .... 152

FIGURE 75. MOST COMMON MONOSACCHARIDES THAT ARE COMPONENTS OF GLYCANS IN VERTEBRATES. FIGURE ADAPTED FROM VARKI <i>ET AL.</i> <sup>285</sup> (2009) .....	155
FIGURE 76. MAIN CLASSES OF GLYCANS IN MAMMALIAN CELLS. SCHEMATIC ADAPTED FROM PINHO AND REIS (2015). <sup>44</sup> .....	156
FIGURE 77. MASS SPECTROMETRIC ANALYSIS OF <i>N</i> -GLYCANS IN TWO COLORECTAL CANCER CELL LINES. ABERRANT SIALYLATION AND HYPER BRANCHING (BI-, TRI- AND TETRA-ANTENNARY) WAS OBSERVED IN THE COLO320 CELL LINE. COLO205 CELLS EXHIBIT <i>N</i> -LINKED GLYCANS WITH EXCESSIVE FUCOSYLATION AND HYPER BRANCHING (BI-, TRI- AND TETRA-ANTENNARY). IMAGE ADAPTED FROM HOLST <i>ET AL.</i> <sup>295</sup> .....	158
FIGURE 78. DIAGRAM SHOWING METABOLIC LABELLING OF GLYCANS. PERACETYLATED METHYLCYCLOPROPENE MANNOSAMINE (AC <sub>4</sub> MANNCCp) IS TAKEN UP (BY PASSIVE DIFFUSION AND/OR ENDOCYTOSIS) BY CELLS. UPON INTERNALISATION MONOMERIC AC <sub>4</sub> MANNCCp IS DEACETYLATED (MANNOSAMINE CONVERTED TO NEURAMINIC ACID) <sup>302</sup> , ACTIVATED AND INCORPORATED INTO GLYCANS IN THE GOLGI APPARATUS (PURPLE LAMELLAR ASSEMBLY) AS A NEURAMINIC ACID. LABELLED GLYCANS (CONTAINING THE NON-NATURAL SUGAR – RED DISCS) ARE EITHER <i>N</i> -LINKED OR <i>O</i> -LINKED TO PROTEINS (GREEN) AND LIPIDS (BLUE DISCS) AND EXPORTED TO THE CELL SURFACE. ....	160
FIGURE 79. STRUCTURE OF AC <sub>4</sub> MANNCYC AND AC <sub>4</sub> MANNAZ USED BY THE DEVARAJ LAB. ....	163
FIGURE 80. THE CHEMICAL STRUCTURE OF THREE METHYLCYCLOPROPENE MODIFIED MONOSACCHARIDES. ....	164
FIGURE 81. THE CHEMICAL STRUCTURE OF Tz-PEG <sub>11</sub> -DYLIGHT649. ....	168
FIGURE 82. A 3-DAY PROTOCOL FOR METABOLIC LABELLING OF COLO205-D CELLS WITH <b>36</b> (100 μM) AND THEN WITH Tz-PEG <sub>11</sub> -DYLIGHT649 (5 μM, 660 NM) AND MONITORED FOR CELL NECROSIS WITH SYTOX GREEN (50 nM, 530 NM). ON DAY 3, CELLS WERE HARVESTED AND LABELLED WITH Tz-PEG <sub>11</sub> -DYLIGHT649 (5 μM). Tz-PEG <sub>11</sub> -DYLIGHT649 AND SYTOX GREEN (50 nM) CELL FLUORESCENCE WAS ANALYSED BY A BD LSR II FLOW CYTOMETER. ....	168

FIGURE 83. FIGURE SHOWING CONTROLS FOR DMSO (RED), COLO205-D CELLS AUTOFLUORESCENCE (BLUE), FACS BUFFER (ORANGE) AND FACS BUFFER-WASHED CELLS LABELLED WITH SUGAR <b>36</b> (LIGHT GREEN). TZ-PEG <sub>11</sub> -DYLIGHT649 (5 μM) TREATED CELLS ARE ALSO SHOWN: COLO205 CONTROL CELLS (DARK GREEN) AND CELLS LABELLED WITH PERACETYLATED SUGAR <b>36</b> (100 μM, YELLOW). .....	169
FIGURE 84. SCATTER PLOTS OF COLO205-D CONTROL (NO SUGAR, LEFT) AND SUGAR <b>36</b> (100 μM) LABELLED CELLS (RIGHT) LABELLED WITH TZ-PEG <sub>11</sub> -DYLIGHT649 (5 μM) AND SYTOX GREEN (50 nM) FOR 20 MINUTES AT 37 °C.....	170
FIGURE 85. HISTOGRAM PLOT (BELOW) OF COLO205-D CONTROL (NO SUGAR) AND SUGAR <b>36</b> (100 μM) TREATED CELLS (RIGHT) DERIVATISED WITH TZ-PEG <sub>11</sub> -DYLIGHT649 (5 μM) AND SYTOX GREEN (50 nM) FOR 20 MINUTES AT 37 °C. ....	170
FIGURE 86. UNPAIRED MANN-WHITNEY TESTS, SHOWING SIGNIFICANT DIFFERENCE (P = 0.0079, N = 5) BETWEEN COLO205-D CONTROL (NO SUGAR) AND CELLS LABELLED WITH AC <sub>4</sub> MANNCCP (100 μM; 24H) (RIGHT) AFTER TREATMENT WITH TZ-PEG <sub>11</sub> -DYLIGHT649 (5 μM, 20 MIN). VIABILITY DECREASED SIGNIFICANTLY FROM 82 TO 74% (P = 0.0022, N = 6). .....	171
FIGURE 87. OPTIMISATION OF LABELLING TIME WITH TZ-PEG <sub>11</sub> -DYLIGHT649 (5 μM). .....	171
FIGURE 88. OPTIMISATION OF TZ-PEG <sub>11</sub> -DYLIGHT649 CONCENTRATION. ....	172
FIGURE 89. CONFOCAL MICROSCOPY OF FIXED COLO205-D LABELLED WITH PERACETYLATED SUGAR <b>36</b> (100 μM; 24 HOURS) AND LABELLED WITH TZ-PEG <sub>11</sub> -DYLIGHT649 (5 μM; 30 MIN) AND SYTOX GREEN (50 nM; 30 MIN). A) SYTOX <sup>®</sup> GREEN CHANNEL (530 nm), B) mSTRAWBERRY CHANNEL (610 nm), C) DYLIGHT649 CHANNEL (660 nm), D) AN OVERLAY OF ALL THREE AFOREMENTIONED CHANNELS. SCALE BARS = 20 μM.....	173
FIGURE 90. MEAN FLUORESCENCE INTENSITY OF EX-VIVO ORGANS SHOWING NO CONTRAST BETWEEN SUGAR TREATED MICE AND CONTROLS. (N = 5) .....	174
FIGURE 91. COMPARISON OF SBRs OBTAINED WITH SUGAR <b>36</b> DISSOLVED IN DMSO (N = 3) AND SUGAR <b>36</b> DISSOLVED IN PBS (N = 2). A SIGNIFICANT DECREASE IN SBR WAS OBSERVED UPON CHANGING THE DISSOLUTION SOLVENT. (TWO-TAILED WELCH'S T TEST PERFORMED, P = 0.03) .....	175

FIGURE 92. COMPARISON OF SBR UPON COLO205-D LABELLED WITH SUGAR **36** (N = 4, IN DMSO), SUGAR **36** + B-CYCLODEXTRIN (N = 2, 25 MG/M<sub>L</sub> IN PBS) AND SUGAR **36** + B-CYCLODEXTRIN (N = 2, 125 MG/M<sub>L</sub> IN PBS), THEN TREATED WITH Tz-PEG<sub>11</sub>-DYLIGHT649 (5 μM) FOR 1 HOUR AT 37 °C. .... 176

FIGURE 93. FPENM-C2AM HPLC STANDARD- HPLC CHROMATOGRAM - RADIO DETECTOR TOP, 254 NM UV TRACE BOTTOM (PEAK AT 12.183 MIN). C2AM (5 UG, 20 U<sub>L</sub>) PROTEIN WAS INJECTED ON THE COLUMN. .... 234

FIGURE 94. 2. [<sup>18</sup>F]FPENM-C2AM HPLC CHROMATOGRAM - RADIO DETECTOR TOP (PEAK AT 12.797), 254 NM UV TRACER BOTTOM (PEAK AT 11.897 MIN). 20U<sub>L</sub> OF [<sup>18</sup>F]FPENM-C2AM (1.85 UG, 4 MBQ) WAS INJECTED ON THE COLUMN. .... 235

## LIST OF ABBREVIATIONS AND ACRONYMS

Abbreviation	Name
<b><sup>18</sup>F-FAZA</b>	[ <sup>18</sup> F]fluoroazomycin arabinose; radiotracer used for PET imaging hypoxic tumours
<b>[<sup>18</sup>F]FBABM</b>	<i>N</i> -(4-((4-[ <sup>18</sup> F]Fluorobenzylidene)aminooxy)butyl)maleimide
<b>[<sup>18</sup>F]FBAM</b>	4-((4-[ <sup>18</sup> F]fluorobenzylidene)aminooxybutyl)maleimide
<b>[<sup>18</sup>F]FBEM</b>	<i>N</i> -[2-(4-[ <sup>18</sup> F]fluorobenzamido)ethyl]maleimide
<b>[<sup>18</sup>F]FBSEM</b>	<i>N</i> -[2-(4-[ <sup>18</sup> F]fluoro- <i>N</i> -methylbenzenesulfonamido)ethyl]maleimide
<b><sup>18</sup>F-FDG</b>	2-[ <sup>18</sup> F]fluoro-D-deoxyglucose; radiotracer used for PET imaging of glucose uptake – Warburg effect
<b>[<sup>18</sup>F]FMISO</b>	[ <sup>18</sup> F]fluoromisonidazole – tracer for determining tumour hypoxia using PET
<b>[<sup>18</sup>F]FPenM</b>	<i>N</i> -(5-[ <sup>18</sup> F]fluoropentyl)maleimide – radioactive functional group used for labelling of free thiol proteins
<b>[<sup>18</sup>F]FPenM-C2Am</b>	Radiotracer for monitoring cell death used in this study representing the C2Am protein conjugated with [ <sup>18</sup> F]FPenM prosthetic group through a thiol ether bond.
<b>[<sup>18</sup>F]FPPD</b>	1-(4-[ <sup>18</sup> F]fluorophenyl)pyrrole-2,5-dione
<b>[<sup>18</sup>F]FPyME</b>	1-[3-(2-[ <sup>18</sup> F]fluoropyridine-3-yloxy)propyl]pyrrole-2,5-dione
<b><sup>18</sup>F-ICMT-11</b>	( <i>S</i> )-1-((1-(2-[ <sup>18</sup> F]fluoroethyl)-1 <i>H</i> -[1,2,3]-triazol-4-yl)methyl)-5-(2(2,4-difluorophenoxy)methyl)-pyrrolidine-1-sulfonyl)isatin; radiotracer used for PET imaging of cell death by labelling activation of caspase-3
<b><sup>18</sup>F-ML-10</b>	2-(5-[ <sup>18</sup> F]fluoropentyl)-2-methyl malonic acid; radiotracer used for PET imaging of cell death by labelling acidification of cell surface post exposure of phosphatidylserine <sup>1</sup>
<b><sup>18</sup>F-SFB</b>	<i>N</i> -hydroxysuccinimidyl para-[ <sup>18</sup> F]fluorobenzoate
<b>Ac<sub>4</sub>ManNAz</b>	tetra- <i>O</i> -acetyl <i>N</i> -azidoacetylmannosamine
<b>ACN / MeCN</b>	acetonitrile
<b>AF649/AF647</b>	Alexa Fluor® 649 or 647 – fluorescent dye
<b>A<sub>m</sub></b>	molar activity – the amount of radioactivity (measured in MBq) per total amount of compound (measured in μmol); MBq/μmol
<b>AMG</b>	automatic gamma counter
<b>A<sub>s</sub></b>	specific activity – the measured amount of radioactivity (measured in MBq) per total amount of compound; MBq/μg or GBq/mg

<b>ATP</b>	adenosine triphosphate
<b>boc</b>	<i>tert</i> -butyloxycarbonyl amine protecting group
<b>CC3</b>	cleaved caspase-3
<b>cGMP</b>	current good manufacturing practice
<b>CT</b>	computed tomography
<b>CTC</b>	circulating tumour cells
<b>ctDNA</b>	circulating tumour deoxyribonucleic acid
<b>DA<sub>inv</sub></b>	inverse electron demand Diels-Alder reaction
<b>DBCO</b>	dibenzocyclooctyne
<b>DCM</b>	dichloromethane
<b>dd</b>	doublet of doublets
<b>DEA</b>	diethylamine
<b>DIFO</b>	difluorocyclooctyne
<b>DIPEA</b>	<i>N,N</i> -diisopropylethylamine
<b>DMB</b>	4,5-Methylenedioxy-1,2-phenylenediamine dihydrochloride
<b>DMF</b>	dimethylformamide
<b>DNA</b>	deoxyribonucleic acid
<b>DOTA</b>	1,4,7,10-tetraazacyclododecane-1,4,7,10-tetraacetic acid
<b>DR5</b>	death receptor 5
<b>dt</b>	doublet of triplets
<b>DTPA</b>	pentetic acid or diethylenetriaminepentaacetic acid
<b>EDC</b>	1-ethyl-3-(3-dimethylaminopropyl)carbodiimide
<b>eq.</b>	equivalent
<b>FBP</b>	filtered back-projection
<b>GBq</b>	gigabecquerel
<b>GMP</b>	good manufacturing practice
<b>HBS</b>	HEPES buffered saline



<b>H&amp;E</b>	hematoxylin and eosin
<b>HER2</b>	human epidermal growth factor receptor 2
<b>HOMO</b>	highest occupied molecular orbital
<b>HPLC</b>	high performance liquid chromatography
<b>HYNIC</b>	hydrazinonicotinamide
<b>i.v.</b>	intra-venous
<b>IORT</b>	intraoperative radiotherapy
<b>K<sub>222</sub></b>	Kryptofix 222 – cryptand 222 for potassium complexation
<b>keV</b>	kiloelectronvolt (unit of energy)
<b>LOR</b>	line of response – in PET imaging represents the path between two detectors along which resides the radioactive source
<b>LUMO</b>	lowest unoccupied molecular orbital
<b>m</b>	multiplet
<b>MBq</b>	megabecquerel
<b>MeV</b>	megaelectron-volt
<b>Min</b>	minutes
<b>MRI</b>	magnetic resonance imaging
<b>MS</b>	mass spectrometry
<b>MWCO</b>	molecular weight cut off
<b>NEMA</b>	National Electrical Manufacturers Association
<b>Neu5Ac</b>	<i>N</i> -acetylneuraminic acid
<b>Neu5Gc</b>	<i>N</i> -glycolylneuraminic acid
<b>NHS</b>	<i>N</i> -hydroxysuccinimide
<b>NIRF</b>	near infra-red fluorescent
<b>NOTA</b>	1,4,7-triazacyclononane-1,4,7-trisacetic acid
<b>ns</b>	nanosecond
<b>PBS</b>	phosphate-buffered saline
<b>PE</b>	phosphatidylethanolamine

<b>PET</b>	positron emission tomography
<b>ppm</b>	parts per million
<b>PS</b>	phosphatidylserine
<b>ps</b>	picosecond
<b>PTEN</b>	phosphatase and tensin homolog
<b>QMA</b>	quaternary methyl ammonium
<b>r.t.</b>	retention time
<b>R<sub>f</sub></b>	retention factor
<b>RT</b>	room temperature
<b>s</b>	singlet or second
<b>SFB</b>	<i>N</i> -succinimidyl 4-fluorobenzoate
<b>SBR</b>	signal-to-baseline ratio
<b>SPAAC</b>	strain promoted azide-alkyne cycloaddition
<b>SPE</b>	solid phase purification
<b>SPECT</b>	single-photon emission computed tomography
<b>SUV</b>	Standard uptake value
<b>TCO</b>	<i>trans</i> -cyclooctene
<b>TFA</b>	trifluoroacetic acid
<b>THF</b>	tetrahydrofuran
<b>TLC</b>	thin-layer chromatography
<b>TMDIBO</b>	2,3,8,9-tetramethoxy dibenzocyclooctyne
<b>TPHA</b>	tetrapropylammonium hydroxide
<b>TRAIL-R2</b>	tumour necrosis factor (TNF) related apoptosis-inducing ligand receptor 2
<b>TSTU</b>	<i>N,N,N',N'</i> -tetramethyl- <i>O</i> -( <i>N</i> -succinimidyl)uronium tetrafluoroborate
<b>TUNEL</b>	terminal deoxynucleotidyl transferase dUTP nick end labelling
<b>UPLC</b>	ultra-performance liquid chromatography
<b>UV</b>	ultraviolet

# 1 INTRODUCTION

Since 1990 the incidence rate of cancer has gone up by 13%.<sup>2</sup> Despite this alarming increase, non-invasive anticancer therapy assessment is still based on a rather slow process: measurements of decreased tumour size or altered metabolism. Monitoring whether these changes are clinically significant can require weeks. Meanwhile, not only do patients undergo extensive toxic anticancer therapy that could prove ineffective, but the healthcare system is also burdened. Hence it is imperative for clinicians to have access to a non-invasive, fast technique to assess the efficacy of anticancer therapies.<sup>3</sup>

## 1.1 Cancer – a worldwide disease

Cancer is one of the leading causes of mortality worldwide, with 8.2 million deaths and 14.1 million new diagnoses reported in 2012. In the UK, more than 350,000 new cases were reported in 2015 and 160,000 lives were lost to cancer in 2016.<sup>4</sup> Despite the high number of cancer-related deaths and an ever-increasing number of diagnosed patients, cancer survival rates have improved dramatically over the last decades. For example, the 2013 Office for National Statistics UK Report shows that since 2000, the 5-year survival rates for prostate and lung cancer have increased from 59.8% to 81.7% and from 5.5% to 11% respectively.<sup>5,6</sup> Overall, in the past 40 years, cancer survival rates have doubled from 25% to 50% according to Cancer Research UK.<sup>2</sup>

Breast cancer survival rates have doubled in the last 40 years; 78% of women with breast cancer will survive 10 years or more according to the latest Cancer Research UK statistics (2010-2011).<sup>7</sup> A similar trend has been observed in the case of colon cancer.

Despite incidence rates remaining the same throughout the last 30 years, with approximately 41,700 new cases every year, 10-year survival rates have almost doubled, since the early 1970s, reaching 57% in 2010-11. Survivability statistics have improved over the decades but colon cancer is still the 2<sup>nd</sup> most common cause of cancer death in the UK in 2016, with more than 16,000 deaths.<sup>8</sup>

Considerable effort has been made to introduce novel anticancer therapies that make a difference to patients' survival and quality of life. In the case of prostate cancer, the 5-year survival rate increased from 25% to 84% in the last 40 years. This success could be attributed, in part, to the use of the prostate-specific antigen (PSA) blood test. The test could indicate the potential presence of prostate cancer from an early stage. This, in turn, if addressed promptly, can lead to an improvement of the 5-year survival rate.<sup>9</sup> However, the PSA blood test is controversial, as it lacks specificity: 3 out of 4 men with raised PSA levels do not have cancer. Moreover, it also has low sensitivity, as it fails to detect the presence of cancer in 15% of cases, making it a less than ideal cancer detection method.<sup>10</sup>

Since 1990, more than 100 new molecular entities (NMEs) were approved by the Food and Drug Administration (FDA) for use in oncology.<sup>11,12</sup> These can be categorised either as growth factor inhibitors (e.g. trastuzumab)<sup>13</sup>, angiogenesis inhibitors blocking vascular endothelial growth factors (e.g. bevacizumab<sup>14,15</sup>, sunitinib<sup>16</sup> – binds to VEGFs), apoptosis-inducing drugs (e.g. MEDI3039<sup>17</sup> – TRAIL-R2 agonist) and lately immunotherapies (e.g. pembrolizumab – anti PD-1<sup>18,19</sup>; atezolizumab<sup>20,21</sup> – anti PD-L1).<sup>22</sup> One of the first FDA approved growth factor inhibitors, trastuzumab, proved to be particularly effective in a type of invasive breast cancer by targeting the overexpression of proteins generated by the *HER2* oncogene. This oncogene is present in 30% of breast cancer cases.<sup>23</sup> Despite this novel targeting agent, breast cancer can become resistant to trastuzumab. This can happen in two ways: either through a mutation where the cell loses the tumour suppressor function of PTEN or by developing a truncated form of the HER2 receptor (p95HER2) that trastuzumab does not bind to. However, a second line of therapy based on a small molecule inhibitor, lapatinib, can be used.<sup>24</sup>

In 2018 alone, the FDA approved 24 new drugs for oncological use<sup>25</sup> and 62 novel applications for previously approved drugs.<sup>26</sup> All of these have been granted following thorough and lengthy clinical trials where patients were subjected to the therapies for weeks before the outcome could be assessed. It follows that the need for a non-invasive

imaging tool that allows early assessment of treatment efficacy would also be beneficial in the context of clinical trials.<sup>3</sup>

There are also novel technologies that contribute to the fight against cancer. For example, intraoperative electrosurgery using the intelligent Knife (iKnife) can inform the surgeon in real time if the tissue he/she is resecting is cancerous or not. The system works by analysing the vapours from tissue that has been cauterised (electric current to heat the tissue rapidly) using a mass spectrometer.<sup>27</sup> Intraoperative radiotherapy (IORT) that delivers radiation during surgery is another example of technology that contributes to the fight against cancer. Stereotactic radiotherapy such as the Cyber Knife or Gamma knife deliver focused radiation to brain tumours with pinpoint accuracy while minimising radiation dose to adjacent tissue.<sup>28</sup> Moreover, updates of current imaging technologies (in terms of speed, detection resolution and sensitivity) have also had a positive impact in the fight against cancer. For example, a PET scanner with an increased axial field of view (10 times larger than current clinical scanners) was introduced in 2017. This machine has a 40 fold sensitivity gain compared to existing PET scanners and is able to reduce the time required to perform a full body scan from ~20 minutes to less than a minute.<sup>29</sup>

Despite these efforts to introduce novel therapies and technologies, cancer is still the cause of more than a quarter of all deaths in the UK (28% in 2016).<sup>30,31</sup> This is mainly attributed to therapy failing to induce tumour cell death due to the tumours becoming intrinsically resistant to treatment.<sup>24,32</sup> Another major factor that contributes to variable response to therapy is the fact that that tumours are heterogeneous.<sup>3</sup> Liquid biopsies (e.g. circulating tumour DNA<sup>33</sup>, circulating tumour cells<sup>34</sup>), solid tumour biopsies<sup>35,36</sup> and imaging modalities (e.g. [<sup>18</sup>F]FAZA or [<sup>18</sup>F]FMISO PET/CT for monitoring tumour hypoxia levels<sup>37</sup>) have reconfirmed this fact. Tumour heterogeneity also poses increased challenges in assessing the extent to which such tumours respond to treatment. Early detection of tumour heterogeneity post treatment can be used as a predictor of metastatic potential.

Despite considerable technological breakthroughs in the area of cancer detection and ever-increasing diversity of available treatment options, clinicians currently rely on tumour size and altered metabolism to non-invasively assess treatment response in cancer. This is a very slow process: approximately 4-8 weeks are required in order to detect clinically relevant changes in tumour morphology.<sup>38,39</sup> Therefore, the need for early detection of treatment response in cancer is not currently satisfied.

## 1.2 Monitoring of treatment response in cancer

In 1979, The World Health Organisation set out to minimise inconsistencies in reporting the results of tumour response to treatment and published the first standardised report of this kind in 1981.<sup>40,41</sup> Since then, other groups have tried to update these rules, with the most widely used standard to date being RECIST 1.0 (Response Evaluation Criteria in Solid Tumours) published in 2000.<sup>42</sup>

According to RECIST, imaging of cancer response to treatment is based on either an anatomic response (i.e. a decrease in size of the tumour) or a metabolic response (i.e. by monitoring changes in tumour glucose metabolism)<sup>42</sup> Although standardisation and image resolution have been greatly improved over the years, shortcomings such as the extensive time required to observe tumour shrinkage after treatment administration have not yet been overcome.

Anatomic-based tumour treatment response, assessed clinically by computed tomography (CT), can be effectively evaluated at only six to eight weeks post-therapy, according to RECIST 1.0 and 1.1.<sup>42,38</sup> A *partial* response to therapy is categorised as an anatomical decrease in tumour size of at least 30%.<sup>38,39</sup> The latency of this process (partly due to the immune system having to remove apoptotic tumour cells) translates to patients having to receive anti-tumour therapy for weeks without any early indication of its effectiveness. Monitoring of tumour morphology is unable to predict treatment response in real time, meaning that tumours could metastasise while the patient is undergoing ineffective therapy<sup>43</sup>.

Another drawback of monitoring tumour size in order to predict treatment response is the failure to distinguish pseudoprogression from a nonresponder. Pseudoprogression occurs when tumours respond to treatment but initially grow in size due to inflammation caused by accumulation of immune cells. For example, pseudoprogression is encountered in 20% of glioblastoma multiforme cases and if misinterpreted, it can lead to exchange of therapy for a less effective one.<sup>44</sup> Furthermore, there is a subjective human component in assessing the size of lesions. It becomes particularly difficult to keep a consistent diagnosis when tumour shapes are irregular or in cases where an unclear boundary between healthy and tumour tissue occurs.<sup>45</sup>

Another drawback of anatomic based assessment is the lack of a possibility to differentiate between radiotherapy induced inflammation, consolidation (pulmonary

oedema) or benign tumour cavitation (necrotic core that lacks nutrients and oxygenation) in non-small cell lung carcinoma patients treated with bevacizumab (angiogenesis inhibitor).<sup>45,46,47</sup>

Monitoring tumour metabolic response to treatment is an alternative to monitoring tumour anatomic response. This is frequently performed by injecting positron-emitting 2-[<sup>18</sup>F]fluoro-D-deoxyglucose (<sup>18</sup>F-FDG) and imaging its accumulation in glycolytic tumours using Positron Emission Tomography (<sup>18</sup>F-FDG PET).<sup>48,49</sup>

Similarly to RECIST, in 2009, <sup>18</sup>F-FDG PET data has been collated in 2009 in the form of the PERCIST 1.0 (PET Response Criteria in Solid Tumours), a standardised qualitative and quantitative set of imaging guidelines.<sup>50</sup> A successful treatment, according to PERCIST, is usually indicated by a decrease of at least 30% in the standardised uptake value (SUV) compared to pre-treatment scan results. A much higher threshold of 65% is required for lymphomas.<sup>50</sup> Standardised uptake value is a relative measure of radiotracer uptake; it represents the activity concentration ( $r$ ) measured in kBq/ml detected by PET imaging within a specific volume/region of interest (ROI), divided by the injected activity ( $a'$ ) of the radiotracer in kBq divided by weight of the patient ( $w$ ) in grams.

$$\text{SUV} = \frac{r}{a' \times w}$$

The weight is a substitute for volume and it assumes that 1 g is 1 mL; however, some suggest the use of lean body mass for instead of the total weight for <sup>18</sup>F-FDG measurements is more appropriate as fatty tissue uptake is low for this particular tracer. This is also known as the standardized uptake value normalized by lean body mass (SUL) and is used with hydrophilic tracers.

However, imaging metabolic response also has disadvantages. Firstly, <sup>18</sup>F-FDG has low specificity and thus it accumulates in all areas of the body such as liver, kidney and bladder but particularly in the brain and heart. This means that tumour uptake of <sup>18</sup>F-FDG in these areas is not easily quantifiable.<sup>51</sup> Furthermore, radiation-related inflammatory <sup>18</sup>F-FDG uptake (which can occur due to lymphocyte and macrophage accumulation) can lead to a false negative treatment response. One way of minimising this effect is by extending the post-treatment scan to 12 weeks post concurrent chemo-radiotherapy, in order to allow inflammation to clear. In the case of chemotherapy and/or surgery, only a 4 week extension is required.<sup>45</sup>

There are, however, a few examples where monitoring tumour metabolism using  $^{18}\text{F}$ -FDG is desirable. Gastrointestinal stromal cancer treated with Glivec (Imatinib) can be imaged 24 hours post treatment administration.<sup>52</sup> In the case of lymphoma, the effects of therapy can be observed within 72 hours.<sup>53</sup> However, this quick treatment response monitoring is limited to these two particular cancer types.

Other radiotracers have been developed that are specific to certain targets/biomarkers. Figure 1 shows a selection of widely used PET radiotracers for detection and monitoring treatment response of cancers. The selection consists of non-specific (FDG), specific and targeted (PSMA, FAPI, RGD) radiotracers labelled with short half-life (carbon-11, 20.4 min; gallium-68, 67.7 min and fluorine-18, 109.7 min) radioisotopes.

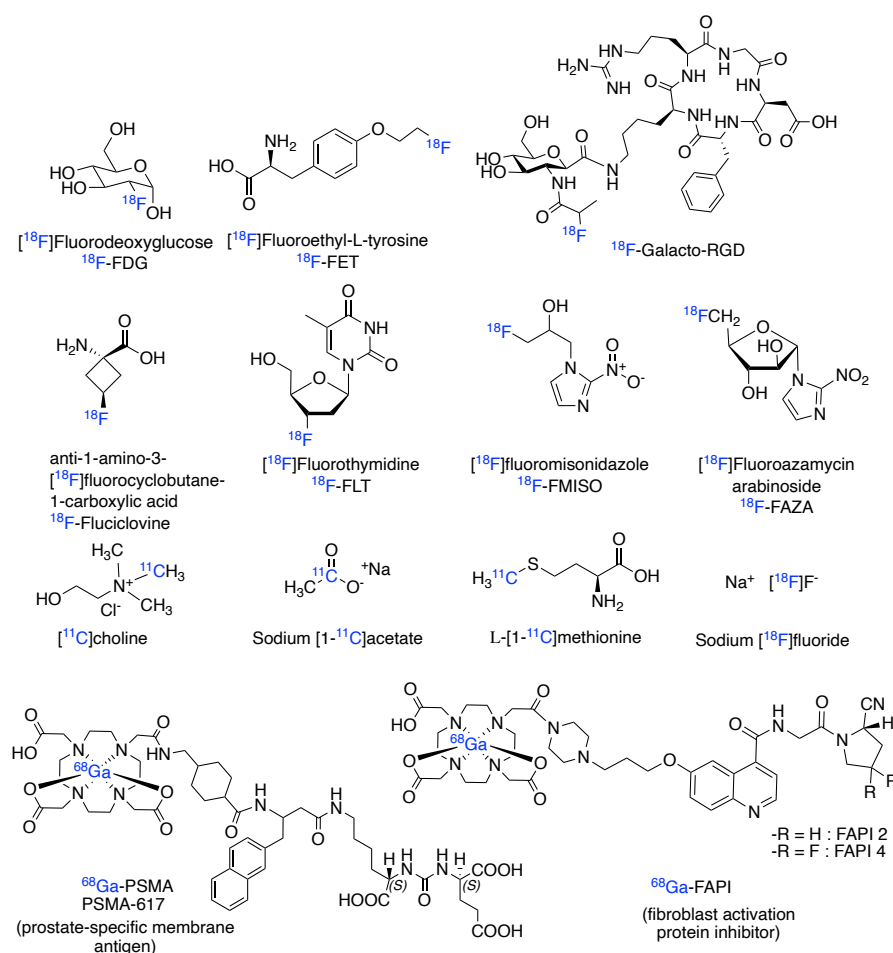


Figure 1. PET tracers routinely used for detection and monitoring treatment response of cancer.

Table 1 summarises the mode of action, clearance and uptake of clinically used radiotracers for the detection of cancer.



Table 1. Selection of PET radiotracers used for detection of cancer

Radiotracer	Mode of action	For PET imaging of	Clearance route/ Uptake organs
<b><sup>18</sup>F-FDG</b>	Non-specific radiotracer. Warburg effect – upregulation of glucose metabolism in cancerous cells results in increased FDG uptake	Majority of cancers (those that are sugar avid) Poor for: high background area (brain), low sugar avid tissue (bronchoalveolar carcinoma, thyroid cancer), no glucose receptors (prostate)	Renal clearance and high uptake in heart and brain.
<b><sup>18</sup>F-FET</b>	Gliomas have upregulated amino acid transporters. <sup>54</sup> <sup>18</sup> F-FET is using the L-amino acid transport system uptake to accumulate in cancerous cells. <sup>18</sup> F-FET is not incorporated into proteins.	Gliomas, lymphoma, intracerebral malignant lymphoma <sup>55,56</sup>	Renal clearance with uptake in liver, kidney and muscle.
<b><sup>18</sup>F-Galacto-RGD</b>	Angiogenesis is the growth of blood supply from pre-existing vessels and it is a key hallmark of cancer. Integrin $\alpha_v\beta_3$ is a transmembrane glycoprotein with a role in proliferation of tumour invasion and metastasis. $\alpha_v\beta_3$ binds to tripeptides such as arginine-glycine-aspartic acid (RGD). <sup>18</sup> F-galacto-RGD is therefore a tracer that used for observing angiogenesis using PET. <sup>57</sup>	Melanoma, late-stage glioblastoma, ovarian, breast cancer, prostate cancer. <sup>58,59</sup>	Renal clearance with uptake in kidney, urogenital tract, liver, spleen and intestine.
<b><sup>18</sup>F-Fluciclovine</b>	Upregulation of human L-type amino acid and alanine-serine-cysteine transporter in carcinomas (prostate cancer included) leads to uptake of <sup>18</sup> F-fluciclovine. Upregulation of these transporters are an indication of aggressive disease. <sup>60,61</sup>	Prostate cancer, carcinomas	Pancreas and liver uptake, some muscle uptake. Clearance is less important as imaging occurs 3-5 minutes post injection. <sup>62</sup>
<b><sup>18</sup>F-FLT</b>	<sup>18</sup> F-FLT is a cellular proliferation tracer. Upon cellular uptake, <sup>18</sup> F-FLT is phosphorylated by thymidine kinase 1 (upregulated in the S phase of mitosis) and trapped as the mono phosphate derivative. Further phosphorylation by thymidylate kinase (TMPK) and nucleotide diphosphate kinase forms triphosphate version. Mono phosphate is then degraded back to FLT by deoxynucleotidase which results in efflux of FLT. ~30% represents triphosphate which remains cytosolic. Since FLT lacks 3'-OH it can't be incorporated into DNA. <sup>63,64</sup>	Gliomas (glioblastoma multiforme, anaplastic astrocytoma) <sup>65</sup>  Gastro-oesophageal cancer but limited due to high background generated by the liver. <sup>66</sup>	Renal clearance, metabolised by liver (glucuronidation) <sup>67</sup>
<b><sup>18</sup>F-FMISO</b>	First tracer to image tumour hypoxia. Nitro group on <sup>18</sup> F-FMISO is reduced to a primary amine in the reducing environment of hypoxic tissue and partly binding covalently to macromolecules intracellularly. <sup>68</sup> Slow tracer accumulation and clearance results in 2-4 hours delay before scanning. <sup>69</sup>	Head and neck, glioma, squamous cell carcinoma, non-small cell lung cancer. <sup>70,71</sup>	Renal clearance with minor uptake in liver, brain and colon. <sup>72</sup>

Targeted Imaging Agents for Detecting Tumour Cell Death following Therapy

Radiotracer	Mode of action	For PET imaging of	Clearance route/ Uptake organs
<b><sup>18</sup>F-FAZA</b>	Same uptake mechanism as <sup>18</sup> F-FMISO however shows faster clearance and better tumour-to-background ratio over <sup>18</sup> F-FMISO.	Multiple studies show uptake in head and neck, high-grade glioma, squamous cell carcinoma, non-small cell lung cancer. No uptake in prostate, lymphoma and limited in cervical cancer. <sup>73</sup>	Renal clearance with uptake in liver, kidneys and muscle <sup>69</sup>
<b>[<sup>18</sup>F]Fluoride</b>	Sodium fluoride uptake by bones as [ <sup>18</sup> F]F <sup>-</sup> ion exchanges with OH <sup>-</sup> from hydroxyapatite to form fluoroapatite High uptake is an indication of increased perfusion associated with bone lesions/bone metastases.	Benign and malignant bone anomalies, bone metastases	Renal clearance; bone uptake <sup>74</sup>
<b>[<sup>11</sup>C]Choline</b>	Upregulation of phosphatidylcholine (PC) synthesis in cancerous tissue consequently increases uptake of [ <sup>11</sup> C]choline.	Neuroblastoma, low and high grade gliomas <sup>75</sup> , prostate (replaced by <sup>68</sup> Ga tracers)	Renal with uptake in kidney and liver predominantly <sup>75</sup>
<b>[<sup>11</sup>C]Acetate</b>	Acetate is a precursor in the biosynthesis pathway of cholesterol and fatty acids. [ <sup>11</sup> C]Acetate highlights increased lipid metabolism associated with cancer.	Primary brain tumours, hepatocellular carcinoma and prostate <sup>76</sup>	Uptake mainly in the pancreas, spleen and liver <sup>76</sup>
<b>L-[1-<sup>11</sup>C]Methionine</b>	High uptake represents increased protein synthesis metabolism in cancerous lesions. Brain uptake of amino acids (AA) is facilitated across the blood-brain-barrier hence can be used for brain cancers. Pitfall: non-specific uptake in non-tumour lesions – ischemic brain tissue (e.g. cranial hyperostosis) <sup>77</sup>	Low-grade gliomas, lymphomas, head & neck and squamous cell carcinoma. <sup>78,79,80,77</sup>	Hepatic and renal clearance. High uptake in liver and pancreas. <sup>81</sup>
<b><sup>68</sup>Ga-PSMA-11 and <sup>68</sup>Ga-PSMA-617</b>	Increased expression of prostate specific membrane antigen (PSMA) in prostate cancer cells compared to other PSMA expressing tissues (kidney, proximal small intestine, salivary glands)	Prostate cancer	Renal excretion with high uptake in kidneys and lacrimal, parotid, submandibular glands. <sup>82,83</sup> Small intestine, liver and spleen show moderate uptake. <sup>84</sup>
<b><sup>68</sup>Ga-FAPI</b>	A cell surface serine protease (fibroblast activation protein—FAP) is upregulated in cancer. Fibroblast activation protein inhibitor is a targeted tracer that binds to FAP highlighting areas within the body with upregulated levels of protein.	Uptake in 28 cancers types: SUV <sub>max</sub> >12 seen in breast, sarcoma, esophageal, cholangiocarcinoma and lung cancer. Average SUV <sub>max</sub> (6-12) in hepatocellular, colorectal, head-and-neck and ovarian carcinoma, pancreatic and prostate cancer. <sup>85</sup> Also used for observing healing tissue heart infarction <sup>86</sup> , liver and lung fibrosis. <sup>85</sup>	Predominantly renal. Healthy tissue shows minimal uptake.

For the past 20 years, short lived radioisotopes such as fluorine-18 and carbon-11 have become increasingly popular for detection of cancer. Recently, the trend for the use of fast labelling kits has been increasing. This method is preferred due to the ability to generate high specific activity, high purity radiotracer in a relatively short time (5-10 minutes). The main advantage of using a kit to produce a radiotracer is its simplicity therefore reducing the burden on the operator and limiting errors. In addition, the required radioisotopes can be obtained on site from a benchtop generator (germanium-68 generators for gallium-68 are readily available) avoiding the need of an expensive cyclotron and synthesis modules.

The use of gallium-68 has increased worldwide due to significant technical breakthroughs in the area of PET imaging of prostate cancer. Radiochemistries were developed to enable chelation of gallium-68 to yield radiotracers such as [ $^{68}\text{Ga}$ ]Ga-PSMA-HBED-CC (known as  $^{68}\text{Ga}$ -PSMA-11)<sup>87,88</sup> which was first used in humans in 2011<sup>89</sup>, followed by [ $^{68}\text{Ga}$ ]Ga-DOTA-PSMA (known as PSMA-617), [ $^{68}\text{Ga}$ ]Ga-PSMA-THP<sup>90</sup> and others.<sup>82,91</sup> The successful chelation chemistry and usage of  $^{68}\text{Ga}$ -PSMA-617 as a radiotracer, in particular, has enabled PSMA to become a theranostic agent. Theranostics, also termed radiotherapeutics, are targeted imaging agents that, besides being labelled with an imaging isotope (e.g. gallium-68 for PET imaging), have a chelate chemistry that also permits facile loading with a radionuclide for radiotherapy that can double as a SPECT imaging agent. Theranostic agents based on radionuclides used for therapy were produced to chelate either  $\alpha$  (e.g. actinium-225) or  $\beta^-$  (e.g. lutetium-177; notably  $^{177}\text{Lu}$ -PSMA-617) emitters.<sup>92,93</sup>

The collective advantages and drawbacks of the aforementioned clinical tracers and imaging methods for measuring tumour treatment response can also shed light on the *desiderata* for an improved imaging method. Firstly, we would like to have a non-invasive imaging method that identifies treatment response within a short period of time – preferably hours – post therapy administration. This is because patients' cancer prognosis would be improved by detecting as early as possible whether the administered anticancer therapy (e.g. chemotherapy, immunotherapy) is effective or not. Early assessment of treatment response would not only reduce the risks of following an ineffective treatment but it would also eliminate the unnecessary side effects caused by a non-beneficial therapy. Early assessment of treatment response would then also lead to a significant reduction of healthcare costs.<sup>3</sup>

Secondly, this imaging method should also reliably identify treatment response irrespective of cancer type and stage, as well as be compatible with any therapy type (chemotherapy, radiotherapy, immunotherapy *etc.*). In this thesis, we suggest that cell death monitoring is an imaging method that encompasses all of the important properties identified above in order to accurately predict therapy outcome.<sup>3</sup>

### 1.3 Targeted cell death imaging as a marker of early treatment response in cancer

Increased levels of tumour cell death have been shown to correlate with higher survivability in breast<sup>94</sup> and cervical cancer<sup>95</sup>. There is a strong correlation between the extent of cell death post treatment and a positive outcome.<sup>96,97</sup> In early treatment of breast cancer, 69% of the responders to chemotherapy showed a 50% increase in apoptotic index (% of apoptotic cells in a biopsy), whereas 75% of the non-responders showed no significant increase of apoptotic index.<sup>98</sup> Therefore, tumour cell death could be used as an indication of therapy outcome. However, currently, no imaging agents that monitor cell death exist in clinical use.<sup>99,100</sup>

The next sections will summarise the essential biological processes and tracers used to image cell death.

#### 1.3.1 Phosphatidylserine, an early stage cell death biomarker

Phosphatidylserine (PS – Figure 2) is a negatively charged phospholipid that is part of the inner leaflet of every cell plasma membrane and has multiple roles; in neuron axon terminals, PS helps synaptic vesicles to bind to the presynaptic membrane in the presence of calcium to initiate exocytosis of neurotransmitter in the synaptic cleft.<sup>101</sup> PS has an important role in blood-clotting by externalising PS in thrombin activated platelets which results macrophage recruitment and fibrin formation.<sup>102</sup> PS also induces membrane curvature, initiates receptor endocytosis, formation of vesicles and most importantly it is an important part of the ‘eat me’ signal, upon cell apoptosis, to activate phagocytes.<sup>103,104,105,106</sup>

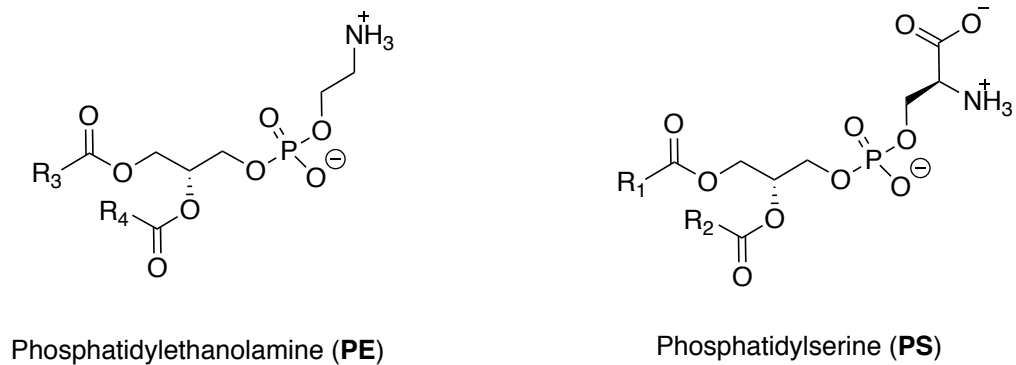


Figure 2. The structure of phosphatidylethanolamine (left) and the negatively charged phosphatidylserine (right). One of the fatty acids represented by the R substituent groups is often stearic acid and the other is often an unsaturated fatty acids: oleic acid (C<sub>18</sub> monounsaturated), arachidonic acid (C<sub>20</sub> tetraunsaturated) or docosahexaenoic acid (C<sub>22</sub> hexaunsaturated).<sup>107,108</sup>

There are two main ways in which cell death can occur following therapy: apoptosis or necrosis. The latter is a non-regulated, energy independent event that is initiated upon permanent disruption of the integrity of the plasma membrane. This can occur through infection, toxins, radiation exposure (radionecrosis), physical intervention (by generating shear stress) or a rapid change in: pH, osmotic pressure or temperature.<sup>109,110</sup>

Apoptosis, on the other hand, is a chain of complex events that lead to an organised breakdown of the cell. It was first characterised by Kerr, Wyllie, and Currie in 1972 as a cascade of events that leads to an energy-dependent controlled cell death.<sup>111</sup> Apoptosis can occur in two ways: via an intrinsic or extrinsic mechanism. The intrinsic pathway is characterised by mitochondrial outer membrane permeabilization which releases cytochrome *c* triggering the formation of the apoptosome which leads to activation of executioner caspase-3 and -7 which leads to apoptosis.<sup>112,113</sup> It can be triggered as a result of DNA damage, aberrant cell-cycle, endoplasmic reticulum stress, hypoxia or metabolic stress. The extrinsic pathway is regulated via the tumour necrosis factor (TNF) receptor superfamily. Upon ligand binding, these receptors crosslink, triggering a p53-independent activation of the caspase cascade that leads to activation of caspase-8 which in turn activates the executioner caspase, caspase-3. This then executes programmed cell death (apoptosis).<sup>112,114</sup>

One morphological event that occurs early during programmed cell death is the exposure of phosphatidylserine (PS) and phosphatidylethanolamine (PE). In healthy cells, flippase enzymes use ATP to actively maintain 96% of PS in the inner leaflet of the cell

membrane. To maintain an equilibrium of phospholipids numbers, an enzyme called floppase uses ATP to flip phosphatidylcholine, sphingolipids and cholesterol against their concentration shifting them from the intracellular to the extracellular space.<sup>115</sup> In apoptotic cells, a third type of enzymes called scramblases become active and rapidly flip phospholipids resulting in exposure of PS on cell surface.<sup>116</sup> The exposure of PS on the cell surface occurs early, prior to membrane permeabilization and blebbing, cell shrinkage, nuclear condensation and DNA degradation. Its role is to initiate phagocytosis (i.e. clearing up of apoptotic cells by macrophages) by triggering the immune system.<sup>117</sup> One important fact is that PS externalisation occurs whenever a cell dies, regardless of how cell death was initiated.

PS is an exceptional biomarker for early indication of cell death. First of all, it only becomes available on the cell surface upon initiation of programmed cell death. Therefore, targeted imaging agents have facile access to PS since they don't have to cross the plasma membrane to reach it. Secondly, PS is an abundant target in apoptotic tumour cells and its tissue concentration has been determined (assuming a 1:1 binding of C2A to PS) in EL4 and MDA-MB-231 to be 277 and 127  $\mu\text{M}$  respectively.<sup>99</sup> Thirdly, it remains present on the cell surface for as long as the apoptotic body is present in the tumour. In addition, treated tumours accumulate necrotic cells that increase the local PS concentration.<sup>118</sup> Since tumours are large and cell death is extensive during therapy, macrophages require time to clear apoptotic and necrotic cells from lesions. This means that there is a wide window for imaging cell death, making PS an ideal candidate to be used as a biomarker for cell death.<sup>100</sup>

Currently, in the clinic, apoptosis can only be identified by biopsy sampling and *ex-vivo* labelling of biomarkers such as cleaved caspase-3 (CC3 – a cytosolic biomarker for late-stage apoptosis). Biopsies are invasive and have risks associated with them: local discomfort, damage to surrounding tissue and increased possibility of infection. Moreover, biopsies are unable to sample the whole tumour and thus heterogeneous areas of cell death might not be identified.<sup>119</sup>

Non-invasive methods such as imaging probes for CC3 are currently being assessed in a clinical setting on breast cancer patients pre- and post-chemotherapy using [<sup>18</sup>F]ICMT-11;<sup>120</sup> however, CC3 is a cytosolic biomarker therefore access to it is challenging due to the need for the imaging agent to cross the plasma membrane. Moreover, CC3 is a transient biomarker, meaning there is only a narrow timeframe when

imaging cell death is possible. This timeframe is characteristic to each cancer type as they respond differently to therapy. Therefore, it is inconvenient to use CC3 as a biomarker for cell death, as it would require further optimisation of the imaging protocol for each cancer type.

### 1.3.2 Imaging cell death – a clinical challenge

Non-invasive imaging of cell death (either through apoptosis or necrosis) following therapy is the end goal of this thesis. No such imaging agents have been approved for routine clinical scans as of today. In what follows, we aim to provide a synopsis of relevant imaging agents, some that failed clinical trials and some that are promising candidates for clinical trials.<sup>100,121</sup>

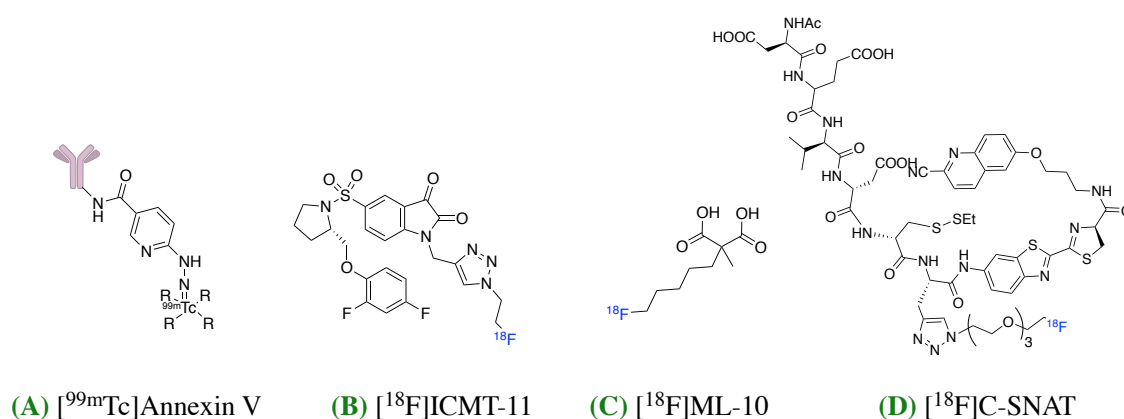


Figure 3. Four representative tracers for imaging cell death. From left to right: (A)  $[^{99m}\text{Tc}]$ Annexin-HYNIC-V, a gold standard in pre-clinical studies that failed clinical trials; (B)  $[^{18}\text{F}]$ ICMT-11, which failed to show a correlation between uptake and positive treatment response; (C)  $[^{18}\text{F}]$ ML-10 and (D)  $[^{18}\text{F}]$ C-SNAT, both showed gut uptake, hepatobiliary and renal excretion thus limiting their application to upper body cancers (e.g. breast, neck, brain);

By far, the most studied agent for detection of cell death is based on a 36 kDa protein named annexin V. It detects cell death by binding to PS as a hexamer with nanomolar affinity. It was introduced in 1998 as a successful non-invasive imaging agent for monitoring cell death in murine models of cardiac transplant rejection, hepatic apoptosis and treated lymphoma.<sup>122</sup> Annexin V quickly became a very popular tool for pre-clinical imaging of cell death following chemo/radiotherapy.<sup>123</sup>

*In vitro* and *in vivo* studies showed promising results for cell death imaging using [<sup>99m</sup>Tc]Annexin V (see Figure 3, **A**) as a SPECT tracer.<sup>124,125,126,127</sup>

Despite being a promising candidate for clinical use, it failed clinical trials II/III due to non-specific binding to organs, slow blood clearance and accumulation in kidneys.<sup>128,129</sup> Despite efforts to improve the specificity of labelling, by the introduction of unique modifiable amino acids by site-directed mutagenesis, and thus its biodistribution, kidney accumulation was still excessively high resulting in the kidney being dosed with high levels of ionising radiation.<sup>130,131</sup>

[<sup>18</sup>F]ICMT-11 (Figure 3, **B**) is a small molecule that crosses the cell membrane and labels cleaved caspase-3 (CC3), which is an alternative cell death biomarker to PS. Despite targeting an intracellular protein, the biodistribution profile of [<sup>18</sup>F]ICMT-11 looked promising for PET/CT clinical translation.<sup>132</sup> In a human study involving treatment of invasive ductal carcinoma (breast cancer), 4 out of 15 patients showed apoptosis dominant signature by PET however only 3 were correlated with the histological assessment by cleaved caspase-3 (the 4<sup>th</sup> patient PET predicted stable disease whereas histology showed partial response). 9 out of 15 showed a necrotic dominant signature by PET and 7 out of these correlated with histological assessment. Finally, 2 out of 15 patients showed no voxel intensity change pre- and post-therapy however tumour localisation was possible with one of the patients and the noted prediction of partial response was confirmed by histology.<sup>120</sup> However, the major drawback of this study is that no patients with progressive disease were studied.

[<sup>18</sup>F]ML-10, known as 2-(5-[<sup>18</sup>F]fluoropentyl)-2-methyl malonic acid (Figure 3, **C**), is a small molecule that targets cell death by crossing the plasma membrane and accumulating in cells showing a characteristic apoptotic membrane imprint.<sup>133</sup> This imprint is defined as activation of membrane phospholipid scrambling, acidification caused by membrane depolarisation, negatively charged phosphatidylserine exposure on the cell surface and irreversible loss of intracellular pH control. [<sup>18</sup>F]ML-10 was first used to label cerebral infarction-associated cell death in 2008, showing a 6-10 fold higher uptake in the affected area compared to background.<sup>133</sup> First in human studies in 2011 showed promising biodistribution, stability, dosimetry (urinary bladder being the limiting organ for dose activity distribution) and renal clearance, with a short plasma half-life of ~1 hour.<sup>1</sup> Multi-centre clinical trials have been underway since then. One clinical trial in China unfortunately showed that there was no significant difference between [<sup>18</sup>F]ML-10



uptake pre- and post- Cyber Knife stereotactic radiotherapy, despite tumours showing a positive treatment response by MRI, 2 to 4 months post radiotherapy.<sup>134</sup> Another problem with this tracer is the optimisation of the imaging protocol. Recently, it was shown in a murine head and neck cell carcinoma xenograft model that no significant [<sup>18</sup>F]ML-10 uptake occurred at 1-day post chemotherapy. However, at 3-7 days post chemotherapy, the uptake of [<sup>18</sup>F]ML-10 became significant. The authors conclude that further optimisation of the time point for imaging post therapy is required with this radiotracer.<sup>135</sup>

A more sensitive tracer and alternative to [<sup>18</sup>F]ML-10 is [<sup>18</sup>F]C-SNAT, which is a peptide tracer (see Figure 3, **D**) that binds to CC3 via cyclisation and causes nanoaggregation.<sup>136</sup> However, due to its hepatobiliary and renal excretion route *in vivo* shown in pre-clinical studies, its use is limited to monitoring cell death in the upper half of the body (e.g. breast cancer).<sup>137</sup>

In 2016, a pre-clinical 19 amino acid peptide SPECT tracer called [<sup>99m</sup>Tc]duramycin was used to image another extracellular biomarker of cell death; phospholipid PE. Radiotherapy, chemotherapy and a combination of both were used to induce cell death in murine colorectal xenograft study. [<sup>99m</sup>Tc]duramycin uptake in mice bearing Colo205 colorectal cancer xenografts showed oxaliplatin treated tumours uptake of duramycin correlated strongly with apoptosis determined by CC3 ( $P < 0.001$ , Pearson  $r = 0.85$ ) and TUNEL ( $P < 0.001$ , Pearson  $r = 0.81$ ) staining. In the case of radiotherapy [<sup>99m</sup>Tc]duramycin uptake correlated well again with CC3 and TUNEL staining ( $P < 0.001$ ; Pearson  $r = 0.88$  and  $0.73$  respectively).<sup>138</sup>

The Pearson correlation (Pearson R test) measures the strength of linear correlation between two variables. The test outcome is a variable with a value between -1 and 1. A positive linear correlation would represent a value of 1, 0 meaning no correlation and -1 a negative linear correlation.

Despite the development and preclinical evaluation of numerous tracers for imaging tumour cell death, no agent has yet been approved for routine clinical use. This is generally due to poor biodistribution and off-target binding.

We therefore propose an alternative solution to these major drawbacks by using a small 14 kDa protein, the C2A domain of Synaptotagmin I, which due to its smaller size shows a much faster biodistribution and clearance compared to Annexin V.

### 1.3.3 C2A protein, the subunit of Synaptotagmin I

C2A, which binds PS, is one of two C2 domains of the protein synaptotagmin I, a  $\text{Ca}^{2+}$  sensor situated in the presynaptic nerve terminal. Synaptotagmin I protein consists of an N-terminal transmembrane region (TMR), a variable linker and two C-terminal C2 domains: C2A and C2B. Its role is to crosslink membranes upon  $\text{Ca}^{2+}$  binding, and it initiates fusion of vesicle membranes with the plasma membrane of the presynaptic axon terminal.<sup>139</sup> The fact that C2A binds with high affinity to PS in a calcium-dependent manner was discovered by Davletov and Sudhof in 1993.<sup>140</sup> Calcium ion binding has a role in changing the protein's electrostatic potential and neutralising aspartate residues, rather than changing its conformation. This favours interaction with negatively charged phosphatidylserine.<sup>141</sup>

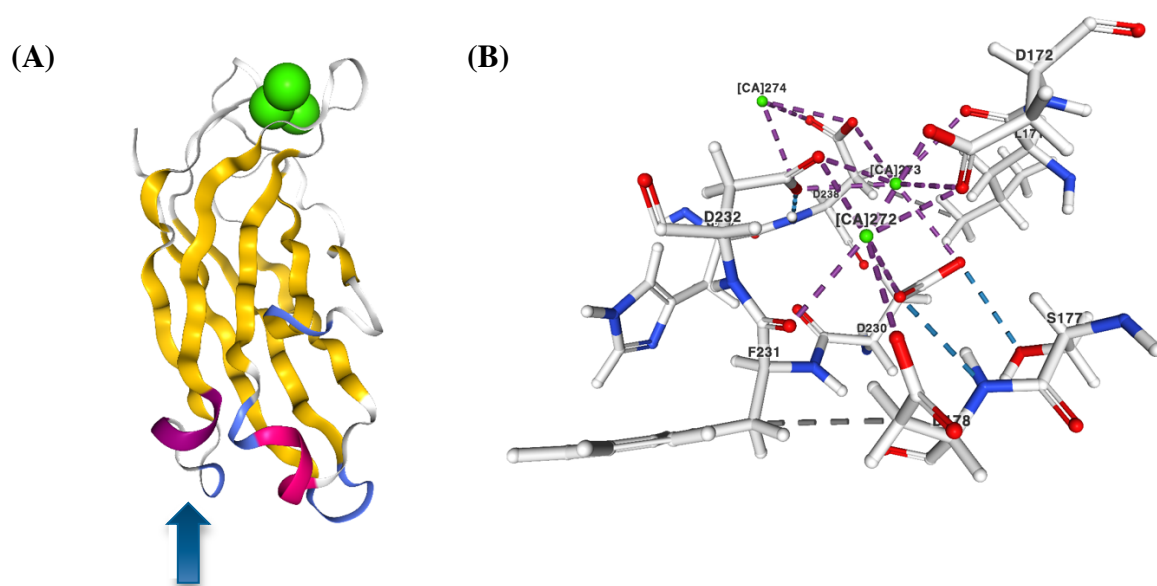


Figure 4. (A) C2Am protein NMR solution structure. The blue arrow indicates the mutated site at position 78, opposite to the binding site in order to minimise effects on affinity for PS, where serine has been replaced by a cysteine residue to enable conjugation with maleimide prosthetic groups. (B) Amino acid representation of the binding site. The three green spheres represent  $\text{Ca}^{2+}$  ions coordinated by aspartate residues.<sup>142</sup>

*In vitro* studies showed that fluorescently labelled C2A has a 5-fold lower binding to viable cells (thus improved specificity for apoptotic cells) compared to an equivalent fluorescently labelled Annexin V.<sup>99</sup> That means that despite having a lower binding affinity for PS (20 nM)<sup>143</sup> compared to Annexin V (0.3-15 nM)<sup>99</sup>, C2A has a reduced off-

target binding to viable cells and organs, thus making it a more specific probe for labelling cell death.

C2A protein has been modified using site-directed mutagenesis at position 78 (position 217 on synaptotagmin I) in order to replace a serine residue with cysteine, which allows single Michael addition reactions to occur via the only thiol present, as detailed in Figure 4.<sup>99</sup>

The Brindle group has been labelling the C2A protein for *in vivo* imaging of tumour cell death using, super-paramagnetic iron oxide (SPIO)<sup>144</sup>, Gd<sup>3+</sup>-DTPA<sup>143</sup> SPECT radioligands (technetium-99m and indium-111)<sup>99</sup> and optoacoustic<sup>145</sup> probes. Here we have developed C2Am as a PET radiotracer as this promised an improved biodistribution profile through the use of radiolabelled organic prosthetic groups rather than chelates.

## 1.4 Positron Emission Tomography (PET)

The existence of antimatter (positron) was first predicted by Paul Dirac in 1928.<sup>146</sup> Ernest Lawrence proved that particles can be accelerated in a circular path, leading to the development of the cyclotron for which he received the Nobel prize in 1939.<sup>147</sup> His contribution was the unique way to accelerate protons to high energies in a very limited space, by proposing a circular path rather than using a straight line. These two discoveries were the cornerstone to advances in nuclear science and form the basis of nuclear medicine and molecular imaging. In the early 1950s, the first positron emission imaging experiment was performed by Gordon Brownell and Charles Burnham at the Massachusetts General Hospital (positrons are anti-electrons). Positron emission imaging was refined in 1961 by James Robertson's ring detector, which is similar to that found in today's PET scanner. However, it was only after the successful use of <sup>18</sup>F-FDG in 1976, in which a study on two volunteers showed <sup>18</sup>F-FDG uptake in the brain, that PET became widely accepted.<sup>148</sup>

Positron emission tomography is a medical imaging technique used to detect the position of a positron emitter radiotracer within a subject. The principle of PET imaging is detailed in Figure 7; a positron is emitted upon radioactive decay of certain radioisotopes due to the conversion of a proton into a positron ( $\beta^+$ ), neutron and a neutrino ( $\nu_e$ ). For example, fluorine-18 decays to oxygen-18:  ${}^{18}_9\text{F} \rightarrow {}^{18}_8\text{O} + \beta^+ + \nu_e$ .

The positron then travels a short distance ( $\sim 1$  mm), which is highly dependent on the environment and the energy of the positron, and collides with an electron. The annihilation event that occurs upon this collision produces 2 gamma photons of 511 keV each, travelling at  $\sim 180^\circ$  with respect to each other and perpendicular to the initial trajectory of the positron. These two photons are detected coincidentally by opposing detectors; see Figure 5. These are called true coincidences; see Figure 6.<sup>149</sup>

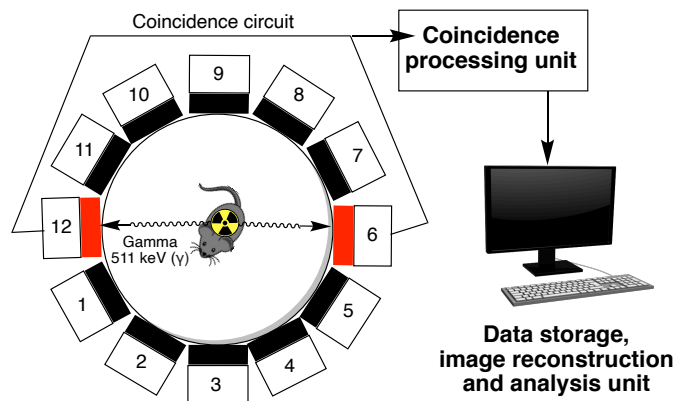


Figure 5. Schematic of the Mediso nanoScan PET detector: A positron-emitting isotope (radiation warning trefoil) generates a positron ( $\beta^+$ ) particle which upon annihilation with an electron situated in the near proximity produces two 511 keV gamma photons (wavy black arrows) at  $180^\circ$  with respect to each other. A static circular array of detectors (black rectangle = crystal arrays, numbered boxes = PMT), detects the two opposing  $\gamma$  photons as a coincidence event (red rectangles). This is then processed by the coincidence unit which will reconstruct the trajectory of these photons thus determining the spatial position of the source.

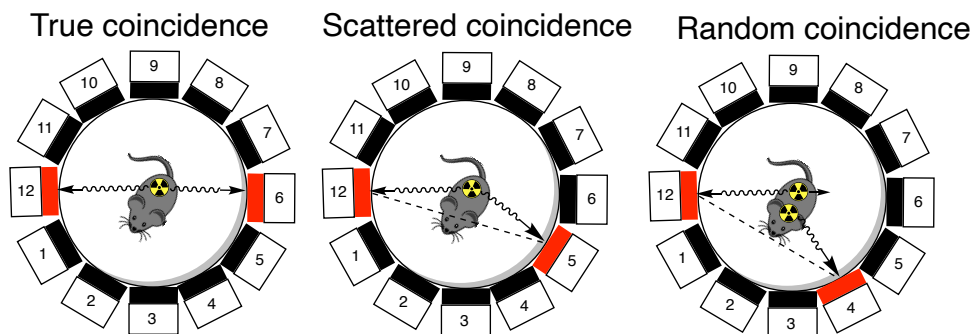


Figure 6. Different types of coincidences. True coincidence occurs when the two gamma photons following an annihilation process end up exciting two detectors opposite each other ( $180^\circ$ ). Scattered coincidence occurs due to change of travel direction of one of the gamma photons due to interaction with surrounding electrons (Compton effect). As a result, the generated LOR is misleading as it does not contain the site of annihilation. A random coincidence occurs when two different annihilation sites emit gamma photons that reach detectors within the coincidence time leading to the formation of an erroneous LOR between them. The static circular array of detectors (black rectangle = crystal arrays, numbered boxes = PMT), detects the two opposing  $\gamma$  photons as coincidence events (red rectangles).<sup>149</sup>

Multiple coincidences generated by activation of more than two detectors within the same interval are not allowed as assigning Line of Responses (LORs) would not be possible. The narrow volume between the two detectors, where the positron-electron annihilation occurs, is called the LOR; see Figure 7.

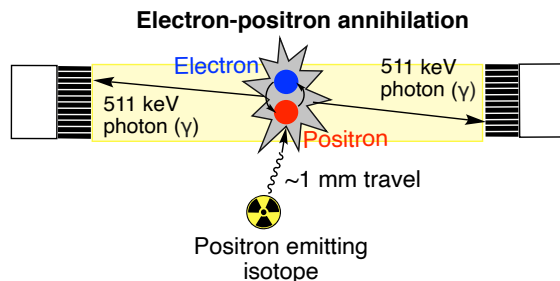


Figure 7. Electron-positron annihilation diagram. Positron (red) travels  $\sim 1$  mm and annihilates with an electron (blue) to generate two 511 keV gamma photons at  $\sim 180^\circ$  to each other. Gamma photons are detected by opposing detectors composed of a crystal array (black rectangles) and a photomultiplier tube (white box). Line of response volume is highlighted in yellow.

Significant advances have been made throughout time that lead to increased sensitivity, resolution and data storage management. Early models of PET had axial collimators installed; these were restricting detection of gamma photons within the same ring or adjacent rings. This is called a 2D acquisition mode. 3D mode became available in the late 1980s by improving the capacity of processing coincidence events between different detector rings. The more LORs are used in a reconstruction process the higher the sensitivity of the scan.

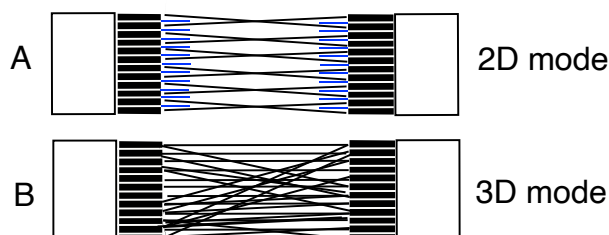


Figure 8. Acquisition using 2D (A) and 3D (B). In 2D mode, collimators limit gamma photons access to scintillators reducing the LOR to adjacent rings. In the 3D mode, detectors can be reached by any gamma photon. Detectors are composed of collimators (blue lines; A) a crystal array (black rectangles; A&B) and a photomultiplier tube (white box A&B).<sup>150</sup>

As a result of the 3D mode acquisition, sensitivity increased by a factor of 4-6 however removing the septa increased scatter coincidence detection from 10-15% to 30-40%.<sup>150</sup>

Scanning volume and sensitivity can be adjusted by increasing LOR density. This can be done by adjusting the PET's detector mode. (Figure 9) Once data is acquired, detector mode can be selected again for the reconstruction. A 1-5 scan can be reconstructed using a 1-5 mode but also be binned down to 1-3 or 1-1 modes as required.

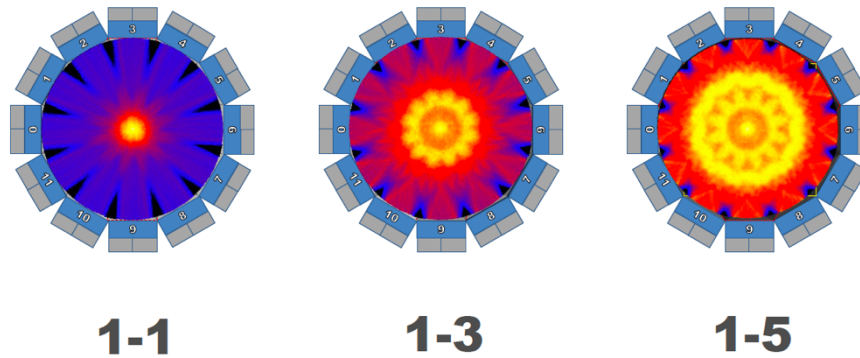


Figure 9. PET acquisition and reconstruction detector modes. 1-1 mode means that 1 detector is accepting coincidence events from just 1 opposing detector. A 1-3 mode means 1 detector accepts coincidences from 3 adjacent and opposing detectors. For example detector 0 accepts coincidences from 5,6 and 7. 1-5 mode means that 1 detector accepts coincidences from 5 opposing detectors. Acquisition and reconstruction can be done in three different modes: 1-1, 1-3 and 1-5. This directly affects sensitivity, the higher the mode the higher the sensitivity. Notably, raw data increases significantly upon using a high detector mode. Picture taken from the Mediso nanoSCAN PET manual.

Significant improvement of image quality was attributed to the use of Cerium-doped lutetium oxyorthosilicate (LSO) scintillation crystal detectors. LSO is a high-density material (high photoelectric fraction) that can stop high energy gamma photons more efficiently. LSO and Cerium-doped lutetium yttrium orthosilicate (LYSO) have higher light yield compared to its predecessors Bismuth germanate oxide (BGO) and Cerium-doped gadolinium orthosilicate (GSO); see Table 2 for more details. A high percentage of light emission per unit of energy absorbed is desirable as it increases the signal-to-noise ratio. Fast crystal excitation following absorption of a 511-keV photon, emission of light and decay of scintillation light is an important characteristic of modern detectors.<sup>150</sup> Short decay time of scintillation light facilitates narrow coincidence detection time of 4-12ns consequently reducing dead time losses. Dead time loss occurs when the crystal being saturated with light is hit by another gamma photon. As a result, the latter photon absorption is not detected as a separate event thus not counted. Dead time loss events occur upon using high activity (high count rate).<sup>149</sup>

Table 2. Scintillation materials used for making PET detectors. LSO and LYSO materials are superior to bismuth germanate oxide (BGO) and cerium-doped gadolinium orthosilicate (GSO) regarding light yield and decay of light. Adapted from Slomka et al (2016).<sup>150</sup>

<b>Material</b>	<b>Density (g/cm<sup>3</sup>)</b>	<b>Light yield (% of NaI(Tl) light)</b>	<b>Decay of scintillation light (ns)</b>
<b>NaI(Tl)</b>	3.67	100	230
<b>BGO</b>	7.13	8	300
<b>GSO</b>	6.71	16	60
<b>LSO</b>	7.4	75	40
<b>LYSO</b>	5.37	75	53

Photomultipliers (PMTs) capture crystal scintillation light, amplify it and convert it to electrical signal. Their function is to characterise photon energies, resolve its position accurately and discriminate rapidly between different events. Conventional PMTs were large and covered several crystals at a time leading to low spatial resolution. Digital photomultipliers made of silicon (SiPMs) couple individually to each scintillation crystal. This results in higher spatial and timing resolution.

PET data acquisition occurs as list mode where the detector pairs (position), energy and time of each coincidence event is recorded in a separate file. Using this information, images are then reconstructed by harnessing the multi-core power of graphics processing units (GPUs). Images are then anatomically co-registered for ease of interpretation. Image reconstruction includes a series of corrections: decay, attenuation correction, scatter correction and random events. PET/CT scanners use computed tomography (CT) to perform an attenuation correction during image reconstruction. Attenuation happens when gamma photons emitted by radiotracers are scattered and/or absorbed by tissue, which can be up to 90% in areas where electron density and tissue thickness is high.<sup>151</sup> Attenuation correction takes into account the position of the radiotracer, as well as, the volume and tissue density of the body shielding it and corrects its effects. The decay of the radiotracer is important and easy to correct for. Provided that the right radioisotope is added in the decay calculation (i.e. half-life is known), the correct concentration of radiotracer at any given time can be accurately determined throughout the scan.<sup>149</sup>

Scatter correction can be done based on the Compton principle. Scattered photons lose significant energy in the process. This energy loss can be detected by PMTs. Therefore photon pairs (coincidences) with high difference in photon energy can be discarded. Random correction is done based on the coincidence event delay window of 5-12 nanoseconds (depending on manufacturer). If two single events reach detectors at more than 5-12 ns apart, they are discarded.<sup>149</sup>

### 1.4.1 Latest PET equipment development

Powerful computers, fast electronics and photomultipliers combined with high density, fast decaying scintillation crystals enabled the redevelopment of time-of-flight (TOF) PET in the early 2000s. TOF-PET was initially built in the early 1980s; however, the crystals had low stopping power (low density) and using large PMTs resulted in low spatial resolution therefore its applicability was limited to research. Development and widespread use of LSO/LYSO crystals and fast photomultipliers lead to the development of the first commercial TOF-PET system (Phillips Gemini TF PET/CT) in 2006.<sup>152,153</sup>

The differences in photon travel times, resulting from an annihilation, are measurable. This time difference can be used for a the better localisation of the initial annihilation event. (see Figure 10) Fast coincidence detector systems are the key to the success of this measurement. The Phillips Gemini TF scanner has a coincidence timing resolution of 585 ps.<sup>153</sup>

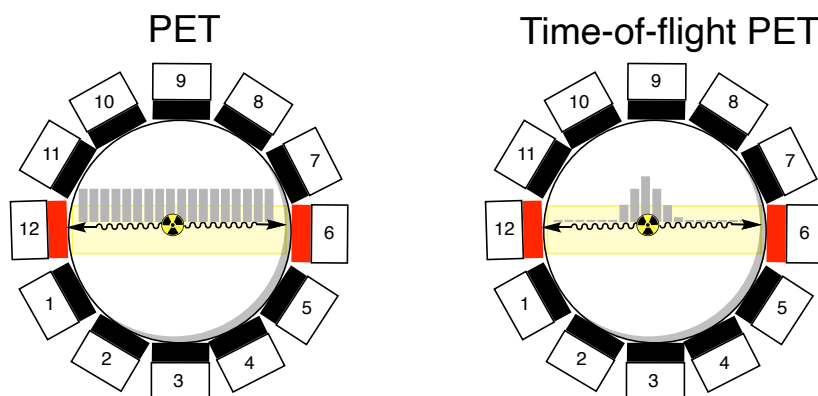


Figure 10. Comparison between PET and time-of-flight PET imaging. The static circular array of detectors (black rectangle = crystal arrays, numbered boxes = PMT), detects the two opposing  $\gamma$  photons as coincidence events (red rectangles), LOR (yellow background), grey bars represent the probability of containing the initial annihilation event and its location within the LOR. In the case of TOF-PET, the higher the grey bar the higher the probability. Adapted from Vandenberghe et al.<sup>152</sup>



This technology promises to reduce the signal-to-noise ratio, reduce the overall image noise and increases quantitative accuracy in small lesions while offering a better image quality. Such performance translates directly to clinical outcomes such as better images in heavy patients (i.e. where attenuation of signal poses a significant hurdle). It also reduces the scanning time or the dose required to obtain an image.<sup>152</sup>

Positron emission tomography/magnetic resonance imaging (PET/MRI) is an emerging technology and it combines the anatomical and quantification power of the MRI with the physiologic data obtained by the PET. Challenges in building such a system consisted mainly of building an appropriately shielded PET detector that can withstand the strong magnetic field of an MRI scanner. PMTs are susceptible to the magnetic field, therefore special silicon photomultipliers (SiPMs) that have high gain ( $10^6$ ), fast response time (100 ps) and are insensitive to magnetic field have been used to overcome this problem.<sup>154</sup> The first whole body PET/MRI was installed in 2010 and since then the number of studies using them grew exponentially. Table 3 provides a comparison between PET/CT and PET/MRI, highlighting their strengths and limitations.

Table 3. Summary of key advantages and limitations of PET/MRI and PET/CT. Table adapted from Ehman et al.<sup>155</sup>

	<b>Advantages</b>	<b>Limitations</b>
<b>PET/CT</b>	<ul style="list-style-type: none"> <li>• Widely available</li> <li>• Established imaging protocols</li> <li>• Evidence proven indications</li> <li>• Familiarity among equipment providers</li> <li>• Quantitative accuracy well established</li> <li>• Imaging of small pulmonary nodules</li> <li>• Exams performed in as little as 30 minutes</li> </ul>	<ul style="list-style-type: none"> <li>• Limited soft tissue contrast</li> <li>• Fast CT exam does not provide extra time for PET acquisition</li> <li>• IV contrast not routinely used</li> <li>• If focused MRI needed, must be additional exam</li> <li>• Ionizing radiation from CT component</li> </ul>
<b>PET/MRI</b>	<ul style="list-style-type: none"> <li>• Improved soft tissue contrast</li> <li>• Added value of diffusion weighted acquisitions</li> <li>• Increased available time to collect PET data</li> <li>• Better motion correction</li> <li>• Convenience and time savings with combined exams</li> <li>• Use of MRI specific contrast agents</li> <li>• No ionizing radiation from MRI component</li> </ul>	<ul style="list-style-type: none"> <li>• Limited availability</li> <li>• Protocols and indications still in development</li> <li>• Requires knowledgeable radiologists in both nuclear medicine and MRI</li> <li>• Quantitative accuracy still being determined</li> <li>• Exams may take 1 hour or longer</li> <li>• Limited evaluation of pulmonary parenchyma</li> </ul>

As of 2017, a full body PET scanner has been produced at the University of California, Davis, and this significantly reduces scanner time to a few minutes and 40-fold sensitivity increase for a total body scan just by extending the field-of-view (FOV) from 20 cm to 200 cm.<sup>29</sup> This significant increase in sensitivity compared to current PET

scanners is due to the fact that current scanners only cover an eighth of the body within the FOV and thus the signal outside this area is not recorded. Coupled with the fact that only 3-5% of the emitted gamma radiation is detected as coincidence events, as the rest is either out of the range of detectors, attenuated or scattered.<sup>29</sup> As a consequence of increased sensitivity, shorter times are required in the scanner which in turn translates to less artefacts generated by potential patient movements. Finally, this results in less activity required to acquire a scan thus lower dose given to the patient. The construction and usage of the total body PET is a strong argument for the future use of PET imaging.

However, the fact that the radionuclides cannot be stored (thus having to be used immediately) can be a drawback. Furthermore, production and usage require special facilities (e.g. cyclotron, radiochemistry lead shielded lab) and specially trained radiochemists to produce the desired radiopharmaceuticals, limiting the availability of this technology.<sup>156</sup>

PET is constantly increasing in popularity in the medical imaging field mainly due to its high sensitivity (as low as femtomoles) and short-lived radiotracers, which minimise the radiation dose. High-energy gamma photons, emitted from the positron-electron annihilation, are able to penetrate tissue, organs and bones; making PET a suitable modality for deep body imaging. The main advantage of PET is its inherent strong signal-to-noise ratio (SNR), which can be achieved due to the very low natural background radiation coming from body tissue. Moreover, radioactive organic compounds (e.g. antibodies) can be targeted at specific sites.

#### 1.4.2 Single-photon emission computed tomography (SPECT)

PET is not the only imaging technique in clinical usage. Other imaging methods are available, each of them with advantages and disadvantages, e.g. speed, resolution, cost and sensitivity. A detailed comparison of these imaging modalities can be found in Table 4 (Adapted from Baker *et al.* 2010).<sup>157</sup> The alternative radionuclide imaging modality is single-photon emission computed tomography (SPECT). The SPECT scanner, depicted in Figure 11, consists of three gamma cameras that rotate around the patient and detect the gamma photons emitted by injected sources. A sodium iodide crystal produces light photons when struck by gamma photons which have been filtered through a lead collimator. The light signal is then converted to an electrical signal by photomultiplier tubes. By knowing the position of the camera, the image can then be

reconstructed and the position of the radiation source can be accurately determined. Pre-clinical systems (e.g. Bioscan NanoSPECT/CT) have up to four cameras to boost sensitivity and resolution. Recently, this technology has been used in clinical scanners using a multi-camera SPECT with other imaging modalities such as PET and CT within the same scanner (Mediso AnyScan TRIO).<sup>158</sup>

### Mediso AnyScan SPECT Scanner

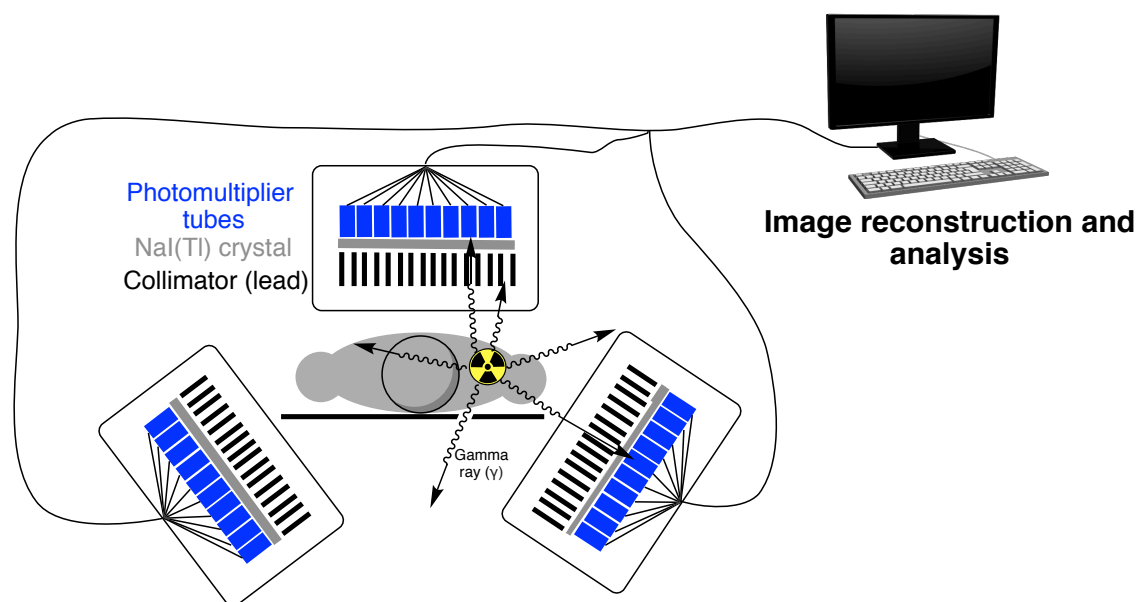


Figure 11. Schematic of the latest Mediso AnyScan TRIO gamma camera SPECT scanner. Gamma photons (wavy black lines) are collimated to a NaI(Tl) thalium doped sodium iodide crystal, signal being picked-up and amplified by photomultiplier tubes and converted to an electrical signal. The image is then reconstructed for analysis. The scanner has the capability to use multi modal imaging by combining three different modalities in one scanner. It has the possibility to combine SPECT, CT and PET all in one scanner.<sup>158</sup>

The resolution of a SPECT scanner depends on the size of the pinholes of the collimator (see Figure 11). Moreover, the lower gamma photon energies (140 keV for  $^{99m}\text{Tc}$ ) used in SPECT causes more pronounced attenuation artefacts compared to PET, especially in larger patients. These are caused by tissue (diaphragm, breasts) between the gamma camera and the imaged organ (e.g. heart).<sup>156,151</sup>

One major drawback with current clinical SPECT systems is that no quantitative imaging can be performed i.e. the voxel intensity detected cannot be converted to an activity. This is a strong argument for the usage of PET to monitor and quantify the biodistribution of a tracer which can be accurately and non-invasively determined. On the

downside, the initial investment for a PET scanner is much higher than for a SPECT one. Another drawback of PET is the requirement for a local cyclotron, which is an expensive asset and high maintenance costs therefore limited to a few locations within a country. Since most research facilities do not have access to a cyclotron, mobile isotope generators are much desired. The most widespread generator is the molybdenum-99 – technetium-99 metastable. Recently, the first gallium-68 generator to be used for human productions (GalliaPharm, Eckert & Ziegler) was approved by the European Medicines Agency for use in 14 European countries in 2014 and by the FDA in 2016 for use in the US.<sup>159</sup> It sparked a revolution in the area of PET imaging of prostate cancer (more details in subchapter 2.1.2).

By comparing the advantages and shortcomings of the two imaging modalities, we have concluded that PET would be a more suitable modality for studying cell death following therapy using the C2Am protein.

Modality	Label	Signal	Advantages	Disadvantages	Initial cost	Speed	Sensitivity (mols detected)	Resolution (mm)
PET	Radiolabelled molecule	$\gamma$ - ray	High sensitivity, high scanning speed with total body PET <sup>29</sup>	Radiation exposure	High	Low	$10^{-15}$	1-2
SPECT	Radiolabelled molecule	$\gamma$ -ray	More than one isotope can be used at once	Radiation exposure	High	Low	$10^{-14}$	1-2
CT	None	X-ray	Fast, anatomical detail	Limited resolution of soft tissue	Moderate	Moderate	N/A	0.05
MRI	Gadolinium based tracer	Magnetic field	No radiation, soft tissue imaging, hyperfine resolution with INUMAC 11.7 tesla scanner <sup>160</sup>	Slow acquisition, movement artefacts near heart	High	Low	$10^{-9}$ to $10^{-6}$	0.05
Optical	Bioluminescent or fluorescent	Light, infra-red	Molecular events can be monitored. No radiation	Low resolution, penetration depth	Low	High	$10^{-12}$	1-2
Photo-acoustic	Probe with high molar extinction coefficient ( $\epsilon$ ) and low quantum yield ( $\phi$ )	Light & Sound	Better depth resolution than light. No radiation exposure	Not yet optimised for clinical use	Low	High	$10^{-12}$	0.05
Ultra-sound	Microbubbles	Sound	No radiation exposure	Operator involved. No air-containing structures	Low	High	$10^{-8}$	0.05

Table 4. Imaging modalities compared by cost, resolution, speed and sensitivity (adapted from Baker *et al.* 2010)<sup>157</sup>

## 2 LABELLING OF C2AM FOR PET IMAGING

The main aim of this work was to design, synthesise and evaluate an  $^{18}\text{F}$ -labelled PET radiotracer. This chapter introduces the challenges of selecting and synthesising the optimum  $^{18}\text{F}$ -labelled prosthetic group for protein thiol labelling but first, the advantages of protein conjugation via cysteine amino acids are presented.

### 2.1 Protein bioconjugation for molecular imaging

Proteins are nature's control switches that regulate events in living cells and organisms. They play an important role in intra and extracellular signalling, structural support, transport, DNA replication, and as enzymes they catalyse a myriad of metabolic reactions.

Proteins differ from each other due to their primary structure (i.e. their amino acid sequence). However, due to their need to fulfil multiple roles, proteins have an added level of complexity where the structure and function are often modified after synthesis. This late event is called post-translational modification (PTM). These modifications include: protein glycosylation (important in cell-cell recognition); acetylation and phosphorylation, which can act as on/off switches; acylation with fatty acids, which

can control solubility and membrane docking; and ubiquitinylation - a marker for protein degradation.<sup>161</sup>

In order to better understand the biochemical processes that proteins undergo in live cells, their concentration and stability need to be monitored and quantified over time. Through site-selective chemical modification, often termed bioconjugation, synthetic labels can be introduced that allow the study of the proteome (e.g. identification by mass spectrometric analysis, affinity purification, amino acid analysis) and biochemical characterisation.<sup>162</sup> Proteins can also be chemically labelled with toxic ‘warheads’ (therapeutic payload)<sup>163</sup> and thus be used as therapeutic agents e.g. an anti-HER2 monoclonal antibody conjugated through a maleimide moiety to the maytansinoid drug DM1 – trastuzumab-SMCC-DM1.<sup>164</sup>

Proteins involved in the study of biochemical processes can be conjugated to imaging labels such as fluorescent and optoacoustic<sup>145</sup>, paramagnetic<sup>143</sup> or radioactive<sup>99</sup> tags.<sup>165</sup> Therefore, the biodistribution and pharmacokinetics of these proteins in the body can be monitored and quantified non-invasively using a variety of imaging modalities.

Radiolabelling of proteins for studying the degradation and excretion of proteins (e.g. globulins, albumin, human growth hormone) was introduced in the 1940s and early 1950s.<sup>166,167</sup> These early studies used iodine-131 to label tyrosine side chains of amino acids. However, it was shown that installation of multiple iodine labels per protein molecule increased its degradation and excretion whereas 0.5 iodine molecules per protein was found to be ideal.<sup>166</sup>

To facilitate protein labelling, chemistries used in the area of metabolic imaging have been adopted. For the past three decades bioorthogonal reactions – a term coined by Bertozzi *et al.* in the early 2000s<sup>168,169</sup> – have increased in popularity, especially in the area of metabolic glycan imaging. A subtype of these bioorthogonal reactions, more specifically the 3+2 cycloaddition of an azide to a strained alkyne in the absence of any copper catalyst – known as strain promoted azide-alkyne cycloaddition (SPAAC) – has been used for the study of glycans and their metabolism.<sup>170,171,172</sup> It has also been used in the context of PET imaging using 2-[<sup>18</sup>F]fluoroethylazide.<sup>173</sup>

Nevertheless, the most popular reactions for covalently linking proteins to synthetic molecules remain bioconjugation reactions with native amino acids such as lysine and cysteine.

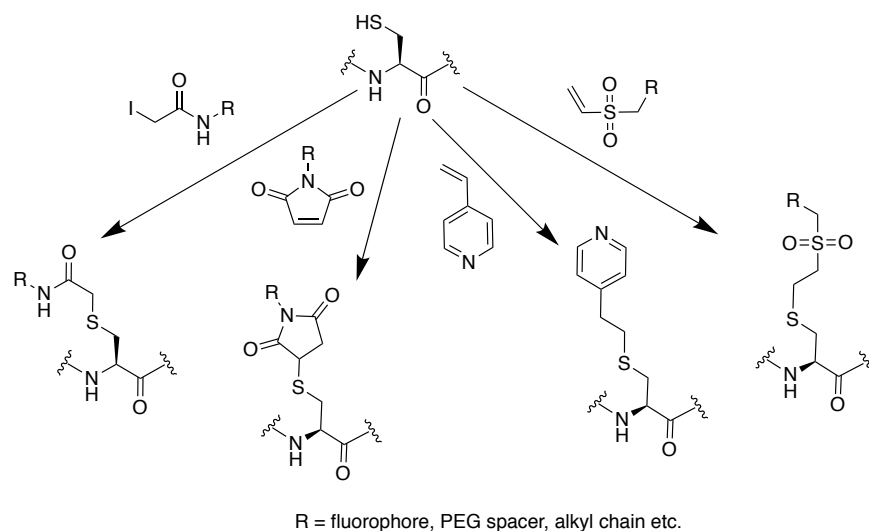
### 2.1.1 Protein bioconjugation via thiol labelling

One of the most commonly used amino acids for modification is lysine due to its primary  $\epsilon$ -amino side chain that can react with multiple chemical partners (e.g. NHS esters). Lysines are abundant<sup>174</sup> in native proteins (5.8% in human proteins<sup>175</sup>) and most of them are available for reaction, therefore labelling a small number of these lysines per antibody is relatively easy. Labelling proteins and peptides with *N*-succinimidyl *para*-[<sup>18</sup>F]fluorobenzoate ([<sup>18</sup>F]SFB) has been attempted on many occasions; however the radiochemical yield was always low and multiple lysines are labelled leading to a heterogenous mixture of tracers.<sup>176,177</sup> Moreover, the latter is not the most elegant approach since multiple labels can hinder the targeting ability of the protein, increase immunogenicity, alter protein pharmacokinetics and pharmacodynamics significantly and also interfere with subsequent quantification.

Because of the limitations inherent in conjugation to lysine residues, selective methods for conjugating small molecules to proteins often use cysteine instead. Cysteine is an amino acid with a relatively low natural abundance in proteins (3% in human proteins<sup>175</sup>).<sup>174</sup> Common roles are to form disulphide bridges and to bind metals. As a result it is usually found embedded in the core of proteins, making it unavailable for conjugation.<sup>178</sup> Solvent exposed cysteines can be introduced into recombinant proteins<sup>99</sup> using site-directed mutagenesis.<sup>179,180</sup> This can ensure that the amino acid to be modified is accessible and the modification does not interfere with the protein's active site.

Chemical modification of proteins via cysteine labelling can be performed in two ways: either by alkylation using an  $\alpha$ -halocarbonyl (e.g. 5-iodoacetamidofluorescein or monobromobimane) or by conjugation with Michael acceptors such as maleimides, vinyl sulfones, 2-vinylpyridines or 4-vinylpyridines. (Scheme 1).





Scheme 1. From left to right: alkylation of cysteine with iodoacetamide, conjugation of cysteine with *N*-alkyl-maleimides, 4-vinylpyridines and vinyl sulfones.

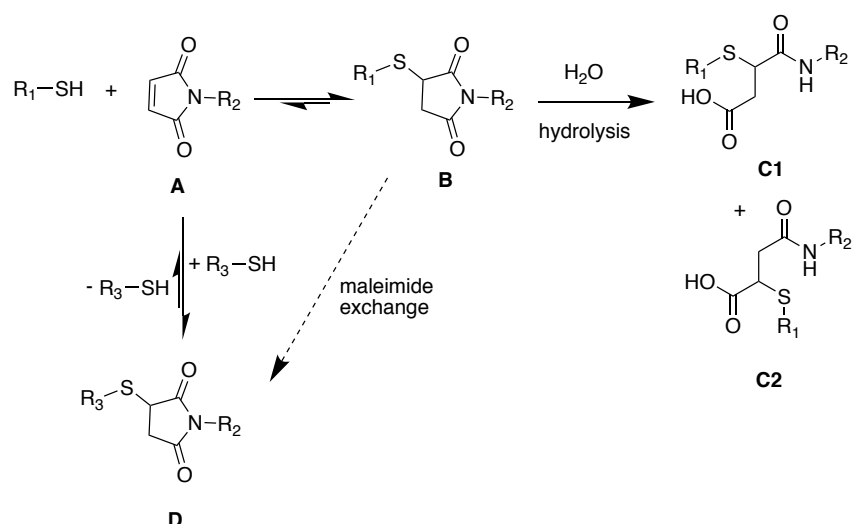
Alkylation with iodoacetamide is a relatively slow reaction, 3 orders of magnitude slower than maleimide conjugation under comparable conditions.<sup>181,182</sup> Maleimides are biocompatible compounds that conjugate to thiols with high specificity and fast kinetics, which make them good prosthetic group candidates for protein labelling. Conjugation of the thiol of tripeptide L-glutathione (GSH) to 2-vinylpyridine is 500-fold slower than to maleimides.<sup>183</sup> This makes vinylpyridines too slow for the purpose of this study. Vinyl sulfones reacting with GSH at pH 6.5-8.5 have half-lives of between 69 and 6 minutes, approximately 6000-fold slower than maleimides.<sup>184</sup>

Michael addition of GSH to *N*-ethylmaleimide has a very high rate constant of  $\sim 1500 \text{ M}^{-1} \text{ s}^{-1}$  at pH 7, as estimated by Gorin *et al.* in 1966.<sup>185</sup> This translates to a half-life of  $\sim 2.6$  seconds at pH 7 and a concentration of 1 mM. These results have been confirmed experimentally in this study using *N*-(5-fluoropentyl)maleimide (synthesised in-house) and GSH (see subchapter 2.2.3).

Fast reactions are crucial for conjugation of prosthetic groups bearing short-lived radioisotopes (e.g. carbon-11, fluorine-18). The speed of the Michael addition reaction is dependent on the thiolate concentration, reaction conditions (e.g. temperature, pH), degree of steric hindrance and  $\text{pK}_a$  of the thiol. The effect of pH on the conjugation rate of reaction is related to thiolate formation, as described by Gorin *et al.*<sup>185</sup> and Bednar<sup>181</sup>. Thiol (-SH) is  $5 \times 10^{10}$ -fold less reactive than thiolate (-S<sup>-</sup>) towards maleimides.<sup>181</sup>

Therefore, pH determines the speed and specificity of the conjugation reaction. Slightly basic pH (7.5 - 8.5) can partially deprotonate (deionise) the  $-\text{NH}_3^+$  group of lysine side chains, which thus become nucleophilic and compete with thiolate ions from cysteines for maleimide conjugation. The  $\text{pK}_a$  of the lysine side chain primary amine is 8.95 which is very close to the cysteine's thiol of 8.4. Therefore, at  $\text{pH} > 8-8.5$  maleimide conjugation to primary amines can become significant.<sup>186,187</sup>

A drawback of the Michael addition reaction is its reversible nature. Once conjugated, maleimides can undergo retro-Michael addition (i.e.  $\beta$ -elimination of the thiol). This can lead to loss of maleimide label by thiol exchange with other thiols present in higher concentrations in the same solution. (Scheme 2.) However, the half-life of the retro-Michael reaction of GSH with *N*-ethylmaleimide was shown to be 350 to 400 hours,<sup>188,189</sup> which is slower than the half-life of fluorine-18 (109.8 minutes). Once conjugated, the retro-Michael addition can be minimised by hydrolysis of the maleimide to the equivalent maleamic acids. These conjugates have increased stability and consequently will not undergo thiol exchange.<sup>190,191</sup> This is due to maleamic acids showing very low rate constants for the retro-Michael reaction.<sup>192,189</sup> The *N*-linked side chain of the maleimide has a direct influence on the hydrolysis reaction rate. An electron withdrawing side chain will increase the hydrolysis rate by increasing the electrophilicity of the maleimide carbonyls. These carbonyl groups are therefore prone to hydroxyl/water attack, whereas an electron donating *N*-substituent does the opposite and decreases the rate of hydrolysis.<sup>189,188</sup>



Scheme 2. Maleimide **A** reacting with a R<sub>1</sub>-SH yields conjugate **B**. This can undergo hydrolysis to permanently generate maleamic acid conjugates **C1** and **C2**. The conjugation of maleimide **A** to R<sub>1</sub>-SH can be reversed and undergo thiol exchange in the presence of a second thiol, R<sub>3</sub>-SH, to obtain a second conjugate **D**. Adapted from Baldwin and Kiick.<sup>189</sup>

To conclude, the covalent reaction of maleimides with a cysteine thiol is the best choice for obtaining quantitative and time-efficient labelling of peptides or proteins. The decision was based on their high reaction rate constant, high thiol specificity and no toxic by-products (*c.f.* iodoacetamide, which produces toxic iodide ions). In addition, maleimides allow a great diversity of functional groups (fluorescent probes, spacers, good leaving groups that can be <sup>18</sup>F-labelled) to be introduced *via* the side-chain on the nitrogen atom. Maleimides have been used extensively in diverse applications. As an example, a common medical application is generating antibody drug conjugates (ADCs) by linking the targeting agent (antibody) to their toxic payload via Michael addition. ADCs have been observed to increase or decrease their activity depending on the hydrolysed or cyclic state of their maleimide.<sup>192</sup>

Native C2A contains 14 lysine and no cysteine residues. For the purpose of specific conjugation reactions, a mutant form, C2Am, was created previously, with a single surface-exposed cysteine residue at the opposite end of the protein active site.<sup>99</sup> Thiol pK<sub>a</sub> values are generally close to neutral: in the case of cysteine it is 8.4 whereas in the context of GSH the thiol is less acidic with a pK<sub>a</sub> of 9.7.<sup>193</sup> The calculated pK<sub>a</sub> of the free thiol cysteine (C95) of C2Am is 10.3 and it is significantly lower compared to the pK<sub>a</sub> of cysteine (C315) on a site-directed mutant of Annexin V, another PS-binding

protein that has been used for imaging<sup>194,195,196</sup>, is  $\sim 14$ . These values were estimated using the constant pH Molecular Dynamics simulations of Matos *et al.*<sup>197</sup> At physiological pH 7.4, the higher the  $pK_a$  of the thiol, the lower the thiolate concentration will be. Experiments have shown that the maleimide conjugation rate constant increases with thiolate concentration.<sup>181</sup> This means that the conjugation rate will be slower for Annexin V than for C2Am.

We shall now focus on the justification for selecting fluorine-18 as the radionuclide of choice, based on the properties of an ideal radiotracer.

### 2.1.2 Radioisotope of choice, radiotracer properties and radiosynthesis

There is a diverse range of radioisotopes that decay via positron emission. Some of them have been used extensively for PET imaging. (Table 5) The choice of radioisotope should be made based on a number of properties that a novel radiotracer must fulfill in order to satisfy the application's requirements.<sup>198, 199</sup>

Table 5. Selection of radionuclides emitting positrons used for PET imaging.<sup>198</sup>

Radionuclide	Half-life (min)	Positron decay (% $\beta^+$ )	Positron energy (MeV)		Positron travel in water (mm)	
			Maximum	Mean	Maximum	Mean
<sup>11</sup> C	20.4	99.77	0.96	0.39	4.1	1.1
<sup>18</sup> F	109.8	96.7	0.63	0.25	2.4	0.6
<sup>64</sup> Cu	768	17.87	0.65	0.28	2.9	0.64
<sup>68</sup> Ga	68.3	87.7	1.90	0.84	8.2	2.9
<sup>89</sup> Zr	4704	23	0.9	0.4	4.0	1.18

Firstly, the radiotracer should be labelled with an isotope with an adequate half-life that allows sufficient time for radiosynthesis, local transport and PET imaging. PET imaging refers to administration of radiotracer, biodistribution (pharmacokinetics, pharmacodynamics), binding to the target, clearance from the blood pool (generating

contrast), excretion and scanning time. All of these steps require time to be completed and this has to be accounted for and be compatible with the radiotracer's decay half-life.

Secondly, the radiotracer should demonstrate an adequate biodistribution profile. It must be soluble in saline or biocompatible aqueous buffers in order to be administered systemically. Moreover, it must be stable under physiological conditions (pH 7.4, 37 °C), distribute rapidly in the body, be metabolized (if required) and finally the unbound material must be excreted rapidly to generate contrast.

An ideal tracer should bind its abundant target with high (nanomolar) affinity and it should also show high selectivity for one biomarker with minimal off-site binding.<sup>99</sup> C2Am has a lower affinity (20-50 nM)<sup>99</sup> for its target (phosphatidylserine) compared to Annexin V's multimeric binding (0.03-15 nM)<sup>200,201</sup>. However, this is probably offering C2A an advantage as it binds less to viable cells than Annexin V. The desired radiotracer should show excellent stability in its final formulation to accommodate transport and delivery. Once injected, its stability should not be compromised by the reduction-oxidation potential of blood, physiological pH, or partial pressure of oxygen. In terms of pharmacodynamics, a successful imaging agent should not have any effect on the body.

In order to achieve maximum tumour contrast, the PET radiotracer should be prepared with high molar activity ( $A_m$ ) and be imaged at the ideal time window for binding to the target with maximum contrast. Molar activity is the amount of radioactivity (measured in GBq) per total amount of compound (measured in  $\mu\text{mol}$ ) (e.g.  $A_m = 50000 \text{ MBq}/\mu\text{mol}$ ).

In terms of cell death, it has been suggested that there are two time-points where cell death can be detected. One time-point occurs 1-2 hours post-administration of chemotherapy when there is an initial wave of cell death, and the other 24-48 hours later when there is further cell death.<sup>202</sup>

One advantage of using short lived isotopes (e.g. fluorine-18) is that repeat scans can be performed, if necessary, at relatively short time intervals (e.g. every 24 hours). Previously, the Brindle group have shown that C2Am generates cell death-dependent tumour contrast within two hours of intravenous administration, due to its fast

biodistribution profile.<sup>100,203</sup> Therefore, labelling the C2Am protein with short lived radionuclides such as fluorine-18 would be sensible.

Fluorine-18 is a pure positron emitter (96.7% of decays emit a positron) that has a relatively short half-life of 109.7 minutes, decaying to a non-toxic element, oxygen-18. For comparison, with gallium-68, only 87.7% of the emissions release a positron. This is reflected in a lower sensitivity (~15%) compared to fluorine-18.<sup>204</sup> However, the higher median energy of gallium-68 positron means that there is less attenuation and therefore higher sensitivity for internal organs; however, a higher positron mean energy can reduce resolution, particularly in pre-clinical systems, due to the longer distance of positron travel. Fluorine-18 has a lower mean positron energy (0.25 MeV) than gallium-68 (0.84 MeV) and this translates into a shorter positron travel distance (0.6 mm and 2.9 mm, for fluorine-18 and gallium-68, respectively, Table 5.) and thus higher spatial resolution. Lower positron energy also means lower dosimetry, i.e. less radiation exposure for the patient.

Thirdly, the radiosynthesis should be reproducible and as rapid as possible, typically being finished within a half-life of the radioisotope. Numerous chemistries have been proposed over the past decades that make real-time radiochemistry feasible.

Ideally, radiochemists prefer to include fluorine-18 as a late-stage step in the fluorination reaction. However, fluorination using fluorine-18 often requires a multi-step synthesis. Choosing the correct labelling method and reaction type are critical steps. Reactions should to be rapid enough to reach an acceptable yield within a short time, typically within a half-life of fluorine-18, i.e. ~1 hour. A successful radiosynthesis will also yield a radiotracer with high molar specific activity.

In order to be able to perform radiosynthesis in a safe, reproducible and fast manner, a module-assisted (automated) synthesis device is used. Using these contained shielded modules, radiochemists can work with high activities whilst minimizing radiation exposure of the operator. Larger quantities of radioactive agents can be produced and shipped to locations within a wider travel distance. Moreover, automation increases reproducibility, limits human error, improves efficiency and speed of

production, leading to shorter, more consistent synthesis times and more reproducibly synthesised tracers, particularly when implemented under cGMP.

### 2.1.3 Radioactive maleimides used for protein labelling

Over the past three decades, a significant number of maleimides have been  $^{18}\text{F}$ -labelled. Notable examples, reported to have been used for labelling proteins and peptides include:  $^{18}\text{F}$ FPPD (1989)<sup>205</sup>,  $^{18}\text{F}$ FBAM (2003)<sup>206</sup>,  $^{18}\text{F}$ FPyME (2005)<sup>207</sup>,  $^{18}\text{F}$ FBEM (2006)<sup>208</sup>,  $^{18}\text{F}$ FPenM (2013)<sup>209</sup>,  $^{18}\text{F}$ FBSEM (2017)<sup>210</sup> (Figure 12).

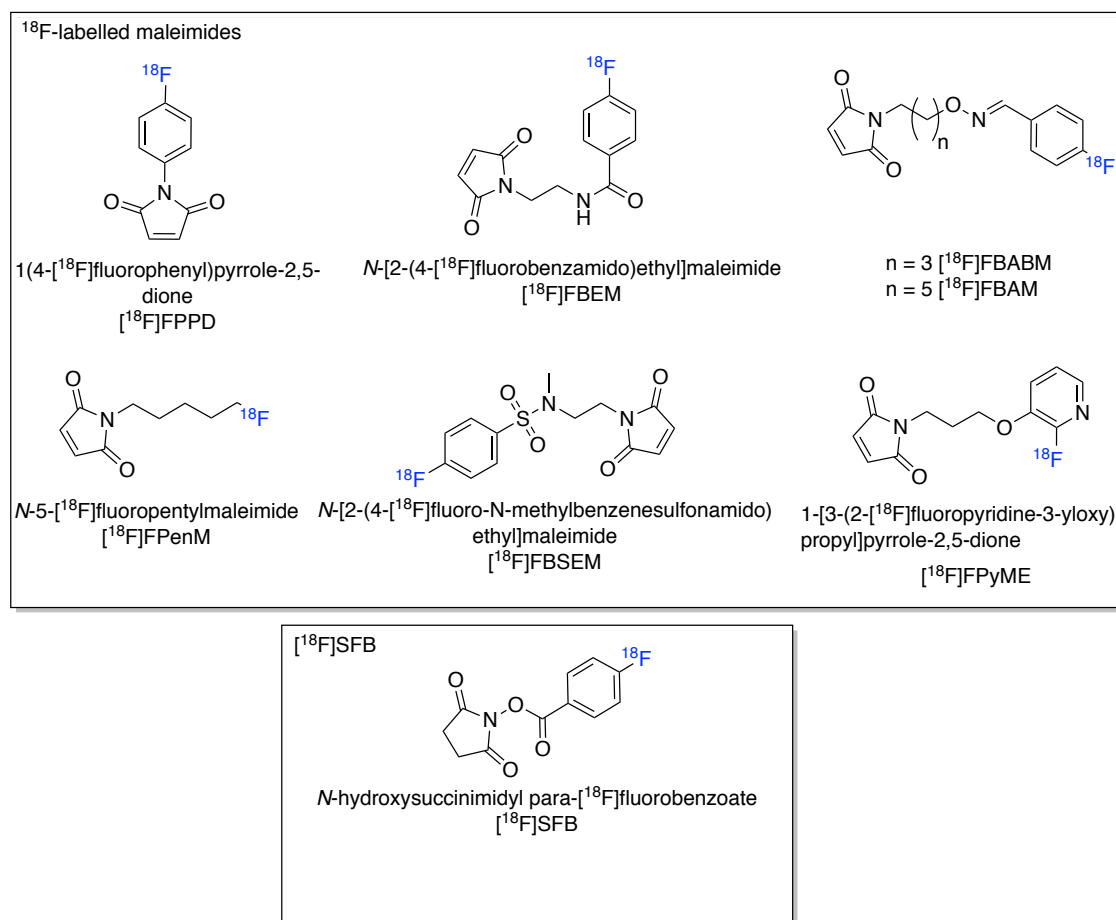
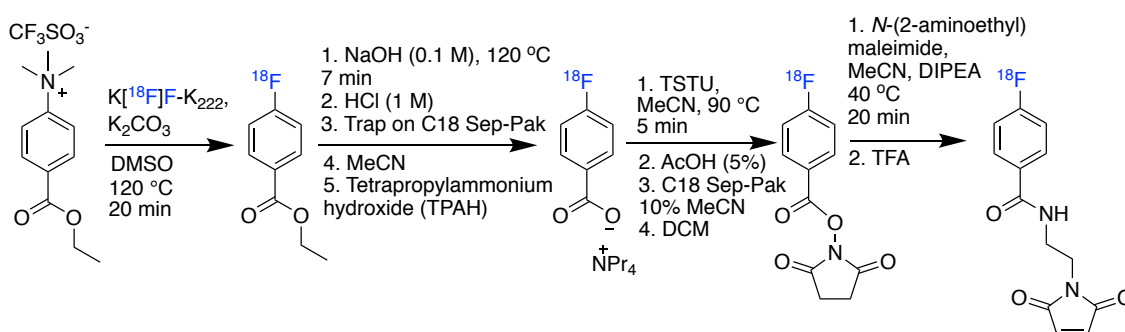


Figure 12. Examples of  $^{18}\text{F}$ -labelled maleimides for protein thiol labelling and also the structure of  $^{18}\text{F}$ SFB intermediate for the synthesis of  $^{18}\text{F}$ FBEM.

The  $^{18}\text{F}$ FBEM maleimide prosthetic group is derived from  $^{18}\text{F}$ SFB. The latter requires 3 steps, 2 reaction pots and 80 min to synthesise using the updated synthesis protocol of Vaidyanathan and Zalutsky.<sup>177</sup> By adding 2-aminoethyl maleimide to  $^{18}\text{F}$ SFB,  $^{18}\text{F}$ FPEB is synthesised. The first radiosynthesis of  $^{18}\text{F}$ FPEB described by

Cai *et al.* (2006, Scheme 3.)<sup>208</sup> was extensive, at 150±20 minutes, and low yielding (RCY 5±2%) but it was quickly adopted by the community.<sup>211,212,213,214</sup> An automated radiosynthesis described by Kiesewetter *et al.*, used a 2-pot synthesiser, 3-step synthesis (*c.f.* 4 steps, 150±20 minute synthesis of Cai *et al.*<sup>208</sup>) and required 95 min to complete (not including 10-15 min HPLC purification) and gave a radiochemical yield of 17.3±7.3%.<sup>215</sup>

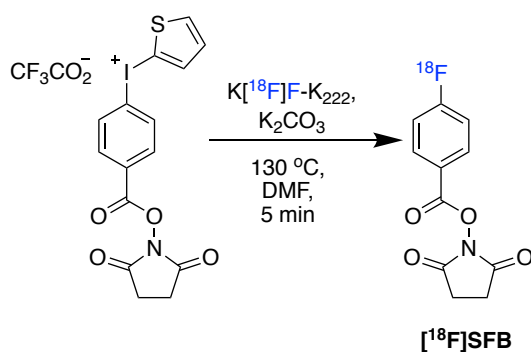


Scheme 3. Production of [<sup>18</sup>F]FBEM according to Cai *et al.*'s procedure.<sup>208</sup>

A simplified 3-step 1-pot synthesis was first described by Kabalka *et al.* in 2008.<sup>216</sup> The production is complete within 60 minutes. The key hydrolysis/saponification step uses an aqueous tetrapropylammonium hydroxide solution. The downside is that this method requires a second time-consuming azeotropic distillation before the final *N*-succinimidyl moiety is added.

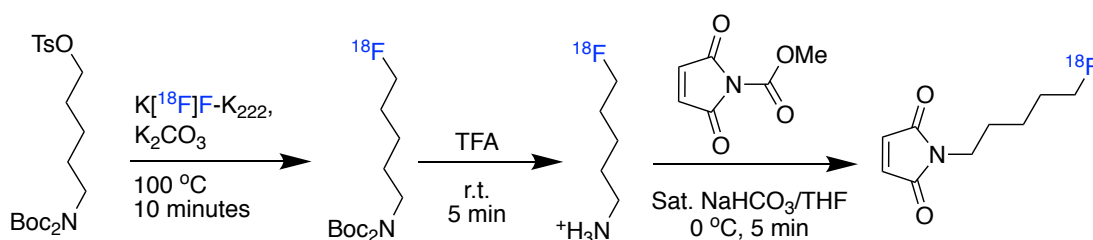
An alternative to the 1-pot, 3-step [<sup>18</sup>F]SFB production, is the 1-pot 1-step fluorination of a 2-thiophenyl iodonium salt. (Scheme 4.) The Carroll and Aigbirhio labs were the first to produce [<sup>18</sup>F]SFB *via* this method in 2008, with a radiochemical yield of 4-23% (n = 8).<sup>217</sup> The simple 1-pot, 1-step production was then filed for patenting later that year.<sup>218</sup> Diaryliodonium precursors are difficult to handle but tracers such as [<sup>18</sup>F]flumazenil, used to visualise areas with reduced GABA<sub>A</sub> receptor activity in patients with epilepsy, have been produced by <sup>18</sup>F-fluorination of a thiophenyl diaryliodonium salt.<sup>219</sup>





Scheme 4. Production of  $[^{18}\text{F}]\text{SFB}$  from (4-((2,5-dioxopyrrolidin-1-yl)oxy)carbonyl)phenyl)(thiophen-2-yl)iodonium trifluoroacetate precursor.<sup>217</sup>

Finally, an attractive alternative to  $[^{18}\text{F}]\text{FBEM}$  was  $[^{18}\text{F}]\text{FPenM}$  due to its facile  $^{18}\text{F}$ -labelling. However the original synthesis of  $[^{18}\text{F}]\text{FPenM}$  required a 3-step synthesis, 2 synthesis pots and 110 minutes, with an overall uncorrected radiochemical yield of 11-17% according to Yue *et al.*<sup>209</sup>

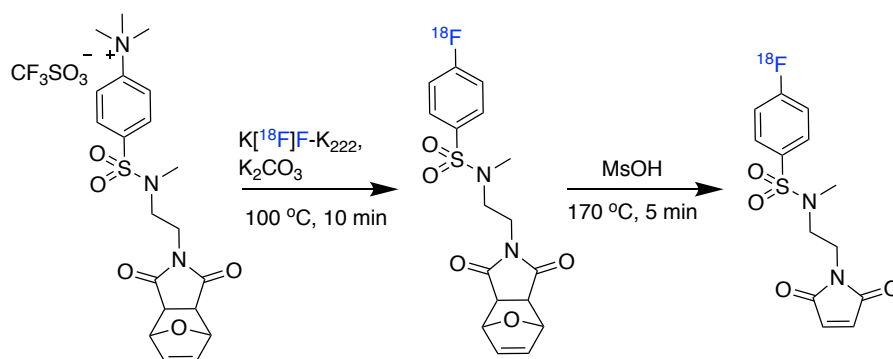


Scheme 5. Synthesis of  $[^{18}\text{F}]\text{FPenM}$  according to Yue *et al.*'s method.<sup>209</sup> Fluorination of tosylate precursor, followed by Boc deprotection and finally transimidation to produce  $[^{18}\text{F}]\text{FPenM}$ .

The synthesis requires 2 pots and removal of basic reagents from the initial fluorination reaction; hence 2 reactors and an elaborate procedure are required. This is due to the fact that maleimides are not stable under fluorination conditions and have to be added after the fluorination step. Since this method had to be automated and transferred to a single pot automated synthesiser (GE TRACERlab FX<sub>FN</sub>), the whole protocol had to be simplified.

A considerable advance on the original  $[^{18}\text{F}]\text{FPenM}$  synthesis was suggested in a patent by Hamamatsu,<sup>220</sup> but Fujita's paper (2017)<sup>210</sup> provided the key details to a successful synthesis (see Scheme 6). These publications use furan protected maleimide

precursors to yield a  $^{18}\text{F}$ -labelled maleimide prosthetic group. The chemistry involved represents a significant simplification of previous procedures using a time efficient 1-pot, 2-step radiosynthesis that did not required purification between the two steps and can be achieved within 65 minutes (including HPLC purification and formulation).



Scheme 6. Maleimide radiotracer formation in Fujita *et al.*'s work.<sup>210</sup>

An alternative to maleimide labelling of proteins is the use of SPAAC chemistry and 2- $^{18}\text{F}$ fluoroethyl azide. The  $^{18}\text{F}$ -labelled azide has been used previously to label small molecules and peptides.<sup>221</sup> The triazole product of the SPAAC reaction is stable to acidic, basic and oxidative conditions and therefore it is a very popular reaction in metabolism studies.<sup>222,223,170</sup> 2- $^{18}\text{F}$ Fluoroethyl azide was used in conjunction with strained alkynes in a pre-targeted labelling method.<sup>173</sup> The main drawback of this approach is the relatively slow reaction rate between azides and strained alkynes. With reaction rate constants of less than  $0.1 \text{ M}^{-1} \text{ s}^{-1}$ , achieving 50% labelling using a very concentrated C2Am protein solution of 1 mM (16.2 mg/mL) would require 166 minutes. Therefore, the radiolabelling of proteins via this method could be relatively slow.

#### 2.1.4 Microfluidic (Advion NanoTek) vs batch (GE TRACERlab FX<sub>FN</sub>) radiochemistry

The NanoTek Microfluidic Synthesis System is a modular, liquid-flow-based microfluidic chemistry system with the ability to combine both microscale process steps. Modular components give the user maximum flexibility for both research and clinical applications.<sup>224</sup> The NanoTek flow system is capable of remotely adding small fractions of liquids and mixing them efficiently in a heated loop. This allows for rapid optimisation of reaction conditions. It also allows the use of higher temperatures than the solvent

boiling point due to adapters that generate backpressure. This in turn allows superheating of solvents and reduces the reaction time compared to batch chemistry, while giving comparable yields. However, these advantages come with a major drawback. Due to the narrow tubing, purposely built for low volumes and laminar flow that increases diffusion mixing, the system is prone to frequent blockages.

An alternative system is the batch system designed by GE called the TRACERlab FX<sub>FN</sub>. The two systems are compared in Table 6. This completely different system showed none of the above drawbacks however it was lacking the capability to quickly optimise reaction conditions, therefore limiting the number of daily reactions. It was decided that due to its superior versatility, lack of blockages and the possibility of using semi-prep purification the GE TRACERlab FX<sub>FN</sub> synthesizer represented the best choice of module system.

Table 6. Advantages and disadvantages of microfluidic vs. batch automated synthesisers

	<b>Advantages</b>	<b>Disadvantages</b>
GE TRACERlab FX <sub>FN</sub>	Reproducibility Robust methods No blockages of PE tubing (I.D. of 1 mm) HPLC purification	One set of reaction conditions possible per batch of activity Only one reactor (vial) available for synthesis
Advion NanoTek Flow micro-reactor	Fast optimization of reaction conditions Multiple reactions possible with one batch of radioactive material Superheating solvents by increasing their boiling point using backpressure regulators	Frequent blockages due small internal diameter tubes (0.14 mm I.D.)

## 2.2 Synthesis of precursors to prosthetic groups

The two iodonium precursors **1** and **2** (from Figure 13.) were received from Dr Mike Carroll (Newcastle University) and were used without further purification. Precursor **1** was used for the production of [<sup>18</sup>F]SFB, **2** is a precursor for the production

of [ $^{18}\text{F}$ ]FPPD and was received with its own HPLC standard. *N*-succinimidyl 4-fluorobenzoate (**6**), the standard reference for fluorination of precursor **1**, was synthesised in-house. Precursors **3**, **4** and **5** were synthesised in-house along with the appropriate standards **6**, **7**.

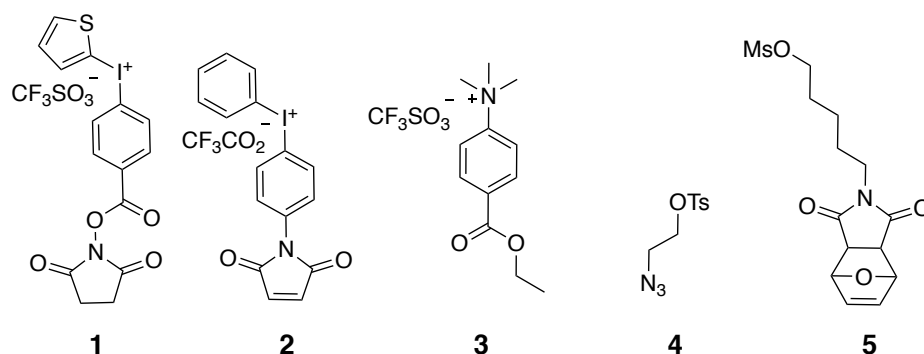
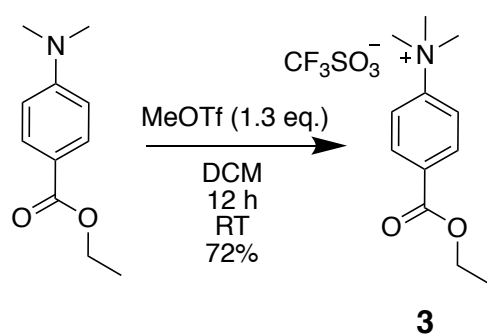


Figure 13. Precursors arranged in the order that were considered for  $^{18}\text{F}$ -fluorination in this study. Compounds **1** and **3** are precursors for [ $^{18}\text{F}$ ]FBEM, **2** for [ $^{18}\text{F}$ ]FPPD, **4** for 2- [ $^{18}\text{F}$ ]fluoroethylazide and **5** for [ $^{18}\text{F}$ ]FPenM.

### 2.2.1 Precursors synthesis

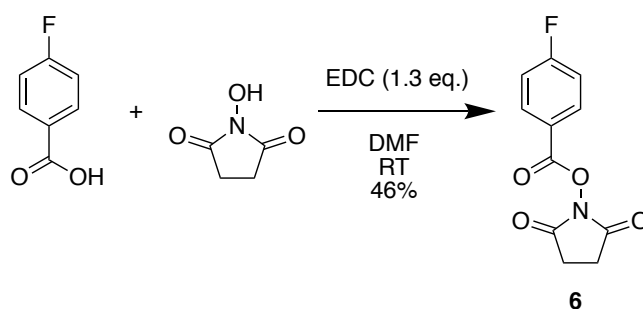
The synthesis of aryltrimethylammonium triflate **3** was from Guhle *et al.*'s work.<sup>225</sup> Methyl trifluoromethanesulfonate (1.3 eq.) was added to ethyl 4-(dimethylamino)benzoate and the product was filtered and recrystallised from  $\text{Et}_2\text{O}$  to give **3** in good yield (72%). (see Scheme 7)



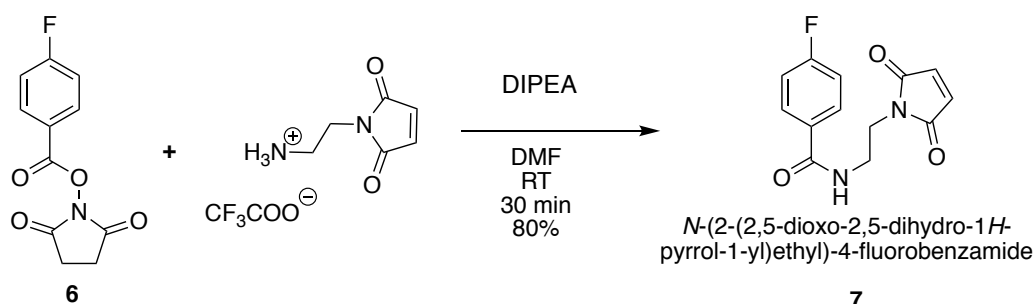
Scheme 7. Ethyl 4-(trimethylammonium triflate) benzoate precursor (**3**) synthesis

HPLC standards for [ $^{18}\text{F}$ ]SFB and [ $^{18}\text{F}$ ]FBEM production were required and these were synthesised according to Vaidyanathan and Zalutsky (1992)<sup>226</sup> and adapted from

Lacroix *et al.*<sup>213</sup> respectively. (Scheme 8, Scheme 9) 4-Fluorobenzoic acid was coupled to *N*-hydroxysuccinimide using EDC (1.3 eq.) dissolved in DCM. After a quick silica plug purification, the desired product **6** (Scheme 8.) was obtained as a white crystalline solid and was used to synthesise the other HPLC standards. *N*-(2-Maleimidylethyl)-4-fluorobenzamide standard **7** to validate [<sup>18</sup>F]FBEM synthesis was synthesised and purified by HPLC to yield a white solid (80%).

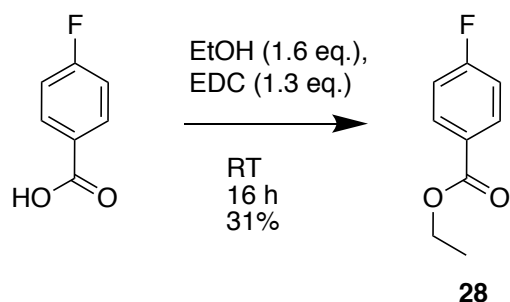


Scheme 8. Synthesis of *N*-succinimidyl 4-fluorobenzoate from 4-fluorobenzoic acid and *N*-hydroxysuccinimide.



Scheme 9. Synthesis of *N*-(2-maleimidylethyl)-4-fluorobenzamide HPLC standard **7**

An HPLC standard for the <sup>18</sup>F-fluorination step of benzoate precursor **3** was required. It was synthesised by esterification of 4-fluorobenzoic acid with ethanol using the carboxyl activating agent EDC (1-ethyl-3-(3-dimethylaminopropyl)carbodiimide) to yield ethyl 4-fluorobenzoate **28** (31%) . (Figure 8.)

Figure 14. Synthesis of ethyl 4-fluorobenzoate HPLC standard **28**

Precursors **4**, **8**, **9**, and **10** were synthesised by adapting the protocol reported by Evans *et al.*<sup>227</sup> 2-Azidoethanol and triethylamine (5 eq. excess) were stirred at room temperature for 12 hours with tosyl chloride (1.5 eq.). Flash column chromatography was used to purify the product and after solvent evaporation, the pure tosylate precursor **4** was isolated as a colourless liquid (83%).<sup>227</sup>

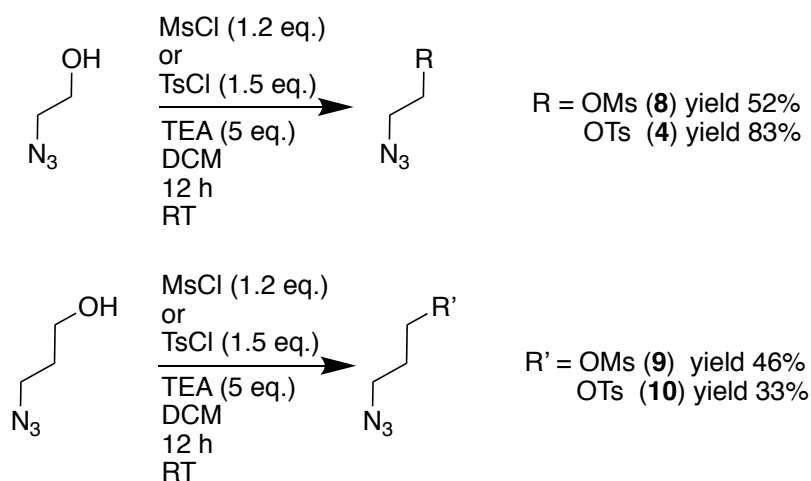


Figure 15. Azido sulfonate precursors synthesis

2-Fluoroethyl azide was synthesised for use as an HPLC standard. 2-Fluoroethanol was added to methanesulfonyl chloride (1.2 eq) and triethylamine (2 eq.) and the resultant mixture was stirred at room temperature under nitrogen for 16 hours. The solvent was evaporated *in vacuo* to yield crude 2-fluoroethyl methanesulfonate **8**, which was carried through to the next step without further purification. To a stirred solution of 2-fluoroethyl methanesulfonate in DMF, sodium azide (2 eq.) was added and the suspension was stirred at room temperature for 48 hours. The reaction mixture was filtered to remove the white precipitate (sodium azide). The filtrate was used without further purification as pure 2-

fluoroethyl azide is unstable and could decompose by explosion, therefore solvent was not removed.  $^1\text{H}$  and  $^{19}\text{F}$  NMR spectra were acquired to confirm production of the desired product and compared to a previously published synthesis.<sup>227</sup>

2-Azidoethyl sulfonate precursors **8-10** were also synthesised. Manual  $^{18}\text{F}$ -fluorination was tested with all of the precursors, however no significant improvement in conversion rates was observed hence precursor **4** was taken forward to automation. **4** was less volatile than the product, hence distillation can be used to purify and separate product 2- $^{18}\text{F}$ fluoroethylazide from its precursor.

### 2.2.2 Synthesis of precursors for $^{18}\text{F}$ FPenM

A more facile radiosynthesis was required for automation and ease of conjugation to C2Am. Labelling of a furan-protected maleimide was described in the Hamamatsu Photonics patent<sup>220</sup> and in Fujita's work<sup>210</sup>. These two publications describe furan-protected maleimides that are stable during basic  $^{18}\text{F}$ -fluorination conditions.

Three precursors, **5**, **14** and **25** (see Figure 16.) were synthesised by adapting Coleman's procedure.<sup>228</sup>

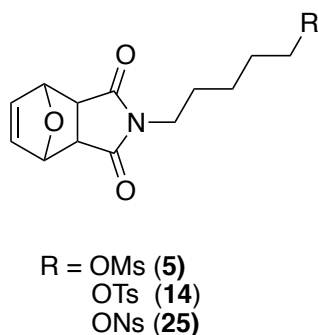


Figure 16. Three protected maleimide precursors synthesised in this study.

In order to explore the best yielding fluorination reaction three leaving groups have been used: mesyl **5**, tosyl **14** and nosyl **25**. Both **5** and **14** precursors were initially synthesised by Connor Willmington-Holmes (Part III student). More material was soon needed and therefore scale-up reactions have been required and were performed by myself. Of the three leaving groups, mesylate worked best (see below) and the synthesis of the mesylated precursor has since been further scaled-up for cGMP production and that

is the work presented here. Highly pure starting materials have been used and careful purification using an automated flash chromatography system has been performed in order to avoid any human-related errors and also to increase the reproducibility and robustness of the process. (Scheme 10)

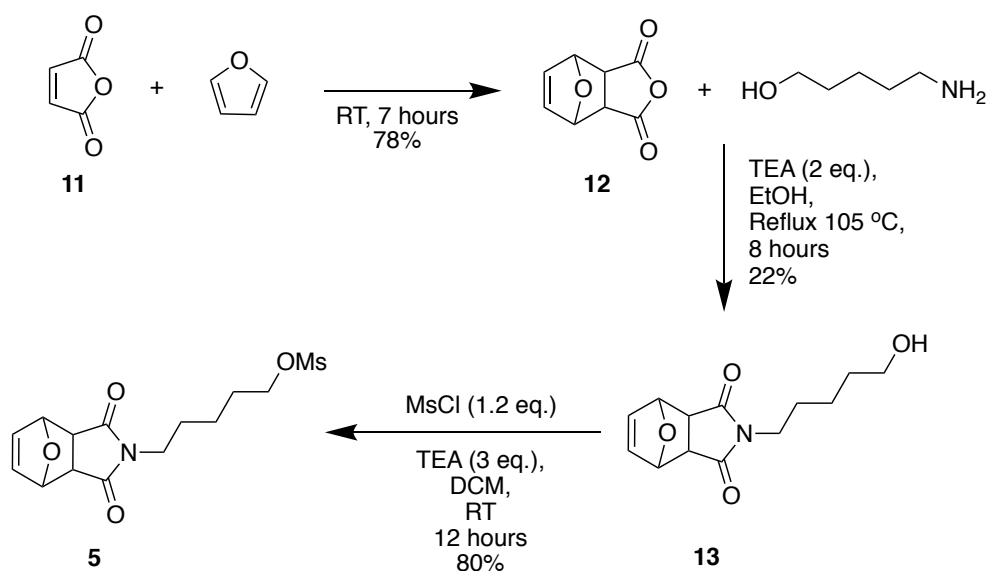
Maleic anhydride **11** was added to furan in a Diels-Alder reaction to yield furan protected maleic anhydride **12**. This reaction was adapted from a synthesis of maleimide polymers.<sup>229</sup> Purification by recrystallisation from ethyl acetate was sufficient to ensure good purity.

5-Aminopentan-1-ol and **12**, in the presence of triethylamine and EtOH were heated at 105 °C to induce cyclisation and promote elimination of water to form **13**. This method was based on Coleman *et al.*<sup>228</sup> but adaptations were made in an attempt to increase the yield. Despite lowering heat (*c.f.* 170-180 °C in Coleman *et al.*) to 105 °C yields were still very low (22%). Radical scavenging was not attempted as the previously mentioned papers attempted this using hydroquinone and p-t-butylcatechol and were unsuccessful.

It was noted that the part III student used lower temperatures (90 °C) and shorter times 4-6 h and yet obtained better yields (up to 50%). Therefore, it may be that heat induced polymerisation can be a major contributor to the poor yield.

Imide **13** was purified using flash column chromatography and reacted with either mesyl chloride, tosyl chloride or nosyl chloride to yield **5**, **14** and **25**. These were purified again using flash column chromatography to yield pure precursors ready for <sup>18</sup>F-labelling.

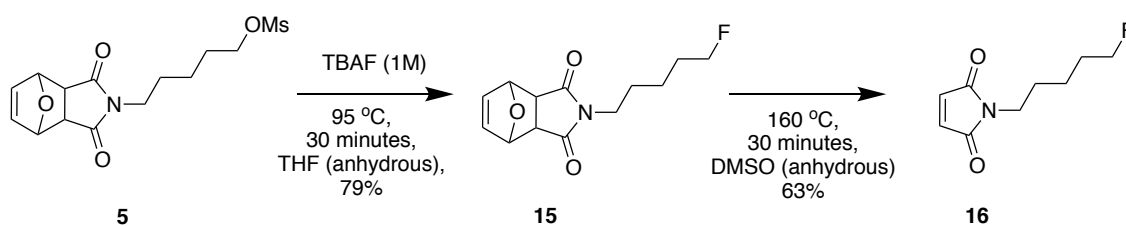




Scheme 10. Three-step synthesis of precursor **14**.

An *N*-(5-fluoropentyl)maleimide **16** HPLC standard was required to confirm the production of the equivalent radioactive molecule and to generate a concentration-absorbance calibration plot for determining its molar radioactivity.

A simple 2-step synthesis (Scheme 11) of the standard was followed to yield **16** as a volatile oil. (details in Subsection 2.6.1) The first step was to fluorinate mesylate **5** using tetrabutylammonium fluoride (TBAF) for nucleophilic substitution ( $S_N2$ ) replacing the methanesulfonate leaving group yielding **15** in a good yield. This was purified by flash column chromatography. Furan-protected maleimide **15** was dissolved in a high boiling point aprotic solvent (DMSO) and heated at 160 °C to remove the furan protecting group and to yield **16**. The temperature required for the retro Diels-Alder deprotection step does cause polymerisation, reducing the yield therefore limiting the duration of the reaction increased the yield.<sup>230,228</sup> Finally, **16** was purified by flash column chromatography and used as an HPLC standard for radiosynthesis.



Scheme 11. Synthetic route to *N*-(5-fluoropentyl)maleimide **16**.

C2Am (1.29 mM) freshly reduced was added to **16** (9  $\mu$ M,  $\sim$ 1000 eq.) in PBS to yield FPenM-C2Am conjugate standard for HPLC analysis. Conjugated protein was purified by spin filtration (Amicon Ultra 0.5 mL 3 kDa centrifugal filter cartridge) and concentrated to a final solution of FPenM-C2Am (1.29 mM). Mass spectrometry on the protein samples were run on a Waters Xevo SQR2 instrument to confirm the mass of the conjugate ( $m/z = 16408.5$  [MH]<sup>+</sup>).

### 2.2.3 Kinetics of *N*-(5-fluoropentyl)maleimide conjugation with L-glutathione

As described in section 2.1.1 maleimides react readily with solvent exposed thiols through Michael-addition to generate covalently linked conjugates. The rate constant for the Michael-addition conjugation reaction of L-glutathione (GSH) with **16** was determined by stopped-flow UV spectroscopy.

Overlaid UV-vis spectra of GSH (1 mM) and **16** (1 mM; 0.5 mM)

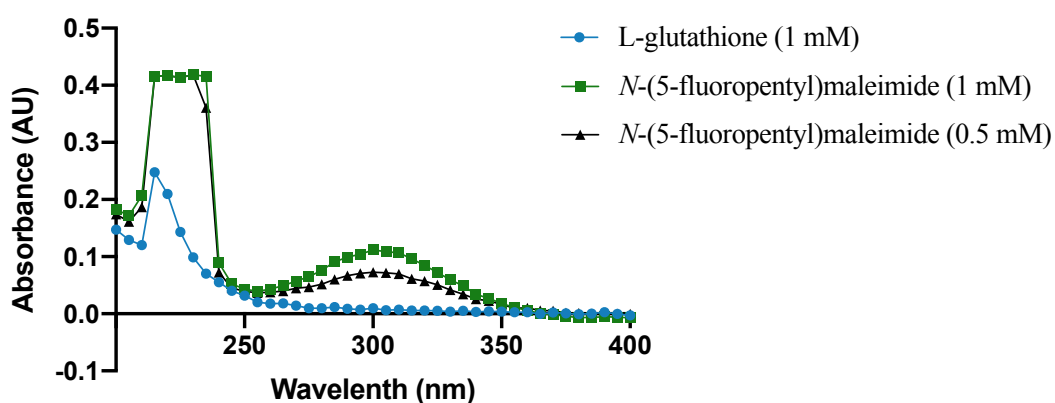


Figure 17. Superimposed UV-vis (200 to 400 nm) spectra of **16** (1 mM and 0.5 mM) and GSH (1 mM). **16** absorbs light at 300 nm while GSH does not.

Kinetic experiments were performed on an automated SX18.MV stopped flow spectrometer, which can analyse reactions that reach equilibrium within milliseconds of mixing. GSH and **16** were mixed in different concentrations in a 1:1 ratio as detailed in Table 7. Further details of the experiment can be found in the Experimental 2.6.1 and Table 11.

Maleimide conjugation to thiolates is a second order reaction and first order with respect to each reactant.<sup>231</sup>

$$\text{Reaction rate} = k [\text{GSH}] [N\text{-}(5\text{-fluoropentyl})\text{maleimide}]$$

Where  $k$  is the rate constant. As GSH and **16** have the same initial concentrations and react in a 1:1 ratio, the rate law becomes

$$\text{Reaction rate} = k [N\text{-}(5\text{-fluoropentyl})\text{maleimide}]^2$$

Finally, the integrated rate law is:

$$\frac{1}{[N\text{-}(5\text{-fluoropentyl})\text{maleimide}]_t} = kt + \frac{1}{[N\text{-}(5\text{-fluoropentyl})\text{maleimide}]_0}$$

By plotting  $1/[N\text{-}(5\text{-fluoropentyl})\text{maleimide}]$  against time, the rate constant  $k$  is equal to the slope of the graph (Figure 18., Figure 19., Figure 20.). Experiments were run in triplicate and the rate constant  $k$  is an average of the three runs shown in Figure 18, Figure 19 and Figure 20. Rate constants are displayed in Table 7.

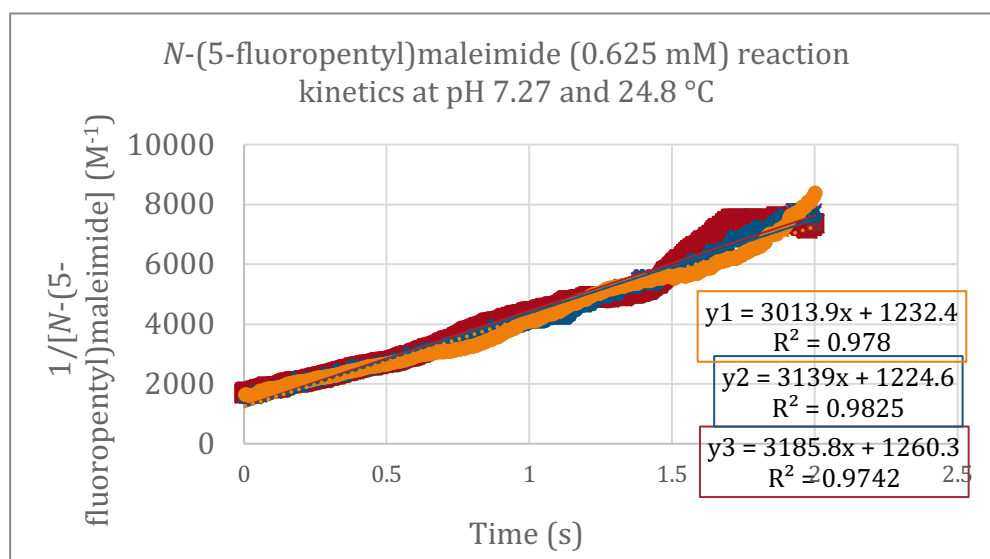


Figure 18. Plot showing  $1/\mathbf{16}$  concentration with time following conjugation with GSH at pH 7.27 and 24.8 °C. Initial concentration of **16** = GSH = 0.625 mM

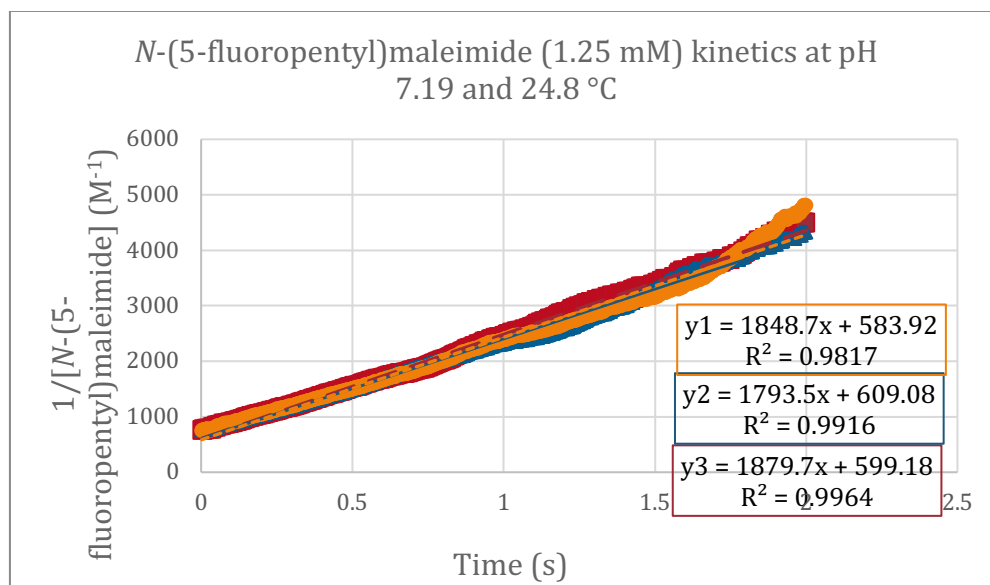


Figure 19. Plot showing 1/**16** concentration with time following conjugation with GSH at pH 7.19 and 24.8 °C. Initial concentration of **16** = GSH = 1.25 mM

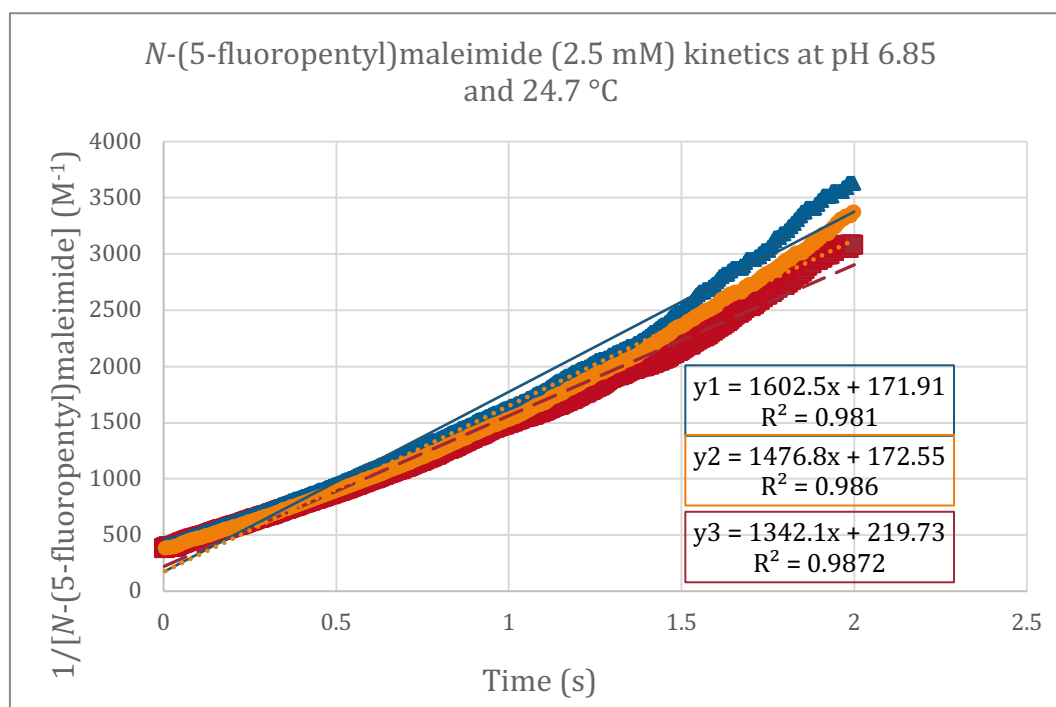


Figure 20. Plot showing 1/**16** concentration with time following conjugation with GSH at pH 6.58 and 24.7 °C Initial concentration of **16** = GSH = 2.5 mM

Table 7. Kinetics of **16** conjugation with GSH and the effects of pH

Initial [GSH] <sub>0</sub> and [N-5-fluoropentylmaleimide] <sub>0</sub>	Average rate constant k (M <sup>-1</sup> s <sup>-1</sup> )	Final solution pH	Temperature (°C)
2.5 mM	1474 ± 106	6.85	24.7
1.25 mM	1841 ± 36	7.19	24.8
0.625 mM	3113 ± 73	7.27	24.8

The effects of pH described in literature are consistent with the experimental data shown in Table 7. Higher pH leads to an increase in the rate constant due to increased thiolate concentration. Finally, the reaction time required for the conjugation to reach 90% completion is less than 5 seconds at pH 7.19 and 1 mM; therefore, the speed of maleimide conjugation is more than sufficient for the purpose of labelling proteins.

The conjugation product of **16** and GSH (Experimental 2.6.1) was analysed by NMR, LC-MS and accurate mass ESI. (spectra attached in the Appendix 8.21)

## 2.3 Radiosynthesis of prosthetic groups

All protocols for the synthesis of <sup>18</sup>F-labelled functional groups were developed at the Molecular Imaging Chemistry Laboratory (MICL) in the Wolfson Brain Imaging Centre (WBIC) on the Cambridge Biomedical Campus.

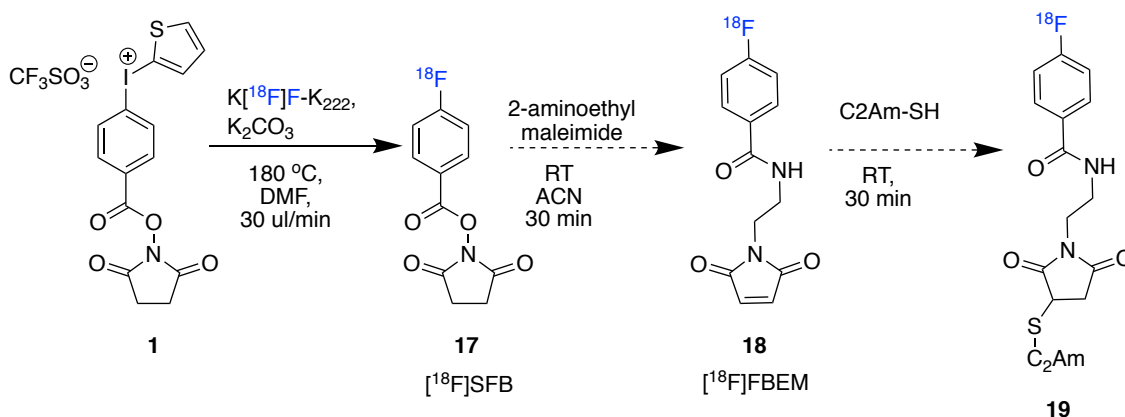
### 2.3.1 <sup>18</sup>F-Fluorination of iodonium salts to yield [<sup>18</sup>F]SFB

Initially, a high-risk high-reward project was initiated by <sup>18</sup>F-labelling iodonium triflate (**1**, Scheme 12), synthesised by Carroll's lab (Newcastle), to obtain [<sup>18</sup>F]SFB **17**<sup>232</sup>,<sup>233</sup> followed by amide bond formation with *N*-(2-aminoethyl)maleimide to yield the [<sup>18</sup>F]FBEM **18**. This would then be used to conjugate to C2Am. <sup>18</sup>F-Fluorination of diaryliodonium salts promised to reduce the synthesis time and simplify the production protocol for [<sup>18</sup>F]SFB compared to the traditional 3-step multi-pot method. <sup>18</sup>F-labelling was attempted by both manual synthesis and a module-assisted microfluidic synthesis rig in order to generate [<sup>18</sup>F]FBEM. We wanted to reproduce Carroll *et al.*'s paper<sup>217</sup> and Olma and Shen's patent<sup>218</sup> by <sup>18</sup>F-fluorination of 2-thiophenyl iodonium triflate and

automate the production process using either the Advion NanoTek microfluidic system or the batch synthesiser GE TRACERlab FX<sub>FN</sub>.

Initially, manual <sup>18</sup>F-fluorination of **1** (3 mg in DMF) was attempted at 130 °C in DMF for 10 minutes, however no peaks other than that of K<sub>222</sub>, K[<sup>18</sup>F]F were observable on the radio-HPLC chromatogram.

Upon using the NanoTek Advion liquid flow reactor, <sup>18</sup>F-fluorination of **1** generated one peak (9.7 min) other than the K[<sup>18</sup>F]F peak (4.1 min), as shown on radio chromatograms in Figure 21. The peak at 9.7 min was only generated at high temperatures, 180 or 190 °C and slow flow rate (5 μL/min) through the heated coil reactor loop. Conversion was very poor at 160 °C but the results were consistent with the remarks of Reed *et al.*<sup>233</sup>



Scheme 12. Proposed labelling of C2Am using <sup>18</sup>F-labelling of iodonium precursor **1**.

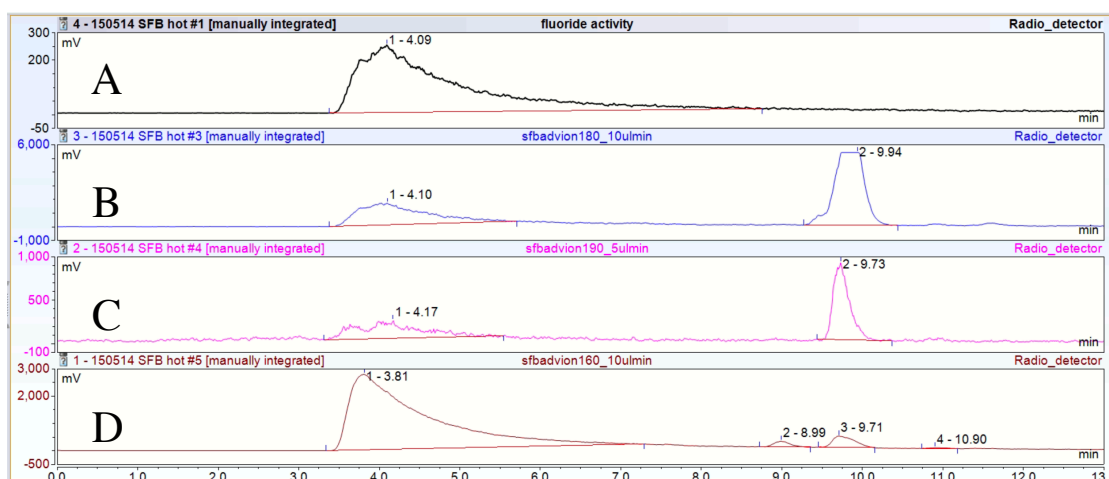


Figure 21. Radio-chromatograms of 4 samples post Advion synthesis of [ $^{18}\text{F}$ ]SFB starting from iodonium precursor **1**. The radio-chromatograms show:  $^{18}\text{F}$ -fluoride only (**A**); then reaction mixtures heated at 180 °C (**B**), 190 °C (**C**) and 160 °C (**D**).

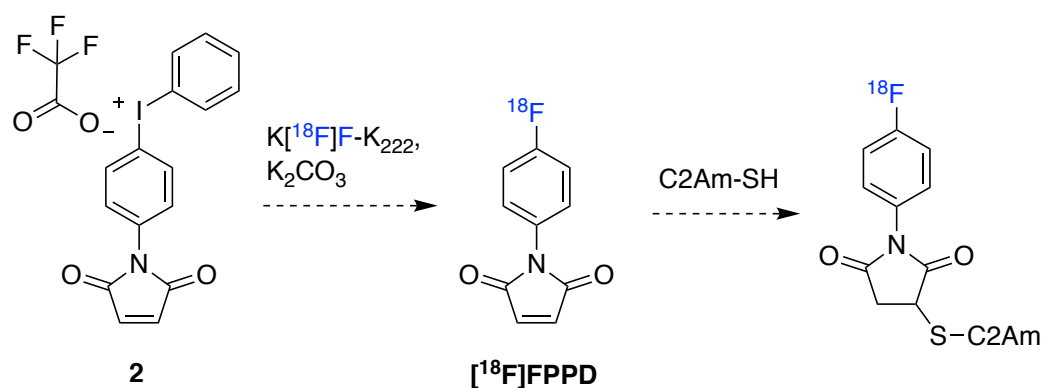
However, this peak did not match the UV peak of the SFB HPLC standard. Hence the production of [ $^{18}\text{F}$ ]SFB could not be confirmed. However, SFB is prone to hydrolysis under reverse-phase HPLC aqueous conditions. It is therefore believed that the HPLC conditions may have degraded the SFB. The HPLC should have been run using a normal phase column, which was not available at that time.

Finally, the process was abandoned as a result of line blockages occurring every run. This was consistent with the remarks of Reed *et al.*<sup>234</sup> Blockages still occurred frequently despite an increase in backpressure from 250 psi to 350 psi. These were probably caused by insoluble potassium bicarbonate, which blocked the very narrow microfluidic lines (ID = 0.14 mm).

In the meantime, iodonium trifluoroacetate precursor **2** arrived from the Carroll laboratory. This already contained a maleimide attached to the para position of the aryl moiety of the iodonium salt. (Scheme 13.)

This is another very interesting radiotracer to label C2Am due the possibility of a one-step fluorination. Unfortunately, after several attempts it was concluded that no product can be isolated and this could be due to the harsh basic conditions that hydrolyse the maleimide. This is not the only reason. It is known that electron-withdrawing groups linked to the nitrogen heteroatom of the maleimide decrease their stability to hydrolysis.

Therefore, it would have been very challenging to produce a maleimide radiotracer directly from an iodonium precursor without protecting the maleimide moiety from  $F^-$  and  $OH^-$  attack.



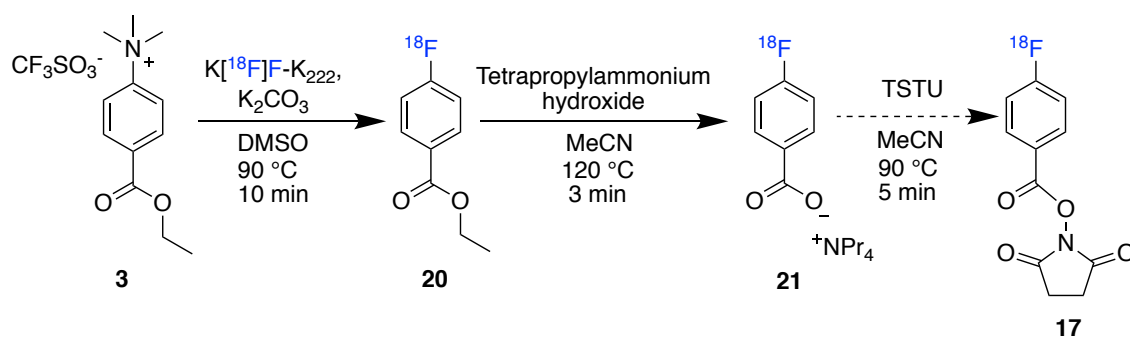
Scheme 13. Proposed fluorination of precursor **2** and conjugation to C2Am

Following the problems with blockages with the narrow microfluidic lines on the Advion, the batch synthesiser GE TRACERlab FX<sub>FN</sub> was considered a better choice of automated equipment. The radiosynthesis that follows was optimised for the TRACERlab FX<sub>FN</sub>.

### 2.3.2 Production of [<sup>18</sup>F]SFB by <sup>18</sup>F-fluorination of ethyl 4-(trimethylammonio)benzoate

Ethyl 4-(trimethylammonio)benzoate (precursor **3**, see Scheme 14) was used for manual [<sup>18</sup>F]SFB synthesis. The first <sup>18</sup>F-fluorination step occurred with excellent conversion (>95%) following manual synthesis. It was then decided to automate the sequence. However due to the complicated protocol of Cai *et al.*<sup>208</sup>, a dual reactor setup was required to separate the aqueous saponification steps, using NaOH and HCl (later using Scott and Shao's protocol<sup>235</sup> with TPAH), from anhydrous *N*-hydroxysuccinimide addition.





Scheme 14. Automated synthesis of [ $^{18}\text{F}$ ]SFB, inspired by the work of Scott and Shao (2010).<sup>235</sup>

The GE TRACERlab FX<sub>FN</sub> synthesis rig was modified to couple an externally heated Wheaton V-vial acting as an external reactor. Initially, this system was modified for  $^{18}\text{F}$ -labelling of precursor **3**. We sought to separate the  $^{18}\text{F}$ -fluorination from the rest of the synthesis to facilitate purification, monitoring of subsequent products and avoiding time consuming reactor cleaning steps. Therefore, the second reactor was intended to be used for ester hydrolysis, succinimidyl formation and *N*-(2-aminoethyl)maleimide coupling. This reactor also had remote temperature control functionality thus subsequent steps that required variable temperatures could be completed.

The radiosynthesis was automated up to the point of product **20** (conversion rate 74%, Figure 22.) and hydrolysis of the ethyl ester to [ $^{18}\text{F}$ ]FBA was attempted but could not be confirmed against the fluorobenzoic acid standard due to quick elution on a reverse phase HPLC column.

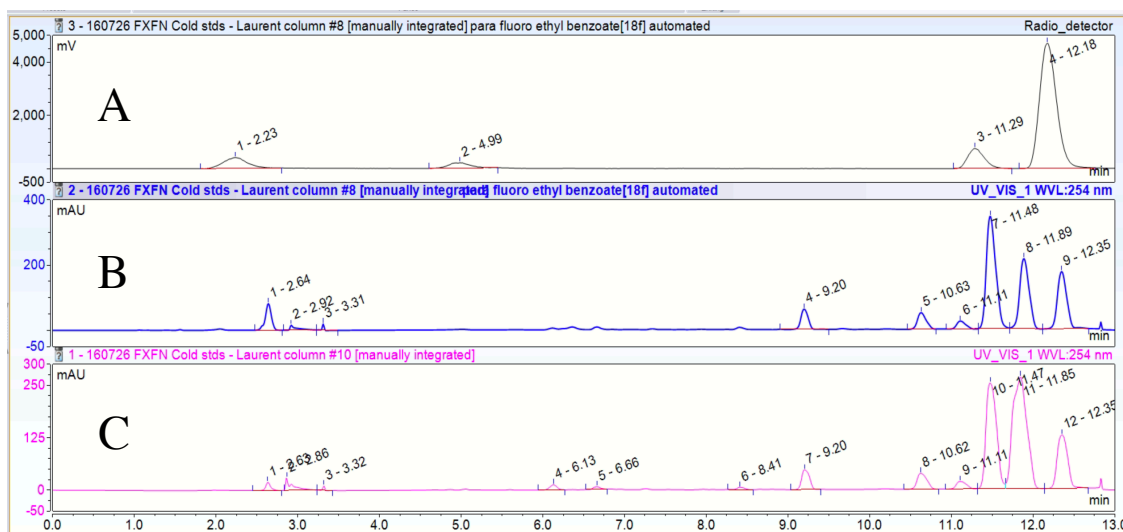


Figure 22.  $^{18}\text{F}$ -fluorination of precursor **3**. Radio-chromatogram (A) showing ester **20** eluting at 12.1min (peak 4). UV chromatogram (B) showing UV absorbance (254 nm) of the crude  $^{18}\text{F}$ -fluorination reaction to yield **20** (peak 8 at 11.8 min). UV chromatogram (C) showing UV absorbance (254 nm) of the crude  $^{18}\text{F}$ -fluorination reaction to yield **20** co-injected with ethyl 4-fluorobenzoate standard **28** (peak 9 at 11.8 min).

The dual reactor automated system setup is shown in Figure 23. Modifications from the standard setup (shown in Figure 24) were as follows:

The external V-vial reactor was manually set to 95 °C before the start of synthesis and this temperature was adequate for both drying target water containing fluorine-18 and for  $^{18}\text{F}$ -fluorination of precursor **3**. For this to happen, 4 lines were set up through the septum lid:

1. Helium line for drying and pressurising reactor 1 – line coming from V31 from the HPLC bottles was used;
2. Vacuum for drying the fluoride was provided through a line going to reactor 2, which is directly coupled to the vacuum pump. A charcoal trap was also set-up between the two reactors to prevent any gaseous contamination of the second reactor. A manually controlled valve was installed along this line to control/limit vacuum to reactor 2 when required, for example when transferring contents from reactor 1 to reactor 2 by vacuum.

3. Line connecting vial 1 (Kryptofix K<sub>222</sub> solution) through V13, was moved to reactor 1 to dispense <sup>18</sup>F from QMA directly into the external reactor 1. Line connecting vials 2 and 3 were joined with line 1 and moved to reactor 1 to be able to dispense dry ACN and precursor to the external reactor 1.

4. A line connecting the two reactors was set up to allow content transfer and was controlled externally by a 2-way valve.

It was quickly recognised that the next precursor, furan-protected maleimide precursor yielding [<sup>18</sup>F]FPenM, was a much better alternative to the extensive protocol required to synthesise [<sup>18</sup>F]FBEM.

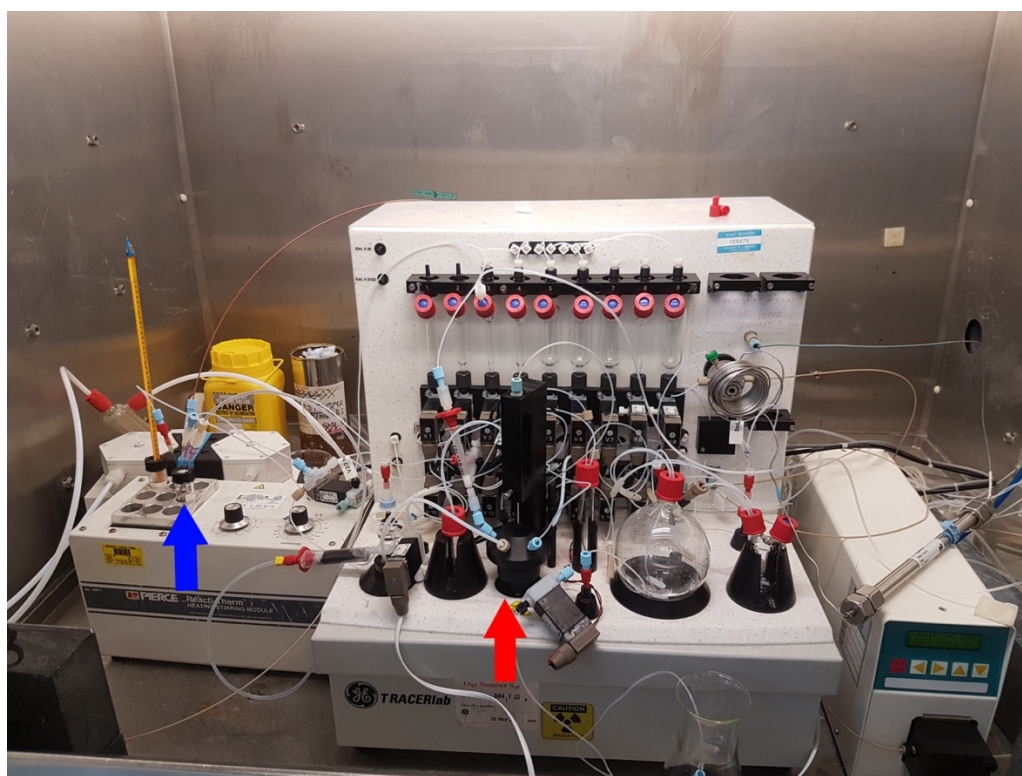


Figure 23. GE TRACERlab FX<sub>FN</sub> modified to mimic a GE TRACERlab FX<sub>N</sub> PRO (dual reactor) automated synthesizer. Picture showing reactor 1 (blue arrow – left) and reactor 2 (red arrow - right)

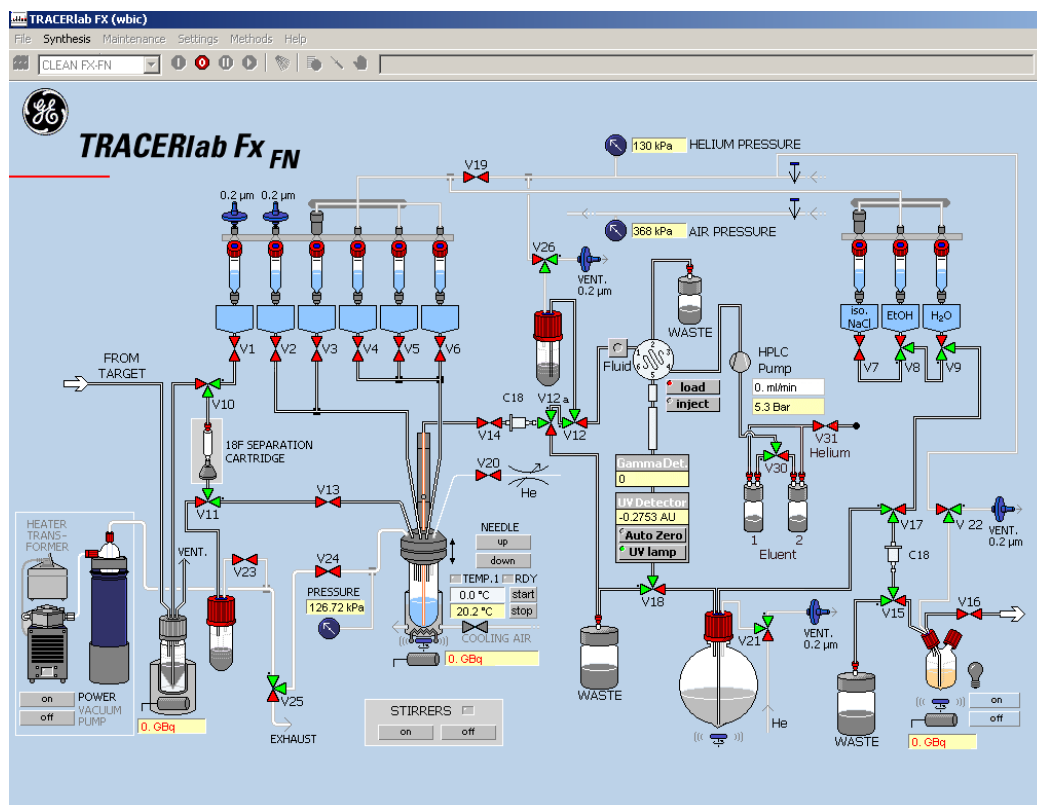


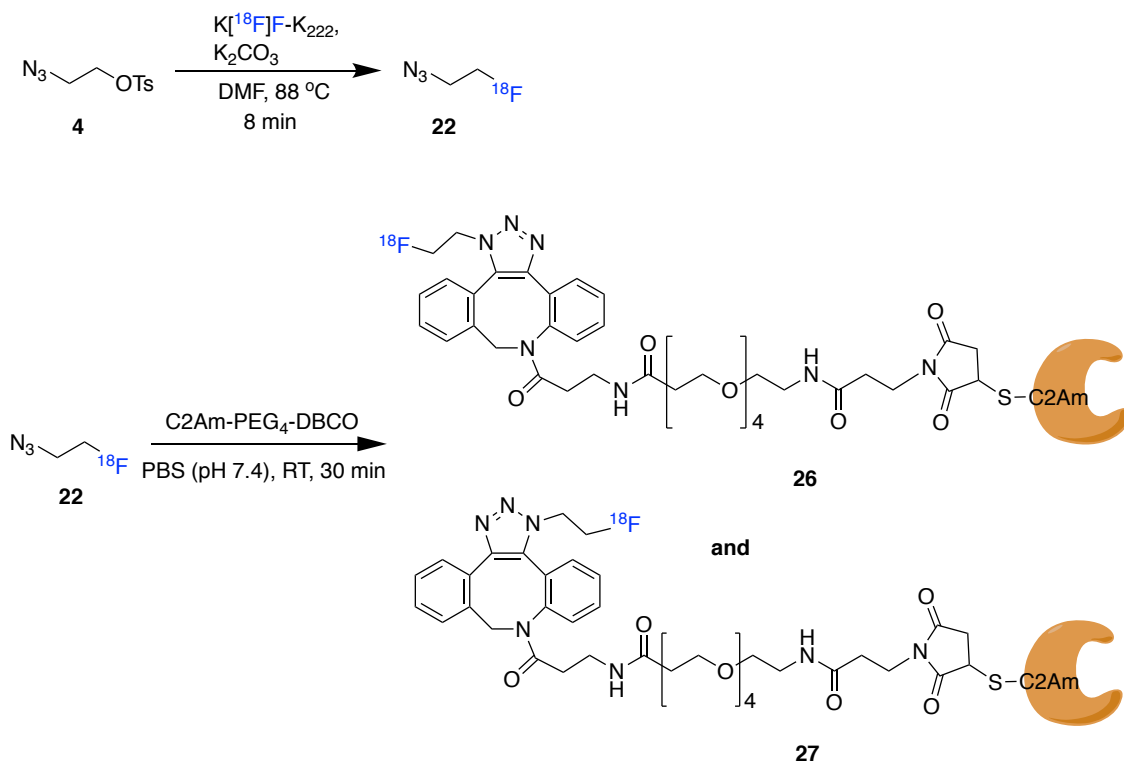
Figure 24. GE Healthcare TRACERlab Fx<sub>FN</sub> control screen showing the default line connections. These were modified to accommodate an external reactor as described in the text.

### 2.3.3 2-[<sup>18</sup>F]Fluoroethylazide

An alternative to [<sup>18</sup>F]FBEM conjugation to C2Am is to use a bioorthogonal copper-free click reaction. An attempt to label a strained cyclooctyne (DBCO) prosthetic group on C2Am-maleimide-PEG<sub>4</sub>-DBCO with 2-[<sup>18</sup>F]fluoroethylazide was made using the strain promoted azide-alkyne cycloaddition reaction (SPAAC).

Initially, both mesylate and tosylate precursors were manually <sup>18</sup>F-labelled to yield 2-[<sup>18</sup>F]fluoroethylazide and the RCY of the reactions were analysed by HPLC.<sup>236</sup> The tosylate was chosen as it facilitated separation by vacuum distillation of 2-[<sup>18</sup>F]fluoroethyl azide from the less volatile tosylate precursor. The equivalent propyl mesylate and tosylate precursors were also <sup>18</sup>F-labelled but these required HPLC purification, which is a time-consuming process, so these precursors were not used for further studies.

An automated synthesis using the GE Healthcare TRACERlab FX<sub>FN</sub> module was employed, followed by manual vacuum distillation, to yield 2-[<sup>18</sup>F]fluoroethylazide with >99% radiochemical purity and 8±3% RCY yield (decay corrected, n = 3) (see radiochromatogram in Figure 25).<sup>214,237,173</sup>



Scheme 15. Labelling C2Am using the 2-[<sup>18</sup>F]fluoroethylazide precursor. <sup>18</sup>F-labelled product of **4** was distilled to yield 2-[<sup>18</sup>F]fluoroethylazide (**22**) (top reaction). C2Am-PEG<sub>4</sub>-DBCO was conjugated to **22** to yield [<sup>18</sup>F]C2Am-PEG<sub>4</sub>-DBCO as a mixture of regioisomers (**26** and **27**).

C2Am derivatised with a strained alkyne (dibenzocyclooctyne-amine) was labelled with 2-[<sup>18</sup>F]fluoroethylazide via copper-free SPAAC. (see Scheme 15) C2Am-PEG<sub>4</sub>-DBCO (4.5 mg/ml, 278 μM) labelling with **22** was achieved but the conversion was very low (see Figure 26). This is believed to be due to the purification method used to purify 2-[<sup>18</sup>F]fluoroethylazide. Distillation was employed to separate the volatile radiotracer from its precursor. While this is a time-efficient method, an impurity, possibly azidoethene, which resulted from elimination of the tosylate group, is believed to be distilled with the radiotracer (see Figure 25). This can compete with 2-[<sup>18</sup>F]fluoroethylazide for the click reaction with C2Am-PEG<sub>4</sub>-DBCO.

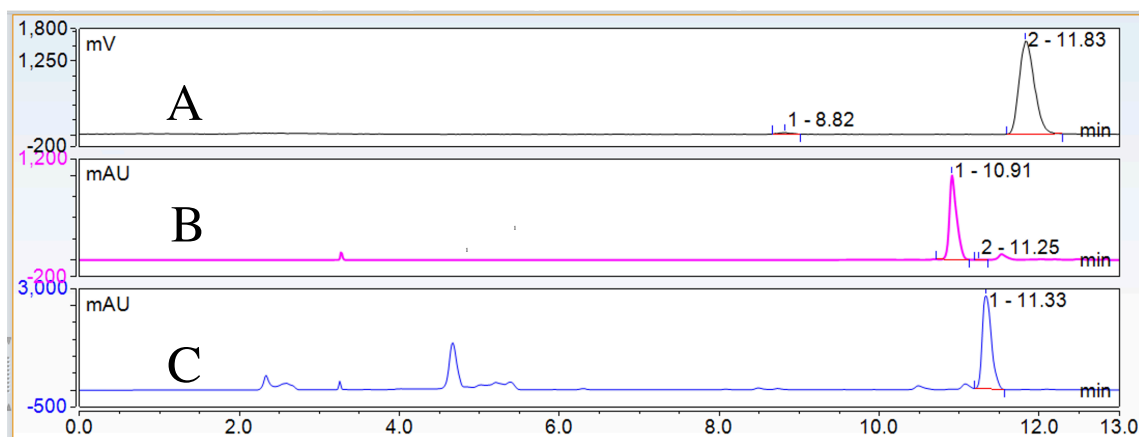


Figure 25. HPLC analysis of distilled 2-[ $^{18}\text{F}$ ]fluoroethylazide.

showing radioactive azide at 11.8 min (top radio chromatogram), possible azido ethene at 10.9 min (B UV at 254 nm chromatogram) and 2-fluoroethylazide HPLC standard (bottom UV at 254 nm chromatogram) showing the azide peak at 11.3 min.

The radio-chromatogram of 2-[ $^{18}\text{F}$ ]fluoroethylazide clicked to the C2Am-PEG<sub>4</sub>-DBCO is shown below (Figure 26). The radiopeak at 11.8 min correlates with UV at 280nm peak of the protein at 11.4 min.

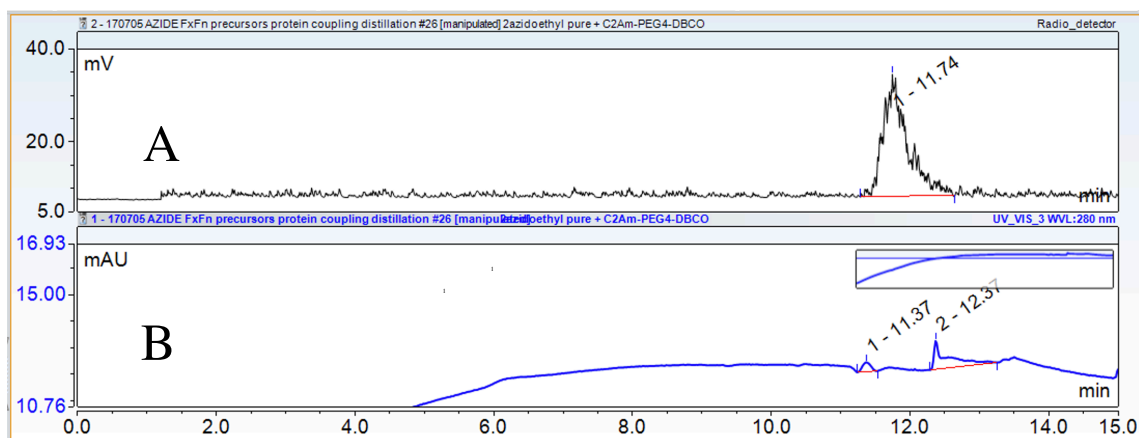


Figure 26. Radio-HPLC chromatogram of the crude click reaction between 2-[ $^{18}\text{F}$ ]fluoroethyl azide and C2Am-PEG<sub>4</sub>-DBCO. The peak at 11.8 min in the radiochromatogram A is the  $^{18}\text{F}$ -labelled C2Am. Chromatogram B (UV 280nm) shows C2Am-PEG<sub>4</sub>-DBCO as a mix of stereoisomers **26** and **27** at 11.4 min.

2-[ $^{18}\text{F}$ ]Fluoroethylazide, being a small molecule, was retained by the size exclusion column designed for separating proteins. Therefore, the click conjugation yield

could not be determined as the 2-[<sup>18</sup>F]fluoroethylazide peak could not be observed within the time frame of the isocratic elution (15 min). Most of the activity was found to be retained on the column. Judging by the low counts of peak 1 in the radiochromatogram in Figure 26 and the fact that most of the activity injected on the column was retained, it was clear that the copper-free click reaction had a very low conversion yield.

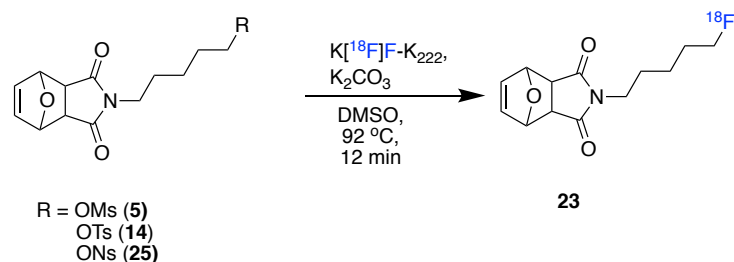
This is supported by the data shown by Evans *et al.* 2012 where 2-[<sup>18</sup>F]fluoroethylazide reacting with different strained cyclooctynes showed very low conversion, even after being heated up to a range of temperatures: 40-90 °C. The only successful reaction in their case was the fastest reacting cyclooctyne, DIFO, which was reacted with 2-[<sup>18</sup>F]fluoroethylazide in acetonitrile (incompatible with proteins) at 90 °C (again too high for proteins) to obtain a good yield (higher than the rest of the cyclooctynes) of 97% and 62% at 40 °C.<sup>227</sup>

#### 2.3.4 Manual production of *N*-(5-[<sup>18</sup>F]fluoropentyl)maleimide ([<sup>18</sup>F]FPenM)

Furan protected maleimide radioactive prosthetic groups promise to be an excellent alternative to the classic [<sup>18</sup>F]FBEM bifunctional group as they are faster and easier to prepare.

This study has combined the incompletely described radiosynthesis of [<sup>18</sup>F]FPenM in the Hamamatsu patent<sup>220</sup> with suggestions from Fujita's work<sup>210</sup>. After formulation in an aqueous buffer, it can be conjugated to thiol-containing biomolecules.

Initially, mesylate **5** was manually <sup>18</sup>F-labelled and gave an excellent radio-HPLC yield in excess of 96%. It was presumed that better leaving groups such as tosyl and nosyl would result in an increased conversion rate. In search of a better conversion yield, tosyl and nosyl precursors were synthesised. These three precursors (see Scheme 16) were tested in parallel by manual <sup>18</sup>F-labelling and the conversion rates monitored by radio-HPLC.



Scheme 16. The three precursors with three different leaving groups that were  $^{18}\text{F}$ -labelled manually.

The first step,  $^{18}\text{F}$ -labelling of the precursor, was described in the patent<sup>220</sup> as occurring between 60-100 °C in 10-15 minutes. The  $^{18}\text{F}$ -labelling conditions attempted in this work were 92 °C, for 10 and 15 minutes and using 5 or 10 mg of precursor. There was a slight increase in conversion between 10 and 15 minutes therefore a middle point of 12 minutes was chosen as the ideal time for labelling. There was no difference in labelling between 5 and 10 mg of precursor therefore 5 mg precursor was adopted, making the process slightly less expensive. Finally, the highest conversion rate, according to the radio-HPLC chromatograms, was observed with the mesylate precursor (>96%). (see Figure 27. and Table 8.

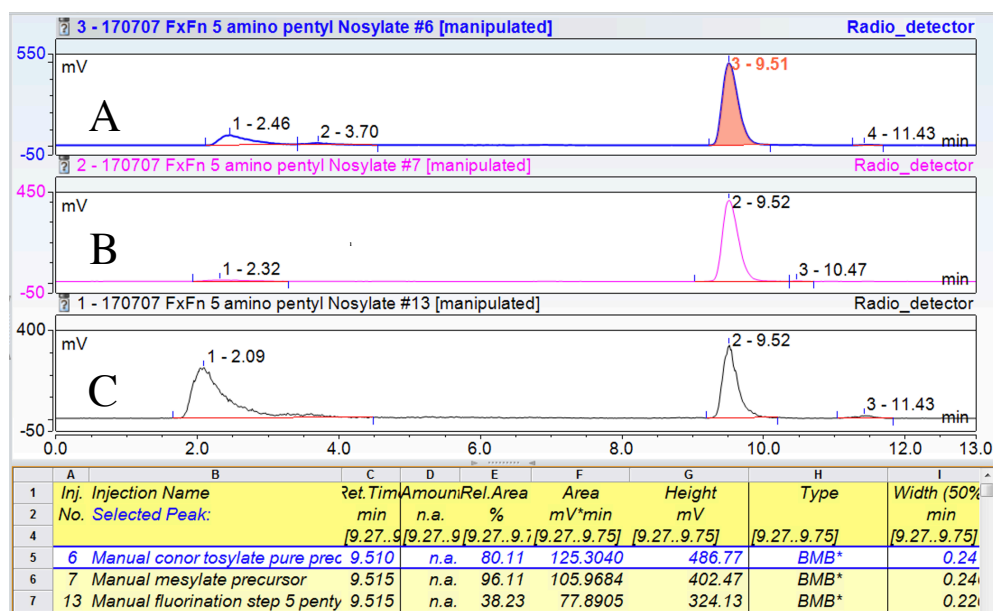


Figure 27. Three radio-chromatograms showing  $^{18}\text{F}$ -labelling of precursors: tosylate **14** (A), mesylate **5** (B), **25** (C) to yield the furan protected maleimide **23**. Peak at 2.3 min represents unreacted  $\text{K}[^{18}\text{F}]\text{F}$  and peak at 9.5 min represents  $^{18}\text{F}$ -fluorinated maleimide **23**.



Table 8. The radio-HPLC conversion yield of three precursors upon  $^{18}\text{F}$ -fluorination using optimised reaction conditions (92 °C, 12 minutes, 5 mg precursor in DMSO)

Precursor	Radio-HPLC conversion (%)
5 (OMs)	96
14 (OTs)	80
25 (ONs)	38

The second step, thermal deprotection of the maleimide by retro-Diels Alder removal of the furan moiety, was described in the patent as occurring between 100-160 °C but preferably between 120-130 °C within 5 to 20 minutes however ideally, 10 to 15 minutes was sufficient. At no point did the patent describe the thermal instability at high temperatures of the maleimides formed. Fujita's work addresses this problem by adding methanesulfonic acid to acidify the solution and inhibit degradation by hydrolysis of the maleimide moiety.

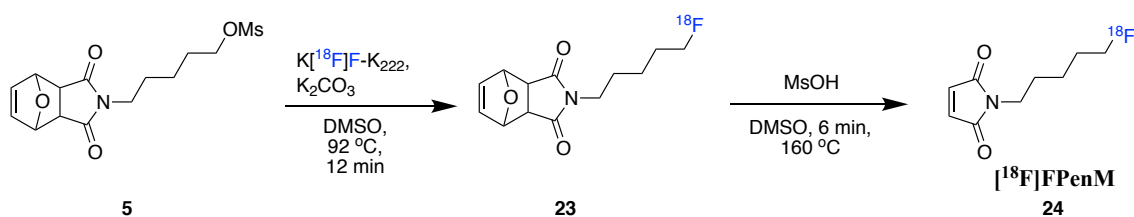
Deprotection temperatures of 120, 150 and 160 °C were investigated for a limited amount of time (6 min) to reduce the possibility of polymerisation of the maleimide. It was concluded that 160 °C is required to completely remove the furan protection within 6 minutes. Despite the high temperatures, no decomposition was observed during the manual synthesis.

The 2-step, single pot preparation (process described before in Scheme 6.) of [ $^{18}\text{F}$ ]FPenM requires 58 minutes (c.f. 95 minutes for production of [ $^{18}\text{F}$ ]FBEM). It is also a simpler process needing 2 steps (fluorination, deprotection) thus fewer starting reagents are required. This requires less reagent vials on an automated system therefore automated systems such as the GE TRACERlab FX<sub>FN</sub> can be used.

### 2.3.5 Automated radiosynthesis of [ $^{18}\text{F}$ ]FPenM for pre-clinical imaging

After optimisation of  $^{18}\text{F}$ -fluorination reaction conditions such as: precursor concentration, temperatures and time required for the 2-step production of [ $^{18}\text{F}$ ]FPenM using manual synthesis, an automated protocol was developed at the Molecular Imaging Chemistry Laboratory (MICL). The remote controlled synthesis rig GE TRACERlab

FX<sub>FN</sub> was used for this purpose following general reaction conditions from the only two patents covering furan protected maleimides.<sup>238,220</sup>



Scheme 17. Reaction scheme for synthesising **24** (*N*-(5-[<sup>18</sup>F]fluoropentyl)maleimide ([<sup>18</sup>F]FPenM)).

Using a preprogrammed sequence to produce [<sup>18</sup>F]FPenM (Appendix 8.2), the maximum activity of [<sup>18</sup>F]fluoride target water was obtained from the Cambridge University cyclotron, complying with the holding capacity specified by the license issued by the UK's Environmental Agency (<30 GBq). [<sup>18</sup>F]Fluoride was trapped on a Sep-Pak QMA cartridge and eluted with Kryptofix 222<sup>®</sup> (known as K<sub>222</sub>) and K<sub>2</sub>CO<sub>3</sub> in ACN/water to increase the reactivity of the fluoride. K<sub>222</sub> dissolved in organic dry solvents is used to provide free fluoride (F<sup>-</sup>) ions by complexing the K<sup>+</sup> ions.<sup>239</sup> K[<sup>18</sup>F]F was then dried using azeotropic distillation using three portions of ACN. The first step of the radiosynthesis was to use the dried K[<sup>18</sup>F]F in an S<sub>N</sub>2 nucleophilic substitution reaction with precursor **5** dissolved in dry DMSO at 92 °C for 12 min to yield furan protected maleimide **23**. The second step was to remove the furan protecting group by retro Diels-Alder cycloaddition at high temperatures (160 °C) to yield the desired maleimide **24** in 6 minutes. It was noted upon scale-up of activity (< 30 GBq), permitted by the use of remote-controlled automated equipment located in lead-shielded 'hot-cells', that no [<sup>18</sup>F]FPenM (**24**) was produced. Despite a successful first <sup>18</sup>F-fluorination step, confirmed by radio-HPLC, [<sup>18</sup>F]FPenM was degrading quantitatively before HPLC purification and formulation. This problem occurred due to extreme temperatures required by the reverse Diels-Alder deprotection step. It was speculated that hydrolysis degraded [<sup>18</sup>F]FPenM. To overcome this problem, methanesulfonic acid was added in DMSO, before the furan deprotection step at 160 °C for 6 minutes, to lower the pH (overcome K<sub>2</sub>CO<sub>3</sub> base used for eluting fluorine-18). This inhibited hydrolysis, as suggested by Fujita *et al.*,<sup>210</sup> and [<sup>18</sup>F]FPenM could be isolated.

Following thermal deprotection, the reaction mixture was then cooled to  $< 35\text{ }^{\circ}\text{C}$  and added to the HPLC vial through a Sep-Pak Alumina N Plus light cartridge to retain residual fluorine-18 and polar side products. The HPLC vial was pre-filled with 150 mM  $\text{NH}_4\text{OAc}$  (pH 4.12) to buffer the acidic reaction mixture. The reactor was washed with DMSO and 150 mM  $\text{NH}_4\text{OAc}$  buffer (pH 4.12) to recover remaining material that had been left on the walls of the reactor and to improve the radiochemical yield. The solution from the HPLC vial, containing the prosthetic tracer, was loaded onto a C18 reverse phase HPLC column (radio-chromatogram in Appendix 8.3) and purified with an isocratic flow of 38% ACN in 50 mM  $\text{NH}_4\text{OAc}$  (pH 5.6) with added ascorbic acid (0.1 mg/mL) to inhibit radiolysis-induced degradation. Radiolysis was first observed upon activity scale-up (Subsection 2.3.7) and it induced hydrolysis and polymerisation, limiting the radiochemical purity, radiochemical yield and the specific activity that can be produced. Upon addition of ascorbic acid (1-2 mg/mL) to all the purification and formulation steps, radiochemical purity and radiochemical yield increased significantly to  $> 95\%$ .

The  $[^{18}\text{F}]\text{FPenM}$  peak eluted at  $14.3\pm 0.3$  min (purification chromatogram in Appendix 8.3) and was collected in the SPE flask containing 50 mM  $\text{NH}_4\text{OAc}$  buffer (pH 5.6) and ascorbic acid 1 mg/mL.  $[^{18}\text{F}]\text{FPenM}$  was then trapped on a pre-activated Sep-Pak Plus Light C18 cartridge and eluted first with ethanol and then HEPES-buffered-saline (20 mM HEPES), as such the final solution contains 23% ethanol. Analysis by UV and radio-HPLC was used to confirm the production of  $[^{18}\text{F}]\text{FPenM}$  **24** by co-injection with unlabelled standard FPenM **16** (see Figure 28). The radiosynthesis, purification and formulation took  $58\pm 5.8$  min ( $n = 12$ ) from start-of-synthesis, with a moderate radiochemical yield ( $12\pm 3\%$ , decay corrected to start-of-synthesis,  $n = 11$ ) and high radiochemical purity ( $95\pm 3.4\%$  by radio-HPLC,  $n = 11$ ).

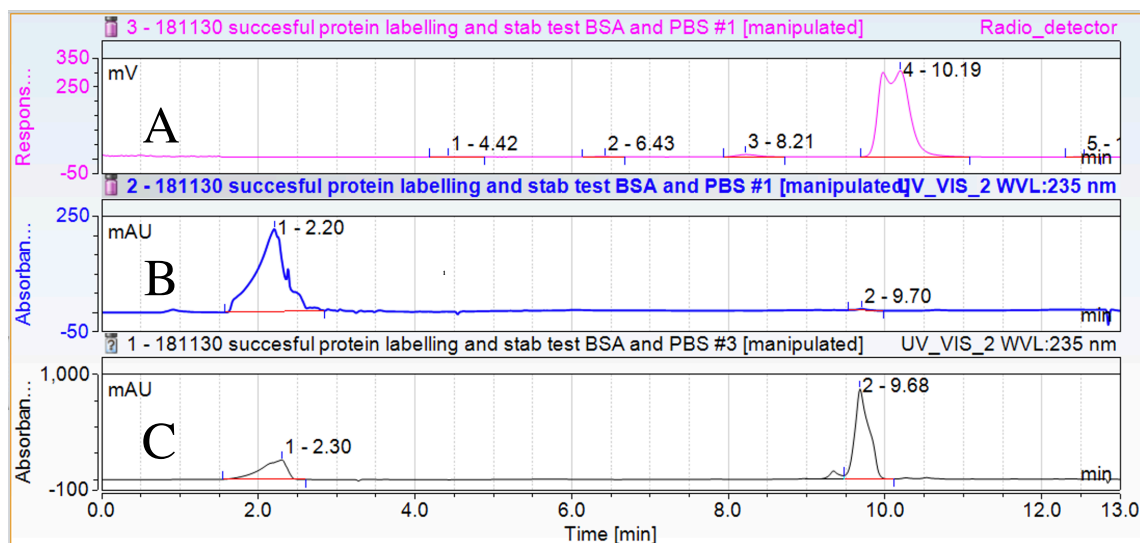


Figure 28. Validation of  $[^{18}\text{F}]\text{FPenM}$  radiosynthesis. Radiochromatogram **A** shows  $[^{18}\text{F}]\text{FPenM}$  eluting at at 10.2 min. Chromatogram **B** represents the UV trace of radiotracer  $[^{18}\text{F}]\text{FPenM}$  and peak 2 at 9.7 min displaying the FPenM residual peak. Chromatogram **C** displays the spiked sample (shown in **B**) with FPenM HPLC standard (peak 2 at 9.7 min).

Specific radioactivity of  $[^{18}\text{F}]\text{FPenM}$  was  $1144000 \pm 161000$  MBq/mg ( $n = 3$ ), molar radioactivity  $212000 \pm 30000$  MBq/ $\mu\text{mol}$  ( $n = 3$ ) and were determined by using the integral of its UV peak at 220 nm against a standard calibration curve.

The current yield was limited to  $12 \pm 3\%$  due to heat and radiation induced polymerisation of the maleimide followed by radiolytic degradation. Radiolysis is discussed in section 2.3.7. High temperature ( $160\text{ }^\circ\text{C}$ ) is required to remove the furan protecting group rapidly, but temperatures above  $100\text{ }^\circ\text{C}$  have been shown to increase levels of polymerisation.<sup>228,230</sup> Radiation induced degradation of maleimide can lead to polymerisation by secondary interaction of radical species ( $\text{H}\bullet$  and  $\text{HO}\bullet$ ) that induce a cascade of reactions (e.g. hydrolysis and radical formation). This then generates up to 5 different radicals, depending on the maleimide.<sup>240</sup> C-H scission in the alkyl side chain and  $\text{H}\bullet$  addition to the maleimide double bond are the most common reactions. These maleimide radicals then attack other radical maleimide monomers to initiate a polymerisation reaction, as shown in Figure 29.<sup>241</sup> In order to improve the current yield, further optimisation of the process is required. Radical inhibitors such as benzoquinone have been shown to inhibit radiation induced maleimide polymerisation and therefore improve the radiochemical yield.<sup>242</sup>

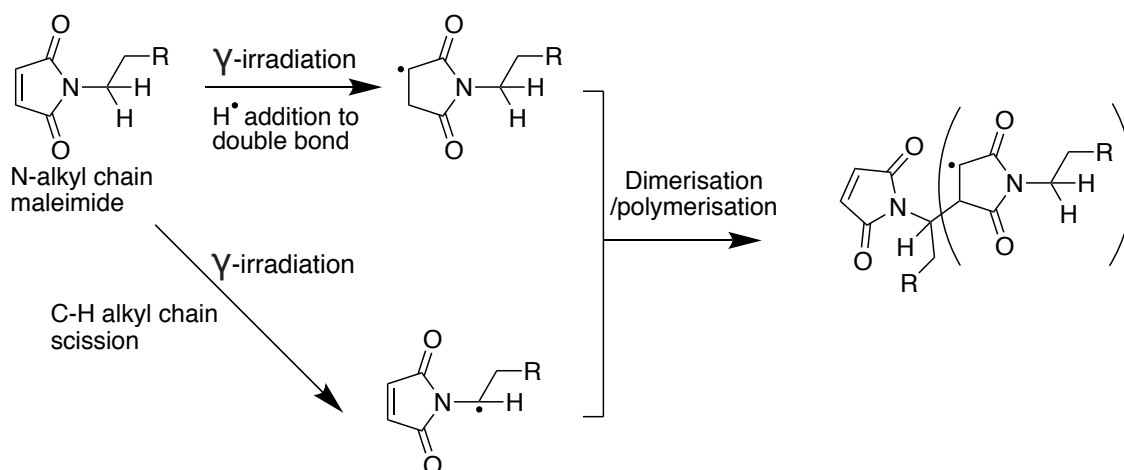


Figure 29. Radical formation and polymerisation of *N*-alkyl maleimides as described by Zott and Heusinger<sup>240</sup> and Kagiya *et al.*<sup>242</sup>

Stability of the maleimides at room temperature in neutral aqueous buffer is challenged by another process: hydrolysis. This is a common stability concern with maleimides as the hydrolysis product, maleamic acid, does not react rapidly with thiols.<sup>189</sup>

In this case, the hydrolysis half-life of the maleimide standard **16** was  $30 \pm 2.2$  hours ( $n = 4$ ) at  $20^\circ\text{C}$  in PBS, pH 7.4. This was determined by monitoring by UV-HPLC the degradation of the maleimide **16** over time a period of 14 hours. Therefore, hydrolysis of [<sup>18</sup>F]FPenM before conjugation with C2Am protein is not a concern, as conjugation occurs over several minutes. Hydrolysis post conjugation to C2Am would be beneficial, as upon hydrolysis, the maleamic acid conjugate does not undergo retro-Michael reaction and thiol exchange.

### 2.3.6 Solid phase extraction (SPE) cartridge and optimisation of [<sup>18</sup>F]FPenM purification

Purification of [<sup>18</sup>F]FPenM produced by automated synthesis was carried out on a reverse phase HPLC column using a 15-minute isocratic run. Simplification of this process was required for the whole tracer synthesis process (including C2Am labelling) to be translatable to cGMP automated synthesisers. Also, by replacing the HPLC purification with SPE purification, the time of synthesis can be reduced by 15 min therefore increasing the decay corrected yield. In order to implement this cartridge

purification method on an automated system, manual optimisation had to be performed first.

Using the crude [ $^{18}\text{F}$ ]FPenM reaction mixture (1.5 mL) synthesised on the GE TRACERLab FX<sub>FN</sub> (radio-chromatogram in Figure 30.), the solution was diluted 10-fold with acetate buffer (50 mM ammonium acetate, 1 mg/mL ascorbic acid, pH 6.0) and was manually loaded 1 mL on each of the Waters Sep-Pak C18 light/plus reverse phase purification cartridges. Using the conditions shown Table 6 and Table 7 below, cartridges were washed with different concentrations of acetonitrile - acetate buffer solutions to elute side products. Activities of the eluted solutions and SPE cartridges were monitored and recorded after each step and all were decay corrected for the start-of-purification. Finally, the product of interest was eluted with an ethanolic HBS solution and analysed by HPLC.

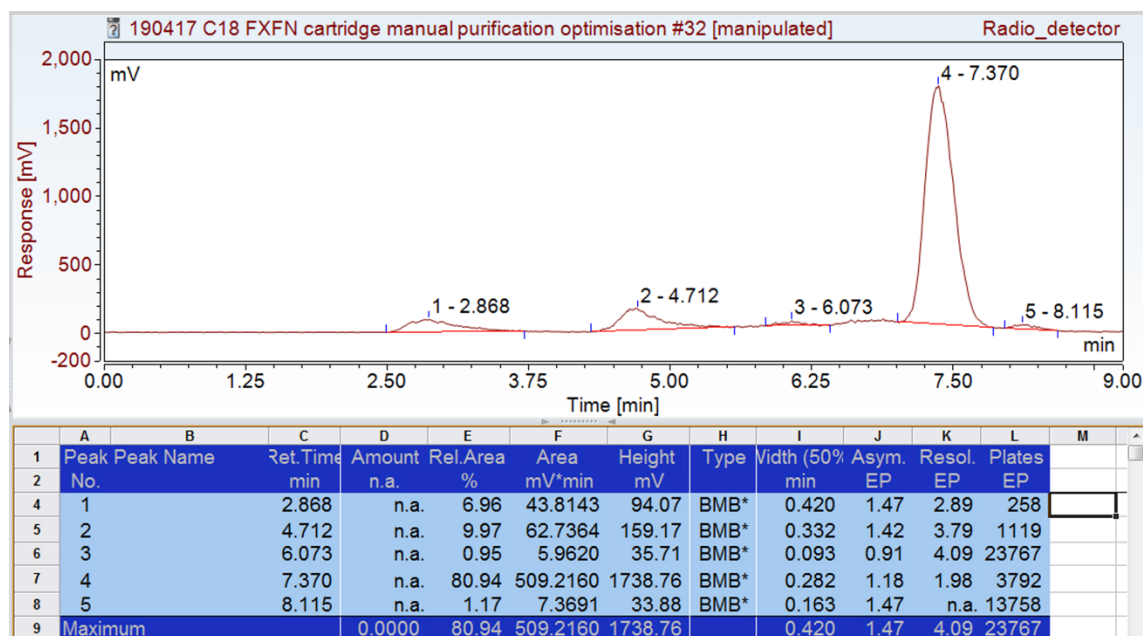


Figure 30. Radio-HPLC chromatogram of the crude [ $^{18}\text{F}$ ]FPenM as eluted from the automated TRACERlab FX<sub>FN</sub> synthesis rig. The chromatogram shows **24** at 7.3 min with 81% radiochemical purity.

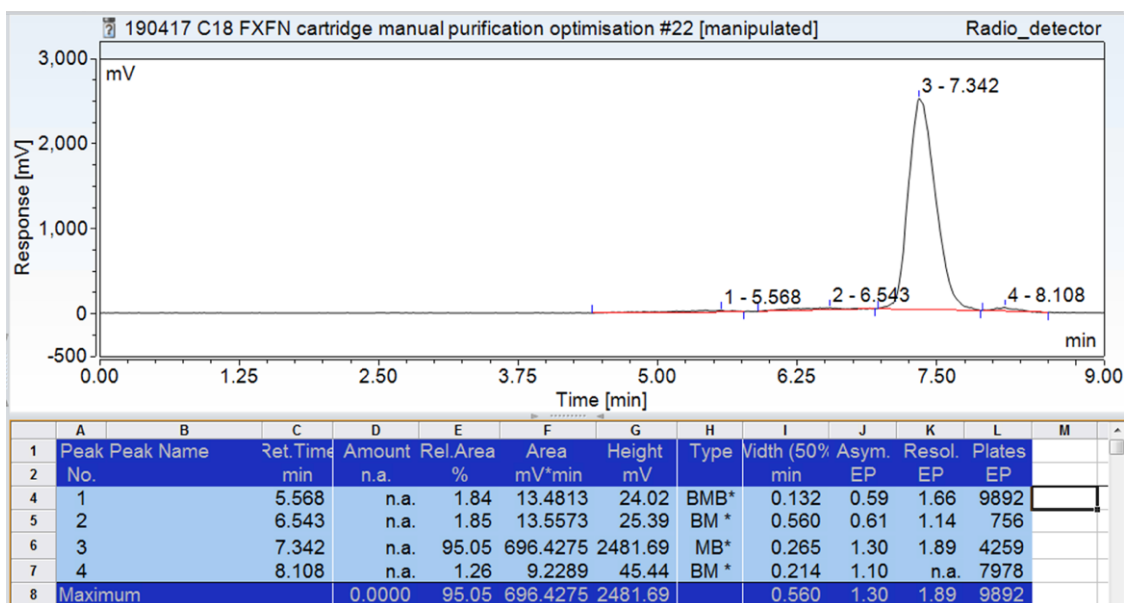


Figure 31. Radio-HPLC chromatogram of the C18 Sep-Pak cartridge-purified [ $^{18}\text{F}$ ]FPenM. The chromatogram shows **24** (7.3 min, > 95% radiochemical purity) as it was ready to be conjugated to C2Am.

A single Waters Sep-Pak light C-18 reverse phase cartridge provided excellent purification (>95% purity by radio-HPLC, Figure 31.) and with 74% recovery of **24** (which was 95% pure by radio-HPLC at the start of the method). This can replace HPLC purification and hence reduce the synthesis time by ~20 minutes. However, a peak at 5.5 min was observed in the UV (210 nm) chromatogram that required investigation as it potentially was 5-(*N*-maleimido)pentanol, which can react with thiols. However, this peak disappeared upon eluting cartridge C18-Light with Method 3: 20% MeCN:Acetate buffer (50 mM). (Figure 32.)

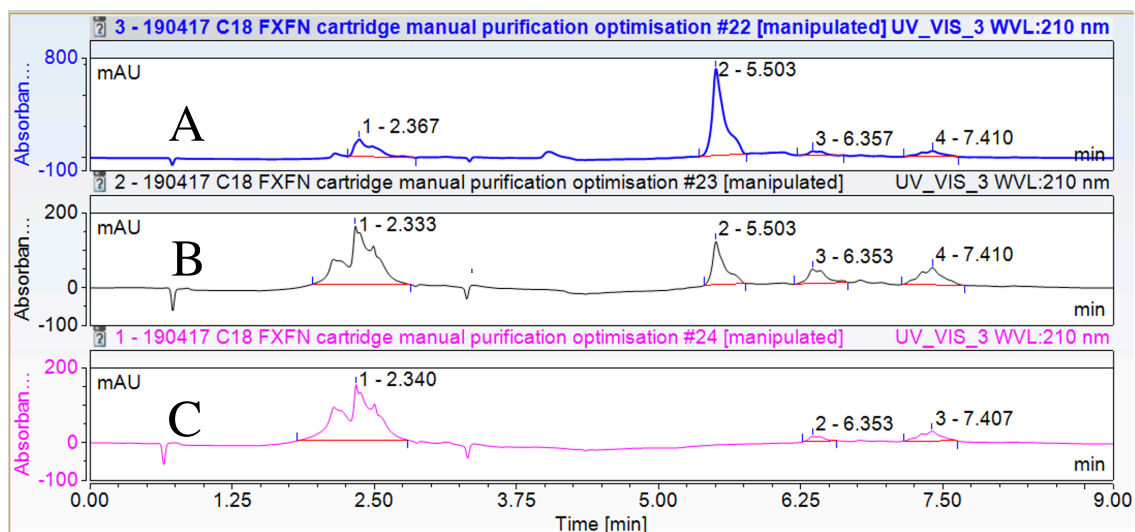


Figure 32. UV-HPLC (210nm) chromatogram of products eluted from the first three Methods using C18 Sep-Pak light cartridges (**A**, **B**, **C** correspond to Methods 1, 2, 3 - see table 6). Peak at 5.5 min is an impurity, potentially 5-(*N*-maleimido)pentanol. Method 3 shown in chromatogram **C** did not show the presence of this particular impurity hence it was selected as the optimum cartridge purification method.

Therefore, this method was used for cGMP production optimisation runs. In the future, if **24** is deemed to be required as a highly concentrated solution, in order to maximise the molar activity of the final [ $^{18}\text{F}$ ]FPenM-C2Am radiotracer, then purification by a distillation method will be investigated. **24** is a volatile organic compound, as was discovered upon attempted concentration by ethanol evaporation during formulation. Therefore, distillation is a feasible purification method.



Table 9. Elution of Waters Sep-Pak C18 light cartridges showed improved recovery of **24** compared to Waters Sep-Pak C18 plus. Activity has been decay corrected for the start-of-purification.

	Method 1 (one C18 light)	Method 2 (one C18 light)	Method 3 (one C18 light)	Method 4 (two C18 light connected in series)
<u>Loading solvent</u>	acetate buffer (50 mM ammonium acetate + 1 mg/mL ascorbic acid, pH 6)			
Volume	1 mL			
Activity not retained on cartridge after loading (passthrough)	15.7 MBq	25 MBq	10 MBq	12 MBq
Activity Cartridge	50 MBq	50 MBq	38 MBq	53 MBq
<u>Washing eluent</u>	5:95 ACN:Acetate buffer	10:90 ACN:Acetate buffer	20:80 ACN:Acetate buffer	20:80 ACN:Acetate buffer
Volume (mL)	0.15 mL ACN and 2.85 mL acetate buffer	0.3 mL ACN and 2.7 mL acetate buffer	0.6 mL ACN and 2.4 mL acetate buffer	0.6 mL ACN and 2.4 mL acetate buffer
Activity side products eluted	42.5 MBq	40 MBq	19.1 MBq	41 MBq
Activity Cartridge	42.5 MBq	40 MBq	19.1 MBq	41 MBq
<u>Eluting solvent</u>	EtOH/HBS with 0.1 mg/mL ascorbic acid			
Volume (mL)	0.3 mL EtOH in 1 mL HBS			0.3 mL EtOH in 1.5 mL HBS
Product eluted (MBq)	37 MBq	35 MBq	16.8 MBq	35 MBq
Leftover cartridge activity (MBq)	5 MBq	4 MBq	2.5 MBq	3.8 MBq
<b>Product recovery (%)</b>	<b>74</b>	<b>70</b>	<b>44</b>	<b>66</b>
Radiochemical Purity (%)	95	96	93	96

Table 10. Elution of Waters Sep-pak C18 plus cartridges showing poor recovery of **24** compared to Waters Sep-pak C18 light. Activity has been decay corrected for the start-of-purification.

	Method 5 (one C18 plus)	Method 6 (one C18 plus)	Method 7 (one C18 plus)	Method 8 (one C18 plus)	Method 9 (two C18 plus in series)
<u>Loading solvent</u>	acetate buffer (50 mM ammonium acetate + 1 mg/mL ascorbic acid, pH 6)				
Volume	1 mL				
Activity Cartridge	37 MBq	50 MBq	36 MBq	34 MBq	23 MBq
<u>Washing eluent</u>	10:90 ACN:Acetate buffer	20:80 ACN:Acetate buffer	30:70 ACN:Acetate buffer	35:65 ACN:Acetate buffer	35:65 ACN:Acetate buffer
Volumes (mL)	0.9 mL ACN and 8.1 mL acetate buffer	1.8 mL ACN and 7.2 mL acetate buffer	2.7 mL ACN and 6.3 mL acetate buffer	3.15 mL ACN and 6.85 mL acetate buffer	3.5 mL ACN with 6.5 mL acetate buffer
Activity side products eluted	11 MBq	28 MBq	32 MBq	31 MBq	20 MBq
Activity Cartridge	26 MBq at	22 MBq	3.5 MBq	3 MBq	3.4 MBq
<u>Eluting solvent</u>	EtOH/HBS with 0.1 mg/mL ascorbic acid				
Volume (mL)	0.3 mL EtOH in 1.5 mL HBS				0.5 mL EtOH in 2 mL HBS
Product eluted (MBq)	12.9 MBq	10.7 MBq	1.7 MBq	1.7 MBq	1.5 MBq
Leftover cartridge activity (MBq)	11.7 MBq	9 MBq	2.3 MBq	1.8 MBq	1.8 MBq
<b>Product recovery (%)</b>	<b>35</b>	<b>21</b>	<b>5</b>	<b>5</b>	<b>7</b>
Radiochemical purity (%)	96	98	65	55	>99

### 2.3.7 Radiolysis of water and effects on [<sup>18</sup>F]FPenM

It has been long known that high molar activity brings an increased risk of radiolytic degradation of radiotracers. Several studies quote radiolysis as being one of the leading factors in radiotracer degradation.<sup>243, 244, 245, 246</sup> The extent of radiolysis damage is mainly proportional to the molar activity and to a lesser extent on the volume, the dose and the pH.<sup>243</sup> Radiolysis dramatically changes with activity and can ultimately be a limiting factor in obtaining a stable formulation for long-distance transport. Radioprotectants (radical scavengers) such as ethanol, benzoquinone, AIBN, thiosulfate, nitrite and ascorbic acid have been suggested as inhibitors of water radiolysis.<sup>245,242</sup>

Radiotracers are formulated in aqueous solutions for injection. Radiolysis of water (Figure 33.) occurs when ionising radiation travels through a bulk aqueous solution and creates a path of electrons that have gained in energy. Depending on this energy, water molecules can ionize (~13 eV), excite (~7.4 eV) or transfer heat. Irradiation of water with high energy photons (e.g.  $\gamma$ - or X-rays) leads to multiple-step excitation/ionisation processes that result in decomposition of water to ions, radicals and highly reactive oxygen species (ROS) and occurs over a short timeframe (nanoseconds).<sup>247,248</sup> The resulting electrons, radicals (e.g. H• and HO•) and ions (H<sub>3</sub>O<sup>+</sup>) generated by the radiolysis of water can react with organic molecules within their proximity and thus generate a variety of side products.

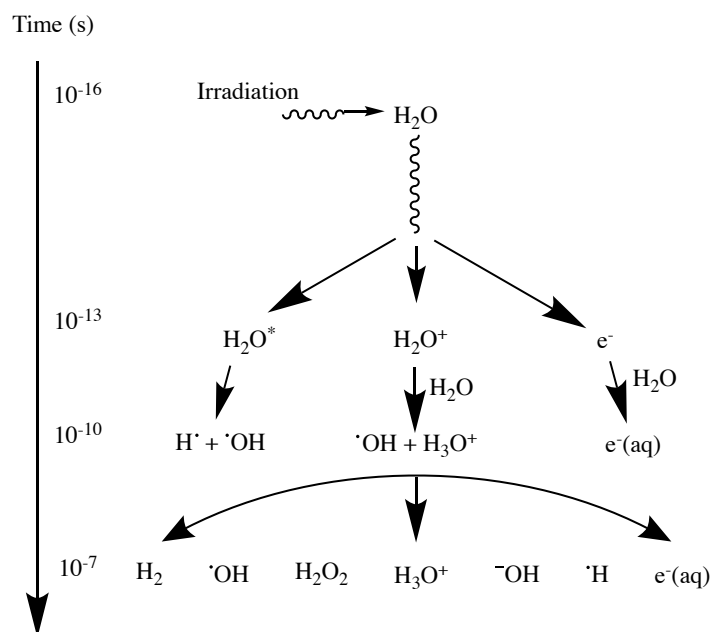


Figure 33. Ionising radiation causing water radiolysis yielding highly reactive radicals, ions and hydrogen peroxide. (adapted from Lousada *et al.*)<sup>247</sup>

In this study, degradation of the [<sup>18</sup>F]FPenM (**24**) was identified during formulation and after the end of the synthesis.

The degradation was detected by radio-HPLC immediately after the end-of-synthesis. A high number of side products were observed, despite the radiotracer undergoing a successful semi-preparative HPLC purification. These side products have only been observed upon radiosynthesis scale-up (from 1 GBq to 30 GBq of fluorine-18 starting activity) hence two main causes are thought to have induced radiolytic degradation: the relatively high molar radioactivity (212000±30000 MBq/μmol) combined with the low formulation volume (1.3 mL) and high activity (~2 GBq at the end-of-synthesis).

Another factor that can increase radiolysis is the formulation method (the formulation process is detailed in Subsection 2.6.2.2). A pre-wetted Waters Sep-Pak C18 light cartridge (~0.2 mL in volume) was used to trap **24** in order to reformulate it in the desired volume and buffer. Petrik *et al.* have shown that irradiation of silicon dioxide (silica; SiO<sub>2</sub>) dissolved in water results in more hydrogen gas production than bulk water on its own.<sup>249</sup> Hydrogen gas is formed from hydrogen radicals (H•), so it is likely that

the radical-mediated degradation of the maleimide molecules will be higher when they are trapped on the C18 silica cartridge.

Radio-HPLC analysis (Figure 34 A) of **24** (r.t = 10 minutes) shows the effects of radiolysis within 15 minutes following semi-preparative purification and formulation (9 other compounds were on the chromatogram with lower retention times). There are three ways to reduce the radiolytic degradation **24**: (i) dispersal of molecules (dilution), (ii) addition of radical scavengers or (iii) cooling the solution down to low temperatures (-78 °C).<sup>230</sup> Out of these measures, adding radical scavengers was the only feasible method in our system. The effects of dilution and cooling would have had a more significant impact on slowing down the maleimide-thiol conjugation than the providing a radioprotection benefit.

Addition of ascorbic acid (1 mg/mL) was included in all the steps involved in the purification of **24** (e.g. HPLC loading vial, dilution flask, HPLC solvent, product collection vial) and shown to inhibit radiolysis significantly, as shown in Figure 34 A.

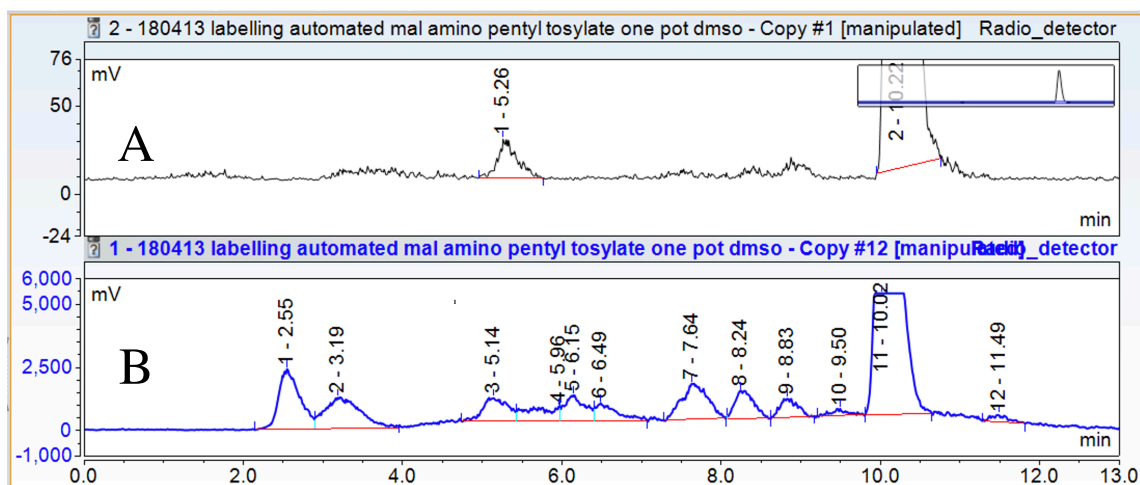


Figure 34. Radiochromatograms of [<sup>18</sup>F]FPenM. **B** (no ascorbic acid added) shows multiple peaks have appeared (15 mins post formulation) despite HPLC purification and formulation. **A** (addition of 1 mg/mL ascorbic acid) shows significantly less side-product formation (15 mins post formulation).

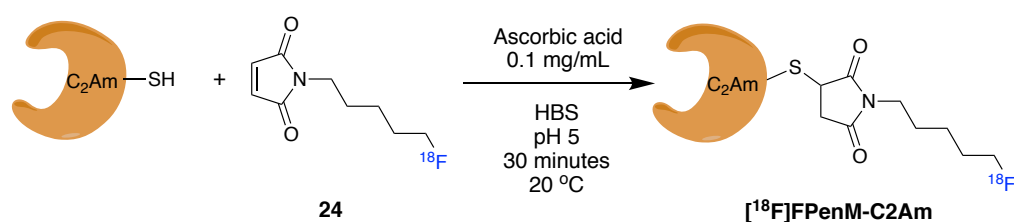
One aspect of product degradation that could be investigated in the future is whether the degradation occurs due to gamma ray photons or due to the high energy fluorine-18 positrons. This can be done by placing a vial with the standard adjacent (1 cm away) to a fluorine-18 positron source (mean <sup>18</sup>F positron travel distance in water = 0.64

mm)<sup>250</sup>. If no degradation of the standard is observed, then it can be safely assumed that gamma derived hydrolysis does not occur and the decomposition is mainly due to positron bombardment.

## 2.4 Labelling C2Am with [<sup>18</sup>F]FPenM

### 2.4.1 [<sup>18</sup>F]FPenM-C2Am radiotracer synthesis

The overexpression and purification of site-directed mutant C2Am, with a single solvent-exposed cysteine residue, has been described previously<sup>99</sup> Free thiol-containing C2Am was reduced with 10 mM DTT for 30 min at 20 °C. Next, [<sup>18</sup>F]FPenM prosthetic group was conjugated to the protein in solution via a Michael-addition reaction at room temperature (20 °C) for 30 min at pH 5. (Scheme 18.) The low pH was generated by addition of ascorbic acid to the buffer (1 mg/mL) and by the ascorbic acid added at the formulation stage (0.1 mg/mL). The low pH stabilised the maleimide, protecting it from hydrolysis and increasing the selectivity of the Michael addition reaction for thiols, by protonating lysine primary amine side chains. However, this measure slows down the overall reaction rate, hence 30 min were required for a nearly quantitative labelling (monitored by radio-HPLC). The typical conjugation radiochemical yield was 87±4.3% (n = 5) determined by radio-HPLC. (87% of the [<sup>18</sup>F]FPenM (**24**) was conjugated to the C2Am)



Scheme 18. C2Am-SH conjugation via Michael addition with **24** to form [<sup>18</sup>F]FPenM.

To determine the percentage of [<sup>18</sup>F]FPenM that had become attached to the protein, the radio-HPLC method was modified with longer runs and 10% acetonitrile added after the first 20 minutes to aid elution of unbound **24**. Therefore, the analytical conditions for [<sup>18</sup>F]FPenM-C2Am production confirmation were 0-20 min 100% PBS,

20-40 min 90:10 PBS:ACN, 40-45 min 100% PBS, on a xBridge BEH 125A 3.5  $\mu$ m size exclusion column (Waters) using a 0.7 ml/min flow rate.

To remove the prosthetic group and any of its hydrolysis side-products, peak 3 in the chromatogram in Figure 36, the protein solution was purified by gel filtration using a Sephadex G-25 desalting cartridge (NAP-5 GE Healthcare Life Sciences). An important point is that this cartridge is unable to separate  $^{18}\text{F}$ -labelled from unlabelled C2Am.

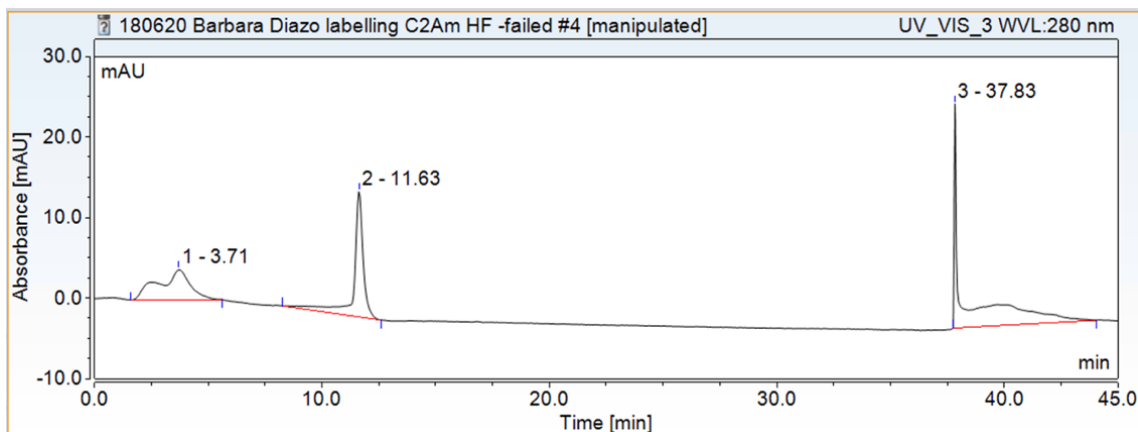


Figure 35. HPLC chromatogram of reduced C2Am-SH. Chromatogram shows the UV absorbance at 280 nm of C2Am peak 2 at 11.6 min. Peak 1 at 3.7 min are presumably aggregates of C2Am. Peak 3 (37.9 min) is due to the HPLC solvent system change at 20 min.

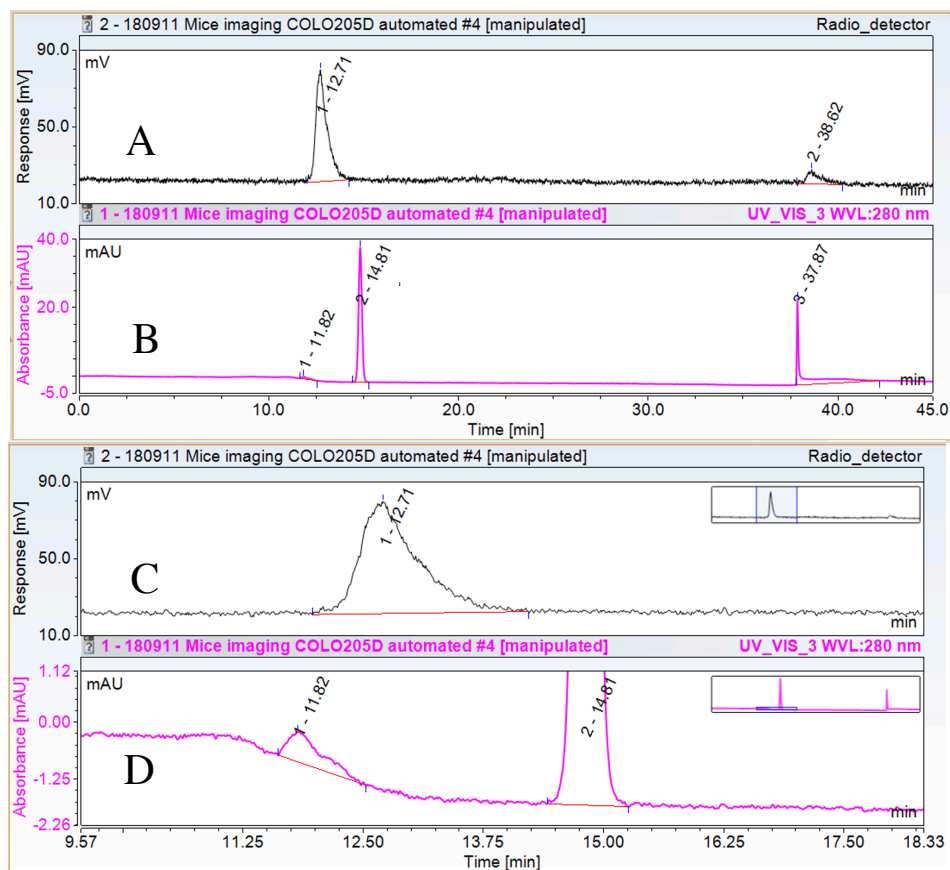


Figure 36. HPLC chromatogram of the crude Michael-Addition reaction between **24** and C2Am-SH yielding [ $^{18}\text{F}$ ]FPenM-C2Am. Radiochromatogram A: [ $^{18}\text{F}$ ]FPenM-C2Am is the first peak (12.7 min), peak 5 (38.7 min) is unreacted **24**. Chromatogram B shows the UV absorbance at 280 nm: the first peak is [ $^{18}\text{F}$ ]FPenM-C2Am (11.8 min), peak 2 represents traces of ascorbic acid (14.8 min), the final peak (37.9 min) is due to the HPLC solvent system change at 20 min. Chromatograms C and D are expanded chromatograms A and B respectively focused on the [ $^{18}\text{F}$ ]FPenM-C2Am peak.

Gel filtration was performed on a column pre-equilibrated with PBS. Three fractions were collected, the first fraction was protein- and tracer-free, the second fraction contained >99% pure by radio-HPLC [ $^{18}\text{F}$ ]FPenM-C2Am (Figure 37), ready for injection, and the third fraction contained some [ $^{18}\text{F}$ ]FPenM-C2Am and unbound **24**. Another radio-HPLC of [ $^{18}\text{F}$ ]FPenM-C2Am was run, this time spiked with a FPenM-C2Am HPLC standard. The UV peak 2 at 12.1 minutes increased which confirms the production of [ $^{18}\text{F}$ ]FPenM-C2Am radiotracer.



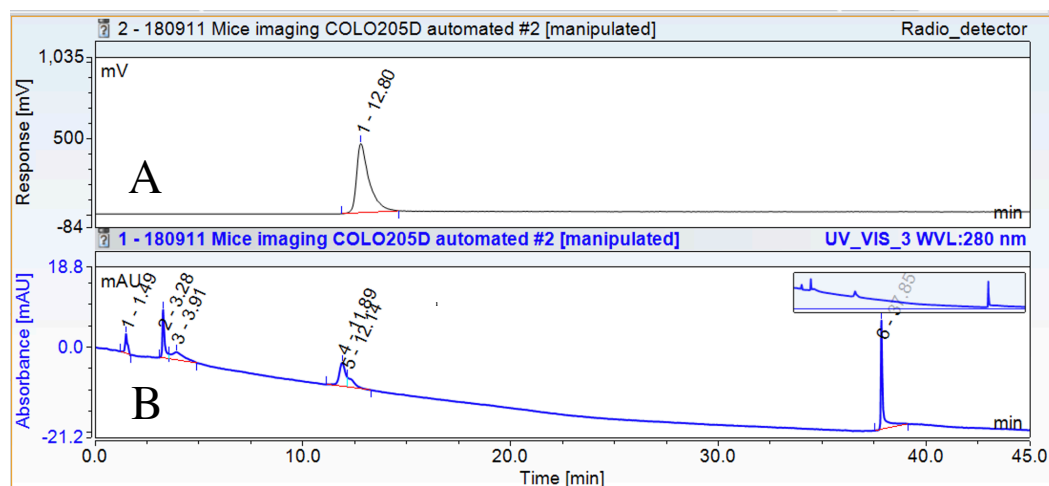


Figure 37. QC chromatogram of pure  $[^{18}\text{F}]\text{FPenM-C2Am}$ . Radiochromatogram (A) represents the radiodetector trace and showed  $[^{18}\text{F}]\text{FPenM-C2Am}$  elution at 12.8 min. Chromatogram B represents the UV (280 nm) trace and showed absorbance of reduced C2Am protein at 11.9 min and 12.1 min (FPenM-C2Am). The peak at 36 min is the solvent front due to the solvent system change at 20 min. Peaks 1, 2 and 3 are probably caused by dimerization of unlabelled C2Am (disulphide bond formation) and hydrophobic interactions promoted aggregation hence the multiple peaks.

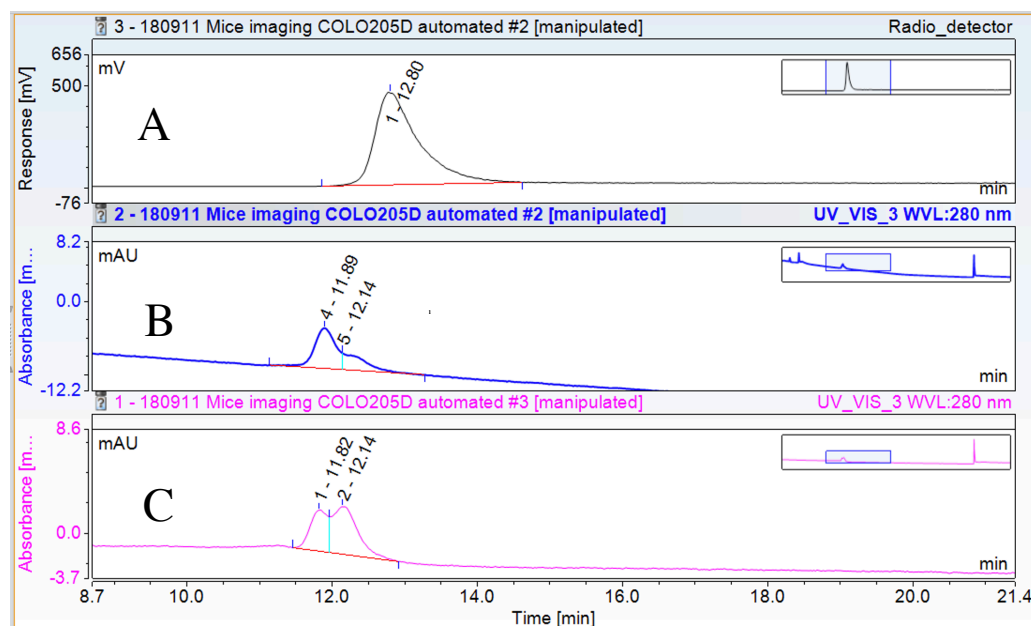


Figure 38. QC chromatogram of pure  $[^{18}\text{F}]\text{FPenM-C2Am}$  with added (spiked) FPenM-C2Am HPLC standard. Chromatogram A represents the radiodetector trace and showed  $[^{18}\text{F}]\text{FPenM-C2Am}$  elution at 12.8 min. Chromatogram B represents the UV (280 nm) trace and showed absorbance of reduced C2Am protein at 11.9 min and 12.2 min (FPenM-C2Am). Chromatogram C represents the UV (280 nm) trace and showed absorbance of reduced C2Am protein at 11.8 min and 12.1 min (FPenM-C2Am spiked with FPenM-C2Am HPLC standard hence the increased peak). The peak at 36 min is the solvent front due to the solvent system change at 20 minutes.

The protein concentration of the injected radiotracer was determined by Merck Direct Detect Infrared spectrometer. Protein recovery after NAP-5 gel filtration cartridge purification was  $33\pm 2\%$  ( $n = 5$ ) of the initial amount of protein added to the reaction. The very low recovery rate was mainly due to the hydrophobicity of the top and bottom polyethylene frits in the cartridge. Another contributing factor to the loss of protein on the NAP-5 is due to dimerization (Figure 39.) and aggregation occurring during the conjugation reaction with maleimide **24**, despite the protein being relatively dilute (0.8 mg/mL). These aggregates are then effectively filtered and retained by the NAP-5 cartridge. (Figure 36) These factors contribute to frit binding despite the fact that the concentration (0.7 mg/ml) is below the maximum loading of 1 mg/ml recommended by the manufacturer. This problem will be avoided in future by shortening conjugation times, hence less aggregate formation, and by purifying the protein using a preparatory size exclusion column directly on the automated GE TRACERlab FX<sub>FN</sub> synthesiser.

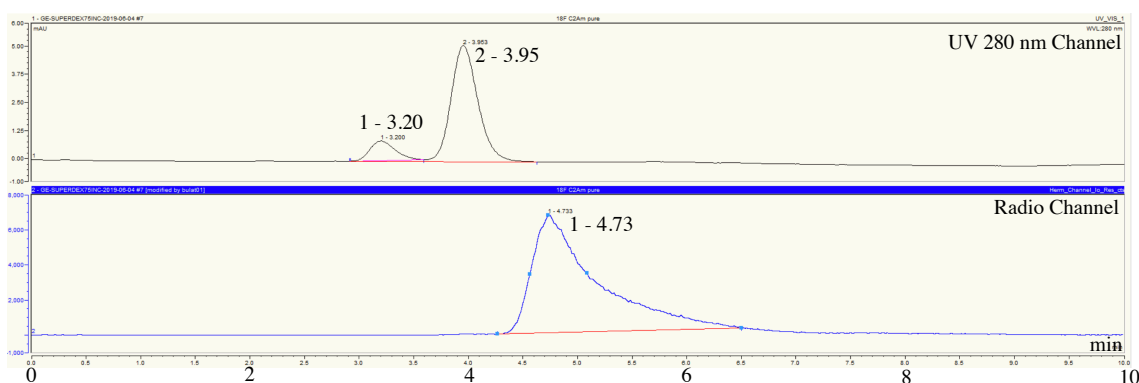


Figure 39. [<sup>18</sup>F]FPenM-C2Am analysed on a UPLC Ultimate 3000 using a GE Superdex 75 (300 mm) analytical column. Top chromatogram (UV 280 nm channel) shows 2 peaks separating oxidised C2Am from C2Am and [<sup>18</sup>F]FPenM-C2Am. The first small peak increases with time, confirming oxidation and dimerization of C2Am with time shown in Figure 40.

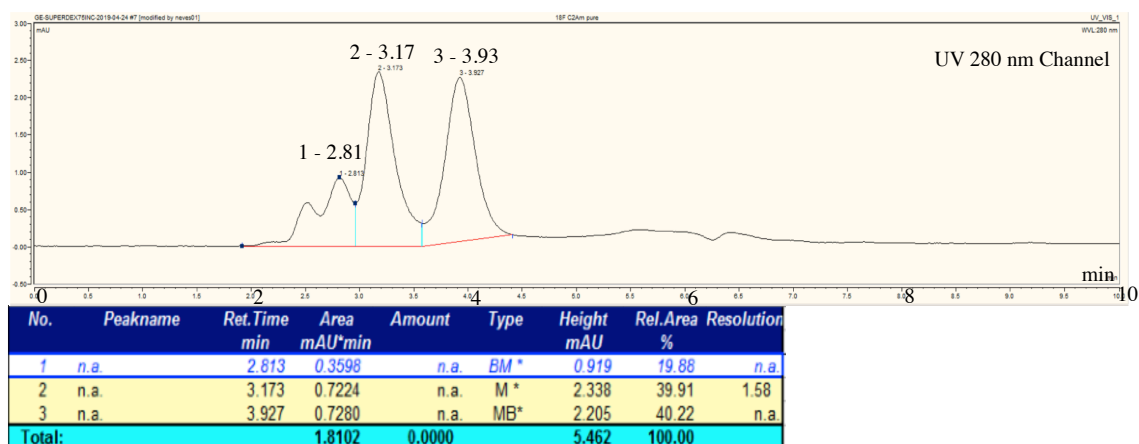


Figure 40. Same [ $^{18}\text{F}$ ]FPenM-C2Am sample as shown in Figure 39 injected again after 24 hours at room temperature. Analysed on a UPLC Ultimate 3000 using a GE Superdex 75 (300 mm) analytical column. UV chromatogram (280 nm channel) shows multiple peaks separating aggregates (peak 1, 20% area), oxidised C2Am (peak 2, 40% area) from conjugated C2Am (FPenM-C2Am, 40% area) seen as peak 3. Chromatograms courtesy of Dr André Neves.

To confirm disulfide bridge formation (dimerisation),  $\text{CuCl}_2$  (50  $\mu\text{M}$ ) was added to a freshly reduced C2Am sample and then analysed by HPLC (see Figure 41).<sup>251,252,253,254</sup> Addition of  $\text{CuCl}_2$  yielded the similar results as oxidation by air upon leaving the C2Am sample overnight at room temperature (see Figure 40).

## Targeted Imaging Agents for Detecting Tumour Cell Death following Therapy

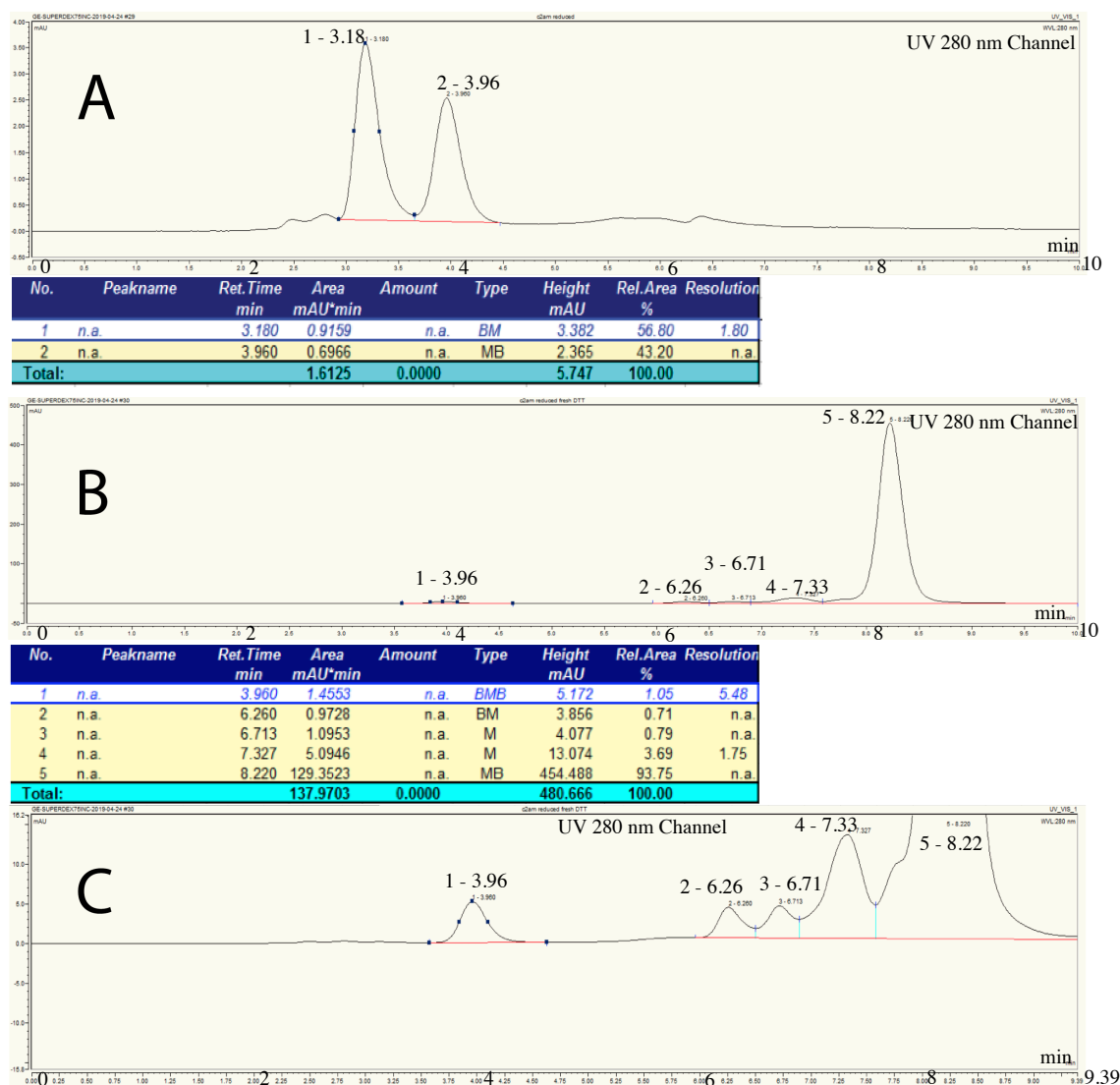


Figure 41. UV chromatograms showing oxidation of freshly reduced C2Am and then subsequent reduction using DTT. Chromatogram A: dimerization of C2Am was accelerated by the addition of  $\text{CuCl}_2$  ( $50 \mu\text{M}$ ) to confirming that peak 1 at 3.2 min is the oxidised C2Am. Chromatogram B: reduction of oxidised C2Am from chromatogram A using DTT (20 mM, 4 min) showed complete reduction of protein. Chromatogram C: expansion of chromatogram B to allow observation of the reduced protein peak 1 at 4 min, the large peak at 8.2 min represents DTT. Chromatograms courtesy of Dr André Neves.

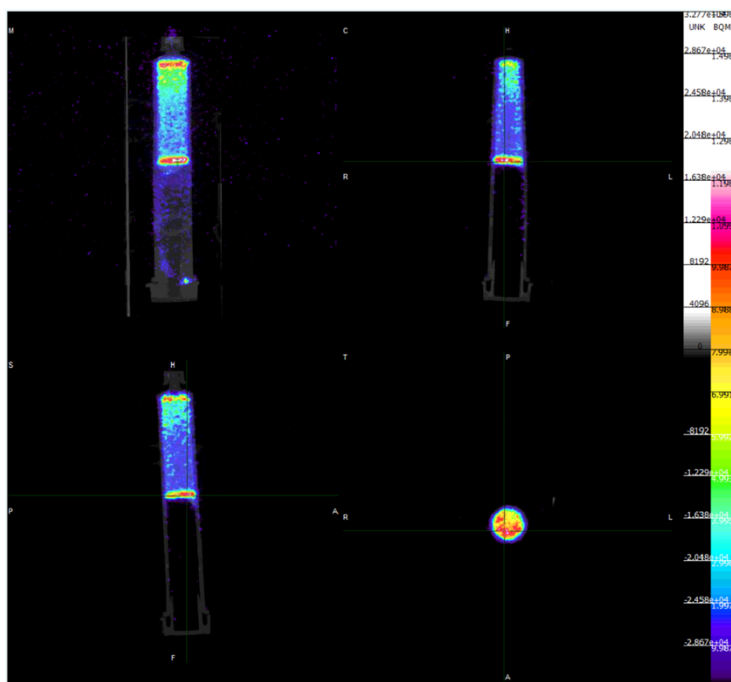


Figure 42. PET/CT scan of a NAP-5 cartridge (column volume 8.3 mL) used for [ $^{18}\text{F}$ ]FPenM-C2Am purification, with 2.71 MBq activity left on the cartridge. The transverse plane (bottom right picture) clearly shows significant activity (in red) on the loading and eluting frits. Maximum-intensity-projection (top left), coronal (top right) and sagittal (bottom left) planes also confirm the presence of activity mainly in the plastic frits. PET images palette shown: Sokolov.

The molar activity of [ $^{18}\text{F}$ ]FPenM-C2Am was calculated by dividing the activity of the pure fraction by the protein concentration and found to be  $29500 \pm 10600$  MBq/ $\mu\text{mol}$  ( $n = 5$ ) ( $1.8 \pm 0.65$  MBq/ $\mu\text{g}$ ) at the end-of-synthesis (conjugation and purification) and  $\sim 16600$  MBq/ $\mu\text{mol}$  ( $\sim 1$  MBq/ $\mu\text{g}$ ) at the time of injection into tumour-bearing mice (typically injected after 1.5 hours after radiosynthesis).

#### 2.4.2 [ $^{18}\text{F}$ ]FPenM-C2Am radiotracer stability test

[ $^{18}\text{F}$ ]FPenM-C2Am radiotracer solution ( $5.7 \mu\text{M}$ ) in PBS was stable for over 3 hours at room temperature and at  $37^\circ\text{C}$ . (Figure 43., Figure 44.) There was no defluorination, nor was [ $^{18}\text{F}$ ]FPenM prosthetic group deconjugation observed. However, unlabelled C2Am was constantly oxidised by atmospheric oxygen and consequently generated dimers and aggregates. Tavaré *et al.* have previously shown the formation of dimeric forms of a cysteine-labelled version of C2A ( $[^{99\text{m}}\text{TcCO}_3]\text{C2AcH}$ ).<sup>255</sup> This suggests that aggregation can occur via the interaction of hydrophobic regions of the C2A protein that are in closer contact following disulphide bridge formation.

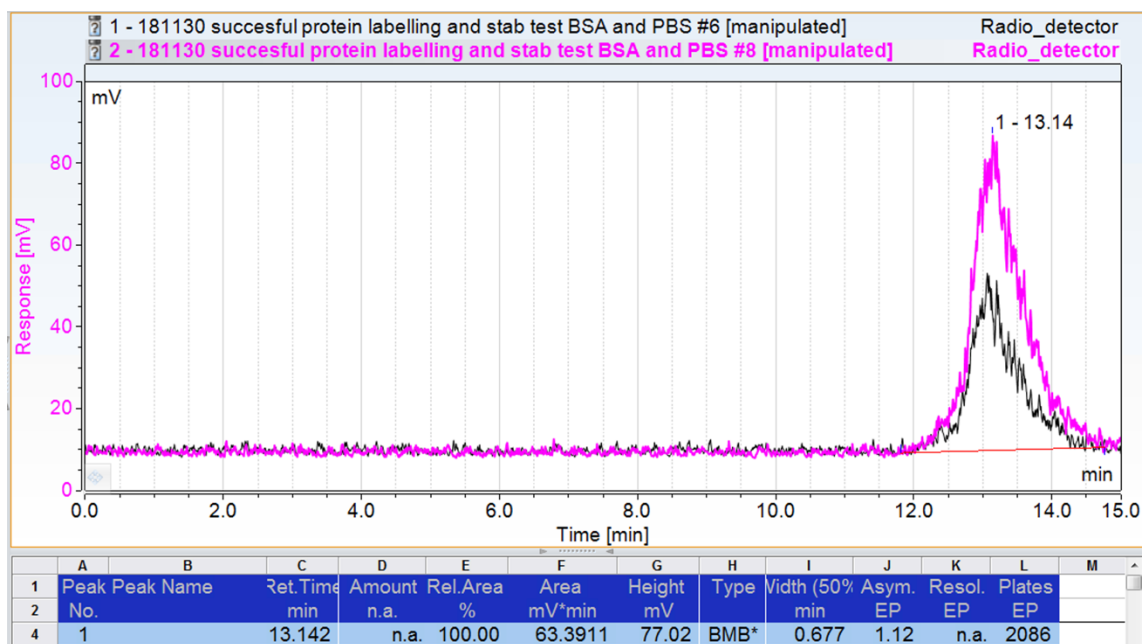


Figure 43.  $[^{18}\text{F}]\text{FPenM-C2Am}$  radiotracer stability test in PBS at 37 °C (black 5 min, pink 1 h after incubation at 37 °C). Peak at 13.1 min is  $[^{18}\text{F}]\text{FPenM-C2Am}$  radiotracer. C2Am concentration was 1  $\mu\text{M}$ . Sensitivity of the radiodetector was increased before analysing the 1-hour sample to compensate for decay and to enable peak observation along with other potential decomposition products.

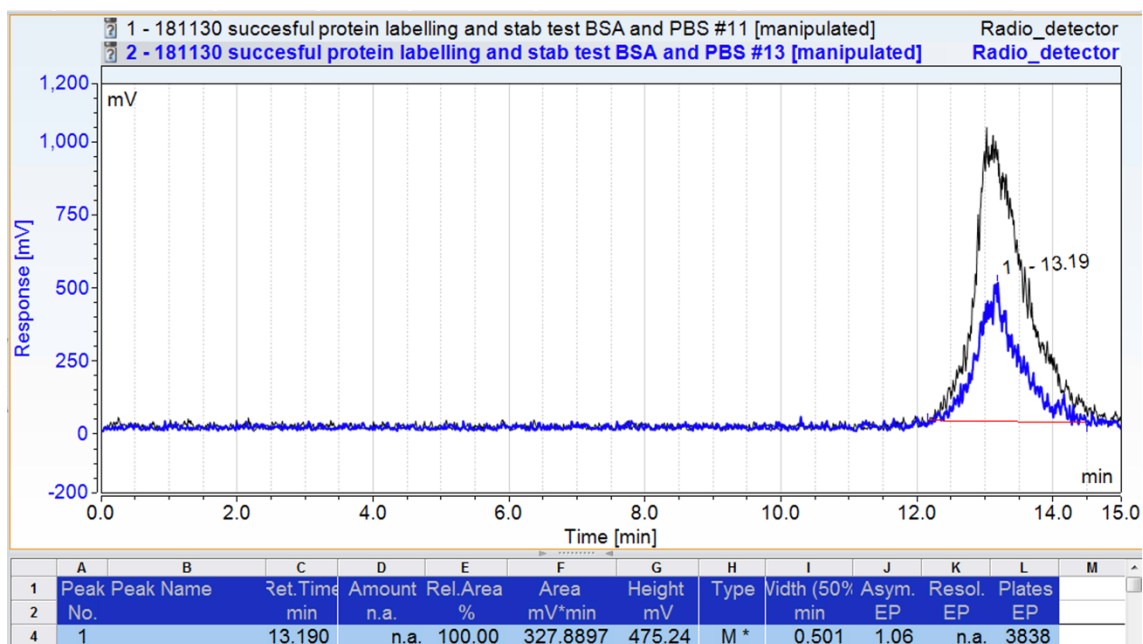


Figure 44.  $[^{18}\text{F}]\text{FPenM-C2Am}$  radiotracer stability in PBS at 37 °C: black 2 h, blue 3 h after incubation in PBS at 37 °C. Peak at 13.2 min is  $[^{18}\text{F}]\text{FPenM-C2Am}$  radiotracer. C2Am concentration was 1  $\mu\text{M}$ .

[<sup>18</sup>F]FPenM-C2Am was also stable in bovine serum albumin (50 mg/mL, C2Am 0.5 μM) for 3 hours at 37 °C. A second small radioactive peak started to appear (at 8.9 mins on the chromatogram) after 1 hour incubation (see Figure 45 and Figure 46). This correlated well with the albumin UV peak at 8.4 min, suggesting therefore that the side product could be the result, to a minor extent, of a thiol exchange reaction, which is specific to maleimides, between C2Am and albumin.

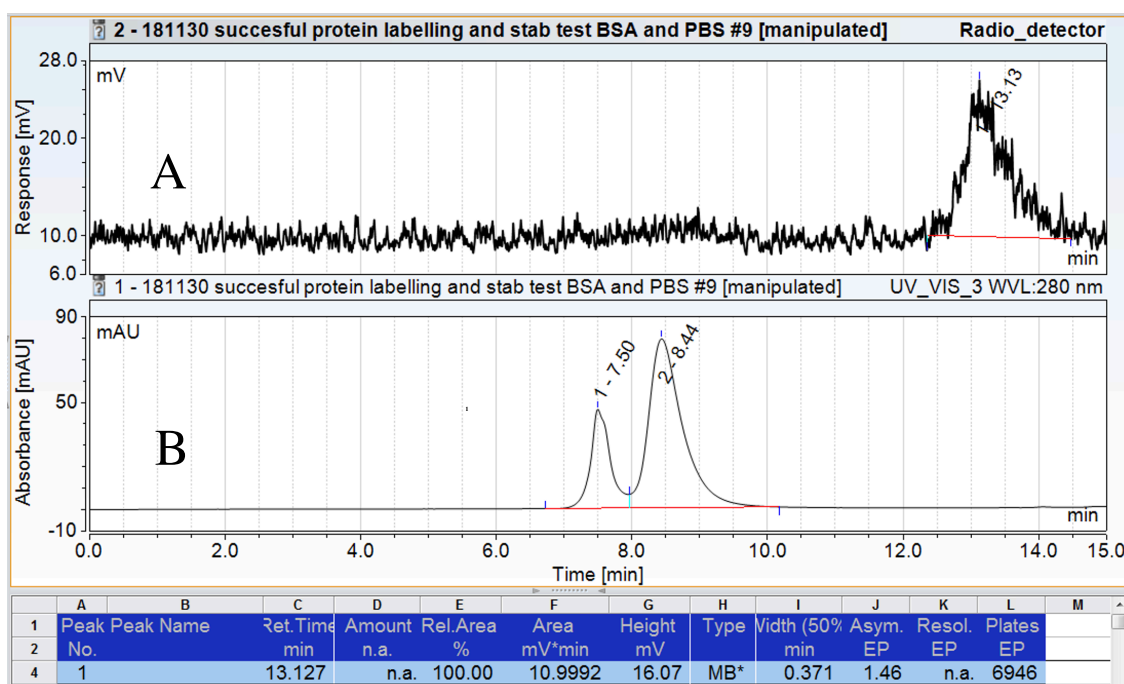


Figure 45. Stability of [<sup>18</sup>F]FPenM-C2Am in a solution of bovine serum albumin (BSA). Radio HPLC chromatogram (A) showing [<sup>18</sup>F]FPenM-C2Am at 13.1 min following incubation in BSA at 37 °C for 1 h. UV trace (B) recorded at 280 nm shows BSA peak 1 at 7.5 and peak 2 at 8.4 min for the 2 h incubation. C2Am concentration was 1 μM.

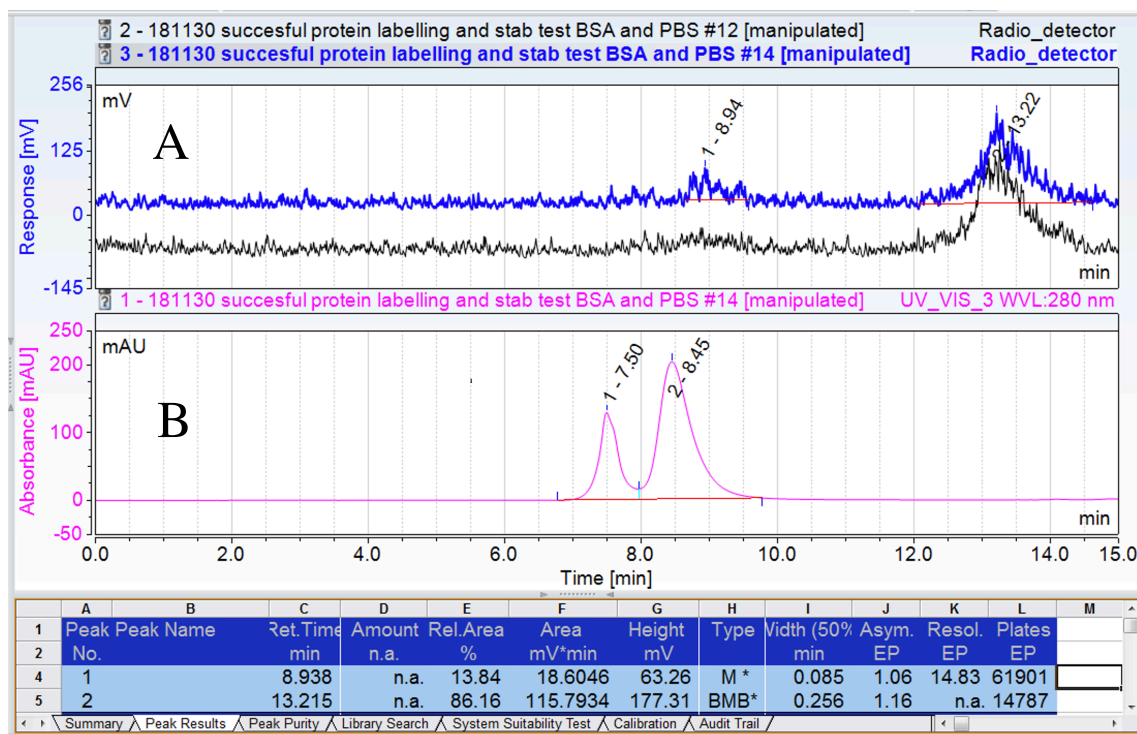


Figure 46. Stability of  $[^{18}\text{F}]\text{FPenM-C2Am}$  in a solution of bovine serum albumin (BSA). Radio HPLC chromatogram (A) showing  $[^{18}\text{F}]\text{FPenM-C2Am}$  following incubation in BSA at 37 °C (black 2 h, blue 3 h). UV trace (B) recorded at 280 nm shows BSA peak 1 at 7.5 and peak 2 at 8.4 min for the 3 h incubation. In the radiochromatogram (A) a peak appears at 8.9 min (14% area) suggesting a product of aggregation of BSA and  $[^{18}\text{F}]\text{FPenM-C2Am}$  or a metabolite. C2Am concentration was 1  $\mu\text{M}$ .

Over the course of a three hour incubation at 8.9 min started to increase in intensity (to (14%)), and therefore the purity of the  $[^{18}\text{F}]\text{FPenM-C2Am}$  radiotracer decreased to 86%, as indicated by radio HPLC. Based on UV and radio detector retention times, this peak has been assigned to the albumin peak at 8.44 on the UV chromatogram. This is not a concern, as no such metabolites have been observed by radio-HPLC in mouse blood serum analysed 10 min post-injection. The maximum blood pool concentration of the radiotracer  $[^{18}\text{F}]\text{FPenM-C2Am}$  is achieved *in vivo* at 10 min post intravenous administration, as determined by Dr André Neves, using time-activity analysis of regions of interest, derived from mouse PET/CT scans.

## 2.5 Conclusion

Several types of  $^{18}\text{F}$ -labelled moieties were considered for tagging C2Am. Initially, synthesis of 4- $[^{18}\text{F}]\text{fluorobenzamido-N-ethylaminomaleimide}$  ( $[^{18}\text{F}]\text{FBEM}$ )



from diaryliodonium precursors was attempted. Then the classic (and lengthy) synthesis of [ $^{18}\text{F}$ ]FBEM was attempted (Section 2.3). In conclusion, [ $^{18}\text{F}$ ]SFB synthesis from iodonium precursors was unsuccessful, both manually and using automated microfluidics modules or GE TRACERlab.

In parallel with this approach, 2-[ $^{18}\text{F}$ ]fluoroethylazide was successfully radiosynthesised and bioorthogonally ‘clicked’ to a dibenzocyclooctyne-PEG<sub>4</sub>-C2Am. Despite initial success, the click reaction was too slow partially labelling C2Am-PEG<sub>4</sub>-DBCO. The resulting radiotracer was unsuitable for PET imaging. (section 2.3.3)

Finally, the *N*-5-[ $^{18}\text{F}$ ]fluoropentylmaleimide ([ $^{18}\text{F}$ ]FPenM) prosthetic group was synthesised manually and optimised for automated synthesis. [ $^{18}\text{F}$ ]FPenM was synthesised in good yield ( $12\pm 3\%$ , decay corrected to start-of-synthesis,  $n = 11$ ), in a short amount of time  $58\pm 5.8$  min ( $n = 12$ ), high radiochemical purity ( $95\pm 3.4\%$  by radio-HPLC,  $n = 11$ ) and excellent molar activity ( $212000\pm 30000$  MBq/ $\mu\text{mol}$  ( $n = 3$ )). Upon scale-up radiolysis and thermal decomposition were inhibited using ascorbic acid and methanesulfonic acid respectively.

The conjugation of [ $^{18}\text{F}$ ]FPenM to C2Am proceeded almost quantitatively ( $87\pm 4.3\%$  ( $n = 5$ ) by radio-HPLC) yielding [ $^{18}\text{F}$ ]FPenM-C2Am with a high molar activity  $29500\pm 10600$  MBq/ $\mu\text{mol}$  ( $n = 5$ ). Reaction proceeded quantitatively due to its fast kinetics. This has been previously investigated and shown that GSH reacted quickly with *N*-(5-fluoropentyl)maleimide ( $3113\pm 73$  M<sup>-1</sup> s<sup>-1</sup> at pH 7.27 and 25 °C) which is consistent with literature. (see section 2.2.3) Despite maleimides undergoing retro-Michael addition, no decomposition of the [ $^{18}\text{F}$ ]FPenM-C2Am was observed in PBS over 3 hours (section 2.4.2.).

Considering all of the above, we concluded that [ $^{18}\text{F}$ ]FPenM-C2Am could be used to image cell death in two tumour models.

## 2.6 Experimental

### 2.6.1 General synthetic chemistry (Department of Chemistry)

All reactions were performed under anhydrous conditions and inert atmosphere (nitrogen) in oven-dried glassware unless otherwise stated. All solvents used were purchased and distilled by technicians in accordance to departmental protocols. Deionised water used for general reactions was supplied by the Department of Chemistry. Deionised water for HPLC was purchased from VWR. Brine and sodium bicarbonate saturated solutions were prepared by departmental technicians. All purchased reagents were used without any further purification. All chemicals were handled in accordance with the Hazard and Precautionary Statements provided by the manufacturer or if unavailable treated as Hazardous, Dangerous and Carcinogenic. Yields of products quoted refer to chromatographically and spectroscopically homogenous materials. All spectra and chromatograms of compounds were attached in Appendix 8.

Thin layer chromatography (TLC) analysis was performed on Merck aluminium-backed plated pre-coated with silica (0.2 mm, F<sub>254</sub>) or Merck TLC silica gel 60 F<sub>254</sub> glass plates. Products were visualised using either fluorescence indicators such as manganese activated zinc silicate which emits green fluorescence upon excitation with UV light  $\lambda = 254$  or by staining with 10% solution of KMnO<sub>4</sub>, Iodine or Ammonium Cerium Molybdate (Hanessian's stain).

Flash column chromatography (FC) was performed on silica gel Merck Kieselgel 60 F<sub>254</sub> 320-400 mesh or Silicagel Fluorochem 60Å pore size and 40-63  $\mu\text{m}$  particle size. Flash chromatography was also performed on either a Teledyne Isco CombiFlash Rf+ or NextGen 300+ automated purification systems. Products were detected using the 200-400 nm inline UV diode array detector and isolated using an automated fraction collector.

Semi-prep HPLC was performed on an Agilent 1100 using a diode array detector (G1315B) set to monitor 254, 210 and 280 nm wavelengths. ChemStation Software revision A.10.02 was used to set-up methods and sequences for the runs. The instrument

was used with a reverse phase Zorbax SB-C18 (250 mm x 10 mm, 5  $\mu$ m; Agilent) semi-prep column.

The purification method was using a 15 minute 5-95% ACN:H<sub>2</sub>O gradient with 0.1% formic acid modifier running at 4 ml/min unless otherwise specified. Analytical HPLC was performed on an analytical Kinetex XB-C18 100A (100 mm x 2.1 mm, 2.6  $\mu$ m; Phenomenex) column using a 10 minute 5-95% ACN:H<sub>2</sub>O gradient with 0.1% formic acid modifier running a flow of 1 ml/min.

<sup>1</sup>H NMR spectra were acquired at 400 MHz on a Bruker AV-400 Avance III. Chemical shifts ( $\delta_{\text{H}}$ ) are quoted in parts per million (ppm), referenced to the appropriate residual solvent peak. <sup>13</sup>C NMR spectra were acquired at 101 MHz on a Bruker AV-400 Avance III and chemical shifts ( $\delta_{\text{C}}$ ) are quoted in parts per million (ppm), referenced to the appropriate residual solvent peak. <sup>19</sup>F NMR proton coupled or decoupled spectra were acquired at 376 MHz on a Bruker AV-400 Avance III and chemical shifts ( $\delta_{\text{F}}$ ) are quoted in parts per million (ppm). NMR data was analysed using TopSpin 4.0.6 version 1.0 or ACD Labs Academic Version.

Liquid chromatography mass spectrometry (LC-MS) was performed on a Waters SQD2 instrument. The UPLC system is an H-Class UPLC (Waters) using an 2.1 x 50 mm Acquity UPLC BEH C18 (2.1 x 50 mm, 1.7  $\mu$ m; Waters) column and a Xevo G2-S QTOF quadrupole MS (Waters) running in positive mode with an electrospray source. For small molecules, UPLC separation was carried out using a 4-minute method using a 10-90 % MeCN gradient over 3.5 mins followed by 100% MeCN flush to 4.38 mins and finally re-equilibration to 10 % MeCN. The MS source had a temperature of 120 °C, capillary voltage of 3 kV and sampling cone voltage of 40 V. Fragmentation MS-MS experiments were run with a collision energy ramp of 15-40 V and fixed masses for detection were selected as appropriate. For proteins the UPLC is running an 8 min 5-95% MeCN:H<sub>2</sub>O gradient at 0.2 mL/min with added 0.1% formic acid modifier.

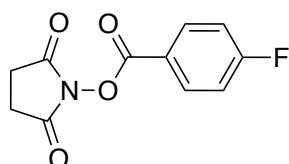
High resolution mass spectrometry (HRMS) was performed on either a Waters Xevo G2-S QTOF or a Waters LCT Premier instruments. The first system uses a UPLC H-Class solvent management system running an 8 min 5-95% MeCN:H<sub>2</sub>O gradient at 0.2 mL/min with added 0.1% formic acid modifier) coupled to an electrospray ionisation

(ESI) tandem mass spectrometer (MS/MS quadrupole and time-of-flight). The MS/MS is calibrated against a leucine-enkephalin internal standard, 1 mg/mL ( $m/z = 556.2771$ ). MassLynx V4.1 software was used to run the samples, interpret the data and deconvolute protein spectra. This instrument was used for both organic small molecules and for proteins.

The Waters LCT Premier instrument is a time-of-flight mass analyser with an Agilent 1100 autosampler and pump for sample injection. The system runs 50:50 ACN:H<sub>2</sub>O isocratic solvent mix with 0.25% formic acid as mobile phase modifier and can analyse organic small molecules ranging from 150 Da to 1500 Da.

An Applied Photophysics SX.18MV stopped flow system was used to determine the rate constant of fast chemical reactions. System was used with 4 bar of nitrogen pressure to drive the plunger mixing the two reagents to be analysed. Temperature surrounding the flow cell and the drive syringes was accurately maintained to 25 °C. Software used to acquire data was the Applied Photophysics Ltd SX.18MV Kinetic Spectrometer Workstation version 4.53. Each run was set to acquired 1000 data points.

#### ***N*-Succinimidyl-4-fluorobenzoate standard (6)**



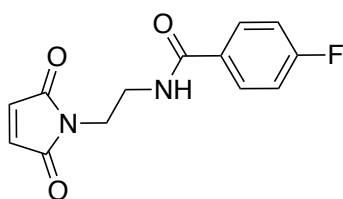
4-Fluorobenzoic acid (150 mg, 1.07 mmol), *N*-hydroxysuccinimide (182 mg, 1.89 mmol, 1.8 eq.) and 1-ethyl-3-(3-dimethylaminopropyl)carbodiimide (140  $\mu$ L, 1.39 mmol, 1.3 eq.) were dissolved in DCM (3 ml). The reaction mixture was left to stir for 24 h at r.t. The solution was then concentrated *in vacuo*, loaded on a silica plug and eluted using 1% MeOH in DCM. The solvent was removed *in vacuo* to give the desired ester 6 as a white crystalline solid (118 mg, 46%).

$\delta_H$  (400 MHz,  $\text{CDCl}_3$ ): 2.93 (4H, s,  $\text{CH}_2$ ), 7.19-7.24 (2H, m, CH), 8.17-8.20 (2H, m, CH)

$\delta_C$  (100 MHz,  $\text{CDCl}_3$ ): 25.7, 116.3 (d,  $J = 22$  Hz), 121.4 (d,  $J = 3$  Hz), 133.4 (d,  $J = 10$  Hz), 160.9, 166.9 (d,  $J = 257$  Hz), 169.2

$\delta_F$  (376 MHz,  $\text{CDCl}_3$ ): -102 (proton decoupled)

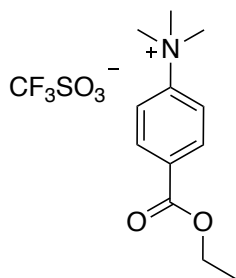
***N*-(2-(2,5-Dioxo-2,5-dihydro-1H-pyrrol-1-yl)ethyl)-4-fluorobenzamide (7)**



*N*-(2-Aminoethyl)maleimide (20 mg, 0.07 mmol, 1 eq) was suspended in DMF (0.8 mL) and DIPEA (10  $\mu\text{L}$ , 0.07 mmol) added, stirring vigorously for 30 min at room temperature. *N*-succinimidyl 4-fluorobenzoate (18 mg, 0.07 mmol) was then added and stirred for 1 h. The product was purified by HPLC according to the standard semi-prep conditions. The product was eluted at 8.05 min and collected. Solvent was removed *in vacuo* to yield amide **7** as a white powder (15 mg, 0.057 mmol, 80%).

$\delta_H$  (400 MHz, MeOD): 3.58 (2H, t,  $J = 6$  Hz,  $\text{CH}_2$ ), 3.75 (2H, t,  $J = 6$  Hz,  $\text{CH}_2$ ), 4.60 (H, s, NH), 6.82 (2H, s, CH=CH), 7.18 (2H, t,  $J = 8.5$  Hz), 7.76-7.81 (2H, m, CH)

$\delta_F$  (376 MHz, MeOD): -111.78

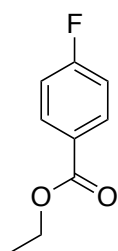
**Ethyl 4-(trimethylammonium triflate) benzoate (3)**

Ethyl 4-(dimethylamino)benzoate (100 mg, 0.51 mmol) was dissolved in DCM (5 mL). Methyl trifluoromethanesulfonate (106  $\mu$ L, 0.65 mmol, 1.3 eq) was added dropwise with a syringe. The solution was stirred for 12 h at room temperature. Solvent was removed *in vacuo* and the white powder was purified by recrystallisation from diethyl ether. Product was collected by suction filtration to yield ethyl 4-(trimethylammonium triflate) benzoate as a white powder (188 mg, 0.37 mmol, 72%).

m.p. = 109-111  $^{\circ}$ C

$\delta_H$  (400 MHz,  $CDCl_3$ ): 1.42 (3H, t,  $J = 7.2$  Hz,  $CH_3$ ), 3.80 (2H, s,  $CH_3$ ), 4.42 (2H, q,  $J = 7.2$  Hz,  $CH_2$ ), 7.95 (2H, d,  $J = 9.2$ , CH), 8.26 (2H, d,  $J = 9.2$ , CH)

$\delta_C$  (100 MHz,  $CDCl_3$ ): 14.2, 57.3, 61.9, 119.9, 132.1, 132.9, 149.8, 164.4

**Ethyl 4-fluorobenzoate standard (28)**

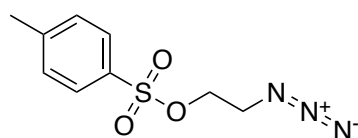
p-Fluorobenzoic acid (150 mg, 1.07 mmol) was dissolved in DCM (1 mL) and stirred at 0  $^{\circ}$ C for 5 min. 1-Ethyl-3-(3-dimethylaminopropyl)carbodiimide (140  $\mu$ L, 1.39 mmol, 1.3 eq) was added and stirred for a further 5 minutes. EtOH (100  $\mu$ L, excess) was added and stirred at RT for 16 hours. Product was purified by flash column

chromatography (50:50 EtOAc: Hexanes), solvent was removed *in vacuo* and product was collected as a colourless liquid (55 mg, 0.33 mmol, 31%).

$\delta_H$  (400 MHz, MeOD): 1.41 (3H, t, J = 7.14 Hz, CH<sub>2</sub>), 4.40 (2H, q, J = 7.14 Hz, CH<sub>2</sub>), 7.12 (2H, t, J = 8.4 Hz), 8.05-8.11 (2H, m, CH)

$\delta_F$  (376 MHz, MeOD): -107

#### 2-Azidoethyl 4-methylbenzenesulfonate (**4**)

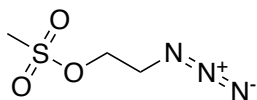


2-Azidoethanol (100 mg, 1.15 mmol) and triethylamine (500  $\mu$ L, 6.81 mmol) were dissolved in DCM (500  $\mu$ L) and p-toluenesulfonyl chloride (285 mg, 1.5 mmol, 1.5 eq) was added. The mixture was stirred at room temperature for 12 h, then diluted with DCM and quenched with water 10 mL. The organic layer was washed with deionised water (10 mL), saturated sodium bicarbonate (10 mL) and brine (10 mL), dried with MgSO<sub>4</sub>, filtered and then solvent was removed *in vacuo*. Purification by flash column chromatography (100% EtOAc) gave tosylate **4** as a colourless liquid (228 mg, 0.95 mmol, 83%).

$R_f$  (100% EtOAc) 0.81

$\delta_H$  (400 MHz, CDCl<sub>3</sub>): 2.45 (3H, s), 3.47 (2H, t, J = 5 Hz), 4.15 (2H, t, J = 5 Hz), 7.36 (2H, d, J = 8 Hz), 7.8 (2H, d, J = 8 Hz)

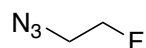
$\delta_C$  (100 MHz, CDCl<sub>3</sub>): 21.7, 49.6, 68.1, 128, 130, 132.6, 145.3

**2-azidoethyl methylsulfonate precursor (8)**

2-Azidoethanol (50 mg, 0.57 mmol) and triethylamine (388  $\mu$ L, 5.29, ) were dissolved in DCM (500  $\mu$ L) in a RBF. Methanesulfonyl chloride (53  $\mu$ L, 0.68 mmol, 1.2 eq.) was added to the mixture and stirred at room temperature for 12 hours. The mixture was diluted with DCM and washed with deionised water (10 mL), saturated sodium bicarbonate (10 mL), brine (10 mL) dried with  $\text{MgSO}_4$ , filtered and then solvent was removed *in vacuo*. Precursor **8** was collected as a yellow oil (50 mg, 0.30 mmol, 52%).

$\delta_H$  (400 MHz,  $\text{CDCl}_3$ ): 3.08 (3H, s), 3.59 (2H, s), 4.35 (2H, s)

$\delta_C$  (100 MHz,  $\text{CDCl}_3$ ): 37.9, 50.0, 67.6

**2-Fluoroethylazide (HPLC standard) (26)**

2-fluoroethanol (0.56 mL, 7.9 mmol) in DCM (15 mL) was added *p*-toluenesulfonyl chloride (2.33 g, 12.2 mmol, 1.2 eq) and triethylamine (1.5 mL, 45 mmol) and the resultant mixture was stirred at room temperature under nitrogen for 16 hours. Crude mixture was diluted with DCM (30 mL) and then washed with  $\text{H}_2\text{O}$  (2 x 10 mL). The solvent was evaporated *in vacuo* to yield an orange oil. Product was recrystallised from hexane to yield 2-fluoroethyl *p*-toluenesulfonate as a white powder (1.583 g, 6.56 mmol, 83%). 2-fluoroethyl *p*-toluenesulfonate (200 mg, 0.92 mmol) in DMF (5 mL) was added sodium azide (179.2 mg, 2.75 mmol) and the suspension was stirred at room temperature for 48 hours. The reaction mixture was filtered to remove the white

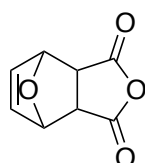


precipitate. The filtrate was used without further purification. Pure 2-fluoroethylazide (**26**) is unstable and could decompose by explosion therefore solvent was not removed.

$\delta_H$  (400 MHz,  $\text{CDCl}_3$ ): 3.51 (2H, dt,  $J = 27$  Hz, 4.4 Hz), 4.58 (2H, dt,  $J = 47$  Hz, 4.4 Hz)

$\delta_F$  (376 MHz,  $\text{CDCl}_3$ ): -224.6

#### **7-oxanorborn-5-ene-2,3-dicarboxylic anhydride (12)**



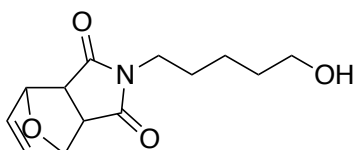
Maleic anhydride puriss  $\geq 99\%$  (10 g, 102 mmol, Lot# STBH5037, Sigma-Aldrich) was added to a round bottom flask and flushed with nitrogen gas. Furan  $\geq 99\%$  (10 ml, 137.5 mmol, 1.35 equivalents, Lot# BCBR7870V, Sigma-Aldrich) was injected dropwise under inert atmosphere ( $\text{N}_2$ ). After 30 minutes, EtOAc  $\geq 99.8\%$  (6 mL, Lot# 1862399, Fisher Scientific) was added to form a suspension. The reaction was stirred vigorously at room temperature for 7 hours. Product was collected by vacuum filtration, washed with EtOAc  $\geq 99.8\%$  (10 mL, Lot# 1862399, Fisher Scientific) and set under high vacuum (1 mbar) for 3 hours to yield 7-oxanorborn-5-ene-2,3-dicarboxylic anhydride as white crystalline powder (13.261 g, 79.82 mmol, 78%).

$R_f$  (100% EtOAc) 0.81

$\delta_H$  (400 MHz,  $\text{CDCl}_3$ ): 3.17 (2H, s), 5.46 (2H, s), 6.58 (2H, s)

$\delta_C$  (100 MHz,  $\text{CDCl}_3$ ): 48.7, 82.2, 137.0, 169.8

**2-(5-hydroxypentyl)-3a,4,7,7a-tetrahydro-1H-4,7-epoxyisoindole-1,3(2H)-dione (13)**



7-oxanorborn-5-ene-2,3-dicarboxylic anhydride (7.661 g, 46.11 mmol) was suspended in absolute ethanol (50 mL, Lot# 18I044016, VWR) in a round bottom flask and purged with N<sub>2</sub> gas. 5-aminopentan-1-ol 95% (6.19 g, 60 mmol, 1.3 eq., Lot# BCBW8001, Sigma-Aldrich) was added to the flask portion wise. Triethylamine ≥99.5% BioUltra (12.8 mL, 92.22 mmol, 2 eq., Lot# STBH8268, Sigma-Aldrich) was then added to the mixture dropwise with stirring. The solution was then set to reflux at 105 °C for 8 hours. Reaction was cooled at room temperature and ethanol was removed *in vacuo* and the resulting yellow oil adsorbed on Merck silica gel 60 (Lot# TA2078685819). Silica was loaded on a Redisep RF 25g solid load cartridge (Cat# 69-3873-240) and initially purified on a Teledyne Isco NextGen CombiFlash 300+ using a 40g HP Silica Gold column (Cat#69-2203-347, Lot# 291117603W) and an isocratic run with 100% EtOAc ≥99.8% (Lot# 1862399, Fisher Scientific). Re-purification was done on a 24g HP Silica Gold column (Cat#69-2203-346, Lot# 282229603W) in 100% EtOAc ≥99.8% (Lot# 1862399, Fisher Scientific) using 40 mL/min.

Fractions 10-19 containing the product were collected and combined, solvent was removed *in vacuo* and product 2-(5-hydroxypentyl)-3a,4,7,7a-tetrahydro-1H-4,7-epoxyisoindole-1,3(2H)-dione (2.56 g, 10.187 mmol, 22%) collected as a white crystalline solid.

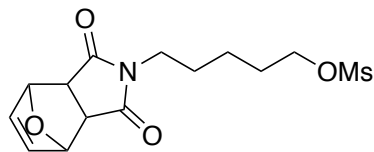
R<sub>f</sub> (100% EtOAc) 0.48

m.p. = 65-67 °C

δ<sub>H</sub> (400 MHz, CDCl<sub>3</sub>): 1.30 (2H, m), 1.54 (4H, m), 1.94 (H, s, -OH), 2.79 (2H, s), 3.44 (2H, t, J = 7 Hz), 3.56 (2H, t, J = 5 Hz), 5.21 (2H, s), 6.47(2H, s)

$\delta_C$  (100 MHz,  $CDCl_3$ ): 22.7, 27.2, 32.0, 38.8, 47.3, 62.3, 80.9, 136.5, 176.4

**5-(1,3-dioxo-1,3,3a,4,7,7a-hexahydro-2H-4,7-epoxyisoindol-2-yl)pentyl methanesulfonate (5)**



2-(5-hydroxypentyl)-3a,4,7,7a-tetrahydro-1H-4,7-epoxyisoindole-1,3(2H)-dione (2.56 g, 10.187 mmol) was dissolved in DCM (50 ml, Lot# 1417944, Fisher Scientific) in a nitrogen flushed round bottom flask. Solution was stirred in an ice bath for 10 minutes. Methanesulfonyl chloride  $\geq 99.7\%$  (946  $\mu$ l, 12.225 mmol, 1.2 eq., Lot# SHBJ4329, Sigma-Aldrich) was injected dropwise under inert atmosphere ( $N_2$ ). Triethylamine  $\geq 99.5\%$  BioUltra (4.256 mL, 30.561 mmol, 3 eq., Lot# STBH8268, Sigma-Aldrich) was added dropwise to the stirring solution. The solution was allowed to warm up at room temperature and stirred for 12 hours. The solvent was removed *in vacuo* and the yellow oil was adsorbed on Merck silica gel 60 (Lot# TA2078685819), loaded on a Rediseq RF 25g solid load cartridge (Cat# 69-3873-240) and purified on a Teledyne Isco NextGen CombiFlash 300+ using a 40g HP Silica Gold column (Cat#69-2203-347, Lot# 291117603W) and an isocratic run with 100% EtOAc  $\geq 99.8\%$  (Lot# 1862399, Fisher Scientific) for 10 column volumes with a flow of 110 mL/min. Fractions containing the product were collected and combined, solvent was removed *in vacuo* to yield 5-(1,3-dioxo-1,3,3a,4,7,7a-hexahydro-2H-4,7-epoxyisoindol-2-yl)pentyl methanesulfonate precursor (2.698 g, 8.192 mmol, 80%) as a white crystalline powder.

$R_f$  (100% EtOAc) 0.65

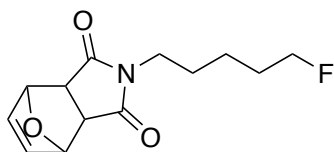
m.p. = 94-96 °C

$\delta_H$  (400 MHz,  $CDCl_3$ ): 1.40 (2H, m), 1.61 (4H, m), 1.76 (2H, q), 2.84 (2H, s), 3.00 (3H, s), 3.49 (2H, m), 4.20 (2H, s), 5.26 (2H, s), 6.51 (2H, s)

$\delta_C$  (100 MHz,  $CDCl_3$ ): 22.5, 26.8, 28.5, 37.4, 38.4, 47.4, 69.6, 80.9, 136.5, 176.3

TOF-ESI-MS: found  $m/z = 330.1122$   $[\text{MH}]^+([\text{C}_{14}\text{H}_{19}\text{NO}_6\text{S}] + \text{H}^+$  requires 330.1011)

**2-(5-fluoropentyl)-3a,4,7,7a-tetrahydro-1H-4,7-epoxyisoindole-1,3(2H)-dione (15)**



5-(1,3-dioxo-1,3,3a,4,7,7a-hexahydro-2H-4,7-epoxyisoindol-2-yl)pentyl methanesulfonate (1.34 g, 4.068 mmol) was dissolved in THF analytical grade (25 mL, Fisher Scientific, Lot# 1691146) and added to a nitrogen flushed RBF. TBAF 1M (6.1 mL, Acros Organics, Lot# A0402228) was added under anhydrous conditions dropwise over 20 minutes while stirring at room temperature. Reaction was set to reflux at 95 °C for 30 minutes. Reaction was cooled to room temperature; solvent was removed *in vacuo* and the resulting yellow oil was adsorbed on Merck silica gel 60 (Lot# TA2078685819). The resulting powder was dry loaded on a Redisep RF 25g solid load cartridge (Cat# 69-3873-240) then it was purified on a Teledyne Isco NextGen CombiFlash Rf+ using an 80g Redisep Rf column (Cat# 69-2203-380, Lot# 272131604X) and 20:80 PetEther:EtOAc gradient (Petroleum spirit 40-60 Cat# 23826.464, Lot# 19B214022, VWR; EtOAc  $\geq 99.8\%$  Lot# 1862399, Fisher Scientific) to 100% EtOAc as per chromatogram in Appendix 8.18 over 5 column volumes. Fractions 5 to 13, containing the product, were collected and combined, solvent was removed *in vacuo* to yield 2-(5-fluoropentyl)-3a,4,7,7a-tetrahydro-1H-4,7-epoxyisoindole-1,3(2H)-dione (819 mg, 3.23 mmol, 79%) as a white solid.

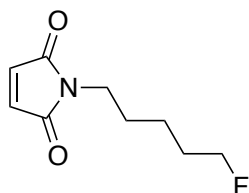
$R_f$  (100% EtOAc) 0.81

$\delta_H$  (400 MHz,  $\text{CDCl}_3$ ): 1.37 (2H, m), 1.67 (4H, m), 2.82 (2H, s), 3.47 (2H, t,  $J = 7$  Hz), 4.40 (2H, dt,  $J = 47$  Hz, 6 Hz), 5.25 (2H, t,  $J = 0.9$  Hz), 6.50 (2H, t,  $J = 0.9$  Hz)

$\delta_C$  (100 MHz,  $CDCl_3$ ): 22.3 (d,  $J = 6$  Hz), 27.1, 29.8 (d,  $J = 20$  Hz) 38.6, 47.4, 80.9, 83.7 (d,  $J = 165$  Hz), 136.5, 176.3

$\delta_F$  (376 MHz,  $CDCl_3$ ): -218.5 (tt,  $J = 47$  Hz, 25 Hz)

**1-(5-fluoropentyl)-1H-pyrrole-2,5-dione (16)**



2-(5-fluoropentyl)-3a,4,7,7a-tetrahydro-1H-4,7-epoxyisoindole-1,3(2H)-dione (732 mg, 2.89 mmol) was dissolved in DMSO  $\geq 99.6\%$  extra dry over molecular sieves (5mL, Lot# 1724013, Acros Organics) in a nitrogen flushed RBF. The flask was heated to 160 °C for 30 minutes with periodic monitoring of reaction progression by TLC. Upon completion, the flask was cooled down by submersion in an ice/water bath. Subsequently, Merck silica gel 60 (Lot# TA2078685819) was added to the RBF and the resulting powder was dry loaded on a Redisep RF 25g solid load cartridge (Cat# 69-3873-240) and purified on a Teledyne Isco NextGen CombiFlash Rf+ using a 40 g Redisep Rf column (Cat# 69-2203-340, Lot# 262217001Y) and an isocratic run with 100%  $Et_2O$  puriss p.a. Ph. Eur.  $\geq 99.8\%$  (Lot# J0080, Honeywell) as per chromatogram in Appendix 8.19 for 8 column volumes with a flow of 30 mL/min. Fractions 6 to 10, containing the product, were collected and combined, solvent was removed *in vacuo* to yield 1-(5-fluoropentyl)-1H-pyrrole-2,5-dione (338.4 mg, 1.827 mmol, 63%) as a colourless oil which crystallises as a white solid upon storing at -20 °C.

$R_f$  (1:1 EtOAc:Hex) 0.78

$R_f$  (100% EtOAc) 0.92

$R_f$  (100%  $Et_2O$ ) 0.98

$\delta_H$  (400 MHz,  $CDCl_3$ ): 1.39 (2H, m), 1.68 (4H, m), 3.53 (2H, t,  $J = 7$  Hz), 4.42 (2H, dt,  $J = 47$  Hz, 6 Hz), 6.68 (2H, s)

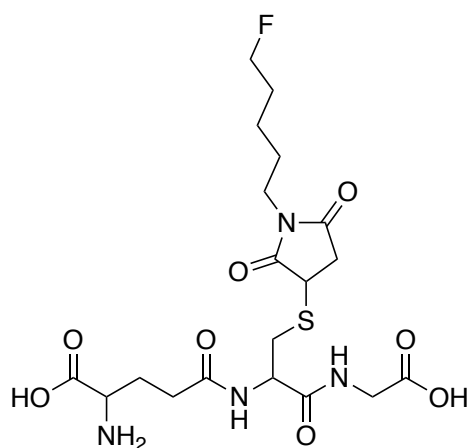
$\delta_C$  (100 MHz,  $CDCl_3$ ): 22.4 (d,  $J = 6$  Hz), 28.1, 29.8 (d,  $J = 20$  Hz) 37.6, 83.7 (d,  $J = 165$  Hz), 134.1, 170.8

$\delta_F$  (376 MHz,  $CDCl_3$ ): -218.6 (tt,  $J = 47$  Hz, 25 Hz)

TOF-ESI-MS: found  $m/z = 186.2220$   $[MH]^+$  ( $[C_9H_{12}FNO_2]+H^+$  requires 186.0930)

LC-MS:  $m/z = 186.2$   $[MH]^+$  detected at 1.49 minutes

***N*<sup>5</sup>-(1-((carboxymethyl)amino)-3-((1-(5-fluoropentyl)-2,5-dioxopyrrolidin-3-yl)thio)-1-oxopropan-2-yl)glutamine (27)**



L-Glutathione reduced  $\geq 98\%$  (153.66 mg, 0.5 mmol, CAS# 70-18-8, Sigma-Aldrich) was dissolved in HBS (100 mL, 20 mM HEPES, 150 mM NaCl, pH 7.49) to yield a final 5 mM solution with a pH of 5.4.

5-fluoropentylmaleimide (9.26 mg, 0.05 mmol) was dissolved in HBS (10 mL, 20 mM HEPES, 150 mM NaCl, pH 7.49) to yield a final solution with a pH of 7.49.

A serial dilution of GSH (5 mM, 2.5 mM, 1.25 mM) in HBS and 5-fluoropentylmaleimide (5 mM, 2.5 mM, 1.25 mM) in HBS were prepared. GSH and 5-fluoropentylmaleimide solutions with equivalent concentration were mixed in a 1:1 ratio,  $\sim 0.5$  mL of each reagent, in a single mixing experiment using the SX.18MV stopped flow spectrometer as per Table 11. The consumption of 5-fluoropentylmaleimide was monitored at 300 nm with strictly maintained temperature at 24.8 °C.

Table 11. L-glutathione and *N*-5-fluoropentylmaleimide solutions mixed

No.	GSH HBS in	<i>N</i> -5-fluoropentyl maleimide in HBS	Mixing ratio	Final mixed solution concentration [GSH] / [ <i>N</i> -5-fluoropentyl maleimide] in HBS
1	5 mM pH 5.4	5 mM pH 7.49	1:1	2.5 mM pH 6.85
2	2.5 mM pH 6.75	2.5 mM pH 7.48	1:1	1.25 mM pH 7.19
3	1.25 mM pH 7.01	1.25 mM pH 7.48	1:1	0.625 mM pH 7.27

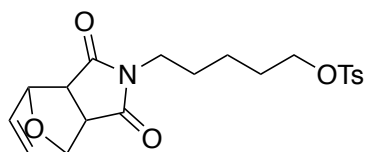
The resulting *N*-5-fluoropentylmaleimide-L-glutathione conjugate was analysed by <sup>19</sup>F-NMR, LC-MS and high-resolution mass spectrometry.

$\delta_F$  (376 MHz, CDCl<sub>3</sub>): -216.6 (ddt, *J* = 47 Hz, 27 Hz, 8.5 Hz)

TOF-ESI-MS: found *m/z* = 493.1755 [MH]<sup>+</sup> ([C<sub>19</sub>H<sub>29</sub>FN<sub>4</sub>O<sub>8</sub>S]<sup>+</sup> H<sup>+</sup> requires 493.1769)

LC-MS: *m/z* = 493.1 [MH]<sup>+</sup> at 1.21 minutes (see LCMS conditions in Experimental 2.6.1)

**5-(1,3-dioxo-1,3,3a,4,7,7a-hexahydro-2H-4,7-epoxyisoindol-2-yl) pentyl 4-methyl-benzenesulfonate (14)**



2-(5-hydroxypentyl)-3a,4,7,7a-tetrahydro-1H-4,7-epoxyisoindole-1,3(2H)-dione (195 mg, 0.77 mmol, 1 eq.) was dissolved in DCM (2 ml) in a round bottom flask. Triethylamine (294  $\mu$ l, 2.1 mmol, 2.7 eq.) was added to the stirring solution. *p*-Toluene sulphonyl chloride (175 mg, 0.924 mmol, 1.2 eq.) was added to the flask and stirred at

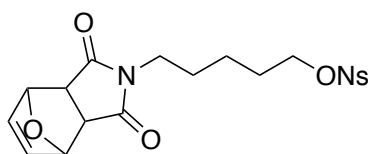
room temperature for 12 hours. Solvent was removed *in vacuo* and the yellow oil was purified by flash column chromatography (100% EtOAc) to yield the 5-(1,3-dioxo-1,3,3a,4,7,7a-hexahydro-2H-4,7-epoxyisoindol-2-yl) pentyl 4-methyl-benzenesulfonate precursor (236 mg, 0.58 mmol, 75%) as a crystalline white solid.

TLC: 100% EtOAc  $R_f = 0.78$

m.p. = 112-113 °C

$\delta_H$  (400 MHz,  $CDCl_3$ ): 1.29 (2H, q,  $J = 7.7$  Hz), 1.52 (2H, q,  $J = 7.5$  Hz), 1.65 (2H, q,  $J = 7.5$  Hz), 2.45 (2H, q,  $J = 7$  Hz), 2.83 (2H, s), 3.43 (2H, t,  $J = 7$  Hz), 3.99 (2H, t,  $J = 6.5$  Hz), 5.25 (2H, s), 6.51 (2H, s), 7.34 (2H, d,  $J = 8.3$  Hz), 7.78 (2H, d,  $J = 8.3$  Hz)

**5-(1,3-dioxo-1,3,3a,4,7,7a-hexahydro-2H-4,7-epoxyisoindol-2-yl) pentyl 4-nitrobenzenesulfonate (25)**



2-(5-hydroxypentyl)-3a,4,7,7a-tetrahydro-1H-4,7-epoxyisoindole-1,3(2H)-dione (450 mg, 1.79 mmol) was dissolved in dichloromethane (10 mL) under inert atmosphere. Triethylamine (502  $\mu$ L, 3.58 mmol, 2 eq.) and 4-nitrobenzene sulphonyl chloride (475 mg, 2.15 mmol, 1.2 eq.) were added to the flask with stirring at 0 °C. The mixture was stirred for 12 hours at room temperature. Solvent was removed *in vacuo* to yield a yellow oil which was purified by flash chromatography using 30:70 (EtOAc: DCM). Product 5-(1,3-dioxo-1,3,3a,4,7,7a-hexahydro-2H-4,7-epoxyisoindol-2-yl) pentyl 4-nitrobenzenesulfonate was collected as a pale yellow waxy solid (357 mg, 0.82 mmol, 45%).

TLC: 100% EtOAc  $R_f = 0.85$

TLC: 30:70 EtOAc:DCM  $R_f = 0.78$

m.p. = 132-133 °C



$\delta_H$  (400 MHz, CDCl<sub>3</sub>): 1.27 (2H, q, J = 7 Hz); 1.51 (2H, q, J = 7 Hz); 1.68 (2H, q, J = 7 Hz); 2.81 (2H, s); 3.42 (2H, t, J = 7 Hz); 4.01 (2H, t, J = 7 Hz); 5.21 (2H, s); 6.49 (2H, s); 8.10 (2H, d, J = 8.4 Hz); 8.38 (2H, d, J = 8.4 Hz)

$\delta_C$  (100 MHz, CDCl<sub>3</sub>): 22.3; 26.7; 28.2; 38.3; 47.4; 71.4; 80.9; 124.5; 129.2, 136.5, 141.9, 150.8, 176.3

TOF-ESI-MS: found  $m/z = 437.1084$  [MH]<sup>+</sup> ([C<sub>19</sub>H<sub>20</sub>N<sub>2</sub>O<sub>8</sub>S]<sup>+</sup> H<sup>+</sup> requires 437.1019)

## 2.6.2 Radiochemistry (in the Wolfson Brain Imaging Centre - Cambridge)

Precursors were synthesised in the Department of Chemistry and transported to the Molecular Imaging Chemistry Laboratory (MICL) radiochemistry facility for <sup>18</sup>F-fluorination. All radioactive work was thoroughly risk assessed, checked that was in accordance with local rules, environmental protection agency (EPA) permit and was agreed upon by the local radioprotection supervisor (RPS).

The cyclotron used for radionuclide production was a GE PETTrace negative ion 16.5 MeV proton accelerator. Fluorine-18 was produced by bombarding <sup>18</sup>O-water (<sup>18</sup>O(p,n)<sup>18</sup>F nuclear reaction) in a silver target (liquid target) with a volume of approximately 1.8 ml. Irradiation with a ramping current of 15-40 uA for 3-21 minutes (depending on amount of fluorine-18 required) produces 1-30 GBq of H[<sup>18</sup>F]F.<sup>256</sup> The activity was eluted into crimped 10 mL vials using chemically pure (CP) grade Helium gas (99.999%).

Cyclotron produced fluorine-18 water and <sup>18</sup>F-labelled organic compounds were measured on a Capintek CRC-15R dose calibrator. Yields of products quoted refer to chromatographically homogenous materials that are decay corrected to the start-of-synthesis unless otherwise specified. Decay correction has been calculated with RadPro online calculator.<sup>257</sup>

The radiochemical yield was then calculated as the ratio between activity of product measured at the end of synthesis decay corrected to the start of synthesis and the  $^{18}\text{F}$  activity at the start of synthesis expressed as a percentage.

Dry solvents and reagents for radiosynthesis were purchased from Sigma-Aldrich, Fisher Scientific and Acros Organics and used without further purification or drying. Deionised water was purified by Merck Synergy UV water purification system providing water with a high resistivity 18.2 M $\Omega$  x cm. Sep-Pak solid phase purification (SPE) cartridges (Waters Sep-Pak C18 Plus Light, Alumina N Plus Light) were purchased from Waters. Before use, the Sep-Pak Alumina N Plus Light cartridge was eluted with 2 mL dry DMSO and the Sep-Pak Plus Light C18 was eluted with 2 mL ethanol followed by 10 mL of deionised water.

The optimised Kryptofix<sup>®</sup> 222 (4,7,13,16,21,24-Hexaoxa-1,10-diazabicyclo[8.8.8] hexacosane) solution containing 2.5 mg K<sub>2</sub>CO<sub>3</sub>, 15 mg K<sub>222</sub>, 1.5 mL (95:5 ACN:water) was used for quaternary methyl ammonium (Waters Sep-Pak Accell plus QMA Carbonate light) cartridge elution for all  $^{18}\text{F}$  drying procedures.

### 2.6.2.1 Manual Radiosynthesis

Cyclotron water (~1.8 mL) containing up to 1 GBq [ $^{18}\text{F}$ ]F<sup>-</sup> was loaded on a Waters Sep-Pak Accell Plus QMA Carbonate light cartridge. Kryptofix<sup>®</sup> 222 solution (1.5 mL solution containing 2.5 mg K<sub>2</sub>CO<sub>3</sub>, 15 mg K<sub>222</sub>, 95:5 ACN:water) was eluted through the cartridge into a Wheaton V-shaped vial. Azeotropic drying was performed at 95 °C under a flow of N<sub>2</sub> (~100 mL/min) using 2 mL dry ACN added in 3 x 0.67 mL portions. Subsequent  $^{18}\text{F}$ -fluorination reactions were carried out in Wheaton V-shaped vials under inert atmosphere (N<sub>2</sub>) using a heating block in a lead lined fume hood.

### 2.6.2.2 Automated Radiosynthesis

Remote controlled module-assisted radiosynthesis was carried on either Advion NanoTek microfluidic system or GE Healthcare TRACERlab FX<sub>FN</sub> automated systems operated in lead shielded 'hot' cells. These modules were used for both optimising reaction conditions and for large-scale tracer production.

The Advion NanoTek system is composed of three individual modules: the NanoTek CE for drying the fluoride, the NanoTek LF that holds 2 reagents in syringes and the MinuteMan LF that holds up to 4 microreactors. Experiments were run remotely from a PC using the Nanotek 1.4.0 software. Nitrogen (2 bar) flow was used to dry fluoride at 95 °C in the presence of Kryptofix<sup>®</sup> 222.

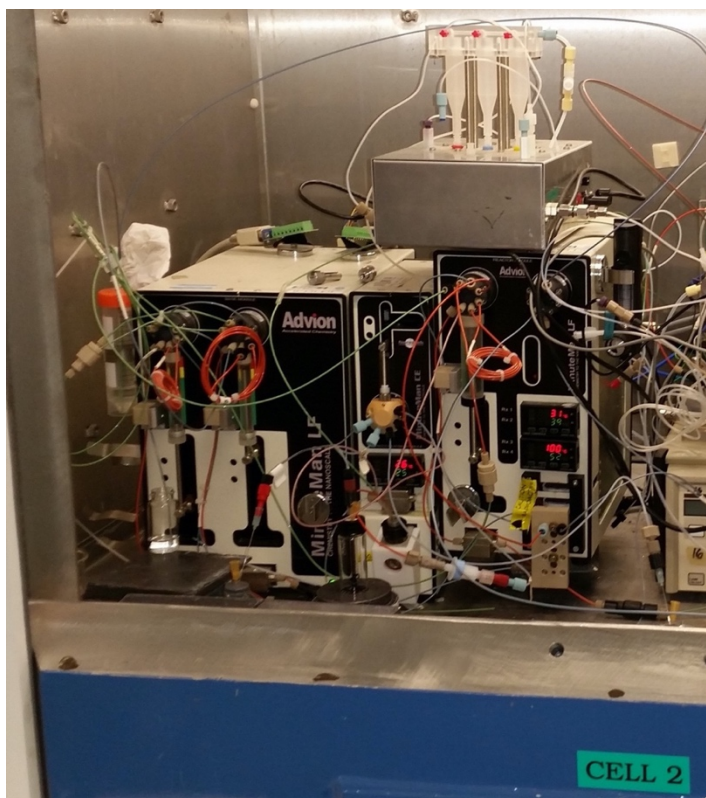


Figure 47. Advion NanoTek modular automated synthesiser in a lead shielded hot cell.

**i. Using Advion NanoTek module to synthesise [<sup>18</sup>F]SFB from 2-thiophenyl iodonium precursor 1**

Below, you can see a diagram (Figure 48.) of the system used for <sup>18</sup>F-fluorination of precursor **1** to produce [<sup>18</sup>F]SFB. P1 is the valve connecting the pump used for iodonium precursor **1** delivery to the flow reactor. P3 is the valve connecting the concentrator V shaped vial used for <sup>18</sup>F fluoride drying to the reactor.

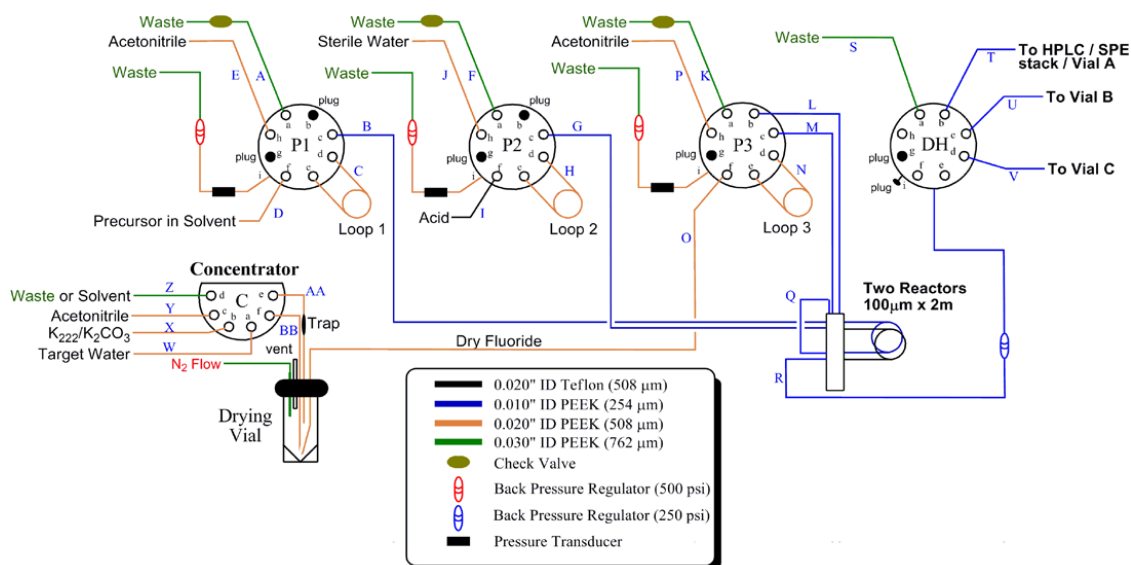


Figure 48. Schematic of the arrangement of pumps, lines and valves on an Advion Nanotek.

The [ $^{18}\text{F}$ ]fluoride water was received in a sealed vial and then placed in the hot cell and connected to the system. The concentrator pump passes the aqueous  $^{18}\text{F}$ -water through a Waters Sep-Pak QMA carbonate light cartridge where it was trapped. A solution of  $\text{K}_{222}/\text{K}_2\text{CO}_3$  (15 mg/2.5 mg) in  $\text{MeCN}/\text{H}_2\text{O}$  (9:1 (v/v)), 450  $\mu\text{L}$  was used to elute the  $\text{K}[^{18}\text{F}]\text{F}$  from the QMA into the concentrator. Upon heating to 95  $^\circ\text{C}$  and using a stream of argon (2 ml/s) the fluoride is dried. It is then resuspended in dry acetonitrile (500  $\mu\text{L}$ ) and loaded in loop 3 by pump 3. The iodonium precursor (5 mg), dissolved in dry DMF or DMSO (500  $\mu\text{L}$ ), is loaded in loop 1. The synthesis begins by mixing both solutions in a 1:1 ratio in the two heated reactor loops with a total volume of 31.4  $\mu\text{L}$  as per the Table 12 below:

Table 12. Reaction conditions used to generate [<sup>18</sup>F]SFB from precursor 1 using Advion NanoTek

Reaction#	Temperature (°C)	Pump volume (μL)	Pump 1: Pump 3 ratio	Rate (μL/min)
1	130	100	1:1	30
2	150	100	1:1	30
3	160	100	1:1	30
4	170	100	1:1	30
5	190	100	1	30

## ii. GE Healthcare TRACERlab FX<sub>FN</sub> synthesis

GE Healthcare TRACERlab FX<sub>FN</sub> automated synthesizer was coupled to an external UV diode array detector set at 220 nm. The automation rig required compressed air (5 bar), nitrogen (2 bar) and helium (1.5 bar) gases for every synthesis. Semi-prep HPLC for radioactive prosthetic groups was performed on a reverse phase Sigma-Aldrich SUPELCOSIL LC-18 (250 mm x 10 mm) column using a SYKAM S1122 dual piston solvent delivery system, which was remotely controlled through the TRACERlab FX<sub>FN</sub> software (see Figure 49).

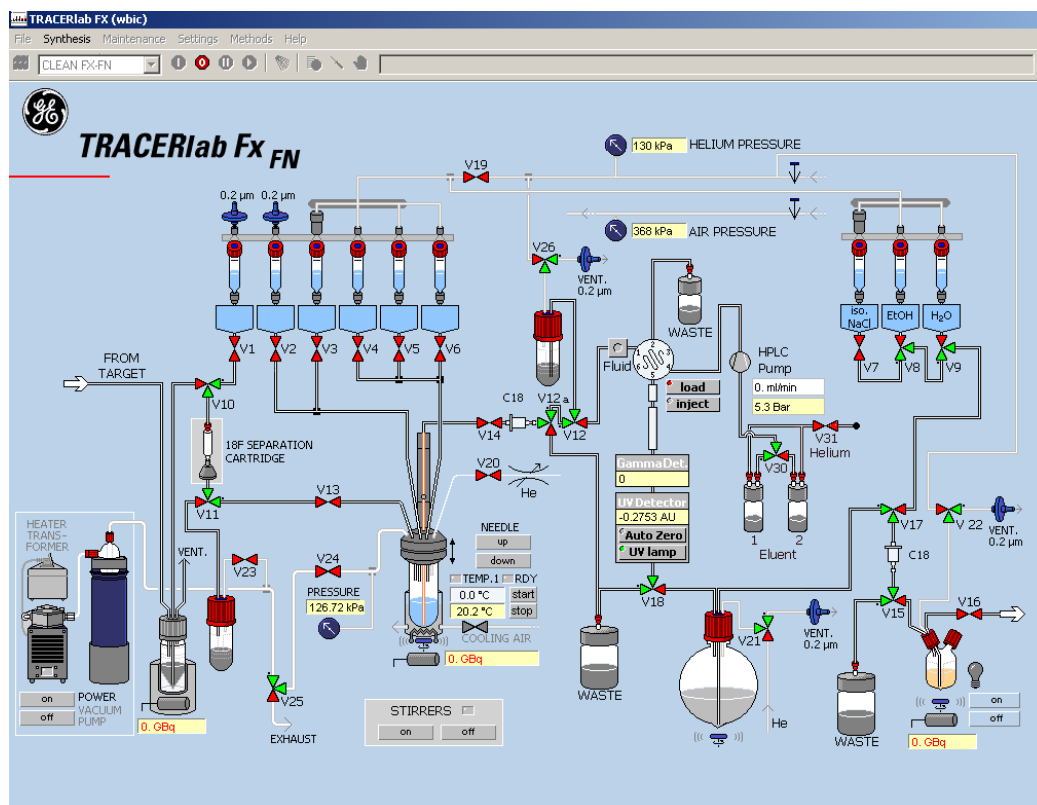


Figure 49. GE Healthcare TRACERlab FX<sub>FN</sub> Windows XP control screen. It allows manual control over each valve and automated control through pre-programmed macros controlling valves, HPLC and gas flow.

A) Vial loading on GE TRACERlab FX<sub>FN</sub> for [<sup>18</sup>F]FBEM preparation (see Figure 49 for position reference)

Cartridge #1 QMA – Waters Sep-Pak Accell Plus QMA Carbonate Plus Light cartridge

Vial 1 – 1.5 mL Kryptofix<sup>®</sup> 222 (2.5 mg K<sub>2</sub>CO<sub>3</sub>, 15 mg K<sub>222</sub>, 1.5 mL 95:5 (v/v) ACN: H<sub>2</sub>O)

Vial 2 – dry ACN (2 mL)

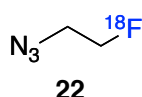
Vial 3 – Ethyl 4-(trimethylammonium triflate) benzoate precursor (5 mg,) in dry DMF (1 mL)

Vial 4 – NaOH (0.1 M, 1 mL), in syringe outside hotcell HCl (1 M, 0.7 mL)

Vial 5 – DMSO (0.5 mL), NH<sub>4</sub>OAc buffer (150 mM, 1 mL, pH 6.8) + ascorbic acid (2 mg/mL) + AcOH (10 µL), final buffer pH 4.12

HPLC Vial – NH<sub>4</sub>OAc buffer (150 mM, 2 mL, pH 6.8) + ascorbic acid (2 mg/mL) and AcOH (20 µL), final buffer pH 4.12

### 2.6.2.3 2-[<sup>18</sup>F]fluoroethyl azide production (22)



Vial loading on GE TRACERlab FX<sub>FN</sub> for 2-[<sup>18</sup>F]fluoroethyl azide preparation (see Figure 49 for position reference)

Cartridge #1 QMA – Waters Sep-Pak Accell Plus QMA Carbonate Plus Light cartridge

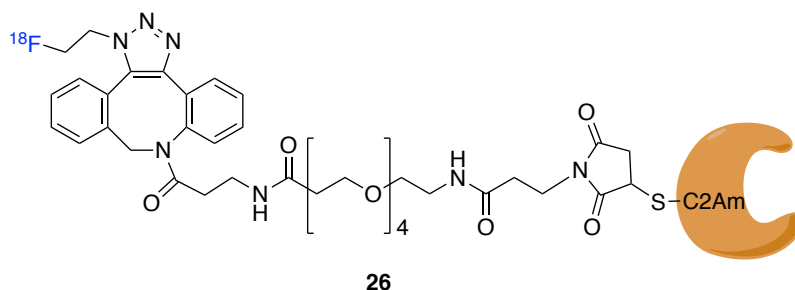
Vial 1 – 1.5 mL Kryptofix<sup>®</sup> 222 (2.5 mg K<sub>2</sub>CO<sub>3</sub>, 15 mg K<sub>222</sub>, 1.5 mL 95:5 (v/v) ACN: H<sub>2</sub>O)

Vial 2 – dry ACN (2 mL)

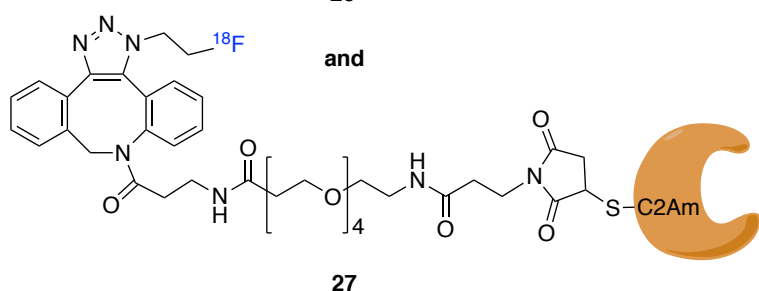
Vial 3 – azide tosylate precursor **4** (5 mg, 15.2 μmol) in dry DMF (1 mL)

Using a preprogrammed sequence (details in Appendix 8.1) on a GE TRACERlab FX<sub>FN</sub>, precursor **4** (5 mg, 15.2 μmol) in dry DMF (1 mL) was added to dried K[<sup>18</sup>F]F-Kryptofix 222 (2 GBq – start-of-synthesis). The mixture was stirred at 88 °C for 10 min then distilled over to a separate vial in an adjacent hot cell. 2-[<sup>18</sup>F]fluoroethylazide was collected with a radiochemical yield of 8±3% (decay corrected, n = 3).

### 2.6.2.4 [<sup>18</sup>F]C2Am-PEG<sub>4</sub>-DBCO (26 and 27)



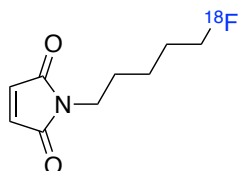
and



A 2-[<sup>18</sup>F]fluoroethylazide solution (260 MBq at end of synthesis) was dissolved in PBS (15 μL) and added to C2Am-PEG<sub>4</sub>-DBCO (4.5 mg/ml, 278 μM, 5 μL) in a ratio of 1:4 v/v to yield a final crude protein solution (1.1 mg/ml, 70 μM) and allowed to react

for 30 min at room temperature. The crude mixture was analysed by HPLC and the UV and radiochromatogram shown in Figure 26.

### 2.6.2.5 [<sup>18</sup>F]FPenM production (24)



24

[<sup>18</sup>F]FPenM

#### i. Vial loading on GE TRACERlab FX<sub>FN</sub> for [<sup>18</sup>F]FPenM preparation (see Figure 49 for position reference)

Cartridge #1 QMA – Waters Sep-Pak Accell Plus QMA Carbonate Plus Light cartridge

Cartridge #2 Intermediate – Waters Sep-Pak Alumina N Plus light cartridge

Cartridge #3 SPE – Waters Sep-Pak Plus Light C18 cartridge

Vial 1 – 1.5 mL Kryptofix<sup>®</sup> 222 elution solution (2.5 mg K<sub>2</sub>CO<sub>3</sub>, 15 mg Kryptofix K<sub>222</sub>, 1.5 mL 95:5 (v/v) ACN: H<sub>2</sub>O)

Vial 2 – ACN (2 mL) dried over molecular sieves

Vial 3 – mesylate **5** (5 mg, 15.2 μmol, 15.2 mM) in dry DMSO (1 mL)

Vial 4 – Methanesulfonic acid (20 μL) in dry DMSO (0.5 mL)

Vial 5 – DMSO (0.5 mL), NH<sub>4</sub>OAc buffer (150 mM, 1 mL, pH 6.8) + ascorbic acid (2 mg/mL) + AcOH (10 μL), final buffer pH 4.12

HPLC Vial – NH<sub>4</sub>OAc buffer (150 mM, 2 mL, pH 6.8) + ascorbic acid (2 mg/mL) and AcOH (20 μL), final buffer pH 4.12

Vial 6 – None

Vial 7 – None

Vial 8 – EtOH (0.3 mL)

Vial 9 – HBS buffer (1 mL, pH 7.4)

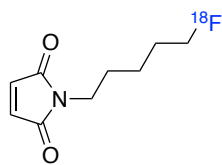
Dilution Flask – NH<sub>4</sub>OAc buffer (50 mM, 30 mL, pH 6.8) + ascorbic acid (1 mg/mL) + AcOH (300 μL), final buffer pH 3.65

Product vial – HBS buffer (100 μL, pH 7.4) + ascorbic acid (1 mg/mL), final buffer pH 4.5

HPLC Solvent – 38:62 ACN (183 mL): NH<sub>4</sub>OAc buffer (50 mM, 30 mL, pH 6.8) + ascorbic acid (0.1 mg/mL) + AcOH (300 μL), final buffer pH 5.6-5.7



## ii. Automated synthesis of [<sup>18</sup>F]FPenM



**24**  
**[<sup>18</sup>F]FPenM**

Using a preprogrammed sequence (details in Appendix 8.2) on a GE TRACERlab FX<sub>FN</sub>, precursor **5** (5 mg, 15.2 μmol) in dry DMSO (1 mL) was added to dried K[<sup>18</sup>F]F-Kryptofix 222 (27±1 GBq – start-of-synthesis). The mixture was stirred at 92 °C for 12 min then added methanesulfonic acid (20 μL) in dry DMSO (0.5 mL) and heated at 160 °C for 6 min. Reaction mixture was cooled down to < 35 °C and moved by positive pressure to the HPLC vial through a pre-activated (by DMSO, 2 mL) Waters Sep-Pak Alumina N Plus light cartridge. The HPLC vial was pre-filled with NH<sub>4</sub>OAc solution (22 mg NH<sub>4</sub>OAc, 2 mL H<sub>2</sub>O) with ascorbic acid (4 mg) and AcOH (20 μL). Reactor was washed with 0.5 mL DMSO and NH<sub>4</sub>OAc solution (11 mg NH<sub>4</sub>OAc, 1 mL H<sub>2</sub>O, 150 mM) with ascorbic acid (2 mg) and AcOH (10 μL). The solution from HPLC vial containing prosthetic tracer (5 mL) was loaded on the HPLC column and purified with an isocratic flow of 3 mL/min of 38% ACN in 50 mM NH<sub>4</sub>OAc (with 1% ascorbic acid and 1% AcOH). The purified peak at around 14 min (see purification chromatogram in Appendix 8.3) was collected and diluted in the SPE flask containing NH<sub>4</sub>OAc solution (50 mM, 115 mg NH<sub>4</sub>OAc, 30 mL, pH 5.6) with ascorbic acid (30 mg) and AcOH (300 μL). The solution was flowed through an ethanol/water (2 mL/10 mL) pre-activated Sep-Pak Plus Light C18. Ethanol 0.3 mL and HBS 1 mL were flowed through the cartridge to elute *N*-(5-[<sup>18</sup>F]fluoropentyl)maleimide ([<sup>18</sup>F]FPenM) (~ 2 GBq – end-of-synthesis, 1.3 mL). This was produced in 58±5.8 min (n = 12) a moderate radiochemical yield (12±3%, decay corrected to start-of-synthesis, n = 11) and high radiochemical purity (95±3.4% by radio-HPLC, n = 11). Specific (1144±161 GBq/mg (n = 3)) and molar activities (212000±30000 MBq/μmol (n = 3)) of [<sup>18</sup>F]FPenM were determined by UV-HPLC monitoring at 220 nm.

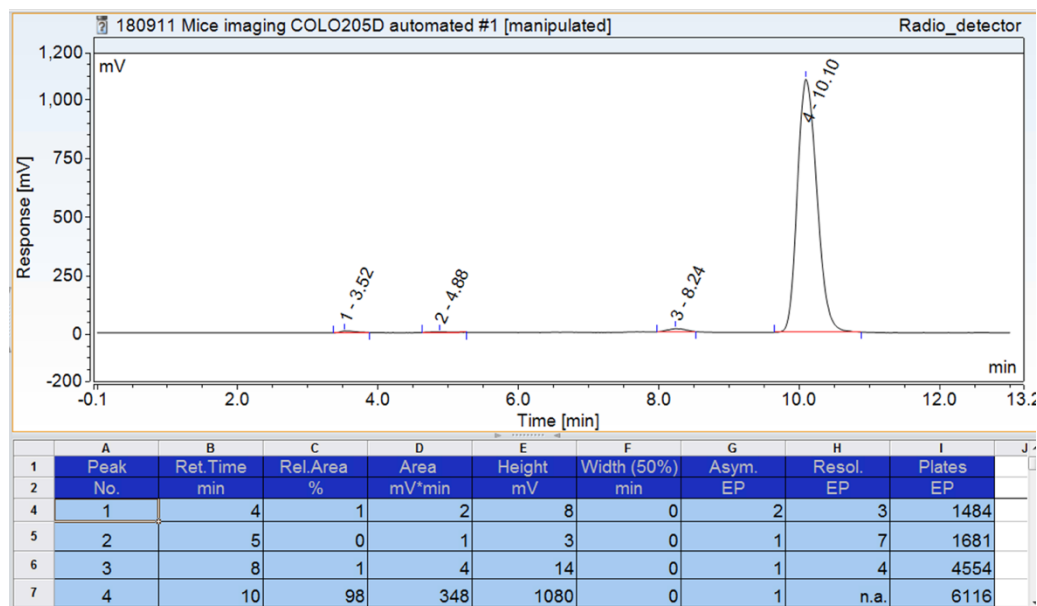
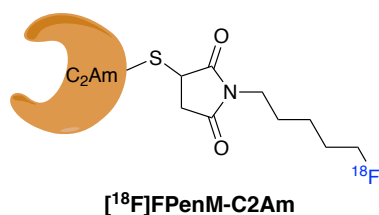


Figure 50. HPLC of [ $^{18}\text{F}$ ]FPenM showing the radiochromatogram. Peak 4 at 10.1 minutes represents [ $^{18}\text{F}$ ]FPenM.

### 2.6.2.6 *N*-(5-[ $^{18}\text{F}$ ]fluoropentyl)maleimide-C2Am ([ $^{18}\text{F}$ ]FPenM-C2Am) bioconjugation



C2Am (123  $\mu\text{g}$ , 25.6  $\mu\text{l}$ , 7.58 nmol, 297  $\mu\text{M}$ ) was conjugated to **24** (150  $\mu\text{L}$ , 359 MBq) to yield, after gel filtration, *N*-(5-[ $^{18}\text{F}$ ]fluoropentyl)maleimide-C2Am (56.1  $\mu\text{g}$ , 3.42 nmol) with a conjugation yield of  $87 \pm 4.3\%$  ( $n = 5$ ) by radio-HPLC. Crude *N*-(5-[ $^{18}\text{F}$ ]fluoropentyl)maleimide-C2Am solution (175.6  $\mu\text{L}$ , 42.7  $\mu\text{M}$ ) was purified by manual loading on a Sephadex G-25 desalting cartridge (PD-10, Illustra NAP-5; GE Healthcare Life Sciences) and gravity filtered and collected 3 fractions. 1<sup>st</sup> fraction was eluted with PBS (300  $\mu\text{l}$ ) was discarded as it did not contain any activity. The 2<sup>nd</sup> fraction ( $\sim 100$  MBq end-of-purification, 56.1  $\mu\text{g}$ , 3.42 nmol, 550  $\mu\text{l}$ , 5.7  $\mu\text{M}$ ) was eluted with PBS (550  $\mu\text{l}$ ) to yield the  $>99\%$  pure (by radio HPLC) [ $^{18}\text{F}$ ]FPenM-C2Am. The molar activity of [ $^{18}\text{F}$ ]FPenM-C2Am was  $29500 \pm 10600$  MBq/ $\mu\text{mol}$  ( $n=5$ ) ( $1.8 \pm 0.65$  MBq/ $\mu\text{g}$ ) at the end-of-synthesis (conjugation and purification) and  $\sim 16600$  MBq/ $\mu\text{mol}$  ( $\sim 1$  MBq/ $\mu\text{g}$ ) at

the time of injection. The 3<sup>rd</sup> fraction (~50 MBq at end-of-purification) was eluted with PBS (1 mL). NAP-5 cartridge (~80 MBq at end-of-purification) was also counted and then discarded. Merck Direct Detect Infrared spectrometer was used to determine protein concentration.

Analytical reverse-phase HPLC was carried out on a UHPLC<sup>+</sup> Thermo Scientific Dionex UltiMate 3000 and data interpreted with Chromeleon 7 software (version 7.2.0.3765). The instrument equipped with a Primesphere C18-HC 110A (250 x 4.6 mm, 5µm; Phenomenex) analytical column was used for HPLC QC analysis of small organic <sup>18</sup>F-labelled prosthetic groups running a 10 minute 5-95% ACN:H<sub>2</sub>O gradient running at 1 ml/min followed by 3 minutes of 5:95 ACN:H<sub>2</sub>O column re-equilibration wash.

An xBridge BEH 125A (7.8 x 300 mm, 3.5 µm; Waters) size exclusion column (SEC) was used for protein HPLC QC runs. 100% PBS isocratic run at 0.7 ml/min flow rate for 45 minutes. 10% acetonitrile was added between 20 and 40 minutes.

### 2.6.3 Protein reduction and storage (CRUK – Cambridge Institute)

All buffers used were made up by the core facilities according to standard recipes. Solvents, reagents and media were used as provided from the vendors without further purification. Thermo Scientific Heraeus Fresco 21 microcentrifuge was used for concentrating reduced C2Am using Amicon Ultra 0.5 mL 3 kDa centrifugal filter cartridges and for forming cell pellets.

Analytical size exclusion HPLC was carried out, in the molecular imaging chemical laboratory, on a UHPLC<sup>+</sup> Thermo Scientific Dionex UltiMate 3000 and data interpreted with Chromeleon 7 software (version 7.2.0.3765). A xBridge BEH 125A (7.8 x 300 mm, 3.5 µm; Waters) size exclusion column (SEC) was used with 100% PBS and 0.7 ml/min flow rate for 45 minutes; 10% acetonitrile was added between 20 and 40 minutes to elute any small organic molecules.

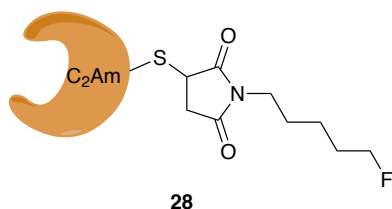
#### 2.6.3.1 C2Am protein reduction reaction and storage

Recombinant C2Am was expressed as a GST fusion protein in *E. coli* and purified by affinity chromatography by Dr André Neves, Senior Research Associate of the Brindle group, and provided as a solution in HBS (20 mM HEPES, 100 mM NaCl, 5mM EDTA,

pH 7.4) containing 5 mM 1,4-dithiothreitol (DTT) and 5 mM ethylenediaminetetraacetic acid (ETDA).

A solution of C2Am (1.43 mg in 50  $\mu$ L, 1.76 mM) was reduced with a 10 mM DTT (0.6 mg, 3.8  $\mu$ mol) in PBS (400  $\mu$ L) at room temperature for 30 minutes. The mixture was loaded in an Amicon Ultra 0.5 mL 3 kDa centrifugal filter cartridge and passed through the filter by centrifugation at 14,000 g for 25 minutes. Protein was dissolved in PBS (400  $\mu$ L) and the spin-filtration wash repeated 2 times. The protein was concentrated to a final solution (70  $\mu$ L, 1.43 mg, 1.29 mM) and aliquoted in 14 low protein binding 0.5 mL Eppendorf tubes, each containing reduced C2Am (5  $\mu$ L, 143  $\mu$ g, 1.29 mM) under inert atmosphere (Argon). Vials were stored in a  $-80$  °C freezer.

### 2.6.3.2 Synthesis of *N*-5-fluoropentylmaleimide-C2Am HPLC standard (28)



#### iii. FPenM-C2Am

To C2Am (7  $\mu$ L, 143  $\mu$ g, 8.8 nmol, 1.26 mM) was added *N*-(5-fluoropentyl)maleimide (0.166  $\mu$ g, 9  $\mu$ M,  $\sim$ 1000 eq.) in PBS (100  $\mu$ L) and left to react at room temperature for 2 hours. The mixture was loaded in an Amicon Ultra 0.5 mL 3 kDa centrifugal filter cartridge and passed through the filter by centrifugation at 14000 g for 25 minutes. Protein was dissolved in PBS (400  $\mu$ L) and the process repeated 3 times. The protein was concentrated to a final solution (75  $\mu$ L, 1.43 mg, 1.29 mM). Mass spectrometry on the protein samples were run in the Department of Chemistry on a Waters Xevo SQD2 instrument. LC-MS and HPLC chromatograms of *N*-(5-fluoropentyl)maleimide conjugated C2Am can be found in the Appendix 8.7, 8.8.

TOF-ESI-MS: C2Am (reduced)  $m/z = 16222.5$  [MH]<sup>+</sup>

TOF-ESI-MS: *N*-(5-fluoropentyl)maleimide-C2Am conjugate  $m/z = 16408.5$  [MH]<sup>+</sup>

# 3 *IN VITRO* STUDIES USING [<sup>18</sup>F]FPENM-C2AM IN BREAST AND COLORECTAL CANCER CELL LINES

## 3.1 Introduction

Alam *et al.*<sup>99</sup> and Xie *et al.*<sup>258</sup> have shown previously that fluorescently-labelled derivatives of C2Am can be used as imaging probes for the detection of cell death, using flow cytometry, following chemotherapy treatment. Cell death, induced by DNA intercalating agents (e.g. doxorubicin and etoposide), was detected in two cancer models, by a membrane integrity marker (SYTOX<sup>®</sup> green nuclear staining) and shown to correlate with increased binding of fluorescently-labelled C2Am-AF647<sup>99</sup>.

Flow cytometry allows heterogenous populations of cells to be discriminated and separated based on their physical properties (e.g. cell size, cell shape, relative fluorescence intensity). Cells are scanned by multiple lasers as they pass individually through a narrow flow chamber. This allows the cytometer to sort cells based on the detected properties. (see Figure 51)

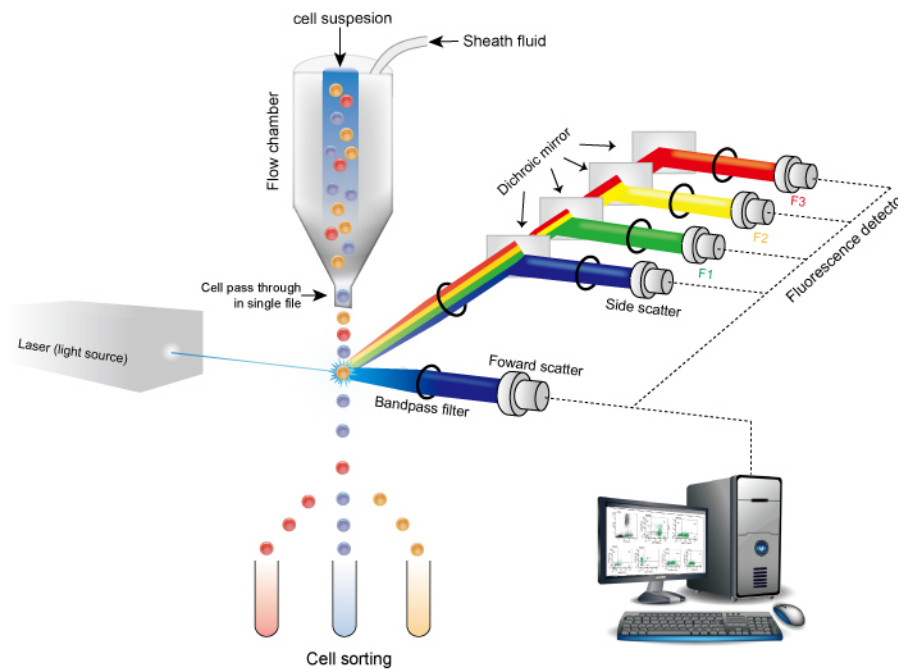
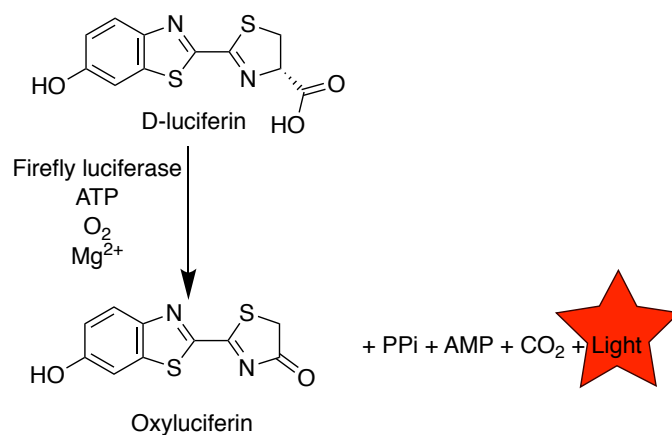


Figure 51. Schematic diagram of a flow cytometer. Cells flow in a single file through a flow chamber where a set of perpendicular laser light beams passes through. The optical properties of cells are detected by analysing scattered incident light. Detectors such as forward-, side-scatter and other fluorescent optical detectors (optical mirrors and filters selectively allow the passage of light of different wavelengths) convert the light into electrical signals which are then interpreted by dedicated software (e.g. BD FACSDiva). Schematic adapted from Creative Diagnostics – Flow cytometry guide.<sup>259</sup>

In this study, the extent of cell death induced by activation of the tumour necrosis factor TNF-related apoptosis-inducing ligand receptor 2 (TRAIL-R2) was assessed. MEDI3039, a TRAIL-R2 agonist, was used to induce apoptosis, via the extrinsic pathway, in models of triple-negative breast (MDA-MB-231-D) and colorectal (Colo205-D) cancer. Apoptosis was assessed indirectly via the reduction in cellular NADH autofluorescence and concomitant increase in SYTOX<sup>®</sup> green nuclear stain fluorescence. Depletion of NADH autofluorescence occurs in dying cells and can be detected in the UV (Excitation  $\lambda = 335\text{-}350\text{ nm}$ ; Emission  $\lambda = 440\text{-}470\text{ nm}$ ) by flow cytometry and used to discriminate between dying and viable cells.<sup>99,260</sup> The DNA damage that occurs as a result of cytotoxic treatment induces the activation of poly-ADP-ribose polymerase (PARP). NAD<sup>+</sup> is a substrate for PARP1, the most abundant family member, which catalyses multiple transfers of the ADP-ribose part of NAD<sup>+</sup> to acceptor proteins thus forming poly(ADP-ribose)-protein. These poly(ADP-ribose) moieties interact with DNA to

facilitate access for the repair mechanism to take place.<sup>261</sup> As a consequence of formation of poly(ADP-ribose), NAD<sup>+</sup> and consequently NADH are depleted from cells.<sup>262</sup>

The two human cancer cell lines, Colo205 and MDA-MB-231 (in short MDA) were chosen because of their fast doubling times *in vitro* and their rapid growth when implanted as xenografts mice. The cell lines were transduced with a lentiviral vector to express firefly luciferase (for bioluminescence measurements, see Scheme 19) and a red-fluorescent protein (mStrawberry). Cells that expressed consistently high levels of mStrawberry were selected by fluorescence-activated cell sorting (FACS).<sup>263</sup> These transfected cell lines have been named Colo205-Dual and MDA-MB-231-Dual and were obtained from Dr Susana Ros, Research Associate in the Brindle group. Bioluminescence imaging (BLI) differs from fluorescence imaging (FLI), in that light is emitted as a result of an enzymatic oxidative decarboxylation reaction rather than from a light absorbing and emitting fluorophore. BLI was performed *in vivo* post implantation of a xenograft in the mouse, and upon intraperitoneal (i.p.) injection of D-luciferin, the substrate for the enzyme (firefly luciferase or fLuc), which requires oxygen and ATP as co-factors. Bioluminescence produced by the tumour cells can be detected and quantified and consequently tumour formation, growth and viability can be assessed non-invasively over time.



Scheme 19. Bioluminescence light emission upon biochemical oxidation of D-luciferin to oxyluciferin in the presence of firefly luciferase. Note that the availability of O<sub>2</sub> and ATP is critical for the reaction.<sup>264</sup> PPi = pyrophosphate ; AMP = adenosine monophosphate

MEDI3039 induces cell death by activating tumour necrosis factor (TNF)-related apoptosis-inducing ligand receptor 2 (TRAIL-R2,<sup>265,17</sup> which are overexpressed in some

human tumour cells, including colorectal and breast carcinomas. Upon activation, the receptor trimerizes, internalizes and triggers a cascade of biochemical pathways which lead to the activation of caspase-8, resulting in apoptosis.<sup>266</sup> Nikolettou *et al.* have suggested that ATP concentration, upon triggering cell death, regulates the balance between apoptosis and necrosis.<sup>267</sup> High levels of ATP are required for the cells to undergo apoptosis, whereas low ATP levels leads to necrosis hence ATP cellular level acts a switch between apoptosis and necrosis.<sup>268</sup> Activating TRAIL-R2 receptors leads to DNA damage, which in turn activates PARP1, consuming the NAD(H<sup>+</sup>) pool, leading to depletion of ATP and triggering of necrosis.

## 3.2 Monitoring cell death following treatment using fluorescence imaging

Colo205-D and MDA-MB-231-D were cultured in RPMI-1640 and DMEM media respectively, both media were supplemented with 10% FBS. Cell viability was determined initially using a Vi-CELL cell viability analyser, which detects viability via the Trypan Blue dye exclusion method<sup>269</sup>. Flow cytometry was then used to accurately determine cell viability 24 hours post treatment with different concentrations of MEDI3039 in the two cancer cell lines, where cell membrane integrity was assessed by staining with SYTOX<sup>®</sup> green (50 nM).

### 3.2.1 Assessment of MDA-MB-231-D cell viability using SYTOX<sup>®</sup> green following incubation of the cells with MEDI3039 (10 pM)

MDA-MB-231-D cells were incubated with MEDI3039 (10 pM) for 24 hours and then with SYTOX<sup>®</sup> green (50 nM) at 37 °C for 10 minutes. Cells were harvested and after washing, the extent of cell death was assessed by flow cytometry.

Data presented in Figure 55 shows NADH autofluorescence (Excitation  $\lambda = 350$  nm; Emission  $\lambda = 475$  nm, measured at 450 nm) and SYTOX<sup>®</sup> green fluorescence (Excitation  $\lambda = 504$  nm; Emission  $\lambda = 523$  nm) (n= 3). The scatter plot of NADH autofluorescence versus SYTOX<sup>®</sup> green fluorescence allowed differentiation of three cell populations: viable, apoptotic, and necrotic cells (Figure 52E and F).



Following MEDI3039 treatment, MDA cell viability dropped significantly from 88 to 17% ( $P < 0.0001$ ) and necrosis increased significantly from 8 to 75% ( $P = 0.0005$ ). Apoptosis increased from 5 to 8% ( $P < 0.01$ ). (see Figure 52 and Figure 55).

Statistical analysis was performed using unpaired two-tailed t-test with Welch's correction. These results suggest that MDA cells die predominantly by necrosis following treatment with the TRAIL-R2 agonist. A confirmation of the viability for the control cells was done using a Vi-CELL cell analyser. This gave a viability of 94.8%, slightly higher than the viability obtained from flow cytometry ( $87.9 \pm 1.6\%$ ).

## Targeted Imaging Agents for Detecting Tumour Cell Death following Therapy

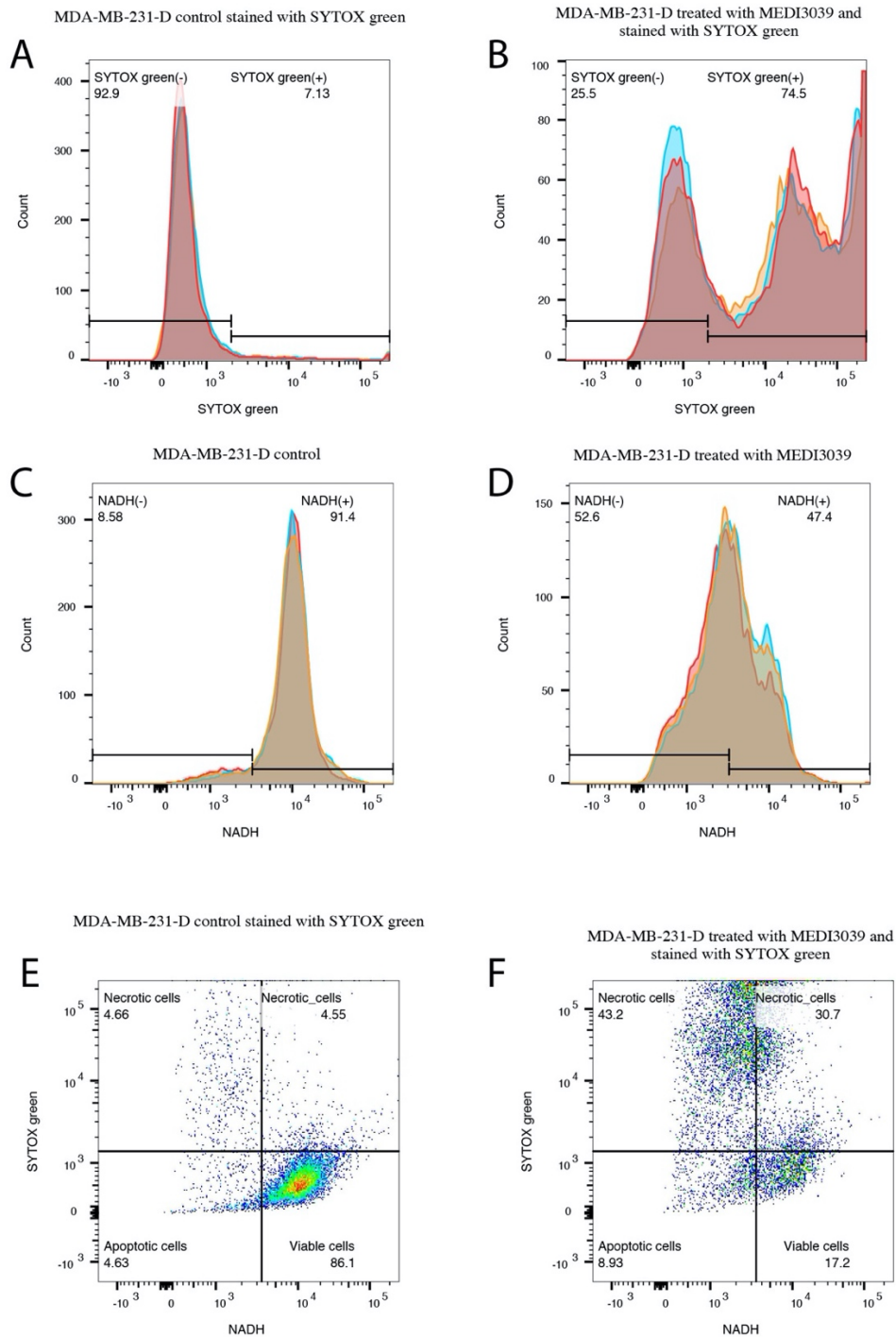


Figure 52. Histograms A (control) and B (treated with MEDI3039 10 pM) show significantly increased SYTOX<sup>®</sup> green nuclear stain emission (530 nm) upon treatment (overlay of 3 replicates). Histograms C (control) and D (treated) show significant reduction of NADH autofluorescence (450nm) upon treatment (overlay of 3 replicates). Scatter plots E (control) and F (treated) showing rectangular gates which split the cell population into viable cells, apoptotic cells and necrotic cells by plotting NADH autofluorescence against SYTOX<sup>®</sup> green fluorescence.

### 3.2.2 Assessment of MDA-MB-231-D cell viability using SYTOX<sup>®</sup> green in cells incubated with MEDI3039 (5 pM)

This experiment used half the concentration of MEDI3039 (5 pM) to induce cell death in MDA-MB-231-D cells for 24 hours and its outcome was assessed by flow cytometry, as described in the previous section (see Figure 53).

In this case viability dropped significantly ( $P < 0.001$ ) from 79 to 38% and necrosis increased significantly from 15 to 49% ( $P < 0.001$ ). Apoptosis increased from 4 to 12% ( $P < 0.05$ ). Further details are presented in Figure 55. These results reinforce the idea that MDA cells undergo cell death via necrosis in the presence of the TRAIL-R2 agonist.

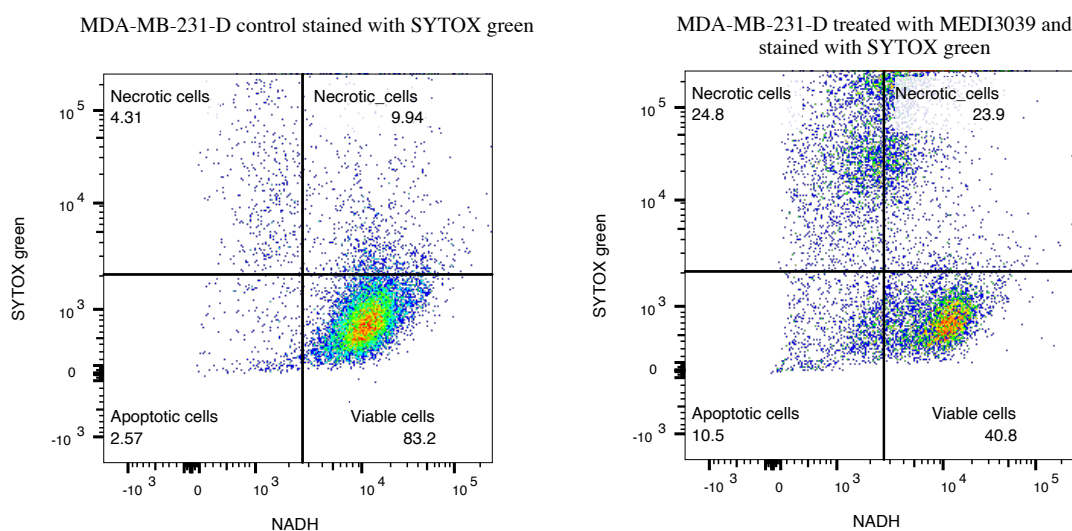


Figure 53. Scatter plots showing SYTOX<sup>®</sup> green (50 nM) stained MDA-MB-231-D control cells (left) and treated cells (right) with MEDI3039 (5 pM). Rectangular gates split the cell population into viable cells, apoptotic cells and necrotic cells by plotting NADH autofluorescence (emission at 450 nm) against SYTOX<sup>®</sup> green fluorescence (emission at 530 nm).

### 3.2.3 Assessment of Colo205-D cell viability using SYTOX<sup>®</sup> green in cells incubated with MEDI3039 (5 pM)

MEDI3039 (5 pM) was used to induce cell death in Colo205-D cells for 24 hours and the outcome assessed by flow cytometry using the same parameters as described previously (see Figure 54).

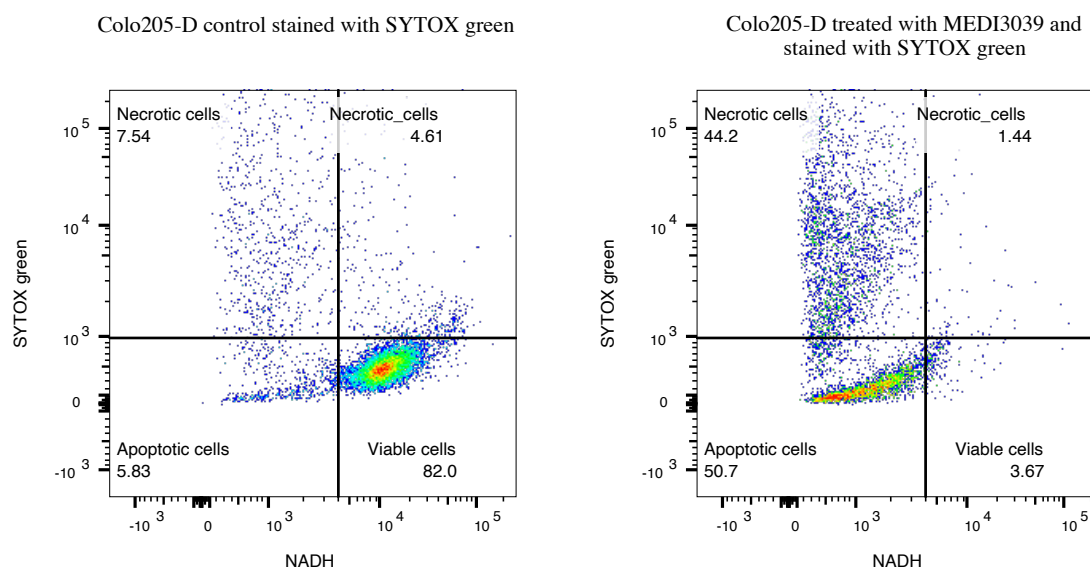


Figure 54. Scatter plots showing Colo205-D cell viability (by NADH UV autofluorescence at 450 nm) and cell membrane integrity (SYTOX<sup>®</sup> green emission at 530 nm) of control (left plot) and cells treated with 5 pM MEDI3039 (right plot).

Colo205-D cell viability dropped significantly, from 83 to 4%. Moreover, cells were undergoing both necrosis 48% and apoptosis 48%. At this drug concentration (5 pM) cell viability was only 4% after 24 hours of treatment. Upon assessing the level of side scatter and forward scatter (area), only 57% of the events detected by the cytometer were cells while the rest were cell debris.

The collated data are shown in Figure 55 for Colo205-D and MDA-MB-231-D cells treated with MEDI3039 (at 5 or 10 pM).

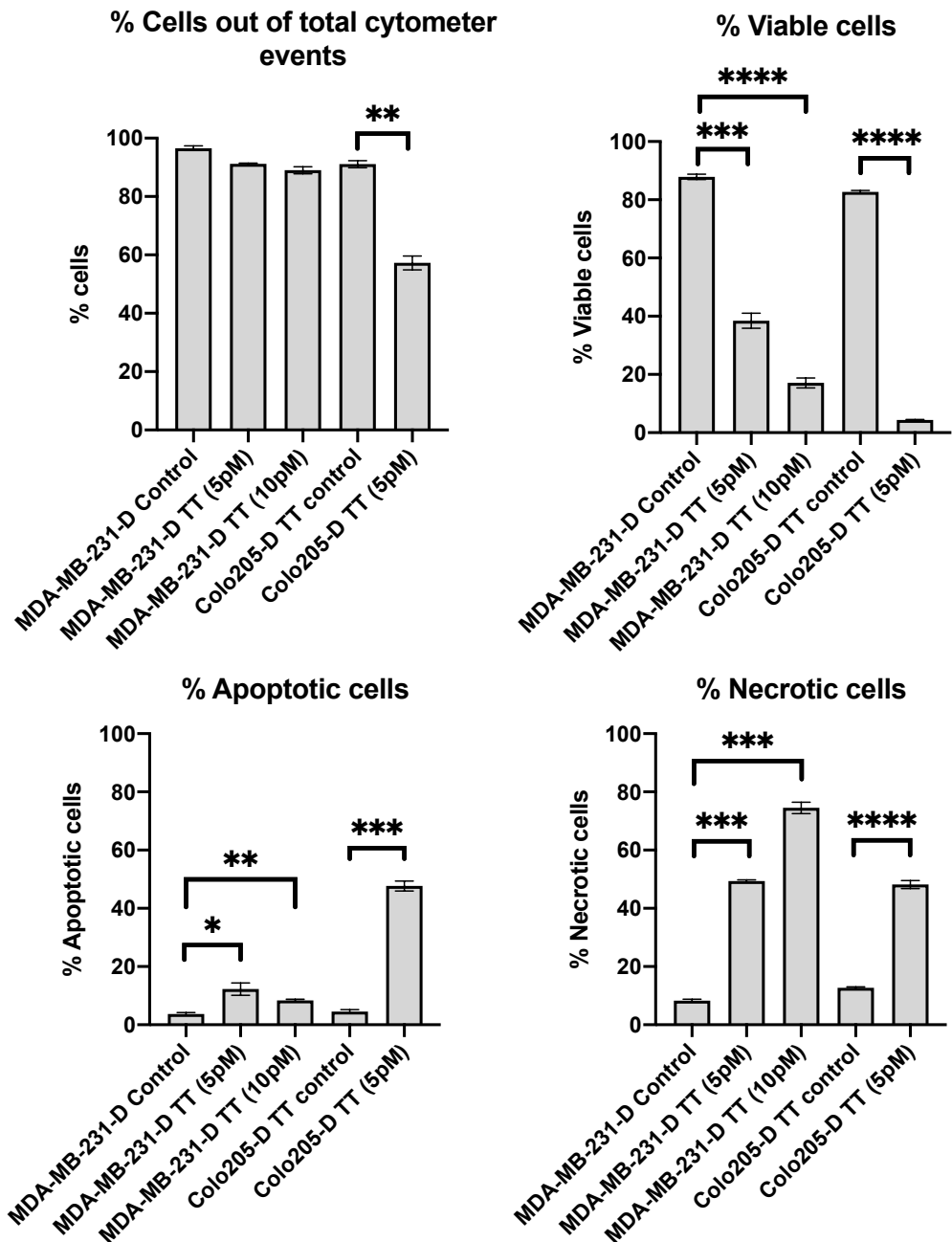


Figure 55. Plots showing extent of cell death upon MEDI3039 treatment of the two cancer cell types. Plot **A** shows the average % of events identified as cells; **B** shows the average % of viable cells. **C** the average % of apoptotic cells; **D** the average % of necrotic cells. Data are mean  $\pm$  SEM (n = 3, per group and the error bars lie within the symbols when not visible). Statistical analysis was performed using unpaired two-tailed t test with Welch's correction. (\*P<0.05, \*\*P<0.005, \*\*\*P<0.0005, \*\*\*\*P<0.0001); TT = treated cells

In conclusion, MEDI3039 induces cell death in both cancer cell lines. MDA cells undergo cell death predominantly by necrosis whereas Colo205-D cells undergo cell death via both apoptosis and necrosis.

Viability of control and treated cells was also assessed by automated (Vi-CELL) cell analyser (Table 13). In the case of MEDI3039 (5 pM) treated MDA-MB-231-D cells, Vi-CELL consistently overestimated viability (87%) compared to flow cytometry (38%). This is due to Vi-CELL not being able to differentiate between healthy cells and apoptotic ones hence it considers them as healthy cells, as it doesn't have the capability to monitor NADH absorbance. It therefore overestimated true cell viability.

A direct comparison between trypan blue staining (assessed with Vi-CELL) and SYTOX green staining (flow cytometry) on MDA-MB-231-D cells treated with MEDI3039 (5 pM) then again Vi-CELL would overestimate the viability showing 87 and 51% respectively. A small contributor to this variability was due to the inherent properties of the cell death markers themselves. A study showed that trypan blue overestimates cell viability by up to 35% upon comparison with acridine orange/propidium iodide.<sup>270</sup>

A similar pattern was observed with Colo205-D where Vi-CELL showed a viability of 68% compared to the true cell viability resulted from the flow cytometry reading of 4%. If compared directly: trypan blue (Vi-CELL) vs SYTOX green staining (flow cytometry) and excluding NADH indicator of apoptosis viability was again overestimated showing 68 (Vi-CELL) and 54% (flow cytometry) respectively.

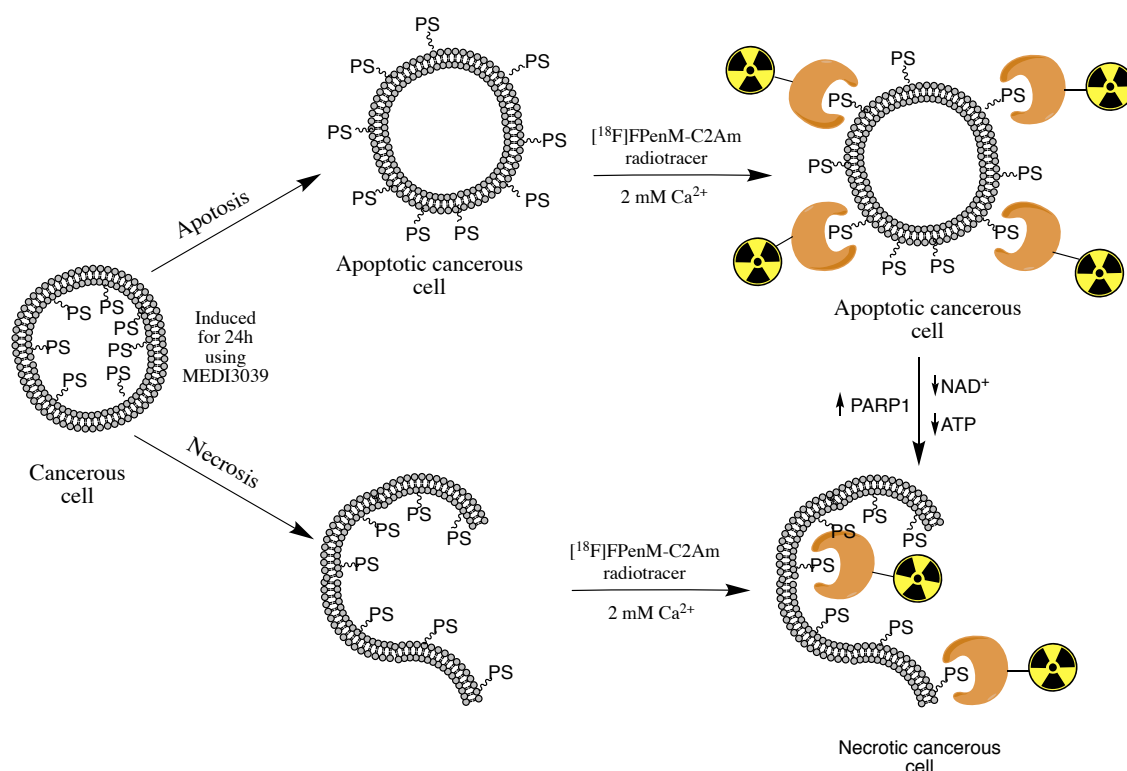
For the Vi-CELL analysis, another observation was that the size of the treated Colo205-D cells decreased after treatment and the apparent number of cells doubled. This was likely the result of the formation of apoptotic cell bodies.

Table 13. Cell viability assessed after MEDI3039 (5 pM) using Vi-CELL analyser.

	Total cells counted	Viable cells counted	Viability (%)	Total cells /ml (x10 <sup>6</sup> )	Viable cells /ml (x10 <sup>6</sup> )	Avg. diam. (microns)	Avg. surface per cell (microns <sup>2</sup> )
MDA-MB-231-D Treated	3346	2920	87.3	3.62	3.16	14.18	632
MDA-MB-231-D Control	4187	4086	97.6	4.53	4.42	14.01	617
Colo205-D Treated	10201	6888	67.5	11.05	7.46	8.99	254
Colo205-D Control	5327	4675	87.8	5.77	5.06	13.48	571

### 3.3 Labelling dying tumour cells using [<sup>18</sup>F]FPenM-C2Am

Cell labelling experiments were performed using the radioactive tracer [<sup>18</sup>F]FPenM-C2Am, described in subchapter 2.4. Radiotracer uptake by MEDI3039-treated and control cells was determined using gamma counting. The labelling process of apoptotic/necrotic cells with [<sup>18</sup>F]FPenM-C2Am at a molecular level is shown in **Scheme 20**.



Scheme 20. Labelling apoptotic and necrotic tumour cells with [<sup>18</sup>F]FPenM-C2Am following MEDI3039 treatment. Phosphatidylserine is exposed by the apoptosis/necrosis induced by MEDI3039 treatment. [<sup>18</sup>F]FPenM-C2Am is represented by the orange c-shape object tagged by the radioactive trefoil. PS = phosphatidylserine

The total activity of [<sup>18</sup>F]FPenM-C2Am added to the cells was measured using a radioisotope dose calibrator (Capintek CRC-15R), which allows a wide range of activities to be detected (0.1 MBq – 200 GBq).

The activity adhering to cells was measured with an Automatic Gamma Counter (AMG, Hidex) equipped with a highly sensitive 3-inch well-shaped NaI scintillation detector with a maximum activity detection of ~0.1 MBq. Activity is detected as light emitted by the scintillation crystal upon exposure to incident high energy gamma photons, beta or alfa particles. This set-up has a higher dead time compared to the ionisation chamber used in the dose calibrator due to the decay time of the scintillation light, which lasts 0.23 μseconds. Since the two radioisotope detectors (gas ionisation vs. scintillation counter) operate over a different activity range calibration against the same source was not possible. Therefore, a serial dilution was performed, starting from a known activity measured by the well counter. The serial dilution was then measured on the AMG and



compared to the measurements on the Capintek dose calibrator to determine the counting efficiency of the gamma counter. The Hidex gamma camera showed a 28% efficiency in relation to the Capintek dose calibrator. All the results reported below are corrected by this factor.

### 3.3.1 Labelling MDA-MB-231-D cells with [<sup>18</sup>F]FPenM-C2Am

Inevitably, due to the very low concentration of [<sup>18</sup>F]FPenM and the presence of fluorine-19 contamination, conjugation of C2Am does not lead to 100% labelled protein. Therefore [<sup>18</sup>F]FPenM-C2Am contains a mixture of [<sup>18</sup>F]FPenM-C2Am, [<sup>19</sup>F]FPenM-C2Am, C2Am, and C2Am-S-S-C2Am dimer. The quoted concentrations for [<sup>18</sup>F]FPenM-C2Am refer to the concentration of the protein in this mixture.

All the radioactivity measurements were decay-corrected to the start time of [<sup>18</sup>F]FPenM-C2Am addition. Background radiation was measured prior to the run and subtracted from the analysed samples.

MDA-MB-231-D control cells and cells treated with MEDI3039 (10 pM for 24 hours) (n = 3, passage no. 15) were harvested, counted and viability assessed with a Vi-CELL analyser. The cells were re-suspended in labelling buffer (1 mL HBS with 1% FBS and 2 mM CaCl<sub>2</sub>) and incubated with [<sup>18</sup>F]FPenM-C2Am (~10, 5 and 1 μM, 11-7 MBq, A<sub>m</sub> = 10500 MBq/μmol at the start of labelling) at 37 °C for 20 minutes. Cell pellets were washed three times with labelling buffer (1 mL) and counted for 1 minute using the AMG set to monitor the fluorine-18 gamma emission (511 keV). The results in Figure 56 show that there was a significant (P = 0.0011) difference in uptake of [<sup>18</sup>F]FPenM-C2Am between control and treated MDA-MB-231-D cells. The error bars were large due to the addition of three different [<sup>18</sup>F]FPenM-C2Am concentrations 1, 5 and 10 μM in each experiment ranging from 7 to 11 MBq which resulted in different activities retained per million cells. However, the activity ratio between control and treated cells was constant at 4.3±0.6 (standard error of the mean, n=3).

**[<sup>18</sup>F]FPenM-C2Am activity retention in the MDAs pellet**

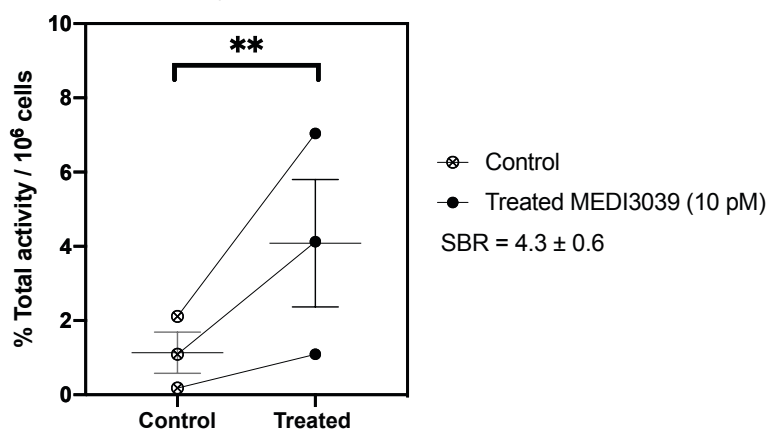


Figure 56. Binding of [<sup>18</sup>F]FPenM-C2Am to control and MEDI3039-treated (10 pM) of MDA-MB-231-D cells. The average % of total activity retained by the cell pellet is shown. Statistical analysis was performed using a paired two-tailed t test (\*\*P<0.005). Average ratio between control and treated, signal to baseline ratio (SBR) was 4.3±0.6. Data are mean ± SEM (n = 3, per group).

The effect of [<sup>18</sup>F]FPenM-C2Am concentration ( $A_m = 24300 \text{ MBq}/\mu\text{mol}$  at start of labelling) is shown in Figure 7. There was consistently more than a 2-fold difference in uptake of [<sup>18</sup>F]FPenM-C2Am between control and treated cells at all the different tracer concentrations.

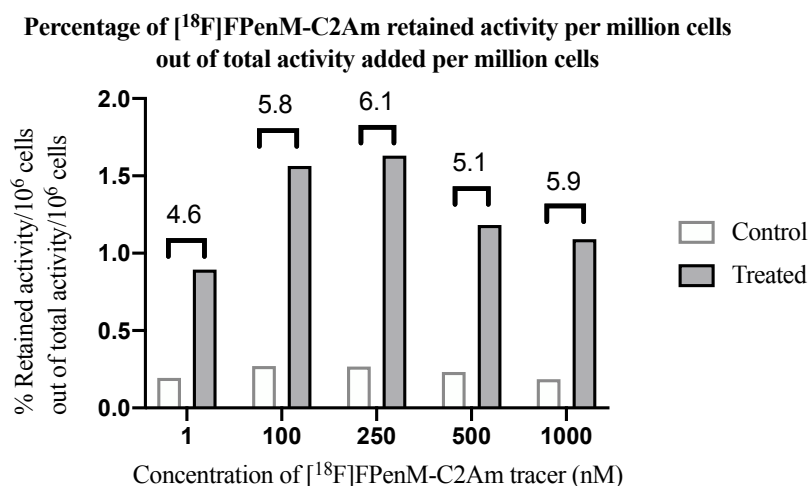


Figure 57. Labelling of MEDI3039-treated and control MDA-MB-231-D cells with different concentrations of [<sup>18</sup>F]FPenM-C2Am. Plots show the % of total activity retained per million cells for each of the five [<sup>18</sup>F]FPenM-C2Am concentrations.

### 3.3.2 Labelling Colo205-D cells with [<sup>18</sup>F]FPenM-C2Am

Colo205-D cells were subjected to the same labelling protocol as the MDA cells. (see Figure 58). However, due to the extensive cell death generated by MEDI3039 treatment (at 5 pM), as shown in the fluorescence experiments, pelleting the cell preparation by centrifugation was difficult. Therefore, washes were performed carefully so as not to remove any apoptotic/necrotic cells. The pellet required double the centrifugation force (1800 vs 900g) compared to MDA cells in order to obtain a pellet. Probably because of this, the data for percentage of retained [<sup>18</sup>F]FPenM-C2Am activity per million cells (Figure 58) out of total activity added per million cells was not as consistent for the Colo205-D cells as it was for MDA-MB-231-D cells. However, the ratio of [<sup>18</sup>F]FPenM-C2Am activity uptake between control and treated cells showed at least a 2-fold increased uptake by treated cells as compared to control cells.

**Percentage of [<sup>18</sup>F]FPenM-C2Am retained activity per million cells out of total activity added per million cells**

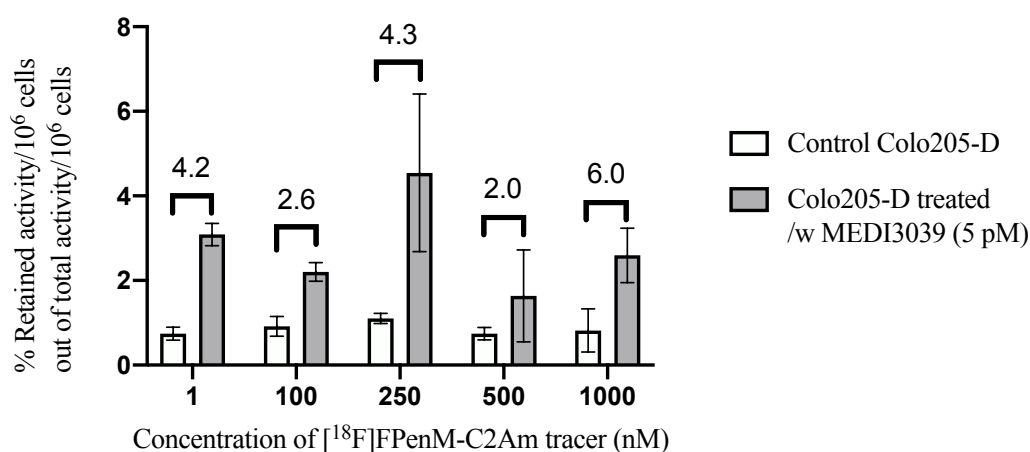


Figure 58. Labelling of MEDI3039-treated (5 pM) and control Colo205-D cells with different concentrations of [<sup>18</sup>F]FPenM-C2Am. Plots showing the % of activity retained per million cells out of the total activity added for each of the five [<sup>18</sup>F]FPenM-C2Am concentrations. The plot also shows the binding ratio for treated and untreated cells for each [<sup>18</sup>F]FPenM-C2Am concentration. Data are mean ± SEM (n = 2, per group)

### 3.4 Conclusion

MDA-MB-231-D and Colo205-D cells showed distinct cell death profiles in response to treatment with MEDI3039 (5 pM). MDA cells died predominantly by necrosis (46±2%) whereas Colo205-D cells showed 48±3% apoptosis and 48±2% necrosis post treatment. Intriguingly, Colo205-D seemed to respond much better than MDA upon MEDI3039 (5 pM) treatment as only 57±4% of events observed on the flow cytometer were cells, the rest were cell debris. Therefore, 5 pM MEDI3039 drug was too high for observation of moderate levels of Colo205-D cell death at 24 hours.

Labelling of MDA-MB-231-D cells with [<sup>18</sup>F]FPenM following treatment with MEDI3039 (10 pM) showed that the percentage of total [<sup>18</sup>F]FPenM activity in the cell pellet was significantly (P<0.005) greater in the treated than the control cells. This was encouraging for the prospect of using [<sup>18</sup>F]FPenM as a PET tracer for imaging cell death *in vivo*.

Finally, Colo205-D was highly apoptotic and necrotic within 24 hours following treatment with MEDI3039 (5 pM) and significant disintegration of the cells had occurred. Cell labelling experiments with a range of [<sup>18</sup>F]FPenM concentrations, from 1 nM to 1000 nM, showed a significant difference in uptake between control and treated cells, confirming the potential of [<sup>18</sup>F]FPenM for imaging cell death *in vivo*.

In conclusion, based on these cells experiments, [<sup>18</sup>F]FPenM-C2Am showed promise as a potential tracer for imaging cell death *in vivo*.

### 3.5 Experimental

All buffers used were prepared by the CRUK Cambridge Institute core facilities. Solvents, reagents and media were used as provided from vendors without further purification. MEDI3039 TRAIL-R2 agonist (85 kDa) was received from MedImmune. SYTOX® green (Invitrogen cat. no. SKU#S7020), 5 mM in DMSO (stored at – 20 °C in 0.5 µL aliquots) was diluted 1000x (0.5 µl in 495 µl of DMSO) to to yield a 5 µM stock solution.

Cell cultures were monitored daily using a Nikon Eclipse TS100 microscope (using a Nikon Plan Fluor 4x 0.13 wide view lens). Cell viability and number were determined using a Beckman Coulter Vi-CELL XR Cell Viability Analyzer 2.04. Cell viability was also quantified using a BD LSRII flow cytometer equipped with 4 lasers (UV – 355 nm, Violet – 406 nm, Blue – 488 nm, Red – 633 nm) and running BD FACSDiva software v8.0.1.

### 3.5.1 Detection of cell death using flow cytometry:

One million MDA-MB-231-D cells (passage number 9) were seeded in Thermo Scientific™ Nunc™ Nunclon™ 6-well cell culture plates (9.6 cm<sup>2</sup> surface area per well) and incubated for 12 hours at 37 °C and 5% CO<sub>2</sub>. MEDI3039 (5 or 10 pM) was added to 90% confluent cells and incubated for 24 hours at 37 °C and 5% CO<sub>2</sub>.

One million Colo205-D cells (passage number 11) were seeded in Thermo Scientific™ Nunc™ T25 flasks and incubated for 12 hours at 37 °C and 5% CO<sub>2</sub>. MEDI3039 (5 pM) was added to confluent cells and incubated for 24 hours at 37 °C and 5% CO<sub>2</sub>.

Cells were then harvested, re-suspended in flow cytometry staining (FACS) buffer (PBS with 1% FBS) and stained with SYTOX<sup>®</sup> Green (50 nM) at 37 °C for 10 minutes on a thermal mixer (Eppendorf Thermomixer R). Cell pellets were then washed 3 times with ice-cold FACS buffer. Cells were re-suspended in ice-cold FACS buffer and analysed on a BD Biosciences LSRII flow cytometer with a minimum of 10000 events counted. For detection of SYTOX<sup>®</sup> Green (absorption/emission peaks at 504/523 nm) the dye was excited with an argon ion laser at 488 nm and its emission monitored at 530 nm. NADH was excited at 355 nm (UV laser) and detected by monitoring its emission at 450 nm. Experiments were run in triplicate and results are presented as an average. Data were analysed using FlowJo software (vs. 10.5.3). Statistical analysis was performed using GraphPad Prism software (vs. 8.0.0).

### 3.5.2 Detection of cell death using [<sup>18</sup>F]FPenM-C2Am:

MDA cells (passage no. 15) were seeded in Thermo Scientific™ Nunc™ T25 or T75 flasks (~1 or 5 million in each depending on flask size) and incubated for 24 hours

at 37 °C and 5% CO<sub>2</sub>. PBS for control cells or MEDI3039 (10 pM) for treated cells was added to the medium and incubated for a further 24 hours.

Colo205-D cells (passage no. 11) were seeded in T25 flasks (~1.5 million in each) and incubated for 24 hours at 37 °C and 5% CO<sub>2</sub>. PBS for control cells or MEDI3039 (5 pM) for treated cells was added to the medium and incubated for a further 24 hours.

Control and treated cells were harvested, counted and viability assessed with a Vi-CELL analyser and re-suspended in labelling buffer (1 mL) (10 mM HEPES, 150 mM NaCl, 1% FBS and 2 mM CaCl<sub>2</sub>, pH 7.4). [<sup>18</sup>F]FPenM-C2Am was added (1, 100, 250, 500, 1000 nM, 5 mM and 10 mM) and incubated at 37 °C for 20 minutes. Cell pellets were washed 3x with labelling buffer (1 mL) and counted for 1 minute using the Hidex AMG.

Hidex AMG was used to count the cell pellets after [<sup>18</sup>F]FPenM-C2Am labelling. The gamma camera was set to detect fluorine-18 gamma emission energy (511 keV) and the cell pellets scanned for 1 minute. Hidex AMG application version 1.5 software was used for collecting and exporting data.

### 3.5.3 General cell culture protocols for Colo205-D and MDA-MB-231-D cancer cell lines:

Colorectal cancer cells – (Colo205-D passage no. 7) and breast cancer cells – (MDA-MB-231-D passage no. 11) were obtained from ATTC culture collection and transfected in house with fLuc by Dr Susana Ros, a senior member of the Brindle group. A mix of Colo205-D adherent and suspension cells were seeded in Thermo Scientific NUNC cell culture flasks (T25, T75 or T175) with a mixture of 90% RPMI Medium 1640 1X (REF 21875-034, LOT 1979014) supplemented with 10% heat inactivated FBS (foetal bovine serum, South American origin). MDA-MB-231-D adherent cells were seeded in Thermo Scientific NUNC cell culture flasks (T25, T75 or T175) with a mixture of 90% DMEM 1X (Dulbecco's Modified Eagle's Medium, REF 41966-029, LOT 1979092) supplemented with 10% heat inactivated FBS (foetal bovine serum, South American origin). Tissue culture flasks were incubated at 37 °C and 5% CO<sub>2</sub> in Thermo Heracell 150 incubators. (Appendix 8 for cell culture protocols)

# 4 *IN VIVO* DETECTION OF CELL DEATH USING [<sup>18</sup>F]FPENM-C2AM IN A MURINE XENOGRAFT MODEL OF COLORECTAL CANCER

## 4.1 Introduction

Novel *in vitro* cell culture techniques that aim to better mimic the basic physiological conditions that exist within an organ such as cell-cell interactions, hormone secretion *etc.* have lately been developed. However, such three-dimensional advanced tissue culture models, termed organoids, still fail to replicate the complex physiological conditions that exist within a higher organism.<sup>271,272</sup> Therefore, animal testing is still used extensively and is paramount for improving safety of pharmaceuticals despite increased opposition from initiatives such ‘Stop Vivisection’<sup>273</sup>, facilitated through the European Citizens’ Initiative mechanism<sup>274</sup>. However, important medical discoveries, such as recent work in cancer immunology and the discovery of programmed death ligand 1 (by James Allison and Tasuku Honjo – Nobel prize in 2018), would have been unachievable without extensive *in vivo* testing in animals. On the other hand, only 8% of candidate drugs that went into clinical trials after promising animal testing were eventually approved.<sup>275</sup> Examples include TGN1412, an anti-CD28 monoclonal antibody for treating multiple sclerosis and certain cancers, (developed by TeGenero), which not only failed to fulfil its therapeutic effect but also caused multiple organ failure despite being tested on multiple animals, including mice, at doses hundreds of times higher than the equivalent delivered to humans.<sup>275</sup>

*In vivo* testing is beset by problems due to differences in physiology between different species but most scientists agree that the benefits outweigh the downsides and by implementing new EU regulations regarding animal usage (directive 2010/63/EU mentioned 3Rs – replace, reduce, refine) their welfare is also ensured.

Advancing a drug from bench to bedside is not a straightforward task. Both the Food and Drug Agency (USA)<sup>276</sup>, and the European Medicines Agency (Europe) and Medicines and Healthcare Products Regulatory Agency (UK) all require a toxicology report demonstrating that no side effects are seen in animals in order to better mitigate risks prior to First-in-Human studies.

In order to demonstrate that [<sup>18</sup>F]FPenM-C2am is capable of detecting tumour cell death *in vivo*, a xenograft athymic mouse model of advanced colorectal cancer, treated with the TRAIL-R2 agonist MEDI3039 for cell death induction, were used in biodistribution and dynamic PET imaging studies.

## 4.2 Biodistribution analysis of [<sup>18</sup>F]FPenM-C2am in Balb/c nu/nu mice bearing Colo205-D tumours

For these experiments, Colo205-D cells were cultured and propagated as described in Chapter 3. Two weeks prior to the biodistribution experiment, six 8-week old Balb/c nu/nu female mice (Charles River Laboratories) were implanted subcutaneously with Colo205-D cells ( $5 \times 10^6$ ). Then, 24 hours before the biodistribution experiment, the control group (n = 3) was treated with drug vehicle (PBS) and the treated group (n = 3) was injected with a single dose of MEDI3039 (0.4 mg/kg, i.v.). Bioluminescence images were acquired prior to treatment as well as 24 hours post-treatment; regions of interest (ROIs) were drawn around tumours and their intensities were measured, which showed lower radiance in the treated cohort (post-treatment) compared to controls (see Table 14).



Table 14. Mouse bioluminescence and injected [<sup>18</sup>F]FPenM-C2Am activity (MBq) details.

Mouse	Treatment Control or MEDI3039 (0.4 mg/kg, i.v.)	Bioluminescence readout* of tumour ROI before treatment	Bioluminescence readout* of tumour ROI after treatment	Injected activity (MBq)	Injected protein mass ( $\mu$ g)
A	Untreated	$1.8 \times 10^8$	$1.7 \times 10^9$	1.218	1.2
B	Treated	$1.5 \times 10^8$	$1.7 \times 10^9$	1.225	1.2
C	Treated	$1.0 \times 10^8$	$2.0 \times 10^7$	2.037	2
D	Treated	$6 \times 10^7$	$8 \times 10^6$	0.969	1
E	Untreated	$2.5 \times 10^7$	$1.3 \times 10^8$	2.494	2.5
F	Untreated	$1 \times 10^7$	$5.6 \times 10^7$	1.967	2

- \*tumour total bioluminescence intensity (photons/sec/cm<sup>2</sup>/sr)

[<sup>18</sup>F]FPenM-C2Am was produced according to the protocol described in Chapter 2 and delivered to the imaging suite at the Cancer Research UK Cambridge Institute (for full details, see Experimental 4.5). Mice were anaesthetised and injected with 200  $\mu$ l of [<sup>18</sup>F]FPenM-C2Am (1–2.5 MBq) solution containing C2Am (1–2.5  $\mu$ g) in PBS. The injected activity and quantity in each mouse is shown in Table 14 and the molar activity at the time of injection was of  $A_m = 16200$  MBq/ $\mu$ mol ( $A_s = 1.0$  MBq/ $\mu$ g at time-of-injection).

[<sup>18</sup>F]FPenM-C2Am showed a favourable biodistribution profile, by gamma counting of mouse organs, at 2 hours after probe administration, as seen in Figure 59, with predominantly renal clearance and minimal retention in an untreated advanced colorectal tumour (0.17 $\pm$ 0.02% ID/g), spleen (0.6 $\pm$ 0.04% ID/g), liver (0.76 $\pm$ 0.09% ID/g), small intestine (0.59 $\pm$ 0.19% ID/g) and kidney (3.83 $\pm$ 0.4% ID/g). In mice treated with MEDI3039 significant retention in the tumours (1.68 $\pm$ 0.15% ID/g) was observed, again with predominantly renal clearance and minimal nonspecific retention in spleen (0.66 $\pm$ 0.05% ID/g), liver (1.05 $\pm$ 0.05% ID/g), small intestine (1.42 $\pm$ 0.2% ID/g) and kidney (4.50 $\pm$ 0.47% ID/g) at 2 hours after probe administration. Significant stomach uptake was observed post treatment which was initially attributed to possible activation

of TRAIL-R2 by MEDI3039 present in mouse stomach and small intestine. TRAIL-R2 in humans (DR5) shares 79% sequence identity with its mouse equivalent (MK) receptors, so an interaction of the MEDI3039 drug with the mouse receptors is plausible.<sup>277</sup> However, no such side effects have been noted previously during extensive testing of the MEDI3039 drug in triple negative breast cancer murine xenografts by Greer *et al.* (2019)<sup>278</sup>. Previous TRAIL-R2 agonists (e.g. G6T8) tested by Swers *et al.* (2013) showed selective binding to human death receptors over mouse TRAIL-R2 receptors.<sup>114</sup> Therefore, the apparent stomach uptake was not observed in any subsequent PET/CT and biodistribution experiments.

**Biodistribution profile of [<sup>18</sup>F]FPenM-C2Am in Balb/c nu/nu mice**

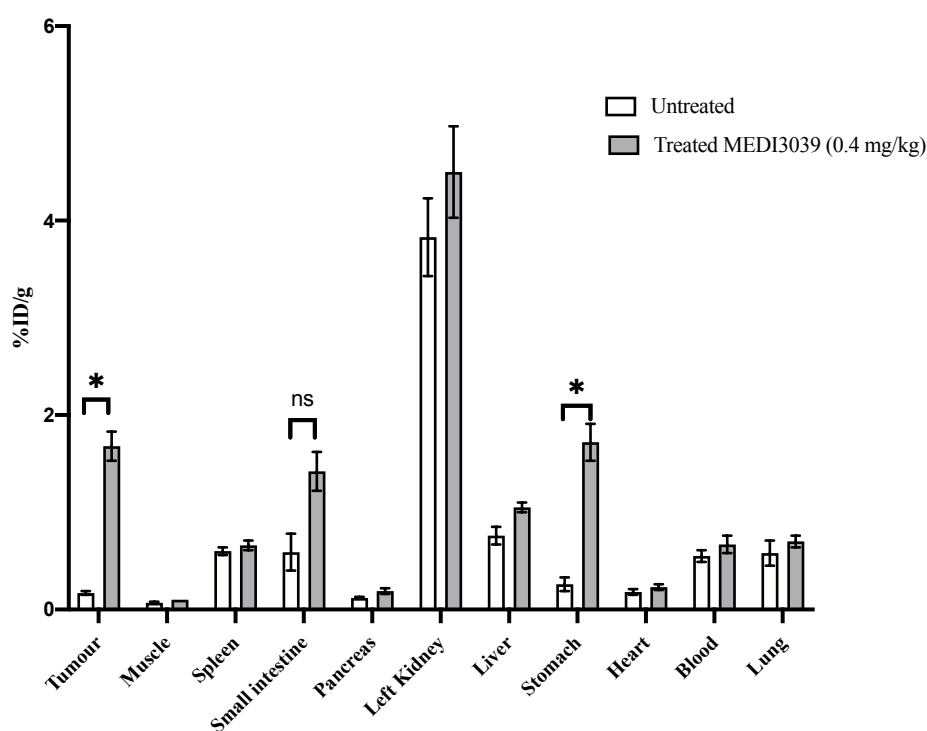


Figure 59. Biodistribution profile of [<sup>18</sup>F]FPenM-C2Am in control and (MEDI3039, 0.4 mg/kg) treated Balb/c nu/nu mice bearing Colo205-D tumours. An unpaired one-tailed t-test showed a significant difference between control and treated tumour (P=0.0006); control and treated stomach (P=0.0022). Data are mean  $\pm$  SEM (n = 3, per group; the error bars lie within the symbols when not visible); (ns >0.05, \*P<0.05, \*\*P<0.005, \*\*\*P<0.0005).

At two hours after administration, [<sup>18</sup>F]FPenM-C2Am generated significant differences between the control and treated tumour-to-muscle (P = 0.0089) and tumour-to-blood (P = 0.093) ratios (see Figure 60).

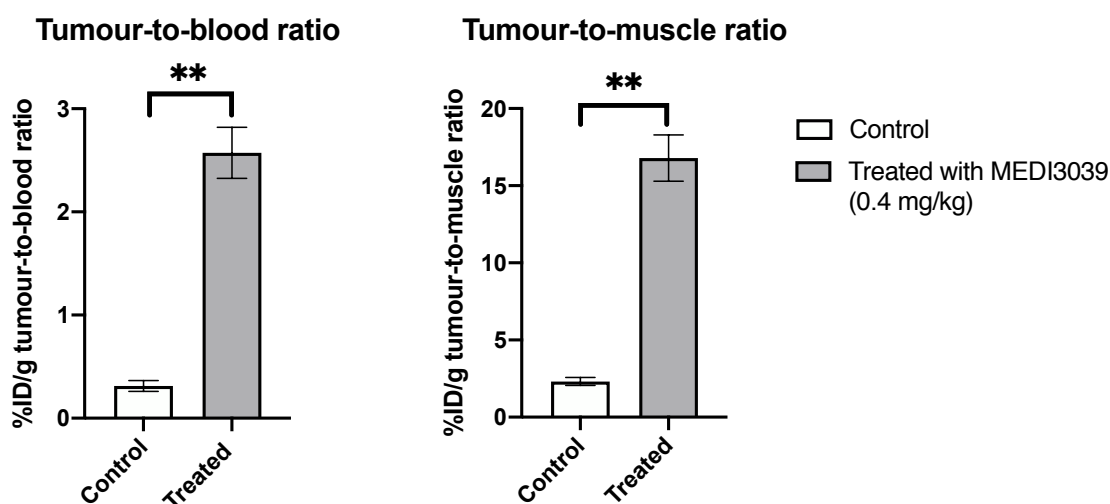


Figure 60. Tumour-to-muscle and tumour-to-blood ratios in control and treated (MEDI3039, 0.4 mg/kg, I.V.) Colo205-D xenograft tumour bearing Balb/c nu/nu mice. Unpaired two-tailed t-tests with Welch's correction showed significant differences (\*\*P<0.01) between tumour-to-muscle and tumour-to-blood ratios between control and treated. Data are mean ± SEM (n = 3, per group)

### 4.3 PET/CT imaging and biodistribution analysis of [<sup>18</sup>F]FPenM-C2am in Balb/c nu/nu mice bearing Colo205-D tumours

PET/CT imaging experiments were performed in a cohort of 8-week old Balb/c female nu/nu mice (n = 5). Animals were implanted with 5 x 10<sup>6</sup> Colo205-D cells and tumours were allowed to grow for 2 weeks. Subsequently, they were subjected to a three-day PET/CT imaging protocol shown in Figure 61. Mice (n = 5) were imaged in two consecutive cohorts (of n = 3 and n = 2) due to the maximum scanner capacity of 3 mice.

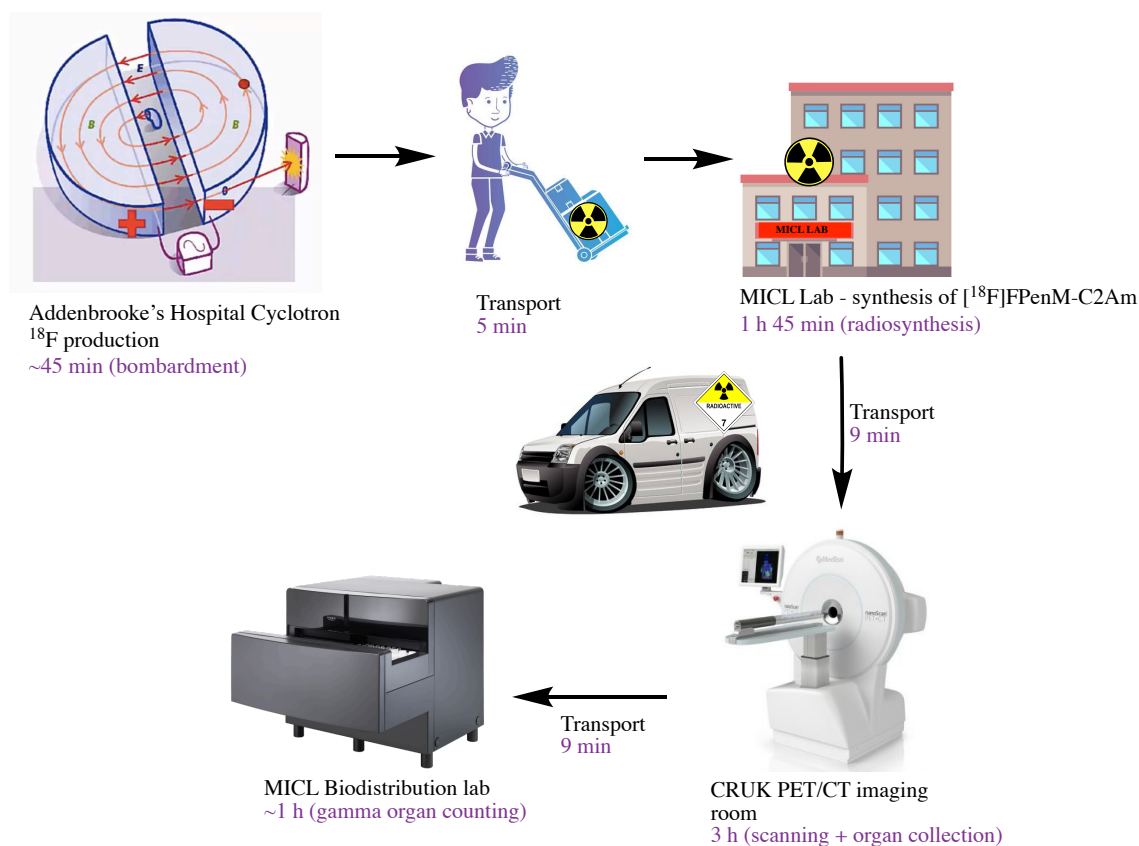


Figure 61. PET/CT imaging protocol pipeline and the times associated with each process. End-of-bombardment to scanner time was less than two hours (approximately the fluorine-18 half-life of 109.7 minutes)

On day one, the first cohort of mice ( $n = 3$ ), were subjected to the PET/CT imaging protocol with the tracer  $^{18}\text{F}$ FPenM-C2am ( $9 \mu\text{g}$ ,  $2.93 \mu\text{M}$ ,  $4.6\text{--}5.2 \text{ MBq}$ ,  $A_m = 10100 \text{ MBq}/\mu\text{mol}$ ) to set a baseline for radiotracer uptake in untreated tumours. On day two (24 hours later) MEDI3039 ( $0.4 \text{ mg/kg}$ ) drug was administered i.v. to induce cell death in the tumours. On day three, 24 hours post-treatment, the PET/CT imaging protocol was repeated using  $^{18}\text{F}$ FPenM-C2am ( $4.6 \mu\text{g}$ ,  $1.43 \mu\text{M}$ ,  $4.9\text{--}6 \text{ MBq}$ ,  $A_m = 18300 \text{ MBq}/\mu\text{mol}$ ) in order to evaluate tracer uptake following therapy (see Figure 62). Details regarding injected radiotracer amounts are summarised in Table 15. Mice were sacrificed 2 hours post-radiotracer injection and their organs were collected for biodistribution and histological assessment.

Table 15. [<sup>18</sup>F]FPenM-C2Am injection doses and amounts before and after treatment.

Mouse	Injection dose pre-treatment (MBq)	Time of injection	Protein amount ug	Injection dose post-treatment (MBq)	Time of injection	Protein amount ug
1	4.66	13:11:45	8	6.07	14:34:37	5
2	5.79	13:14:21	9	4.92	14:33:10	4
3	5.2	13:13:00	8	5.76	14:32:06	5

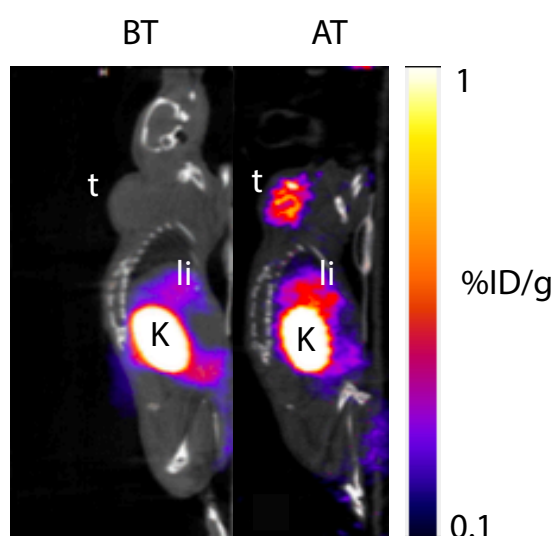


Figure 62. Cell death imaging using [<sup>18</sup>F]FPenM-C2Am. Sagittal PET/CT images of a representative tumour-bearing mouse (first cohort n = 3), before (AT) and 24 hours after MEDI3039 treatment (0.4 mg/kg, i.v.) (BT). Imaging was performed 2 hours after the administration of [<sup>18</sup>F]FPenM-C2Am (0.23 ug/g, 4.9–6 MBq, i.v.). Tumour (t), liver (li) and kidney (k) are shown. PET image palette used: NIH fire. (image courtesy of Dr André Neves)

The imaging protocol for the second cohort of mice (n = 2) was performed as follows: on day one the mice were injected with [<sup>18</sup>F]FPenM-C2Am (4 µg, 2.93 µM, 0.4–1 MBq, A<sub>m</sub> = 3310 MBq/µmol) to set a baseline for radiotracer uptake in untreated tumours. On day two, MEDI3039 (0.2 mg/kg) drug was administered i.v. to induce tumour cell death. On day three, PET/CT imaging was repeated with [<sup>18</sup>F]FPenM-C2am (10 µg, 2.86 µM, 3.3–3.6 MBq, A<sub>m</sub> = 5700 MBq/µmol). Details regarding injected

radiotracer amounts are summarised in Table 16. Mice were sacrificed 2 hours post-radiotracer injection as described above.

Table 16. [<sup>18</sup>F]FPenM-C2Am injection doses and amounts before and after treatment.

Mouse	Injection dose pre-treatment (MBq)	Time of injection	Protein amount ug	Injection dose post-treatment (MBq)	Time of injection	Protein amount ug
4	1.04	16:08:14	5	3.63	17:38:10	10
5	0.39	16:09:41	2	3.37	17:38:37	10

The biodistribution of [<sup>18</sup>F]FPenM-C2am post-PET imaging, shown in Figure 63, is consistent with the experiment presented in subsection 4.2. Nonspecific kidney retention two hours post i.v. injection was very low at  $6.9 \pm 0.5$  %ID/g, suggesting that the probe is excreted rapidly and hence has favourable pharmacokinetic properties. Treated tumour uptake was  $1.19 \pm 0.11$  %ID/g, which was consistent with our previous biodistribution results. Bone uptake was low ( $0.65 \pm 0.15$  %ID/g) and similar to the blood pool ( $0.65 \pm 0.15$  %ID/g) uptake suggesting that no defluorination is occurring during the two-hour scanning period. The main difference compared to the previous results is lower stomach uptake  $0.28 \pm 0.5$  %ID/g (*cf.*  $1.72 \pm 0.33$  %ID/g) post treatment.

### Biodistribution profile of [<sup>18</sup>F]FPenM-C2Am in Balb/c nu/nu mice post MEDI3039 treatment and PET/CT imaging

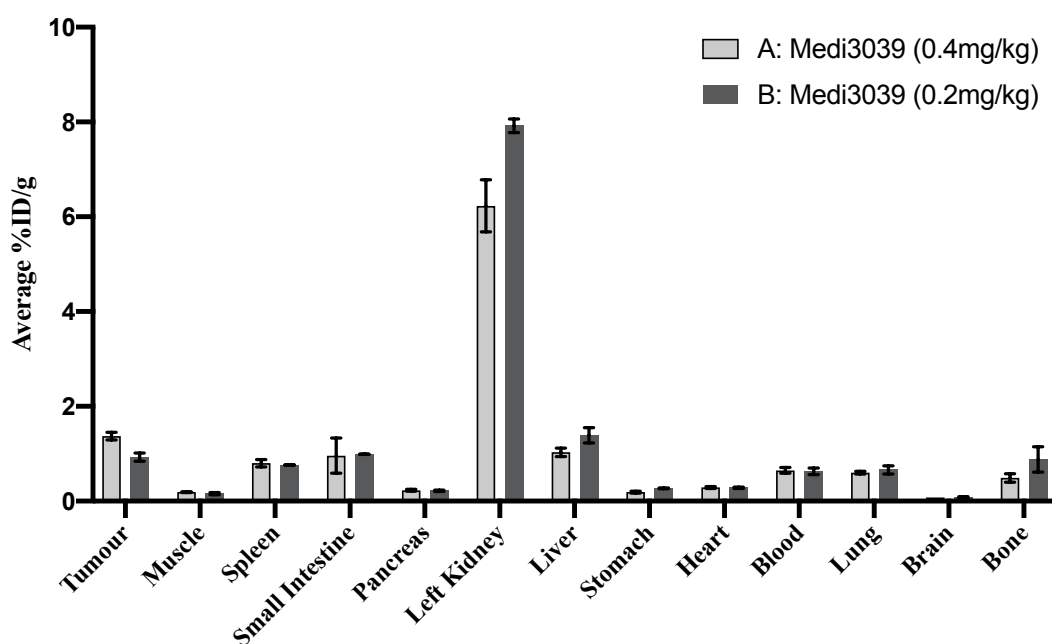


Figure 63. Average %ID/g of [<sup>18</sup>F]FPenM-C2Am (A: 4.6 µg and B: 9.2 µg) injected i.v. in a cohort of (A: n=3 and B: n=2) nu/nu mice bearing Colo205-D tumours that were treated with MEDI3039 (A: 0.4 mg/kg and B: 0.2 mg/kg, i.v.) and imaged using the PET/CT protocol over a 3-day period. Organs were collected for biodistribution, weighed and counted on day three after 2 hours of dynamic PET imaging. Kidney uptake demonstrated a good clearance with low retention (A: 6.2±0.5 and B: 7.9±0.1 %ID/g). Data are mean ± SEM (error bars lie within the symbols when not visible).

PET imaging analysis using [<sup>18</sup>F]FPenM-C2Am, showed mainly renal clearance and minimal retention in the spleen (0.79±0.05 %ID/g), liver (1.18±0.13 % ID/g), small intestine (0.97±0.25 %ID/g) and kidney (6.90±0.56 %ID/g) at 2 hours after probe administration was consistent with the results observed in the experiments presented above. In this Colo205-D colorectal cancer xenograft mouse model, [<sup>18</sup>F]FPenM-C2Am generated tumour-to-muscle and tumour-to-blood ratios following treatment of 6.7±0.8-fold and 1.89±0.23-fold, respectively, at 2 h after administration. PET imaging data was analysed by Dr André Neves. A statistically significant pairwise difference was obtained between the tumour-to-muscle contrast at 2 hours post injection prior to and following therapy (P = 0.0137, unpaired two-tailed t-test) (see Figure 64).

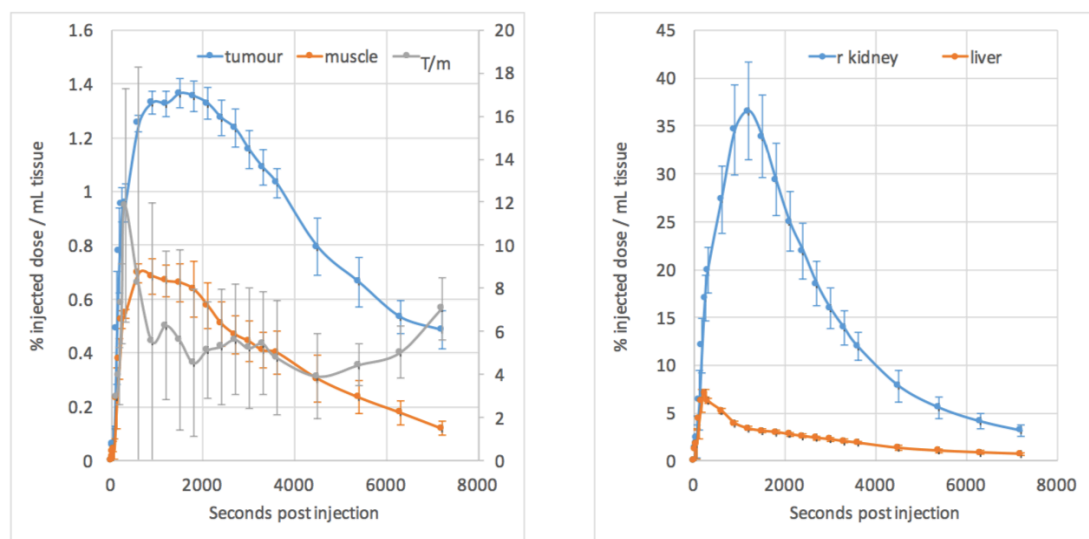


Figure 64. Time activity curves for  $[^{18}\text{F}]\text{FPenM-C2Am}$  post-treatment, shown as tumour-to-muscle ratio (left) and kidney and liver clearance (right). The tumour uptake peaked at 20 minutes following injection, with subsequent clearance. After one hour of administration, the tumour-to-muscle ratio increased thus generating tumour-muscle contrast (grey line, left plot) in the range of 4 to 6-fold ( $n = 5$ ). Kidney uptake peaked at 20 minutes post injection, with subsequent clearance of  $>90\%$  within 2 hours. Liver uptake peaked at 10 minutes post injection, with efficient clearance afterwards. All data has been decay-corrected. (figures courtesy of Dr André Neves)

The partial uptake of the probe in the gallbladder and gut is notable but inconsistent throughout a cohort of mice. Gallbladder uptake was detectable particularly after 30 min of administration, by PET imaging and visible at the two-hour point (see Figure 67). We initially hypothesised that the MEDI3039 drug (DR5 specific TRAIL agonist<sup>17</sup>) could potentially induce cell death in the mouse digestive system. However, subsequent lack of histologic evidence for the presence of cell death in the gallbladder and small intestine, suggested that a more likely explanation for partial retention is partial hepatobiliary excretion of the tracer. This can therefore lead to retention in the small intestine and gallbladder. (see Figure 66 and Figure 67) This matter requires further investigation.



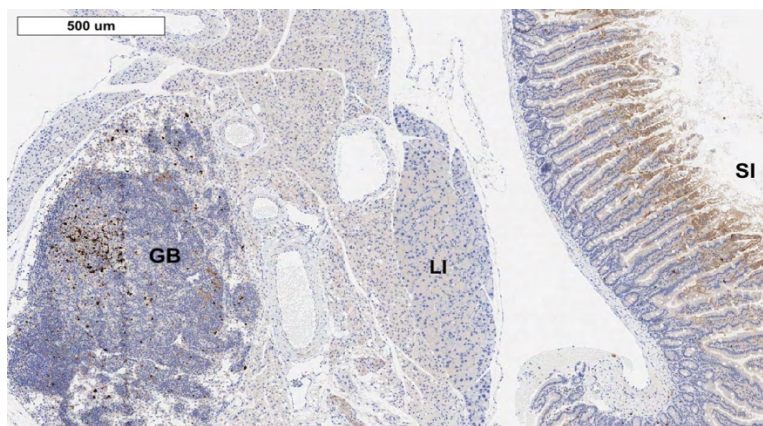


Figure 65. Histology samples stained with cleaved caspase-3 (CC3). Gallbladder (GB)/liver (LI) left and small intestine (SI) on the right. Minimal CC3 staining present was probably due to slow preparation of histological specimens and the fact that the small intestine epithelial cells have a high proliferation and cell death rate.<sup>279</sup>

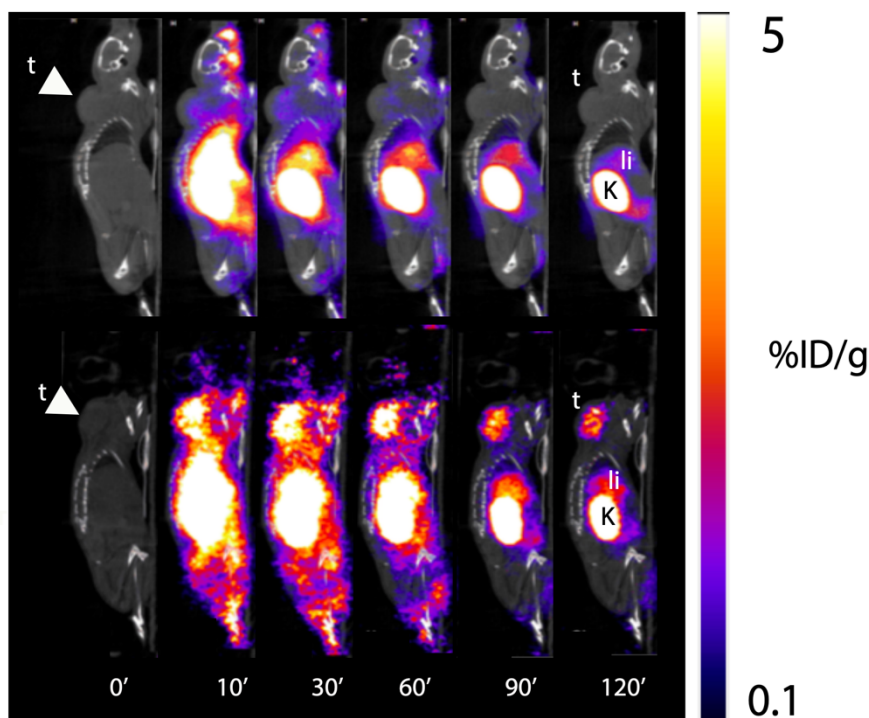


Figure 66. Sagittal PET/CT images of [<sup>18</sup>F]FPenM-C2Am in the same mouse bearing a Colo205D tumour (white arrow) 24 hours before (top row) and 24 hours after treatment (lower row) with MEDI3039 (0.4 mg/kg). Tumour uptake 24 hours after MEDI3039 drug administration (lower row) starts to increase 1-hour post injection. PET palette used: NIH fire. Images courtesy of Dr André Neves.

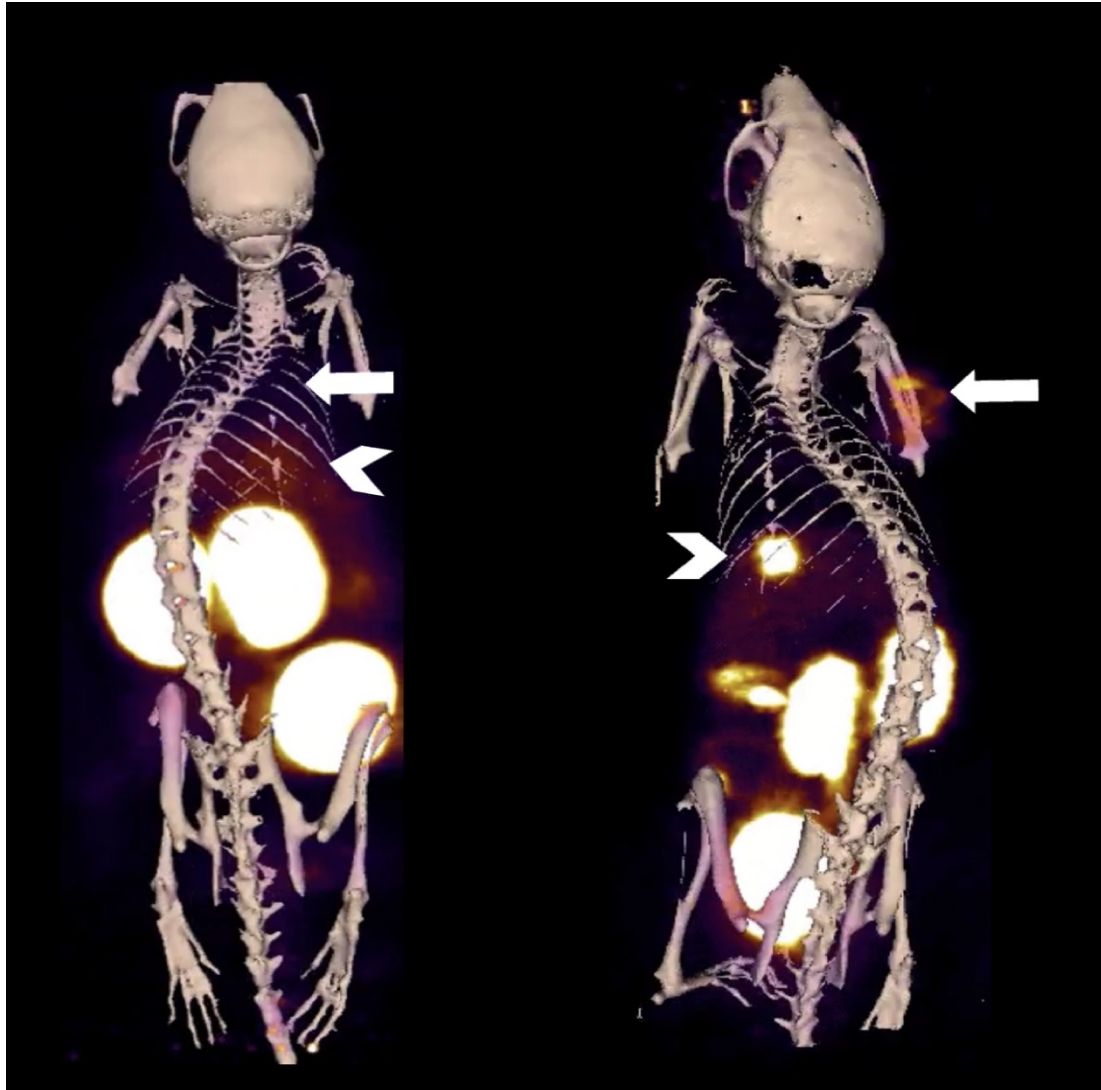


Figure 67. Maximum intensity projection PET/CT images 2 hours post [ $^{18}\text{F}$ ]FPenM-C2Am injection in a Colo205D tumour-bearing mouse. The tumour (white arrow) and gallbladder (white chevron) are indicated. Images were acquired 24 hours before (left image) and 24 hours after treatment with MEDI3039 (0.4 mg/kg) (right image). Images courtesy of Dr André Neves.

There was a good correlation between tumour %ID/g determined by PET at 2 hours and histology CC3 staining (Pearson  $r = 0.82$ ) and TUNEL staining (Pearson  $r = 0.95$ ) confirming the presence of cell death in the mice tumours after treatment ( $n = 5$ ). (Figure 68).

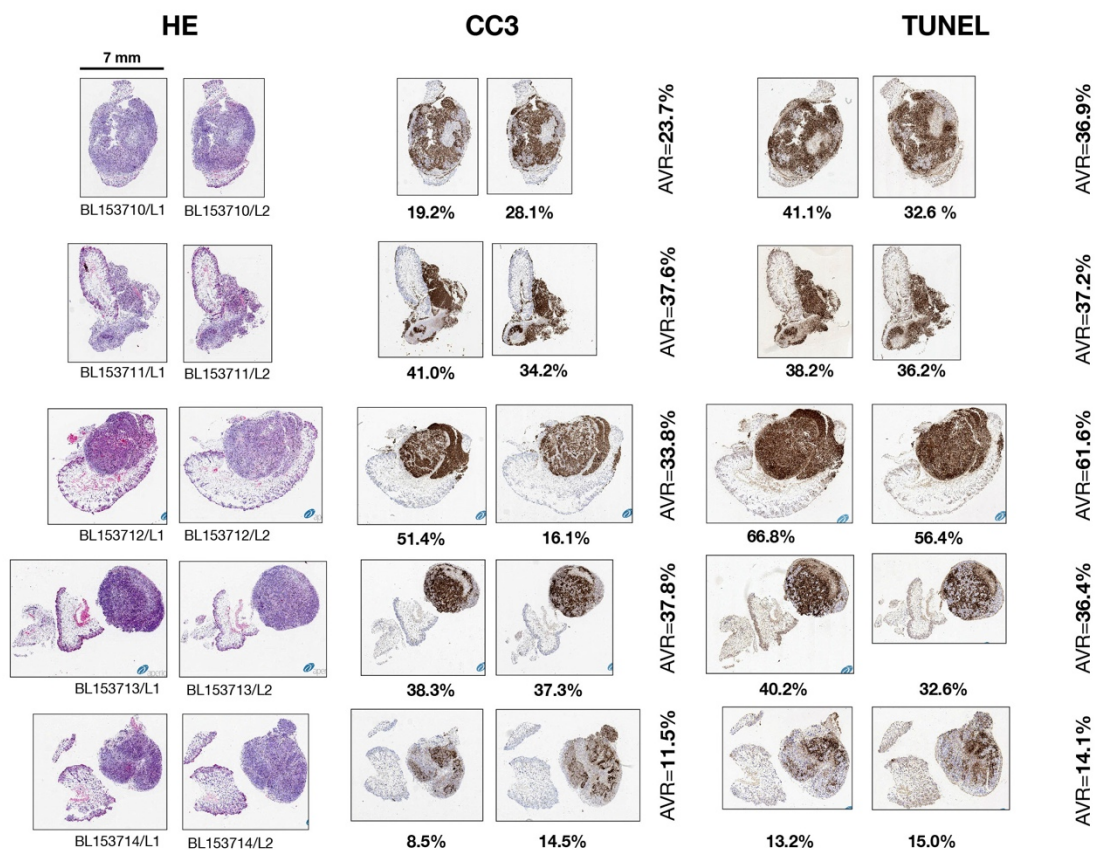


Figure 68. Histology staining of tumours with hematoxylin and eosin (HE), cleaved caspase-3 (CC3) and terminal deoxynucleotidyl transferase dUTP nick end labelling (TUNEL). Images courtesy of Dr André Neves.

## 4.4 Conclusion

[<sup>18</sup>F]FPenM-C2Am showed a favourable biodistribution in treated and control mice bearing human xenografts of advanced colorectal cancer. A statistically significant difference in tracer uptake was found between control and treated tumours. In addition, the radiotracer showed low non-specific retention in organs with predominant renal clearance. These results demonstrate that [<sup>18</sup>F]FPenM-C2Am is a promising radiotracer for PET imaging of cell death following therapy.

Furthermore, we have also developed a reliable and reproducible workflow for the production of [<sup>18</sup>F]FPenM-C2Am that was used successfully in a three day imaging protocol to assess tumour uptake of [<sup>18</sup>F]FPenM-C2Am, before and after targeted treatment. Importantly, images from two-hour dynamic PET scans have shown that post

treatment, the tumour-to-muscle retention ratio of [ $^{18}\text{F}$ ]FPenM-C2Am was significantly higher than prior to treatment in the same animals. Contrast started to develop within one hour of administration of the imaging agent. Time activity analysis showed that radiotracer renal uptake proved to be quick, peaking at 20 minutes post injection, followed by fast excretion, generating good tumour contrast. Intestinal and liver uptake were minimal and potentially represent a minor secondary route of excretion of the radiotracer. Finally, biodistribution was performed at the end of the three-day imaging protocol and results proved to be consistent with the previous experiment in terms of organ tracer uptake, as seen *in vivo* by PET/CT imaging.

## 4.5 Experimental

### 4.5.1 Colo205-D implantation and tumour formation in mice

Athymic BALB/c nu/nu female mice ( $n = 6$ ) were purchased from Charles River Laboratories. All animal procedures were carried out under the authority of project and personal licenses issued by the United Kingdom Home Office under the United Kingdom Animals (Scientific Procedures) Act, 1986, and had been reviewed by the Cancer Research UK, Cambridge Institute Animal Welfare and Ethical Review Body. Colo205-D cells (passage no. 15) were harvested and their viability (98.5%) checked using an automated cell counter (Vi-CELL). *In vivo* PET/CT imaging and biodistribution experiments were carried out with the support of Dr André Neves.

Six 8-week old mice were injected with  $\sim 5 \times 10^6$  Colo205-D cells (passage no. 15, 98.5% viability) two weeks prior to imaging or biodistribution experiments. Bioluminescence imaging was used to monitor tumour growth and tumour response to treatment. This was measured following injection of D-Luciferin (150 mg/kg, i.p.) and measured on an IVIS 200 (Perkin Elmer) fluorescence imaging camera. Mice were

anaesthetised with 3% (v/v) isoflurane for induction and 1.8-2.5% isoflurane for maintenance.

Twenty-four hours prior to the biodistribution experiment, a cohort of ( $n = 3$ ) mice were treated with a single dose of MEDI3039 (0.4 mg/kg). Control mice ( $n = 3$ ) were injected with PBS.

#### 4.5.2 [ $^{18}\text{F}$ ]FPenM-C2Am synthesis for biodistribution experiment

[ $^{18}\text{F}$ ]FPenM (2 GBq at end-of-synthesis) was produced with a good yield of 7.1% non-decay corrected (starting from 28 GBq at start-of-synthesis) with a high radiochemical purity of >99%. (see UV and radiochromatogram in Figure 69)

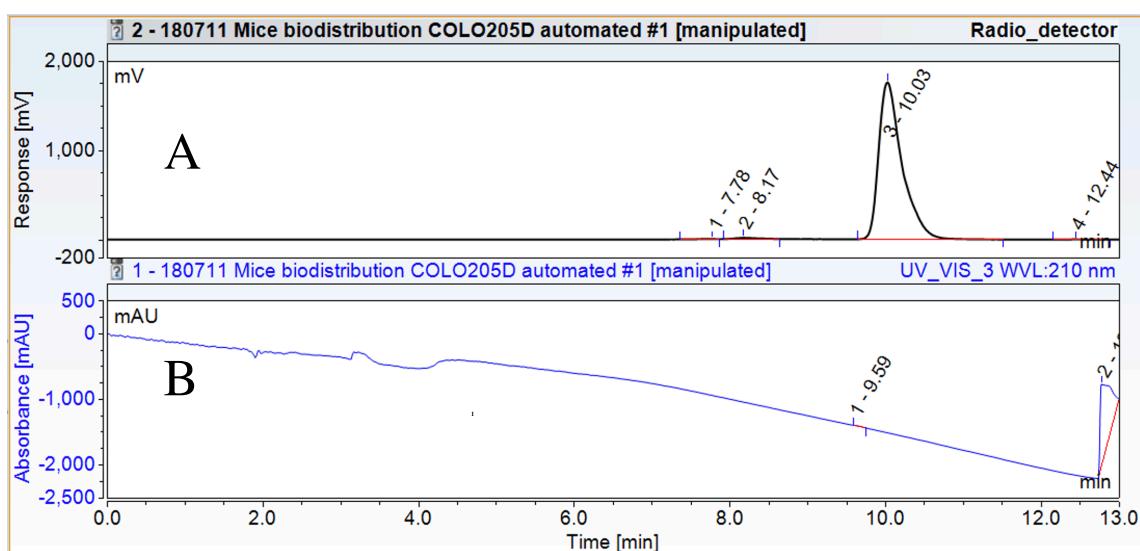


Figure 69. Radiochromatogram (A) and UV chromatogram (B) of the prosthetic group [ $^{18}\text{F}$ ]FPenM prior to C2Am conjugation. The absorbance of the prosthetic group in the UV (at 210 nm) is minimal due to the lack of aromaticity of the *N*-alkylmaleimide ( $^{18}\text{F}$ ]FPenM) molecule.

An aliquot of [ $^{18}\text{F}$ ]FPenM (100  $\mu\text{L}$ , 224 MBq at the end-of-synthesis) was used for conjugation to C2Am (108  $\mu\text{g}$ , 22  $\mu\text{L}$ , 303  $\mu\text{M}$ ), with a final protein concentration of 54.6  $\mu\text{M}$ . After 30 minutes, at RT without stirring, the reaction was analysed by HPLC and >91% of the tracer was bound to the protein. (see UV and radiochromatogram in Figure 70)



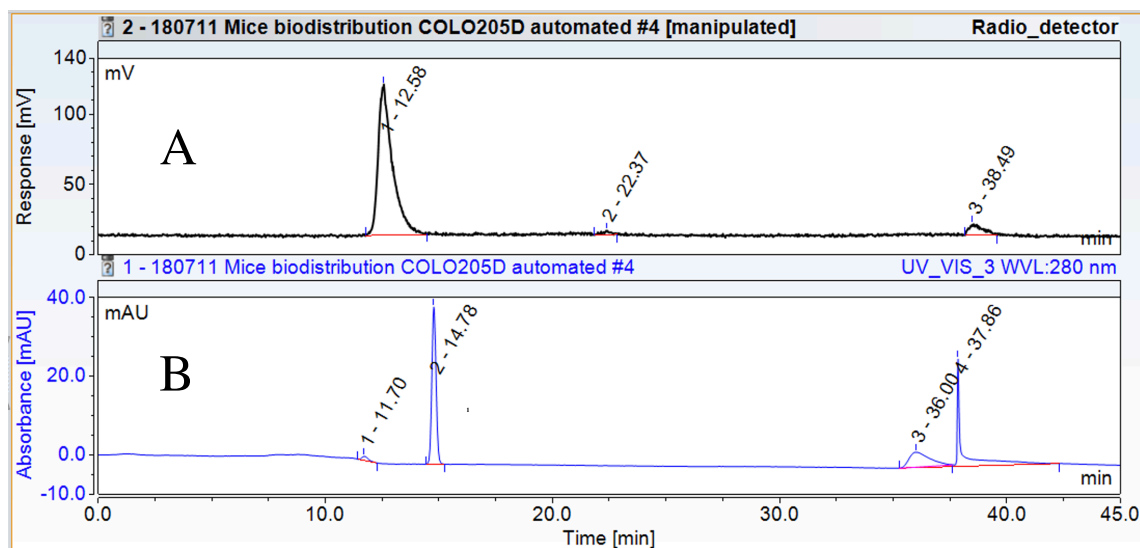


Figure 70. Radiochromatogram (A) of crude [ $^{18}\text{F}$ ]FPenM-C2Am solution prior to desalting (using a NAP-5 cartridge). Peak #1 was the [ $^{18}\text{F}$ ]FPenM-C2Am conjugate, which elutes at 12.6 min; peak #2 was a degradation by-product of [ $^{18}\text{F}$ ]FPenM at 22.4 min and peak #3 was unreacted [ $^{18}\text{F}$ ]FPenM at 38.5 min. UV 280 nm chromatogram (B) showing the [ $^{18}\text{F}$ ]FPenM-C2Am conjugate peak #1 at 11.7 min, peak #2 representing ascorbic acid additive at 14.8 min, peaks #3 and #4 caused by the solvent system changing from 100% PBS to 10% MeCN in PBS and the new solvent front reaching the detector. The estimated conversion yield of the conjugation reaction was >91%. Note that the UV detector is located upstream of the radiodetector in the HPLC system, generating a difference in measured retention times of ca. 0.8 min.

The [ $^{18}\text{F}$ ]FPenM-C2Am/[ $^{18}\text{F}$ ]FPenM mixture (122  $\mu\text{L}$ , 185 MBq) was loaded on to a disposable NAP-5 (GE Healthcare) gravity desalting cartridge and eluted with PBS. Three fractions were eluted: fraction 1 (eluted with 250  $\mu\text{L}$  PBS) did not contain any radioactivity, fraction 2: 70.7 MBq (eluted with 500  $\mu\text{L}$  PBS) contained [ $^{18}\text{F}$ ]FPenM-C2Am with >99% radiopurity according to the HPLC radiochromatogram (see Figure 71). Fraction 3: 0 MBq (eluted with 1000  $\mu\text{L}$  PBS) did not contain [ $^{18}\text{F}$ ]FPenM-C2Am: but contained ascorbic acid.(see Figure 72) Therefore fraction 2 was used for the biodistribution experiment; this fraction contained 32  $\mu\text{g}$  of protein as determined by the Merck Direct Detect Infrared spectrometer and thus protein recovery was 30% after NAP-5 column purification.

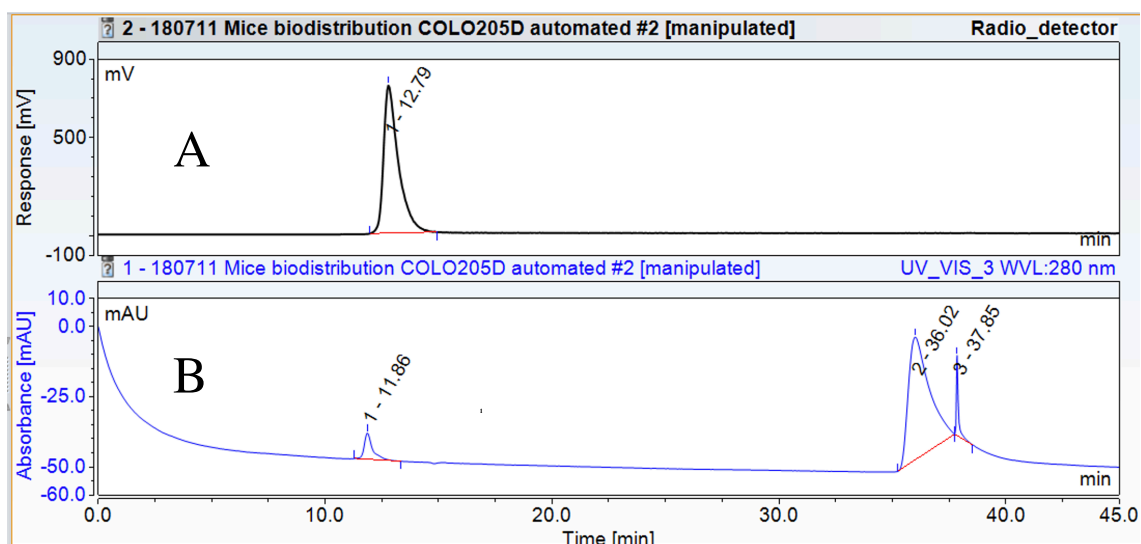


Figure 71. UV and radiochromatogram of >99% pure [ $^{18}\text{F}$ ]FPenM-C2Am conjugate. Peak #1 eluting at 12.8 min radiochromatogram (top) represents [ $^{18}\text{F}$ ]FPenM-C2Am after NAP-5 column purification and was used for *in vivo* biodistribution studies. Peak #1 in the UV 280 nm chromatogram (bottom) eluting at 11.9 min represents the conjugated C2Am. Peak #2 at 36 minutes and peak #3 at 37.9 min are caused by the solvent system changing from 100% PBS to 10% MeCN in PBS thus the new solvent front reaching the detector as peak #2 and #3.

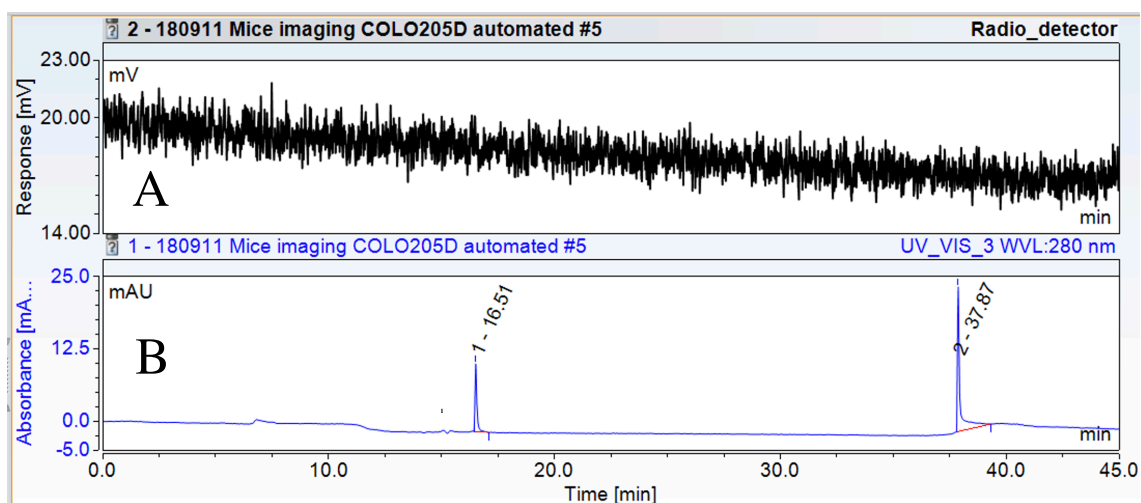


Figure 72. Radiochromatogram (A) and UV (B) of fraction 3 eluted from NAP-5 size exclusion column. Peak #1 eluting at 16.5 min in the UV 280 nm chromatogram (B) represents ascorbic acid, peak #2 at 37.9 min was caused by the solvent system changing from 100% PBS to 10% MeCN in PBS thus the new solvent front reaching the detector.

[ $^{18}\text{F}$ ]FPenM-C2Am tracer (50.59 MBq at delivery) was delivered to the imaging suite as a 410  $\mu\text{l}$  (26.6  $\mu\text{g}$ , 4  $\mu\text{M}$  solution) stock solution in PBS. Protein concentration was determined upon decay, using a Merck Direct Detect Infrared spectrometer, as 65

$\mu\text{g/mL}$  ( $4 \mu\text{M}$ ) with a molar activity of  $31200 \text{ MBq}/\mu\text{mol}$  at time-of-delivery ( $A_s = 1.9 \text{ MBq}/\mu\text{g}$  at time-of-delivery). A solution of [ $^{18}\text{F}$ ]FPenM-C2Am in PBS was made up by diluting  $150 \mu\text{L}$  stock protein tracer with  $1463 \mu\text{L}$  PBS to yield a C2Am solution ( $9.7 \mu\text{g}$ ,  $0.37 \mu\text{M}$  solution,  $1613 \mu\text{L}$ ). Each of the 6 mice were injected with  $200 \mu\text{L}$  solution ( $10 \text{ ml/kg}$ , i.v.) of [ $^{18}\text{F}$ ]FPenM-C2Am containing C2Am ( $1.2 \mu\text{g}$ ,  $0.37 \mu\text{M}$ ) in PBS. The molar activity at the time of injection was  $16200 \text{ MBq}/\mu\text{mol}$  ( $A_s = 1.0 \text{ MBq}/\mu\text{g}$  at time-of-injection)

#### 4.5.3 [ $^{18}\text{F}$ ]FPenM-C2Am synthesis for PET imaging experiment

##### 4.5.3.1 PET/CT imaging before MEDI3039 treatment

[ $^{18}\text{F}$ ]FPenM-C2Am tracer ( $86 \text{ MBq}$  at delivery) was delivered to the imaging suite as a  $500 \mu\text{L}$  ( $47.6 \mu\text{g}$ ,  $5.87 \mu\text{M}$  solution) stock solution (HPLC tracer previously shown in subsection 2.4). Following decay, the protein concentration was determined using a Merck Direct Detect Infrared spectrometer at  $95.2 \mu\text{g/mL}$  ( $5.87 \mu\text{M}$  solution) with a molar activity of  $29300 \text{ MBq}/\mu\text{mol}$  at time-of-delivery ( $A_s = 1.8 \text{ MBq}/\mu\text{g}$  at time-of-delivery). A solution of [ $^{18}\text{F}$ ]FPenM-C2Am in PBS was made up by diluting  $300 \mu\text{L}$  stock protein tracer with  $300 \mu\text{L}$  PBS to yield a C2Am solution ( $28.56 \mu\text{g}$ ,  $2.93 \mu\text{M}$  solution,  $600 \mu\text{L}$ ). The first cohort mice ( $n = 3$ ) were injected with  $200 \mu\text{L}$  of [ $^{18}\text{F}$ ]FPenM-C2Am containing C2Am ( $9.52 \mu\text{g}$ ,  $2.93 \mu\text{M}$ ) in PBS. The molar activity at the injection point was of  $10100 \text{ MBq}/\mu\text{mol}$  ( $A_s = 0.62 \text{ MBq}/\mu\text{g}$  at time-of-injection).



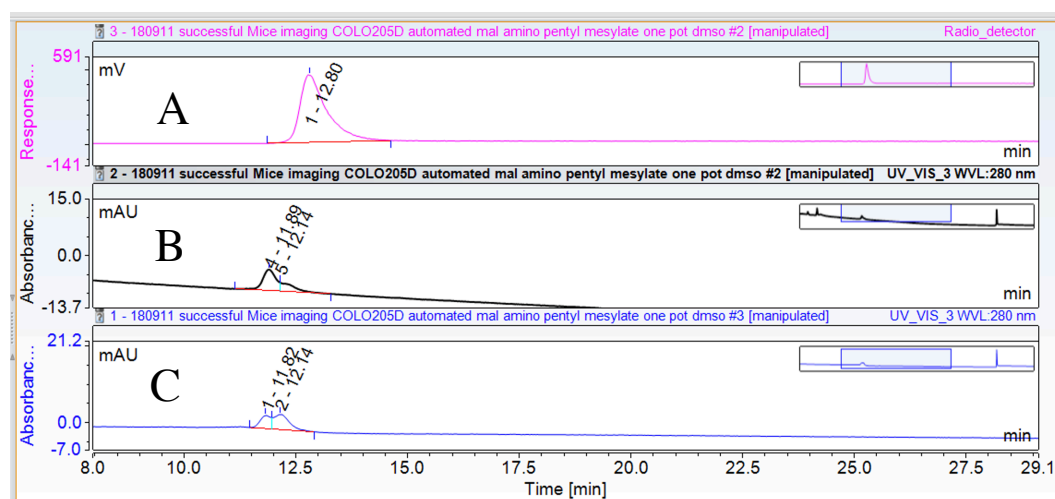


Figure 73. QC chromatogram of pure [ $^{18}\text{F}$ ]FPenM-C2Am with added (spiked) FPenM-C2Am HPLC standard. Chromatogram **A** represents the radiodetector trace and showed [ $^{18}\text{F}$ ]FPenM-C2Am elution at 12.8 min. Chromatogram **B** represents the UV (280 nm) trace and showed absorbance of reduced C2Am protein at 11.9 min and 12.2 min (FPenM-C2Am). Chromatogram **C** represents the UV (280 nm) trace and showed absorbance of reduced C2Am protein at 11.8 min and 12.1 min (FPenM-C2Am spiked with FPenM-C2Am HPLC standard hence the increased peak). The peak at 36 min is the solvent front due to the solvent system change at 20 minutes.

Another solution of [ $^{18}\text{F}$ ]FPenM-C2Am in PBS was made up by diluting 200  $\mu\text{L}$  stock protein tracer with 200  $\mu\text{L}$  PBS to yield a C2Am solution (19  $\mu\text{g}$ , 2.93  $\mu\text{M}$  solution, 400  $\mu\text{L}$ ). The second cohort of mice ( $n = 2$ ) were injected with 200  $\mu\text{L}$  solution of [ $^{18}\text{F}$ ]FPenM-C2Am containing C2Am (9.52  $\mu\text{g}$ , 2.93  $\mu\text{M}$ ) in PBS. The molar activity at the time of injection was of 3310 MBq/ $\mu\text{mol}$  ( $A_s = 0.2$  MBq/ $\mu\text{g}$  at time-of-injection).

#### 4.5.3.2 PET/CT imaging after MEDI3039 treatment

[ $^{18}\text{F}$ ]FPenM-C2Am tracer (112.8 MBq at delivery) was delivered to the imaging suite as a 550  $\mu\text{L}$  (51  $\mu\text{g}$ , 5.8  $\mu\text{M}$  solution) stock solution (HPLC shown below). Following radioactive decay, protein concentration was determined using a Merck Direct Detect Infrared spectrometer at 93  $\mu\text{g}/\text{mL}$  (5.8  $\mu\text{M}$  solution) with a molar activity of 35600 MBq/ $\mu\text{mol}$  at time-of-delivery ( $A_s = 2.2$  MBq/ $\mu\text{g}$  at time-of-delivery). A solution of [ $^{18}\text{F}$ ]FPenM-C2Am in PBS was made up by diluting 150  $\mu\text{L}$  tracer with 450  $\mu\text{L}$  PBS to yield a C2Am solution (13.9  $\mu\text{g}$ , 1.43  $\mu\text{M}$  solution, 600  $\mu\text{L}$ ). The first cohort of mice ( $n = 3$ ) were injected with 200  $\mu\text{L}$  solution of [ $^{18}\text{F}$ ]FPenM-C2Am containing C2Am (4.6  $\mu\text{g}$ , 1.43  $\mu\text{M}$ ) in PBS. The molar activity at the time of injection was 18300 MBq/ $\mu\text{mol}$  ( $A_s = 1.12$  MBq/ $\mu\text{g}$  at time-of-injection). Mice were sacrificed 2 hours post radiotracer injection

by cervical dislocation at an interval of 8 minutes and their organs collected for biodistribution analysis by gamma counting. Tumours were collected and preserved in 4% formalin solution for 24 hours then preserved in 70% ethanol for histological assessment.

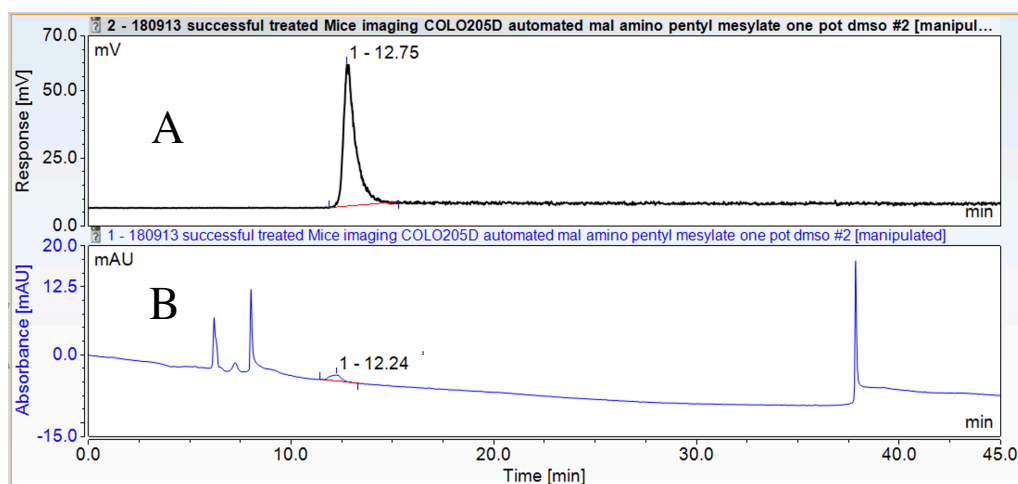


Figure 74. Radiochromatogram of >99% pure  $[^{18}\text{F}]$ FPenM-C2Am conjugate (top) and UV 280 nm chromatogram of  $[^{18}\text{F}]$ FPenM-C2Am conjugate (bottom). Peak #1 shown at 12.7 min in radiochromatogram (A) represents  $[^{18}\text{F}]$ FPenM-C2Am after NAP-5 column purification and used for *in vivo* PET imaging. Peak #1 on the UV 280 nm chromatogram (B) at 12.2 min represents the reduced C2Am. Peaks eluting between 6 and 8 minutes are probably aggregation of dimeric C2Am.

Another solution of  $[^{18}\text{F}]$ FPenM-C2Am in PBS was made up by diluting 200  $\mu\text{L}$  stock with 200  $\mu\text{L}$  PBS to yield a C2Am solution (18.5  $\mu\text{g}$ , 2.86  $\mu\text{M}$  solution, 400  $\mu\text{L}$ ). The second cohort mice ( $n = 2$ ) were injected with 200  $\mu\text{L}$  solution of  $[^{18}\text{F}]$ FPenM-C2Am containing C2Am (9.2  $\mu\text{g}$ , 2.86  $\mu\text{M}$ ) in PBS. The molar activity at the time of injection was 5700 MBq/ $\mu\text{mol}$  ( $A_s = 0.35$  MBq/ $\mu\text{g}$  at time-of-injection). Mice were sacrificed 2 hours post radiotracer injection by cervical dislocation and their organs collected for biodistribution analysis.

#### 4.5.3.3 PET imaging

A Mediso nanoScan PET/CT scanner with a PET ring diameter of 18.4 cm and a single FOV of 10 cm was used for animal scanning. The scanner was used in conjunction with a Minerve 3-place bed for mice was used to acquire CT projection images and PET coincidence detection. CT tomograms were acquired for determination of the 3D volume

for PET reconstruction. Software used was Nucline version 1.4 (Mediso). CT acquisition settings: normal FOV (no zoom), 55 kVp tube voltage, 360 projections, semi-circular, full scan, exposure time 300 ms, 1-4 binning. Reconstruction CT settings: Butterworth, medium voxel size, spatial resolution <30  $\mu\text{m}$ . PET images were normalised and corrected for decay and attenuation. PET acquisition settings: coincidence mode 1-5, single field-of-view (FOV), count rate: normal mode, coincidence time window 5 ns, dynamic PET acquisition for 2 hours, spatial resolution 0.7 mm (using the Tera-Tomo™ 3D reconstruction engine) or 1.2 mm (using filtered back projections (FBP) according to NEMA standards). PET scans reconstruction settings: isotropic 0.6 mm voxel size using a three dimensional mode (Tera-Tomo™ 3D reconstruction engine), energy window 400-600 keV, coincidence mode 1-5, and 23 reconstructed frames at 0.25, 0.5, 0.75, 1, 2, 3, 4, 5, 10, 15, 20, 25, 30, 35, 40, 45, 50, 55, 60, 75, 90, 105 and 120 min. PET/CT images were analysed and time activity curves generated by Dr André Neves using VivoQuant 4.0.

#### 4.5.3.4 Organ/tissue counting

Mice were sacrificed 2 hours post [ $^{18}\text{F}$ ]FPenM-C2am administration and their organs collected post-mortem in pre-weighed screw-top plastic tubes. An automatic gamma counter (AMG, Hidex) was used to count the organs and tissue samples. The gamma camera was set for the fluorine-18 gamma emission energy spectrum (511 keV) to scan cells and organs for 1 minute. Hidex AMG application version 1.5 software was used for collecting and exporting data. After activity decay (generally 24 hours), tubes were collected and reweighed. %ID/g was then calculated by dividing the decay corrected activity of organs by their weight in grams.

#### 4.5.3.5 Histology staining

Staining was performed by the histopathology department within Cambridge Institute for Cancer Research Cambridge. CC3 staining were performed on an automated Leica Bond Max using anti-CC3 antibody (Cell Signalling Tech) in a 1:100 dilution. TUNEL was performed on the same system using a Promega DeadEnd Colorimetric kit. Slices were scanned with a Zeiss Mirax Scan 150 at a resolution of 0.369  $\mu\text{m}/\text{pixel}$  and images interpreted with Aperio ImageScope using Positive Pixel Count algorithm to determine %CC3 and %TUNEL labelling.

# 5 IMAGING TUMOUR GLYCANS

## 5.1 Introduction to glycans and their relevance in cancer

The phenotypical complexity of humans (~21,000 genes)<sup>280</sup> compared to simpler organisms (e.g. *C. elegans* worm ~17,800 genes)<sup>281</sup> has been suggested to be due to extensive post-translational modification (PTM) present in >50% of proteins in the human genome.<sup>282-283</sup> One type of PTM that adds an extra level of complexity to the already diverse proteome is glycosylation,<sup>284</sup> which has been described as the process of glycan addition to proteins and lipids.

Glycans are sugar polymers (termed oligosaccharides) which are composed of a selection of building blocks (monosaccharides) connected to each other by *O*-linked glycosidic bonds. There are twelve common monosaccharides shown in Figure 75 which form the main components of glycans in vertebrates depicted in Figure 76.<sup>285</sup> One of the most common glycan-capping sugars present in vertebrate glycoproteins is sialic acid, which is a general term for acidic sugars, containing a nine-carbon structure. The most common form of sialic acid in humans is *N*-acetylneuraminic acid (Neu5Ac), while *N*-glycolylneuraminic (Neu5Gc) acid is present in other mammals but not in humans due to a mutation in the sequence encoding for the enzyme (cytidine monophosphate (CMP)-*N*-acetylneuraminic acid hydroxylase), which converts Neu5Ac to Neu5Gc.<sup>286</sup>

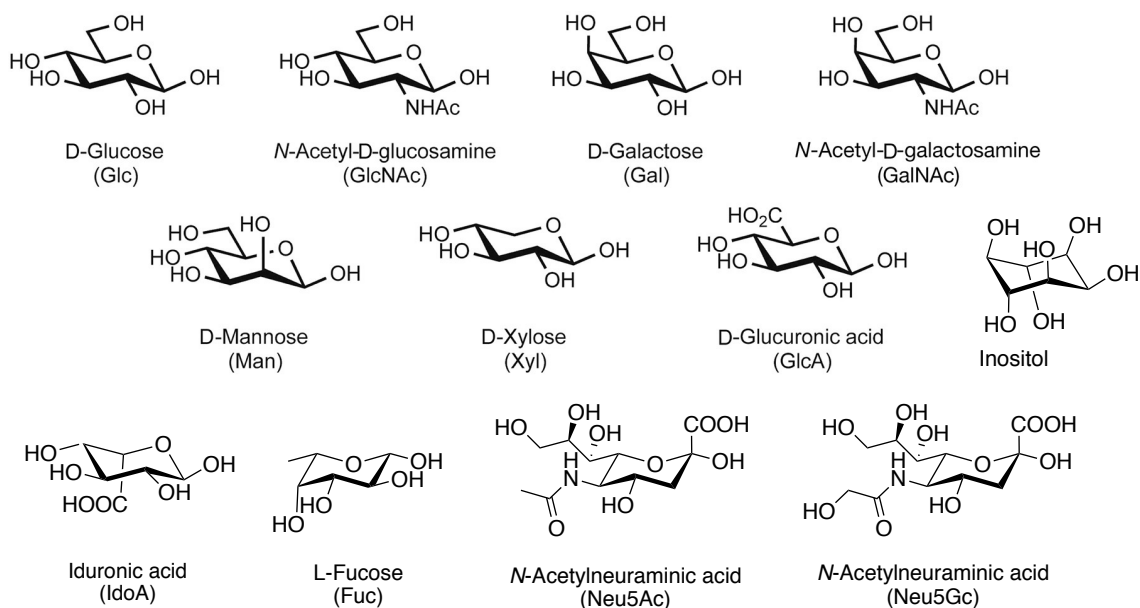


Figure 75. Most common monosaccharides that are components of glycans in vertebrates. Figure adapted from Varki *et al.*<sup>285</sup> (2009)

Glycans are conjugated to proteins and lipids or secreted on their own (e.g. hyaluronan – a component of the extracellular matrix). They have an important role in mediating and regulating the processes of cell recognition, cell adhesion, inflammation, energy storage and pathogen invasion. For example, the ABO blood group system, discovered by Karl Landsteiner at the beginning of the 20<sup>th</sup> century, is determined by glycan epitope antigens (A, B or O) present on the surface of red blood cells and modulated by glycosyltransferases.<sup>285</sup>

There are four types of glycan-conjugated proteins<sup>287</sup>: nitrogen (*N*-), oxygen (*O*-), carbon (*C*-) and sulfur (*S*-) linked glycoproteins. While *N*- and *O*-linked glycans are the most abundant types<sup>285</sup> in eukaryotic cells, *C*-linked glycans are less abundant, examples including RNase II<sup>288</sup> and interleukin-12<sup>289</sup> proteins with  $\alpha$ -mannosyl modifications on the C-2 of tryptophan amino acids. *S*-linked glycans are linked through cysteine<sup>290</sup> and are common in bacteria. Figure 76 shows *N*-linked glycans that are attached to proteins, forming glycoproteins, through amide bonds linking the asparagine (Asn) side chain to *N*-Acetylglucosamine (GlcNAc) at the specific amino acid sequence Asn-X-Ser/Thr (where X represents any amino acid). *O*-linked glycans are attached to proteins by linking either serine or threonine (Ser/Thr) side chains to *N*-acetylgalactosamine (GalNAc).<sup>291</sup> These *O*-linked glycans are present in mucins,<sup>292</sup> which are large megadalton

glycoprotein complexes that play critical roles as barriers on epithelial surfaces and in cell-cell interactions in epithelial tissues (e.g. MUC2 in small intestine). Glycans linked to lipid ceramides, through either galactosylceramide or glucosylceramide, are termed glycosphingolipids and are found embedded in the outer leaflet of the plasma membrane. Glycosphingolipids are also often capped by sialic acids (most commonly *N*-acetylneuraminic acid) and have a role in regulating proliferation via receptor tyrosine kinase (RTK) signaling.<sup>291</sup>

Glycans are synthesised continuously and incorporated into proteins or lipids in the ER and Golgi apparatus by a complex array of glycosyltransferase enzymes that use the intracellular pool of monosaccharides. The glycome, representing the totality of glycans at any given time, is a dynamic pool and its changes have been associated with oncogenic transformation, following environmental and physiological perturbations.<sup>285,291,293</sup>

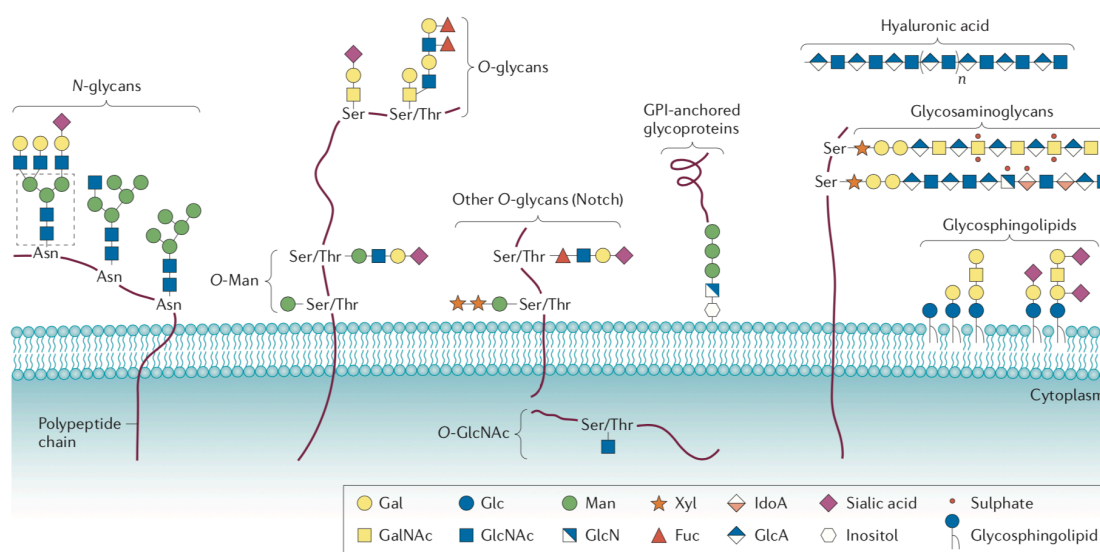


Figure 76. Main classes of glycans in mammalian cells. Schematic adapted from Pinho and Reis (2015).<sup>44</sup>

### 5.1.1 Aberrant glycosylation in cancer

Glycans play an important role in the physiological changes that occur during tumourigenesis and progression; facilitating metastasis, angiogenesis and invasion. Aberrant glycosylation, such as overexpression of sialic acids, fucosylation and hyper

branching (e.g. generating multiple antenna in *N*-linked glycans) of glycans are a key hallmark of cancer. These modifications have a direct impact on cell signalling, adhesion and invasion (metastasis).

In colorectal cancers, overexpression of glycosyltransferases (e.g. sialyltransferases) leads to aberrant glycosylation such as branching and polysialic acid-capped glycans. In colorectal cancer cells, such as Colo205, branching and formation of tri- and tetra-antennary modifications has been observed by mass spectrometry (Figure 77). The latter effect was found to be caused by the overexpression of *N*-acetylglucosaminyltransferases (GnT IV and V), which have a role in extending *N*-glycan branching, and whose overexpression has been associated with malignancy.<sup>294</sup>

Monitoring of these aberrant modifications could prove useful for diagnosis, early detection of the disease and treatment response. Glycan overexpression is known to occur with cancer progression, potentially providing a means to assess disease stage.<sup>294</sup>

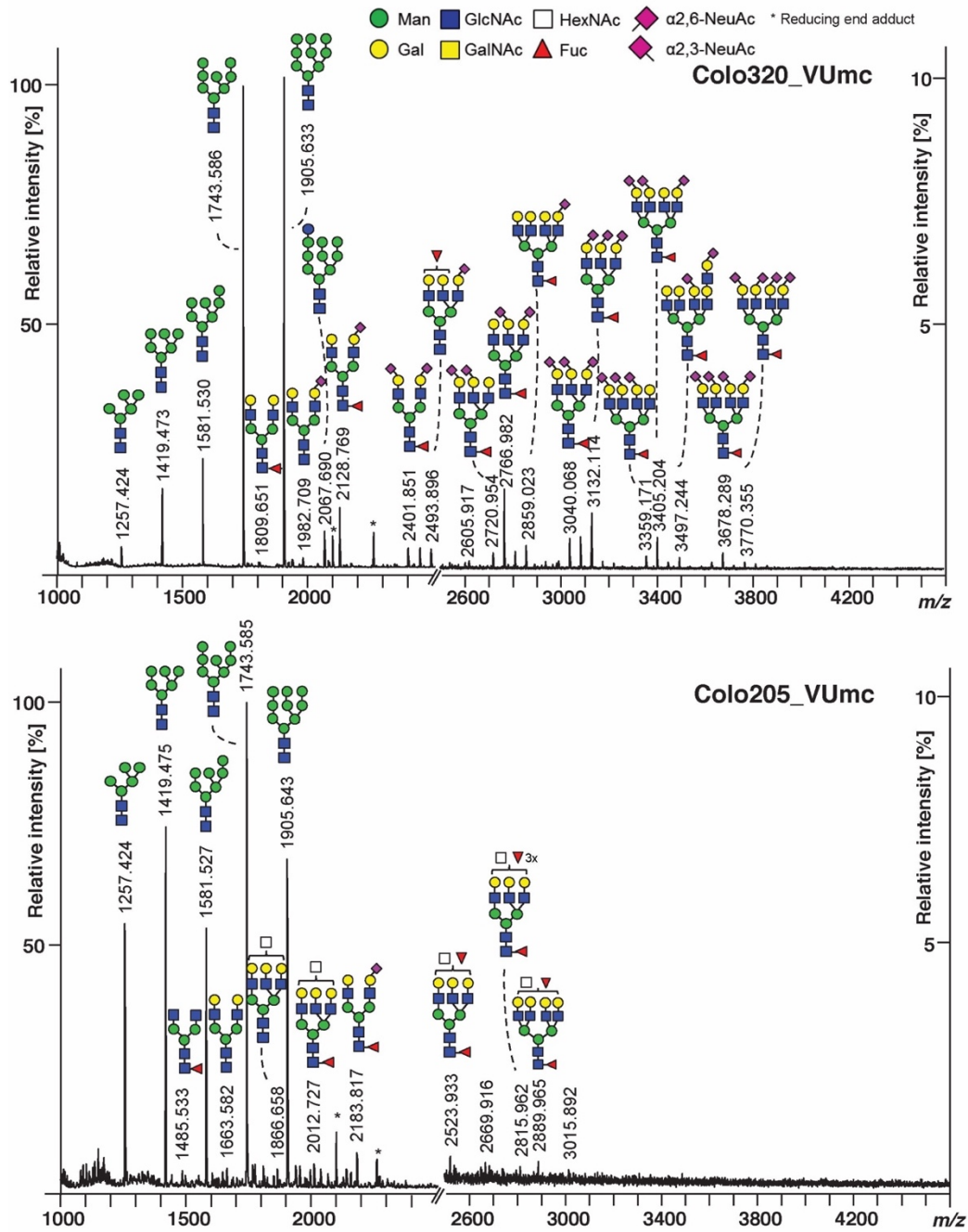


Figure 77. Mass spectrometric analysis of *N*-glycans in two colorectal cancer cell lines. Aberrant sialylation and hyper branching (bi-, tri- and tetra-antennary) was observed in the Colo320 cell line. Colo205 cells exhibit *N*-linked glycans with excessive fucosylation and hyper branching (bi-, tri- and tetra-antennary). Image adapted from Holst *et al.*<sup>295</sup>



### 5.1.2 Imaging of glycans

Glycan imaging has been performed previously using lectins. These are either proteins or glycoproteins capable of binding specific glycan signatures. The detection of high-grade dysplasia in Barrett's oesophagus, a pre-stage to oesophageal adenocarcinoma, has been proposed by the Brindle group as an *in situ* endoscopy imaging method, using topical application of fluorescently labelled lectins<sup>296</sup>. This approach was also used by the Brindle group for differentiating, with high sensitivity and specificity, between benign hyperplastic colon polyps, normal colon epithelium and a range of low- to high-grade dysplasia in colorectal cancer<sup>297</sup>. Lectins are unsuitable for systemic delivery due to slow pharmacokinetics and pharmacodynamics caused by their relatively large size and relatively low affinity towards individual glycans (micromolar range). Moreover, some toxicity can also be exhibited by lectins therefore rendering the systemic administration of these probes unsuitable for *in vivo* imaging.<sup>298</sup> Nevertheless, as topical imaging agents, particularly in the GI tract, lectins may still be useful for the early detection of cancer, having been trialled recently in a Phase-0 study for the detection of oral pre- and malignant lesions.<sup>299</sup>

Since glycosylation is a dynamic post-translational modification, key monosaccharide building blocks can potentially be replaced by reporter-bearing unnatural monosaccharides during biosynthesis. This is the basis of metabolic labelling of glycans using non-natural sugars (see Figure 78). Unnatural monosaccharides and their detection using chemical reporters have been described previously by our research group and used in fluorescence and gadolinium-based MR imaging.<sup>300,301</sup>

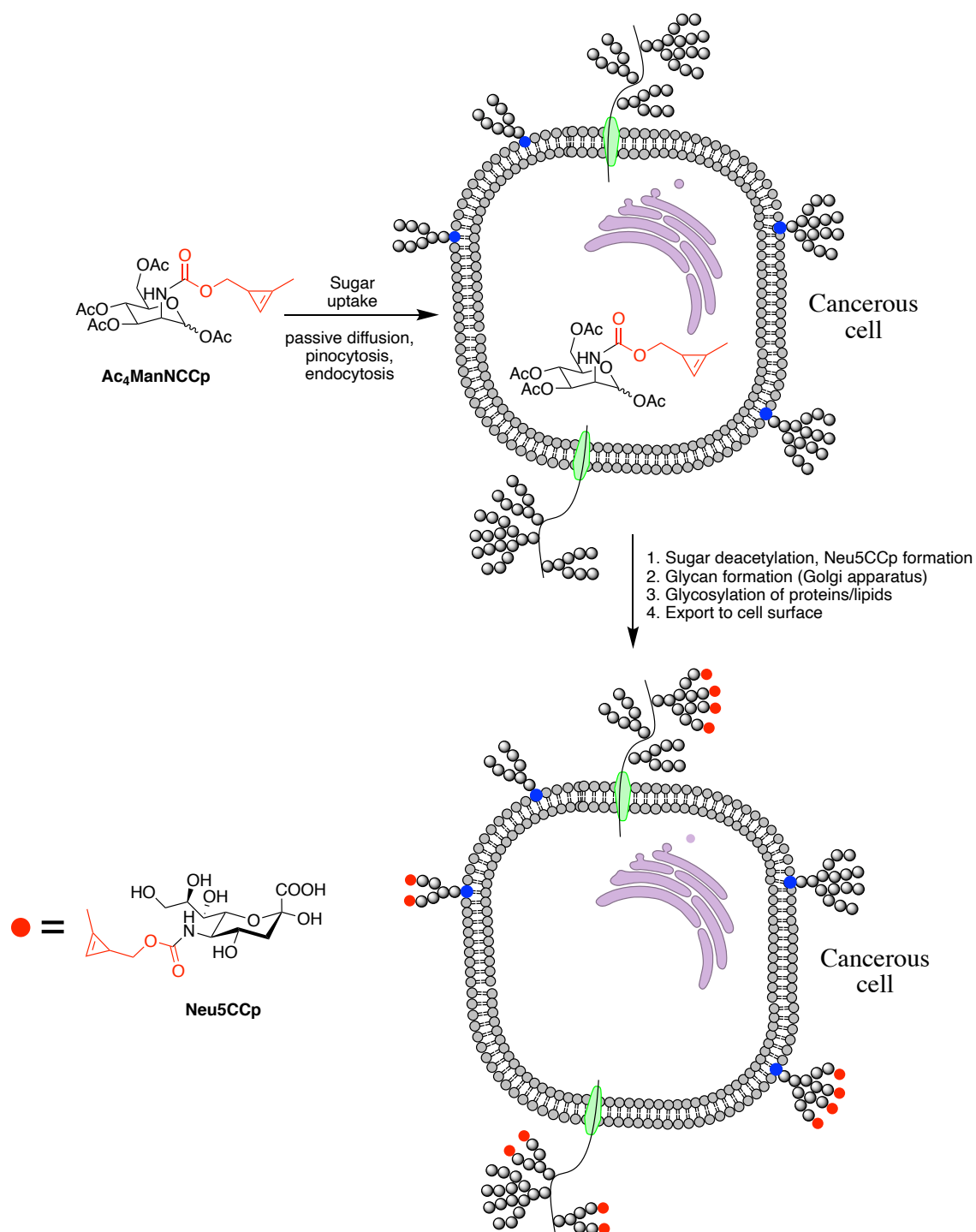
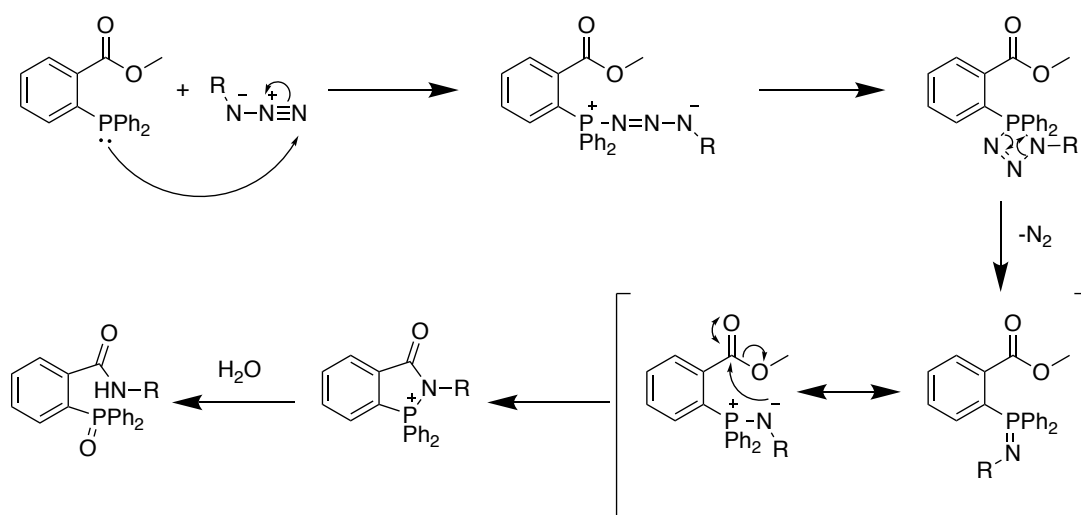


Figure 78. Diagram showing metabolic labelling of glycans. Peracetylated methylecyclopropene mannosamine (Ac<sub>4</sub>ManNCCp) is taken up (by passive diffusion and/or endocytosis) by cells. Upon internalisation monomeric Ac<sub>4</sub>ManNCCp is deacetylated (mannosamine converted to neuraminic acid)<sup>302</sup>, activated and incorporated into glycans in the Golgi apparatus (purple lamellar assembly) as a neuraminic acid. Labelled glycans (containing the non-natural sugar – red discs) are either *N*-linked or *O*-linked to proteins (green) and lipids (blue discs) and exported to the cell surface.

This project investigated the use of *N*-methylcyclopropene amide mannosamine (Ac<sub>4</sub>ManNCCp) as a chemical reporter for fluorescent-tetrazine ligation of *N*-methylcyclopropene neuraminic acid (Neu5CCp) (see Figure 78). The reaction of methylcyclopropenes with tetrazine has previously been used as a bioorthogonal reaction for *in vitro* imaging of glycans.<sup>303-304</sup> However, *in vivo* glycan imaging has yet to be described using this reporter sugar.

### 5.1.3 Bioorthogonal reporter and metabolic labelling strategies

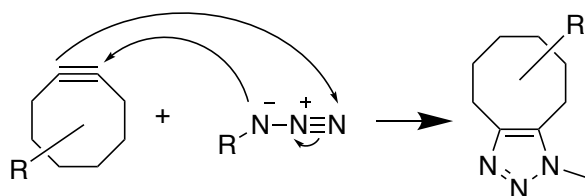
Bioorthogonal is a term used to describe the chemistry undertaken by pairs of synthetic molecules, used for tagging biomolecules, in a living organism. The two component molecules of the bioorthogonal reaction are not affected by the plethora of endogenous molecules present in that organism and are stable under physiological conditions. These molecules should also not interfere with any cellular metabolic processes. The term bioorthogonal was coined by Carolyn Bertozzi in 2003<sup>305</sup> and used the Staudinger ligation (Scheme 21) for *in vivo* labelling of glycans. However, this reaction is not completely bioorthogonal, as the phosphine moiety can reduce disulphide bonds present in proteins. Moreover, the phosphine is prone to oxidation by air, and therefore can be rather unstable.<sup>169</sup> Despite these pitfalls, it has been used successfully *in vivo* for imaging glycans.<sup>222,306</sup>



Scheme 21. Staudinger ligation mechanism.

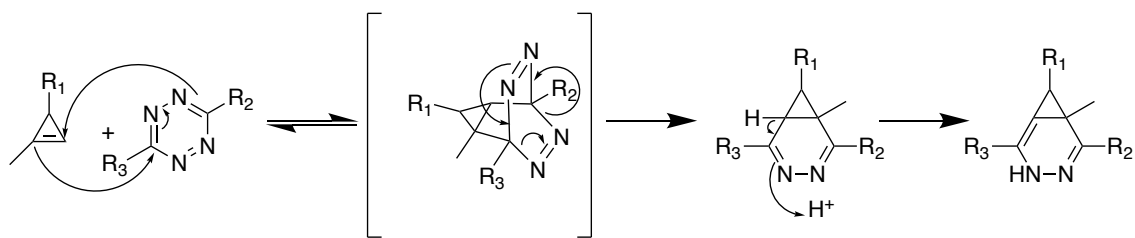
Some bioorthogonal reactions occur through click chemistry. “Click” chemistry refers to ligation reactions that occur reliably in aqueous solvents, irrespective of the nature of the molecules to be ligated. The commonest click reaction occurs when an azide, as a 1,3-dipole, undergoes a [3+2] cycloaddition reaction with a terminal alkyne, using copper (I) as a catalyst.<sup>307</sup> However, ionic copper used as a reaction catalyst is toxic to cells and therefore biocompatible copper-free click chemistry has been developed. One such bioorthogonal reaction is the cycloaddition of an azide to a cyclic, strained alkyne<sup>308</sup> or alkene<sup>309</sup>. The reaction of cyclononynes and cyclooctynes with phenylazide was first described by Wittig and Krebs in 1961.<sup>308</sup> It is now known as strain promoted azide-alkyne cycloaddition (SPAAC) and its mechanism shown in Scheme 22. Cyclic alkynes have a favourable pre-strained structure that favours SPAAC reaction. In addition, a smaller HOMO (azide)-LUMO (alkyne) energy gap compared to acyclic alkynes reaction means that the reaction can proceed without the need for a catalyst.<sup>310,311</sup>

The first bioorthogonal [3+2] cycloaddition between an azide and a cyclooctyne has first been used *in vitro* for cell-surface glycan imaging by Bertozzi *et al.* in 2004.<sup>312</sup> Since then, this particular reaction has been extensively used for metabolic labelling of glycans, by our research groups (Leeper and Brindle)<sup>301,313,314</sup> and others<sup>168,169,312,315,316</sup>.



Scheme 22. The [3+2] cycloaddition between a 1,3-dipole azide and a strained cyclooctyne.

Recently, 1-methyl-3-substituted cyclopropene reacting bioorthogonally with a 1,2,4,5-tetrazine (Scheme 23) has been found to be a faster alternative to SPAAC.<sup>317</sup>



Scheme 23. A typical reaction mechanism of an inverse electron demand Diels-Alder cycloaddition of methylcyclopropene to a 3,6-disubstituted 1,2,4,5 tetrazine derivative.

In 2012, the Prescher lab developed the first methylcyclopropene amide mannosamine named Ac<sub>4</sub>ManNCyc (shown in Figure 79), containing a cyclopropene chemical reporter.<sup>318</sup> This was the first attempt to metabolic labelling of glycans using a methylcyclopropene tagged sugar. In 2013, dual sugar labelling of glycans with Ac<sub>4</sub>ManNCyc and Ac<sub>4</sub>ManNAz was by the Devaraj lab.<sup>319</sup> The two sugars were independently reacted to two different fluorogenic probes, Ac<sub>4</sub>ManNCyc with tetrazine-AlexaFluor-488 and Ac<sub>4</sub>ManNAz with DIBO-647 respectively.

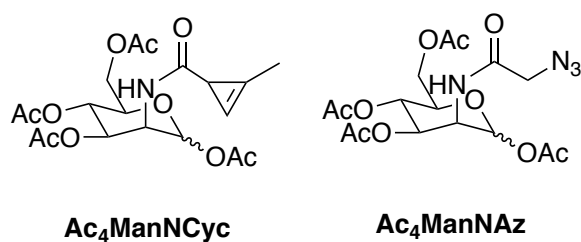


Figure 79. Structure of Ac<sub>4</sub>ManNCyc and Ac<sub>4</sub>ManNAz used by the Devaraj lab.

Following Devaraj's successful work (2012) of labelling live cell membranes using a novel methylcyclopropene carbamate phospholipid<sup>320</sup>, Späte *et al.* used a peracetylated methylcyclopropene carbamate *N*-linked mannosamine (Ac<sub>4</sub>ManNCCp, Figure 80) and a peracetylated azido mannosamine to undertake dual sugar labelling of glycans in HEK 239T cells.<sup>304</sup> Considering the 100-fold faster<sup>320</sup> reaction rates of methylcyclopropenecarbamate to tetrazines compared to SPAAC, the Prescher lab have since used the novel cyclopropene moiety to derivatise three important glycan sugars: mannosamine (precursor to sialic acid), glucosamine and galactosamine. These sugars have been successfully metabolically incorporated into 4T1 breast cancer cells and labelled with a tetrazine-biotin tagging moiety.<sup>321</sup>

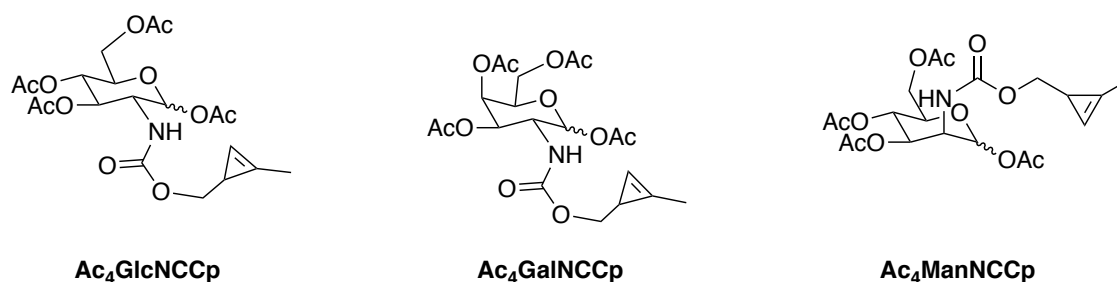
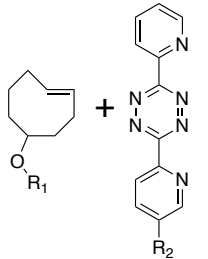
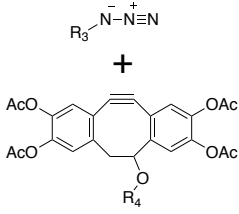
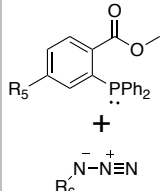
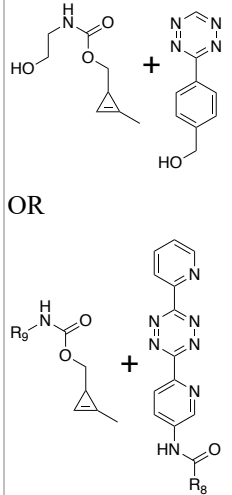


Figure 80. The chemical structure of three methylcyclopropene modified monosaccharides.

Preliminary *in vitro* flow cytometry data were acquired by Dr Yelena Wainmann, using the peracetylated methylcyclopropene carbamate mannosamine **36** (see Scheme 25), synthesised initially by Master's student Beatrice Longo, both members of the Leeper lab. Pilot flow cytometry experiments carried out by Dr Wainman *in vitro* (unpublished work) studied metabolic labelling of LL2 lung carcinoma cells using Ac<sub>4</sub>ManNCCp **36** (100 μM; 24 h). Subsequent labelling of the methylcyclopropene tag using a two-step method using a tetrazine-biotin and NeutrAvidin-DyLight680 (NA680) showed a signal-to-background ratio (SBR) of 30 by flow cytometry. This promising result led to subsequent *in vitro* and *in vivo* testing. However, streptavidin/neutravidin (53 kDa and 68 kDa respectively) based imaging was less favoured for *in vivo* use due to their slow clearance. This can be caused by their large size, low capillary permeability, their immunogenicity and strong non-covalent interaction ( $K_d = 1 \times 10^{-15}$  mol/L)<sup>325</sup> with endogenous biotin found in serum (concentration of 0.5 ng/mL).<sup>326,327</sup> Therefore, an alternative approach was to use a bioorthogonal molecule, *s*-tetrazine-PEG<sub>11</sub>-DyLight649, to label methylcyclopropene neuraminic acid on glycans. This fluorescent probe is compatible with *in vivo* imaging unlike previously used immunogenic streptavidin-tetrazines.<sup>321</sup>

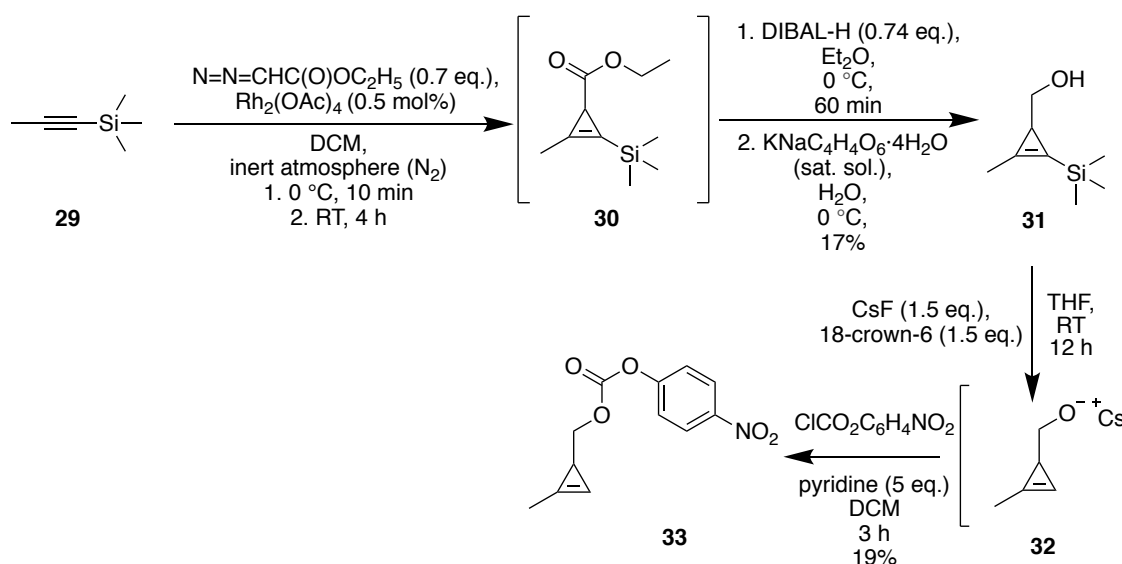
Table 17. Comparison of the kinetics of bioorthogonal reactions, stability, advantages and disadvantages

Bioorthogonal reaction	1	2	3	4
				
Kinetics (rate constant k)	Up to 22000 M <sup>-1</sup> s <sup>-1</sup> (in H <sub>2</sub> O) <sup>322,323</sup>	0.094 M <sup>-1</sup> s <sup>-1</sup> (in 100% MeOH) <sup>171</sup>	2.5 x 10 <sup>-3</sup> M <sup>-1</sup> s <sup>-1</sup> (CDCl <sub>3</sub> )*  *Measured by Dr Stoeckmann and published in his PhD dissertation.	Top: 13±2 M <sup>-1</sup> s <sup>-1</sup> at 30 °C in a solution of water/DMSO (12% DMSO) <sup>320</sup>  OR  Bottom (Tz-R <sub>8</sub> ): 27 ±2 M <sup>-1</sup> s <sup>-1</sup> in TRIS-HCl pH 7.4 with added DMSO (5%) <sup>324</sup>
Stability	trans-Cyclooctene (TCO) stable for up to 2 months -20 °C	TMDIBO stable at room temperature	Phosphine moiety is prone to oxidation. Must be kept under argon. Can be oxidised in vivo by disulphide bonds	Stable for months in the freezer.
Advantages	Very fast reactions	Fast reactions, small functional group	Bioorthogonal reaction	Small chemical reporter, fast reaction with tetrazines
Disadvantages	TCO is a large moiety thus is not easily accepted by the esterases - part of the metabolic labelling cascade of events.  TCO can isomerise to cis-cyclooctene thus unreactive towards tetrazines.	Alkyne moiety increases lipophilicity leading to poor aqueous solubility.	Prone to oxidation.  Relatively slow reaction rates for bioorthogonal reactions	Cyclopropene moiety increases overall molecule lipophilicity leading to poor aqueous solubility.  Unknown in vivo stability. (no peer- reviewed publications)

## 5.2 Synthesis of *N*-cyclopropenyl carbamate mannosamine (Ac<sub>4</sub>ManNCCp)

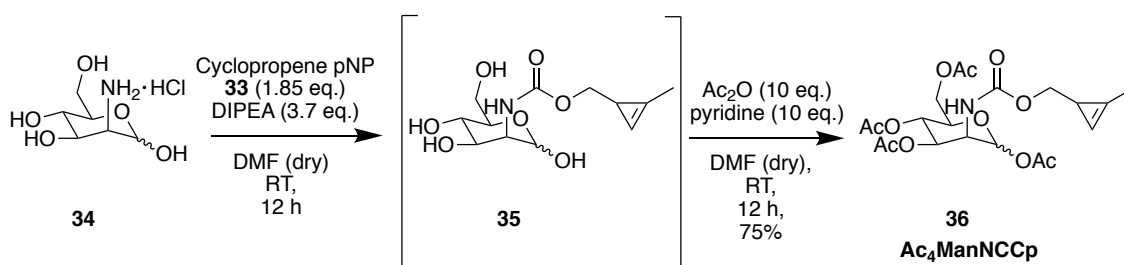
A new batch of methylcyclopropene derivatised mannosamine **36** (Ac<sub>4</sub>ManNCCp) was synthesized for testing *in vitro*. A cyclopropanation reaction between 1-(trimethylsilyl)propyne **29** and ethyl diazoacetate in the presence of rhodium diacetate yielded protected cyclopropene ethyl-ester **30**.<sup>321</sup> Reduction with diisobutylaluminium hydride (DIBAL-H) for 1 hour at 0 °C yielded silyl protected alcohol **31** in a low yield of 17% (cf. 53% yield by Patterson *et al.*<sup>321</sup>) over 2 steps. Alcohol **31** was deprotected with 18-crown-6 and caesium fluoride (CsF) under anhydrous conditions to yield cyclopropene caesium salt **32** as a cloudy solution. This intermediate was unstable and polymerised easily therefore no attempt was made to isolate it. Addition of nitrophenyl carbonate to **32** in the presence of pyridine for 24 hours yielded carbonate **33** in a low yield of 19% (see Scheme 24). The reason for the low yield might be explained by prolonged reaction times used for trimethylsilyl deprotection compared to the literature (12 hours vs 2.5 hours). This increased cyclopropene polymerisation, hence the resulting cloudy solution and the low yield obtained. The challenge with these two steps was to solubilise CsF using cryptands while also keeping the reaction strictly anhydrous. CsF was dried for 1 hour at high vacuum (0.66 mbar) and ~300 °C (using a heat gun). Solvents were dried over freshly activated molecular sieves (4 Å), which had been activated in the same way as drying of CsF.





Scheme 24. Synthesis of methylcyclopropene nitrophenyl carbamate **33**

By reacting D-mannosamine **34** with the activated methylcyclopropene carbonate **33**, as per conditions described by Patterson *et al.*<sup>321</sup>, methylcyclopropene mannosamine **35** was synthesised. The solution quickly turned yellow, indicating the release of the 4-nitrophenolate anion. Peracetylation of **35** using excess acetic anhydride in pyridine yielded Ac<sub>4</sub>ManNCCp **36** in a moderate 75% yield. (see Scheme 25)



Scheme 25. Synthesis scheme of Ac<sub>4</sub>ManNCCp **36** sugar.

### 5.3 *In vitro* metabolic labelling of Colo205-D cells

Ac<sub>4</sub>ManNCCp sugar **36** was dissolved in DMSO and used for metabolic glycan labelling of a colorectal cancer cell line (Colo205-D). A three-day protocol, see Figure 82, was used to label Colo205-D cells with **36**. On day 1, cells were seeded into 6-well

culture dishes with 4 wells left for controls (DMSO vehicle). Passaging of Colo205-D cells was done according to the culture protocol previously described in Chapter 3. On day 2 (16 hours later), **36** (100  $\mu\text{M}$  in DMSO) was added to cells (vehicle – DMSO – to control cells). On day 3, cells were harvested and derivatized with Tz-PEG<sub>11</sub>-Dylight649 (5  $\mu\text{M}$ ) – synthesised by Dr Henning Stoeckmann (Figure 81) – and SYTOX green (50 nM) for 20 min at 37 °C. The SYTOX green stain was used to exclude necrotic cells.

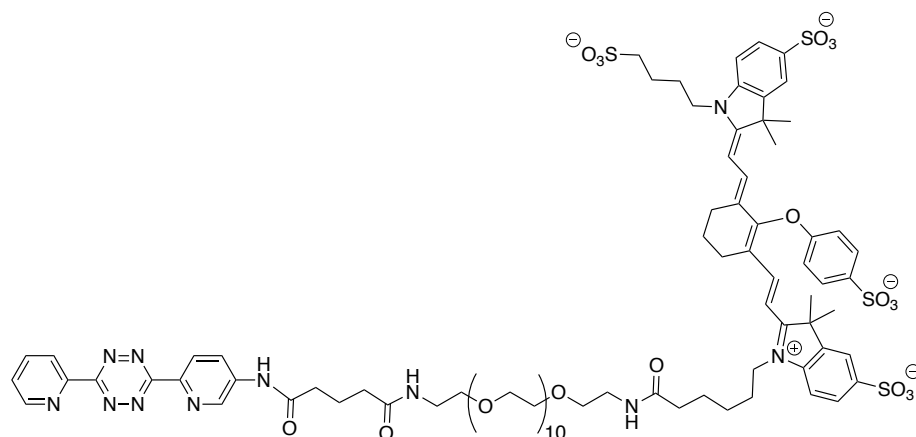


Figure 81. The chemical structure of Tz-PEG<sub>11</sub>-Dylight649.

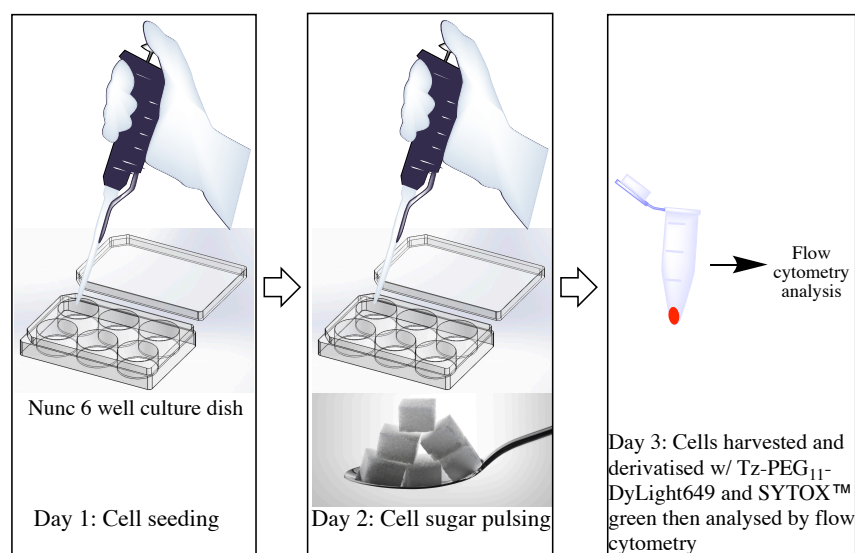
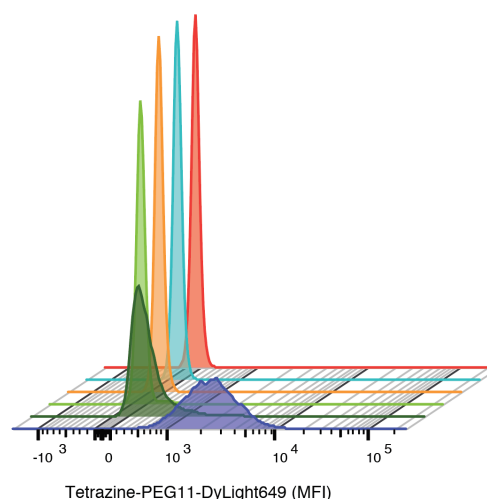


Figure 82. A 3-day protocol for metabolic labelling of Colo205-D cells with **36** (100  $\mu\text{M}$ ) and then with Tz-PEG<sub>11</sub>-Dylight649 (5  $\mu\text{M}$ , 660 nm) and monitored for cell necrosis with SYTOX green (50 nM, 530 nm). On day 3, cells were harvested and labelled with Tz-PEG<sub>11</sub>-Dylight649 (5  $\mu\text{M}$ ). Tz-PEG<sub>11</sub>-Dylight649 and SYTOX green (50 nM) cell fluorescence was analysed by a BD LSR II flow cytometer.

Colo205-D sugar treated cells and controls (DMSO, FACS buffer, unlabelled Colo205-D cells) were analysed by flow cytometry to determine the extent of cell autofluorescence at 660 nm. As shown in Figure 83, no significant fluorescence emission was detected from controls. DMSO, FACS buffer, Colo205-D cells and controls showed a median fluorescence intensity (MFI) of ~35 which is a low value compared to the ~2500 MFI of cells labelled with Tz-PEG<sub>11</sub>-DyLight649 (5  $\mu$ M).



Name	Median : Comp-red 660_20-A
Tz-PEG11-DyLight649 labelled	2452
Tz-PEG11-DyLight649 control	328
FACS buffer control + sugar	39.8
FACS buffer control	35.9
Cells control	34.7
DMSO control	30.8

Figure 83. Figure showing controls for DMSO (red), Colo205-D cells autofluorescence (blue), FACS buffer (orange) and FACS buffer-washed cells labelled with sugar **36** (light green). Tz-PEG<sub>11</sub>-DyLight649 (5  $\mu$ M) treated cells are also shown: Colo205 control cells (dark green) and cells labelled with peracetylated sugar **36** (100  $\mu$ M, yellow).

Scatter plots of Colo205-D cells derivatised with Tz-PEG<sub>11</sub>-DyLight649 (660 nm) against SYTOX<sup>®</sup> green (530 nm) were analysed to quantify the extent of labelling between viable and necrotic control and peracetylated sugar **36** labelled cells. (see Figure 84, Figure 85 and Figure 86) In these experiments SYTOX green has shown very little cell death suggesting that sugar **36** is not inducing necrosis. The signal-to-baseline ratio (SBR) of Tz-PEG<sub>11</sub>-DyLight649 fluorescence (i.e. the ratio of MFIs of sugar-labelled and control cells) was  $7.6 \pm 0.31$  (n = 5) (Figure 86).

This favourable SBR indicates that this probe has the potential to be used for *in vivo* studies. However, cell-viability was significantly affected by the addition of sugar **36** despite no necrosis being recorded, dropping from 82 to 74% ( $P = 0.0022$ ,  $n = 6$ ).

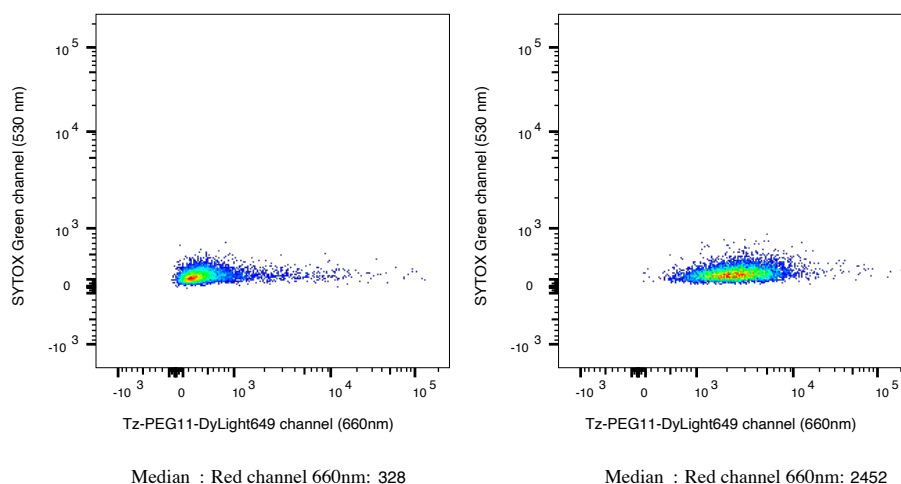


Figure 84. Scatter plots of Colo205-D control (no sugar, left) and sugar **36** (100  $\mu\text{M}$ ) labelled cells (right) labelled with Tz-PEG<sub>11</sub>-DyLight649 (5  $\mu\text{M}$ ) and SYTOX green (50 nM) for 20 minutes at 37 °C.

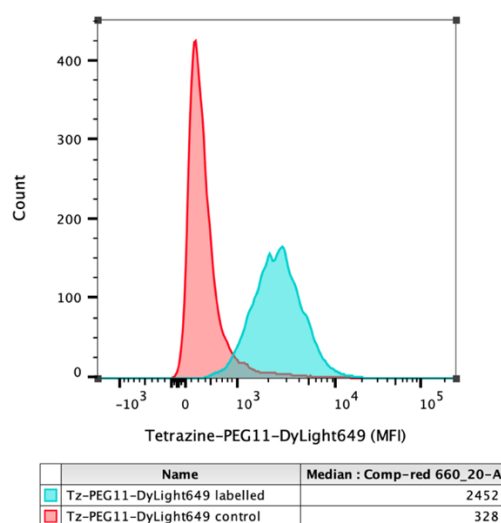
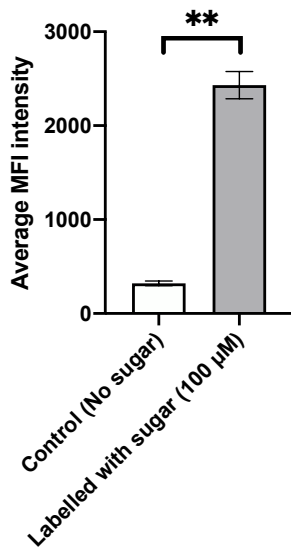


Figure 85. Histogram plot (below) of Colo205-D control (no sugar) and sugar **36** (100  $\mu\text{M}$ ) treated cells (right) derivatised with Tz-PEG<sub>11</sub>-DyLight649 (5  $\mu\text{M}$ ) and SYTOX green (50 nM) for 20 minutes at 37 °C.

**Tz-PEG<sub>11</sub>-DyLight649 labelling of Colo205-D**



**Viability upon Ac<sub>4</sub>ManCCp sugar addition**

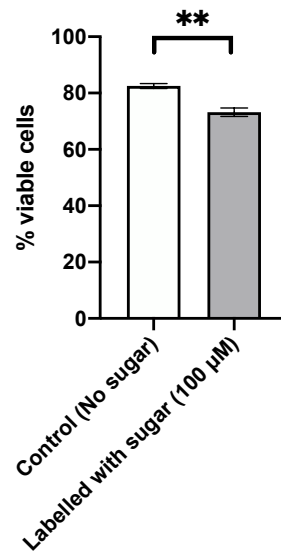


Figure 86. Unpaired Mann-Whitney tests, showing significant difference ( $P = 0.0079$ ,  $n = 5$ ) between Colo205-D control (no sugar) and cells labelled with Ac<sub>4</sub>ManNCCp (100 µM; 24h) (right) after treatment with Tz-PEG<sub>11</sub>-DyLight649 (5 µM, 20 min). Viability decreased significantly from 82 to 74% ( $P = 0.0022$ ,  $n = 6$ ).

Further tests were carried out to optimise the required concentration and time for the fluorescent probe labelling. From Figure 87, it was deduced that 1 hour is sufficient for achieving a close-to-maximal SBR of 14.4 using a solution of Tz-DyLight649/SYTOX<sup>®</sup> green (5 µM / 50 nM).

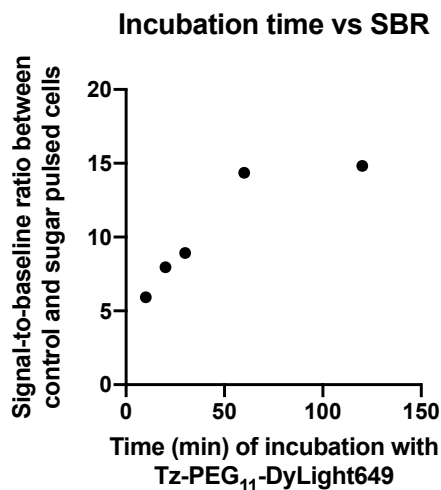


Figure 87. Optimisation of labelling time with Tz-PEG<sub>11</sub>-DyLight649 (5 µM).

Next, different concentrations of Tz-PEG<sub>11</sub>-DyLight649 (5, 10, 20 and 40  $\mu$ M) were used for labelling sugar treated cells for 1 hour at 37 °C: 5  $\mu$ M gave the best SBR of 30 according to the graph shown in Figure 88.

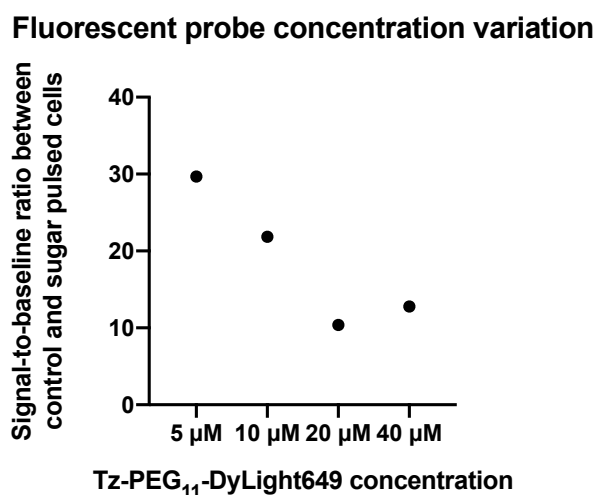


Figure 88. Optimisation of Tz-PEG<sub>11</sub>-DyLight649 concentration.

Confocal microscopy was used to image fixed Colo205-D labelled with peracetylated sugar **36** (100  $\mu$ M) and labelled with Tz-PEG<sub>11</sub>-DyLight649 (5  $\mu$ M) and SYTOX<sup>®</sup> green (50 nM). No image quantification was performed. The images confirm that the Tz-PEG<sub>11</sub>-DyLight649 fluorescence (Figure 89 C) was confined to the cell surface and not distributed throughout the cytoplasm.

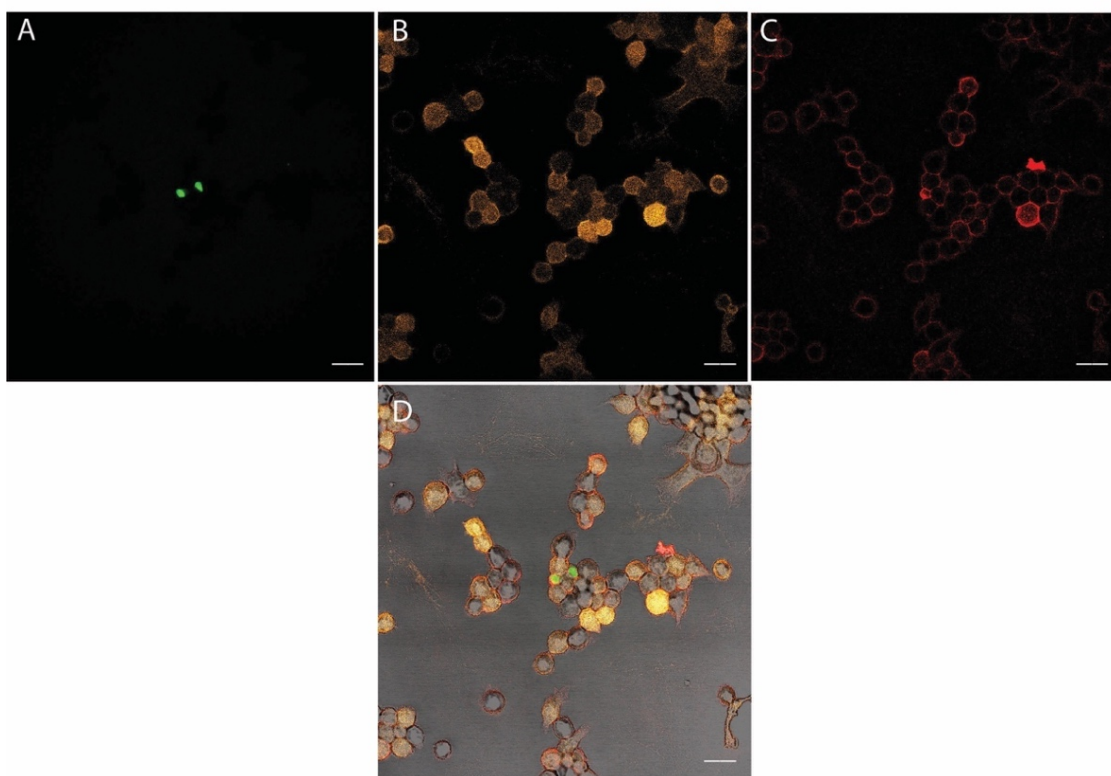


Figure 89. Confocal microscopy of fixed Colo205-D labelled with peracetylated sugar **36** (100  $\mu$ M; 24 hours) and labelled with Tz-PEG<sub>11</sub>-DyLight649 (5  $\mu$ M; 30 min) and SYTOX green (50 nM; 30 min). A) SYTOX<sup>®</sup> green channel (530 nm), B) mStrawberry channel (610 nm), C) DyLight649 channel (660 nm), D) an overlay of all three aforementioned channels. Scale bars = 20  $\mu$ m.

#### 5.4 *In vivo* metabolic labelling of Colo205-D tumours

Female Balb/c nu/nu mice (n = 5) were implanted with Colo205-D cells (~5 million) and tumours were grown for 2 weeks. Mice were dosed by oral gavage with Ac<sub>4</sub>ManNCCp (300 mg/kg) suspension in PBS with 12% DMSO (PBS with 12% DMSO for control mice) for 3 consecutive days. On day 4 mice were injected with Tz-PEG<sub>11</sub>-DyLight649. Mice were sacrificed on day 4 and the fluorescence intensity of the different organs was measured (performed by Dr André Neves). This showed no difference between control and sugar-labelled mice (Figure 90). Thus the *in vivo* experiment failed to replicate the labelling of DMSO dissolved sugar **36** observed *in vitro*. This is most probably due to the fact that **36** was insoluble in PBS (even upon 12% addition of DMSO)

thus it was rather unlikely that it became bioavailable following oral administration. Gavage delivery of sugars was selected in this case as an alternative to intraperitoneal injection. The latter method was extensively used *in vivo* in the past<sup>222,301</sup> to deliver non-natural sugars. However, a previous experiment undertaken by Dr Neves indicated that i.p. delivery of sugar **36** resulted in abdominal non-specific labelling.

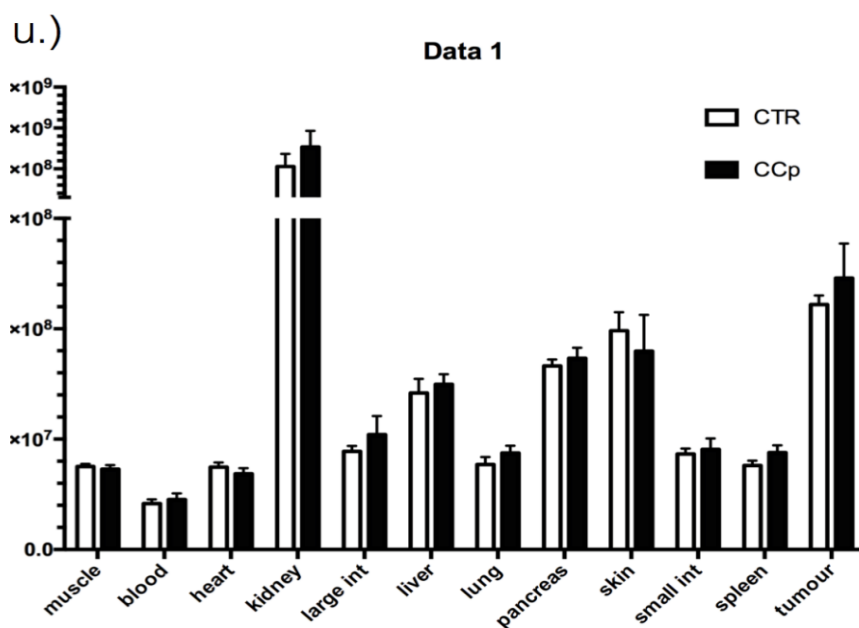


Figure 90. Mean fluorescence intensity of ex-vivo organs showing no contrast between sugar treated mice and controls. (n = 5)

In preparation for *in vivo* delivery for assessing biodistribution and imaging experiments, the **36** was dissolved in PBS (rather than DMSO). The solution became cloudy suggesting that sugar was not fully dissolved. Heating and addition of DMSO up to maximum concentration of 12% (maximum compatible with animal injection) was attempted in order to improve solubility. Using this PBS (with 12% DMSO) dissolution of sugar **36**, *in vitro* flow cytometry labelling was assessed. Upon Tz-PEG<sub>11</sub>-DyLight649 (5  $\mu$ M; 20 min at 37 °C) labelling of cells, a significantly lower SBR of  $3.1 \pm 0.4$  (n = 2) was obtained using the PBS (with 12% DMSO) dissolved sugar **36** compared to the DMSO dissolved one: SBR of  $9.0 \pm 0.2$  (n = 3). (see Figure 91) The poor dissolution is



presumably due to increased hydrophobicity of **36** leading to poor solubility and therefore low incorporation into cells.

#### SBR of sugar formulation in PBS and 12% DMSO

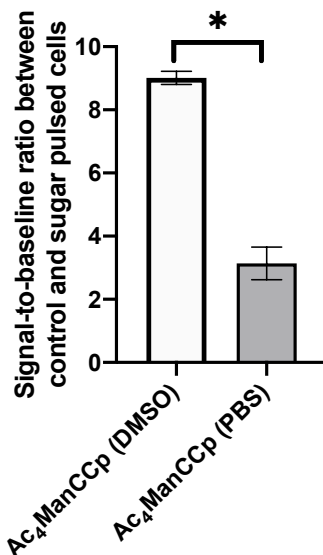


Figure 91. Comparison of SBRs obtained with sugar **36** dissolved in DMSO (n = 3) and sugar **36** dissolved in PBS (n = 2). A significant decrease in SBR was observed upon changing the dissolution solvent. (Two-tailed Welch's t test performed, P = 0.03)

Alternative formulations using 15% polyethylene glycol (PEG-400) in PBS were tested but there was no visible effect on solubility.<sup>328,329</sup> This translated in no sugar-dependent labelling between control and sugar labelled cells upon analysis by flow cytometry. A final attempt at dissolving **36** in PBS was attempted:  $\beta$ -cyclodextrin was added to improve the solubility of peracetylated sugar **36** by entrapping it in its hydrophobic core and therefore increasing its availability for cells to metabolise.  $\beta$ -Cyclodextrin is a cyclic heptasaccharide composed of seven glucopyranose sugars and has been extensively used in formulations for improving solubility.<sup>330,257</sup> Upon using this additive, the SBR dropped from 7 (obtained by dissolving the sugar in 100% DMSO) to 2 when using  $\beta$ -cyclodextrin (25 mg/mL) or 3  $\beta$ -cyclodextrin (125 mg/mL), as shown in Figure 92. One possible explanation is that  $\beta$ -cyclodextrin fails to provide as a reservoir of sugar **36**.

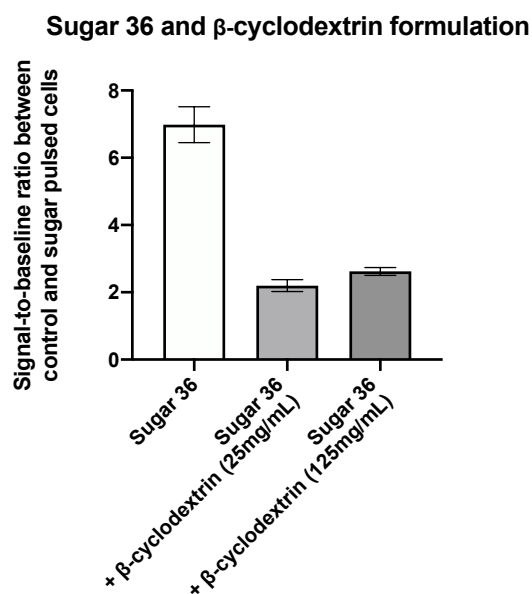


Figure 92. Comparison of SBR upon Colo205-D labelled with sugar **36** (n = 4, in DMSO), sugar **36** +  $\beta$ -cyclodextrin (n = 2, 25 mg/mL in PBS) and sugar **36** +  $\beta$ -cyclodextrin (n = 2, 125 mg/mL in PBS), then treated with Tz-PEG<sub>11</sub>-DyLight649 (5  $\mu$ M) for 1 hour at 37 °C.

## 5.5 Conclusion

Ac<sub>4</sub>ManNCCp **36** is a promising chemical reporter for metabolic labelling of glycans. In this work use, a single tetrazine fluorescent probe Tz-PEG<sub>11</sub>-Dylight649 (5  $\mu$ M) was used *in vitro* to label Colo205-D cells for 1 hour at 37 °C. This was sufficient for achieving a close-to-maximal SBR of 30 between sugar **36** derived cells and control. These results are consistent with findings by Dr Wainman where a similar SBR of 44 was obtained upon metabolic labelling of LL2 Lewis lung carcinoma cells with sugar **36**. However, in that study, the fluorescent tetrazine used to label sugar **36**, required the use of NeutrAvidin-DyLight680 which was incompatible with *in vivo* use due to its immunogenicity. The use of NeutrAvidin-DyLight680 generates better SBR due to the hydrophilic nature of the probe and low non-specific binding to cells.

Despite initial promising results, upon preparation for *in vivo* delivery, it was observed that peracetylated methylcyclopropene-derived mannosamine **36** lacked aqueous solubility. This could be one of the main causes for which this sugar failed to generate contrast in an advanced colorectal tumour *in vivo*. Perhaps this is also the reason

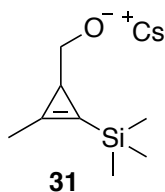
for which none of these peracetylated methylcyclopropene-derived sugars were published *in vivo* publications imaging with these sugars.

Therefore, further improvement of structure-activity relationship (SAR) of sugar **36** was required to improve solubility, bioavailability and potentially facilitate metabolic labelling of glycans. This project was assigned to Shahd Fouad (Master's student). By reducing the degree of acetylation of Ac<sub>4</sub>ManNCCp (mono-, di- and tri- acetylated methylcyclopropene mannosamine) increased aqueous solubility was observed. In her thesis, Shahd showed by flow cytometry that tri-acetylated sugar provided the best SBR (MFI – 13.9±0.9) out of the mono-, di- and tri acetylated sugars upon derivatisation with tetrazine-PEG<sub>11</sub>-AF649 (5 μM) in sugar labelled Colo205-D cells.

## 5.6 Experimental

### 5.6.1 Synthesis of Ac<sub>4</sub>ManNCCp

#### (2-Methyl-3-(trimethylsilyl)cycloprop-2-en-1-yl)methanol (31)



To a suspension of ethynyltrimethylsilane **29** (3.00 mL, 2.274 g, 20.3 mmol) and Rh<sub>2</sub>(OAc)<sub>4</sub> (44 mg, 0.101 mmol, 0.5% mol) in DCM (20 mL) stirred at 0 °C in an inert atmosphere (N<sub>2</sub>), ethyl diazoacetate (1.72 mL (with <15% DCM), 1.62 g, 14.21 mmol, 0.7 eq.) was added dropwise (1 mL/min) with vigorous stirring. The green suspension was warmed to RT and stirred vigorously for 4 hours. The suspension was passed through a silica plug and DCM (20 mL) was used to wash the plug. The fractions collected were combined and concentrated *in vacuo* to approximately 5 mL. The yellow solution containing ethyl ester **30** was added dropwise (0.16 mL/min) to a solution of DIBAL-H (15 mL of a solution 1.0 M in hexanes, 15 mmol, 0.74 eq.) in Et<sub>2</sub>O (30 mL) at 0 °C,

making sure the temperature did not rise above 3 °C. The reaction was monitored by TLC (Hex/EtOAc 9:1,  $R_f$  0.6, potassium permanganate stain) and was stirred until the methylcyclopropene ester **30** was consumed (within 60 min) to yield silyl-protected methylcyclopropene alcohol **31**,  $R_f$ (10:90 EtOAc:Hexanes) 0.3.

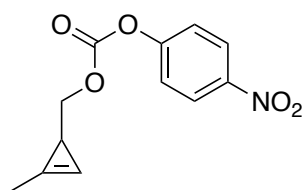
Saturated aqueous Rochelle's salt (10 mL) was then added dropwise, making sure the temperature does not exceed 4 °C. The mixture formed a gel, which was extracted with Et<sub>2</sub>O (3 x 30 mL). The organic layers were combined, washed with brine, dried (MgSO<sub>4</sub>), filtered and concentrated *in vacuo*. The resulting yellow oil was purified by flash column chromatography (eluting with 30% EtOAc in hexanes) to yield **31** (540 mg, 3.45 mmol, 17% over two steps) as a faintly yellow oil. <sup>1</sup>H NMR spectrum was consistent with previously reported data.<sup>320</sup> The <sup>13</sup>C NMR spectrum differed from literature<sup>320</sup> showing one more upfield -CH<sub>2</sub>- adjacent to -O<sup>-</sup>Cs<sup>+</sup> due to Cs shielding (115.5 ppm vs literature 135.9 ppm).

$R_f$ (30:70 EtOAc:Hexanes) 0.51

$\delta_H$  (400 MHz, CDCl<sub>3</sub>): 0.17 (9H, s), 1.56 (1H, t,  $J = 4.6$  Hz), 2.21 (3H, s) 3.47 (2H, d,  $J = 4.6$  Hz)

$\delta_C$  (100 MHz, CDCl<sub>3</sub>): -1.1, 13.4, 22.2, 69.3, 111.3, 115.5.

### (2-Methylcycloprop-2-en-1-yl)methyl (4-nitrophenyl) carbonate (**33**)



**33**

Alcohol **31** (540 mg, 3.46 mmol), 18-crown-6 (1370 mg, 5.19 mmol, 1.5 eq.) and freshly dried anhydrous CsF (784 mg, 5.19 mmol, 1.5 eq) were dissolved in THF (8 mL). The solution was stirred at RT for 12 hours. The reaction was then diluted with DCM (5 mL) and freshly distilled dry pyridine (1.4 mL, 17.3 mmol, 5 eq.) was added. 4-Nitrophenyl chloroformate (1.4 g, 7 mmol, 2 eq.) was added and reaction was monitored

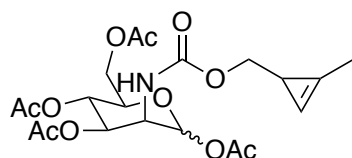
by TLC (30% EtOAc in hexanes, permanganate stain). After 3 hours, the starting material was consumed. The reaction mixture was then diluted with DCM (20 mL), washed with brine (2 x 50 mL), dried (MgSO<sub>4</sub>), gently concentrated in vacuo (>150 mbar) and purified by flash column chromatography (eluting with 10-30% EtOAc in hexanes) to afford the carbonate 33 as a white crystalline solid (162 mg, 0.65 mmol, 19% over two steps). NMR spectra were in accordance to literature.<sup>318</sup>

R<sub>f</sub> (30:70 EtOAc:Hexanes) 0.74

$\delta_H$  (400 MHz, CDCl<sub>3</sub>): 1.71 (1H, dt, J = 5.36, 1.4 Hz), 2.17 (3H, d, J = 0.9 Hz) 4.14 (1H, dd, J = 11.1, 5.5 Hz), 4.21 (1H, dd, J = 11.1, 5.2 Hz, 1H), 6.61 (1H, s), 7.39 (2H, d, J = 9.2 Hz), 8.28 (2H, d, J = 9.2 Hz)

$\delta_C$  (100 MHz, CDCl<sub>3</sub>): 11.7, 16.6, 77.4, 101.7, 120.2, 121.8, 125.3, 145.3, 152.7, 155.8

***N*-(((2-Methylcycloprop-2-en-1-yl)methoxy)carbonyl)mannosamine tetraacetate (36) Ac<sub>4</sub>ManNCCp**



**36**  
**Ac<sub>4</sub>ManNCCp**

Mannosamine HCl salt (75 mg, 0.35 mmol) was dissolved in DMF (0.5 mL) and *N,N*-diisopropylethylamine (226  $\mu$ L, 1.3 mmol, 3.7 eq.) at 60 °C for 30 minutes. The solution was cooled to RT and a solution of carbonate 33 (162 mg, 0.65 mmol, 1.85 eq.) in dry DMF (5 mL) was added. The reaction was monitored by TLC (10:90 MeOH:DCM, permanganate stain) and upon completion (12 hours) pyridine (282.5  $\mu$ L, 3.5 mmol, 10 eq.) and Ac<sub>2</sub>O (330.5  $\mu$ L, 3.5 mmol, 10 eq.) were added. The reaction was stirred for a further 12 hours and then solvent was removed *in vacuo*. The resulting yellow oil was adsorbed on silica gel and purified by flash column chromatography (10:90 MeOH:DCM) to yield Ac<sub>4</sub>ManNCCp 36 (120 mg, 0.26 mmol, 75% after 2 steps) as a white powder. <sup>1</sup>H

NMR spectra were in accordance to literature<sup>321</sup> however some peaks at 4.11 ppm were not fully resolved due to solvent residue covering some peaks.

$R_f$  (10:90 MeOH:DCM) 0.25

$\delta_H$  (400 MHz,  $CDCl_3$ ): (mixture of anomers 2:1  $\alpha$ : $\beta$ )

( $\alpha$  anomer) 1.66 (1H, m), 2.02 (3H, s), 2.04 (3H, s), 2.14 (3H, s), 2.17 (3H, s), 3.95 (2H, t,  $J = 5.1$  Hz), 4.02 (1H, m) 4.26 (1H, dd,  $J = 12.3, 4.3$  Hz), 4.34 (1H, dd,  $J = 8.7, 3.8$  Hz), 5.02 (1H, d,  $J = 4.2$  Hz), 5.20 (1H, t,  $J = 9.9$  Hz), 5.31 (1H, dd,  $J = 10.2, 4.2$  Hz), 6.08 (1H, s), 6.58 (1H, d,  $J = 4.8$  Hz)

( $\beta$  anomer) 1.66 (1H, m), 2.03 (3H, s), 2.05 (3H, s), 2.08 (3H, s), 2.11(3H, s), 2.14 (3H, s), 3.78 (1H, ddd,  $J = 9.6, 5.05, 2.58$ ), 4.02 (1H, m), 4.05-4.08 (m, 2H) 4.26 (1H, dd,  $J = 12.3, 4.3$  Hz), 4.47 (1H, d,  $J = 8.7$ ), 5.02-5.04 (1H, m), 5.10 (1H, s) 5.16 (1H, t,  $J = 9.9$  Hz), 5.84 (1H, s), 6.58 (1H, d,  $J = 4.8$  Hz)

### 5.6.2 Metabolic labelling of Colo205-D with $Ac_4ManNCCp$ and Tz-PEG<sub>11</sub>-DyLight 649 derivatization for flow cytometry analysis

Stock solutions used:

Three peracetylated methylcyclopropene sugar solutions:

1.  $Ac_4ManNCCp$  (110 mM in 100% DMSO) was used for feeding cells for *in vitro* analysis of the sugar probe;
  2.  $Ac_4ManNCCp$  (25 mM in PBS (11.4 mg/mL) with 25 mg/mL  $\beta$ -cyclodextrin);
  3.  $Ac_4ManNCCp$  (16 mM in PBS (7.3 mg/mL) with 120 mg/mL  $\beta$ -cyclodextrin);
- Tz-PEG<sub>11</sub>-DyLight 649 (50  $\mu$ M in PBS) synthesised by Henning Stöckmann, former member of the Leeper lab;
- SYTOX<sup>®</sup> green (30  $\mu$ M in DMSO, Invitrogen cat. no. SKU#S7020)

Derivatisation solution: Tz-DyLight 647 (150  $\mu$ L, 50  $\mu$ M in PBS) diluted 10-fold in FACS buffer (1347.5  $\mu$ L) with SYTOX<sup>®</sup> green (2.5  $\mu$ L, 30  $\mu$ M in DMSO) to generate a working solution Tz-dylight647/SYTOX<sup>®</sup> (5  $\mu$ M/50nM in PBS) sufficient for labelling 15 samples.

### **i. Colo205-D cell seeding and culture**

Colo205-D cells were seeded into Nunc Cell-culture treated 6-well culture dishes, at a density of  $4 \times 10^4$  viable cells/cm<sup>2</sup> ( $\sim 4 \times 10^5$  cells per well). A volume of 2 ml of RPMI-1640 tissue culture medium (with added 10% heat inactivated FBS) was used per well. The area of a single well is 9.6 cm<sup>2</sup>. Cells were allowed to settle on the plate for 16 hours.

### **ii. Cell labelling with Ac<sub>4</sub>ManNCCp**

Ac<sub>4</sub>ManNCCp (11 μL, 110 mM in 100% DMSO) was diluted 10-fold in DMSO (99 μL). Each well (2 mL) was treated with Ac<sub>4</sub>ManNCCp (18.2 μL, 11 mM) to generate a concentration of 100 μM or with DMSO (18.2 μL) for the control cells. Cells were incubated for 24 hours in a 5% CO<sub>2</sub> incubator at 37 °C.

### **iii. Ac<sub>4</sub>ManNCCp derivatisation with Tz-PEG<sub>11</sub>-DyLight649 for flow cytometry**

Colo205-D cells treated with Ac<sub>4</sub>ManNCCp were treated with Gibco 0.25% Trypsin- 1 mM EDTA (0.5 mL) per well and returned to the incubator for 3 minutes to facilitate dissociation from vessel. Cells were then transferred to Eppendorf tubes, washed with FACS buffer (1 mL, PBS containing 1% foetal bovine serum), then reacted with the derivatisation solution (100 μL) containing Tz-PEG<sub>11</sub>-DyLight649 (5 μM) and SYTOX<sup>®</sup> green (50 nM) in FACS buffer for 20 min at 37 °C with shaking at 600 rpm. Cells were pelleted (800 G), washed with FACS buffer (1000 μL) and the process was repeated 3 times. Cells were then set on ice to be analysed by flow cytometry on an LSRII flow cytometer (BD Biosciences). For each sample 10,000 data points were acquired. Cells were analysed in triplicate. Fluorescence emitted by Tz-PEG<sub>11</sub>-DyLight 649 and SYTOX<sup>®</sup> green was analysed using FlowJo software.

Flow cytometer filters used (nm) and their associated photomultiplier voltages: forward scatter – 350V; side scatter – 352V; SYTOX<sup>®</sup> green blue 530nm/30 channel – 400V; mStrawberry blue 610nm/20 channel – 489V; Tz-PEG<sub>11</sub>-DyLight649 red 660nm/20 channel – 500V; NADH UV 450nm/50 channel – 500V; laser/wavelengths used: UV - 355 nm; argon ion laser - 488 nm; violet diode laser - 406 nm; red laser - 633 nm.

**iv. Confocal microscopy imaging**

Colo205-D cells incubated for 24h with Ac<sub>4</sub>ManNCCp (100 μM) were seeded in an ibidi cell culture pot at concentration of  $\sim 5 \times 10^5$  cells/cm<sup>2</sup> and allowed to adhere to the plate surface for 2h. Growth media was washed away with PBS (1 mL) and cells were treated with Tz-PEG<sub>11</sub>-DyLight649 (5 μM) and SYTOX<sup>®</sup> green (50 nM) in FACS buffer (500 μL) and incubated at 37 °C for 20 minutes. Cells were washed with cold FACS buffer (3 x 1 mL) and then fixed with PBS (1 mL) containing 4% formalin at RT for 15 min. Then cells were washed with PBS (3 x 1 mL) and ethanol (1 mL) to dry the slide. The slide was imaged on a Leica TCS SP5 Confocal Microscope (63x objective with oil).



# 6 CONTRIBUTIONS AND FUTURE WORK

## 6.1 Imaging cell death using C2A protein

This work was set out to design and synthesise a PET imaging agent to be used for detecting tumour cell death *in vivo* in response to therapy.

An automated radiosynthesis of 2-[<sup>18</sup>F]fluoroethylazide and labelling of a C2Am-DBCO by SPAAC was achieved however the yield was too low to be used for PET imaging.

A more efficient labelling method, using Michael-addition, an *N*-(5-[<sup>18</sup>F]fluoropentyl)maleimide functional group ([<sup>18</sup>F]FPenM) was successfully conjugated to a free thiol C2Am for the first time. An automated synthesis was developed to produce this fluorine-18 maleimide functional group within a shorter time (58±5.8 min) compared to other maleimides in the literature<sup>209,210</sup>, in a moderate yield (12±3%) and with a high molar radioactivity 212000±30000 MBq/μmol (n = 3). Its speed of conjugation to thiols, determined in this study by reaction with glutathione, was determined to be sufficiently fast for the synthesis of PET imaging agents. FPenM hydrolysis rate was determined to be slow (30±2.2 hours), showing good stability in aqueous media (PBS) thus allowing for conjugation of proteins for an extended period of time. Finally, [<sup>18</sup>F]FPenM was successfully used for conjugation of C2Am protein for the first time, yielding a cell death radiotracer with a high molar activity suitable for *in vivo* PET imaging studies.

[<sup>18</sup>F]FPenM-C2Am was successfully used *in vitro* to detect tumour cell death following treatment with a TRAIL-R2 agonist in two cancer models: a triple negative breast cancer and an advanced colorectal carcinoma.

Biodistribution and PET imaging studies were successfully carried out using [<sup>18</sup>F]FPenM-C2Am in murine xenograft of advanced colorectal cancer using the same

TRAIL-R2 agonist (MEDI3039) for inducing cell death. Cell death was validated by histology using cleaved caspase-3 (CC3) and terminal deoxynucleotidyl transferase dUTP nick end labelling (TUNEL) and were positively correlated with PET imaging tumour uptake values.

Given the favourable biodistribution profile of [<sup>18</sup>F]FPenM-C2Am, and its ability to produce rapid and cell death-specific image contrast, this agent has potential for clinical translation. We have initiated GMP manufacture and toxicology studies required for a Phase 1 trial.

Future work using the [<sup>18</sup>F]FPenM-C2Am will consist of analysing the % increase in probe uptake between pre- and post-treatment and correlation with histological staining with CC3 and TUNEL in a murine breast cancer xenograft model (MDA-MB-231 cells).

Further experiments are planned to extend the scope of [<sup>18</sup>F]FPenM-C2Am radiotracer by varying the cancer type (triple negative breast cancer) and treatment: chemotherapy (5-fluorouracil, doxorubicin) and radiotherapy. In addition, experiments using an inactive version of the C2Am protein (iC2Am) will be used as a better control for imaging cell death post treatment. This will help detect excretion pathways and any non-specific binding.

## 6.2 Imaging tumour glycans in an advanced colorectal cancer using Ac<sub>4</sub>ManNCCp

First, a methylocyclopropene derived sugar (Ac<sub>4</sub>ManNCCp) was synthesised and used *in vitro* to demonstrate glycan sialylation for the first time in Colo205-D cancer cells. This bioorthogonal labelling of glycans used a biocompatible fluorogenic tetrazine which upon flow cytometry analysis showed an excellent SBR of 30. Previous publications that used flow cytometry to study glycan labelling used biotin-streptavidin/avidin/NeutrAvidin labelling methods which generate superior SBRs but are incompatible with *in vivo* testing due to immunogenicity concerns.<sup>318,321</sup>

Labelling glycans using Ac<sub>4</sub>ManNCCp using the biocompatible Tz-PEG<sub>11</sub>-Dylight649 was attempted for the first time in a murine advanced colorectal xenograft model however it failed to generate contrast. Despite the successful *in vitro* detection of glycans, *in vivo* labelling was impossible due in part to poor solubility of Ac<sub>4</sub>ManNCCp in aqueous media. As of 2019, there is no evidence in literature for the use of methylcyclopropene sugars (Ac<sub>4</sub>ManNCCp) for *in vivo* metabolic labelling of glycans and we suspect it's due to their poor solubilities.

Following our Masters' student (Shahd Fouad) successful improvement of the solubility of Ac<sub>4</sub>ManNCCp by using a tri-acetylated equivalent, the project has now been assigned to Daniel Parle (PhD student in the Leeper lab) to investigate the effect on metabolic labelling of glycans using mono- di- and triacetylated sugars.

Dual sugar labelling of glycans *in vivo* using azide and methylcyclopropane derived sugars is the ultimate goal as this can enable better profiling of glycans in cancer cells. "Finger-printing" glycans using non-natural sugars could help to better understand carcinogenesis, invasion and predict prognosis of cancer following therapy.<sup>332</sup>

As of 2019, methylcyclopropene continues to be a highly desirable chemical handle for labelling glycans. The fast nature of the bioorthogonal reaction between a methylcyclopropene and a 3,6-disubstituted-1,2,4,5-tetrazine enables quick *in vivo* labelling reactions. Therefore, an <sup>18</sup>F-labelled tetrazine could be used for the first time to image metabolically labelled glycans by PET.

## 7 REFERENCES

1. Hoglund, J., Shirvan, A., Antoni, G., Gustavsson, S.A., Langstrom, B., Ringheim, A., Sorensen, J., Ben-Ami, M. & Ziv, I.  $^{18}\text{F}$ -ML-10, a PET Tracer for Apoptosis: First Human Study. *J. Nucl. Med.* **52**, 720–725 (2011).
2. Cancer incidence for all cancers combined Cancer Research UK. [<https://www.cancerresearchuk.org/health-professional/cancer-statistics/incidence/all-cancers-combined>, accessed 2<sup>nd</sup> January 2019]
3. Brindle, K. M. New approaches for imaging tumour responses to treatment. *Nat. Rev. Cancer* **8**, 94–107 (2008).
4. Cancer Research UK. Cancer incidence statistics in the UK. [<https://www.cancerresearchuk.org/health-professional/cancer-statistics-for-the-uk#:~:text=Cancer%20incidence,new%20cancer%20cases%20in%202017.> Report accessed 2<sup>nd</sup> January 2019].
5. Office for National Statistics UK. Cancer survival rates, Cancer survival in England, patients diagnosed 1993-1995 and followed up to 2000. Office for National Statistics UK **7**, (2002).
6. Solomon, T., Rachet, B., Drummond, R., Rowlands, S., Brown, P., Bannister, N., Gordon, E. & Coleman, M. P. *Statistical Bulletin Cancer Survival in England: Patients Diagnosed 2007 – 2011 and Followed up to 2012.* **2013**, (2013).
7. Breast cancer statistics | Cancer Research UK. [<https://www.cancerresearchuk.org/health-professional/cancer-statistics/statistics-by-cancer-type/breast-cancer#heading-Four>, accessed 3<sup>rd</sup> January 2019]

8. Bowel cancer statistics | Cancer Research UK. [<https://www.cancerresearchuk.org/health-professional/cancer-statistics/statistics-by-cancer-type/bowel-cancer#heading-Four>, accessed 3<sup>rd</sup> January 2019]
9. Prostate cancer survival statistics | Cancer Research UK. (2019). [<https://www.cancerresearchuk.org/health-professional/cancer-statistics/statistics-by-cancer-type/prostate-cancer/survival#heading-Zero>, accessed 3<sup>rd</sup> January 2019]
10. Prostate cancer - Should I have a PSA test? – NHS. [<https://www.nhs.uk/conditions/prostate-cancer/should-i-have-psa-test/>, accessed 3<sup>rd</sup> January 2019]
11. Kinch, M. S. An analysis of FDA-approved drugs for oncology. *Drug Discov. Today* **19**, 1831–1835 (2015).
12. Monoclonal Antibodies Approved by the EMA and FDA for Therapeutic Use – ACTIP. [<http://www.actip.org/products/monoclonal-antibodies-approved-by-the-ema-and-fda-for-therapeutic-use/>, accessed 10<sup>th</sup> January 2019]
13. Hudis, C. A. Trastuzumab – Mechanism of Action and Use in Clinical Practice. *N. Engl. J. Med.* **357**, 39–51 (2007).
14. Ellis, L. M. Mechanisms of Action of Bevacizumab as a Component of Therapy for Metastatic Colorectal Cancer. *Semin. Oncol.* **33**, S1–S7 (2006).
15. Mukherji, S. K. Bevacizumab (Avastatin). *Am. J. Neuroradiol.* **31**, 235–236 (2010).
16. Faivre, S., Demetri, G., Sargent, W. & Raymond, E. Molecular basis for sunitinib efficacy and future clinical development. *Nat. Publ. Gr.* **6**, 734–745 (2007).
17. Greer, Y. E., Gilbert, S. F., Gril, B., Narwal, R., Peacock Brooks, D. L., Tice, D. A., Steeg, P. S. & Lipkowitz, S. MEDI3039, a novel highly potent tumor necrosis factor (TNF)-related apoptosis-inducing ligand (TRAIL) receptor 2 agonist, causes regression of orthotopic tumors and inhibits outgrowth of metastatic triple-negative breast cancer 11 Medical and Health Scien. *Breast Cancer Res.* **21**, 1–17 (2019).

18. Csőszi, T., Fülöp, A., Gottfried, M., Peled, N., Tafreshi, A., Cuffe, S., Brien, M. O., Rao, S., Hotta, K., Leiby, M. A., Lubiniecki, G. M., Shentu, Y., Rangwala, R. & Brahmer, J. R. Pembrolizumab versus Chemotherapy for PD-L1–Positive Non-Small Cell Lung Cancer. *N. Engl. J. Med.* **375**, 1823–1833 (2016).
19. Arance, A., Grob, J. J., Mortier, L., Lotem, M., Larkin, J., Lorigan, P., Neyns, B., Blank, C. U., Hamid, O., Mateus, C., Shapira-frommer, R., Kosh, M., Zhou, H., Ibrahim, N. & Ebbinghaus, S. Pembrolizumab versus Ipilimumab in Advanced Melanoma. *N. Engl. J. Med.* **372**, 2521–2532 (2015).
20. Markham, A. Atezolizumab : First Global Approval. *Drugs* **76**, 1227–1232 (2016).
21. Bensch, F., van der Veen, E. L., Lub-de Hooge, M. N., Jorritsma-Smit, A., Boellaard, R., Kok, I. C., Oosting, S. F., Schröder, C. P., Hiltermann, T. J. N., van der Wekken, A. J., Groen, H. J. M., Kwee, T. C., Elias, S. G., Gietema, J. A., Bohorquez, S. S., de Crespigny, A., Williams, S. P., Mancao, C., Brouwers, A. H., Fine, B. M. & de Vries, E. G. E. <sup>89</sup>Zr-Atezolizumab imaging as a non-invasive approach to assess clinical response to PD-L1 blockade in cancer. *Nat. Med.* **24**, 1852–1858 (2018).
22. Evolution of Cancer Treatments: Targeted therapy. [<https://www.cancer.org/cancer/cancer-basics/history-of-cancer/cancer-treatment-targeted-therapy.html> accessed 12<sup>th</sup> March 2019]
23. Evolution of Cancer Treatments: Immunotherapy. [<https://www.cancer.org/cancer/cancer-basics/history-of-cancer/cancer-treatment-immunotherapy.html>. accessed 12<sup>th</sup> March 2019]
24. Ellis, L. M. & Hicklin, D. J. Resistance to targeted therapies: Refining anticancer therapy in the era of molecular oncology. *Clin. Cancer Res.* **15**, 7471–7478 (2009).
25. FDA Approved Drugs in Oncology - CenterWatch. [<https://www.centerwatch.com/drug-information/fda-approved-drugs/therapeutic-area/12/>, accessed 10<sup>th</sup> January 2019]

26. Research, C. for D. E. and. Approved Drugs - Hematology/Oncology (Cancer) Approvals & Safety Notifications. [<https://www.fda.gov/drugs/informationondrugs/approveddrugs/ucm279174.htm>, accessed 10<sup>th</sup> January 2019]
27. Balog, J., Sasi-Szabó, L., Kinross, J., Lewis, M. R., Muirhead, L. J., Veselkov, K., Mirnezami, R., Dezsó, B., Damjanovich, L., Darzi, A., Nicholson, J. K. & Takáts, Z. Intraoperative Tissue Identification Using Rapid Evaporative Ionization Mass Spectrometry. *Sci. Transl. Med.* **5**, (194) 1–11 (2013).
28. History of cancer. [<https://www.cancer.org/cancer/cancer-basics/history-of-cancer/cancer-treatment-radiation.html>, accessed 18<sup>th</sup> December 2018]
29. Cherry, S. R., Jones, T., Karp, J. S., Qi, J., Moses, W. W. & Badawi, R. D. Total-Body PET: Maximizing Sensitivity to Create New Opportunities for Clinical Research and Patient Care. *J. Nucl. Med.* **59**, 3–12 (2017).
30. Cancer mortality statistics. Cancer Research UK. [<https://www.cancerresearchuk.org/health-professional/cancer-statistics/mortality#heading-Zero> accessed 19<sup>th</sup> December 2018]
31. Cancer Statistics for the UK. [<https://www.cancerresearchuk.org/health-professional/cancer-statistics-for-the-uk#heading-One> accessed 19<sup>th</sup> December 2018]
32. Galluzzi, L., Vitale, I., Vacchelli, E. & Kroemer, G. Cell death signaling and anticancer therapy. *Front. Oncol.* **1**, (5) 1–18 (2011).
33. Diaz, L. A. & Bardelli, A. Liquid biopsies: Genotyping circulating tumor DNA. *J. Clin. Oncol.* **32**, 579–586 (2014).
34. Alix-Panabieres, C. & Pantel, K. Circulating tumor cells: Liquid biopsy of cancer. *Clin. Chem.* **59**, 110–118 (2013).
35. Bedard, P. L., Hansen, A. R., Ratain, M. J. & Siu, L. L. Tumour heterogeneity in the clinic. *Nature* **501**, 355–364 (2013).

36. Visvader, J. E. & Lindeman, G. J. Cancer stem cells in solid tumours: Accumulating evidence and unresolved questions. *Nat. Rev. Cancer* **8**, 755–768 (2008).
37. Salem, A., Asselin, M. C., Reymen, B., Jackson, A., Lambin, P., West, C. M. L., O'Connor, J. P. B. & Faivre-Finn, C. Targeting Hypoxia to Improve Non-Small Cell Lung Cancer Outcome. *JNCI J. Natl. Cancer Inst.* **110**, 14–30 (2018).
38. Eisenhauer, E. A., Therasse, P., Bogaerts, J., Schwartz, L. H., Sargent, D., Ford, R., Dancey, J., Arbuck, S., Gwyther, S., Mooney, M., Rubinstein, L., Shankar, L., Dodd, L., Kaplan, R., Lacombe, D. & Verweij, J. New response evaluation criteria in solid tumours: Revised RECIST guideline (version 1.1). *Eur. J. Cancer* **45**, 228–247 (2009).
39. Ollivier, L., Padhani, A. R. & Leclère, J. International criteria for measurement of tumour response. *Cancer Imaging* **2**, 31–32 (2001).
40. Organization, W. H. WHO handbook for reporting results of cancer treatment. (1979).
41. Miller, A. B., Hoogstraten, B., Staquet, M. & Winkler, A. Reporting results of cancer treatment. *Cancer* **47**, 207–214 (1981).
42. Duffaud, F. & Therasse, P. New guidelines to evaluate the response to treatment in solid tumors. *Bull. Cancer* **87**, 881–886 (2000).
43. Weber, W. A. Assessing tumor response to therapy. *J. Nucl. Med.* **50 Suppl 1**, 1S-10S (2009).
44. Linhares, P., Carvalho, B., Figueiredo, R., Reis, R. M. & Vaz, R. Early pseudoprogression following chemoradiotherapy in glioblastoma patients: The value of RANO evaluation. *J. Oncol.* **2013**, 9 (2013).
45. Sheikhabaei, S., Mena, E., Yanamadala, A., Reddy, S., Solnes, L. B., Wachsmann, J. & Subramaniam, R. M. The value of FDG PET/CT in treatment response assessment, follow-up, and surveillance of lung cancer. *Am. J. Roentgenol.* **208**, 420–433 (2017).



46. Johnson, B. E. & Mcloud, T. C. State of the Art : Response Assessment in Lung Cancer in the. *Radiology* **271**, (2014).
47. Gill, R., Matsusoka, S. & Hatabu, H. Cavities in the Lung in Oncology Patients: Imaging Overview and Differential Diagnoses. *Appl. Radiol.* (2010). [<https://appliedradiology.com/articles/cavities-in-the-lung-in-oncology-patients-imaging-overview-and-differential-diagnoses> accessed 20<sup>th</sup> June 2019]
48. Delbeke, D., Coleman, R. E., Guiberteau, M. J., Brown, M. L., Royal, H. D., Siegel, B. A., Townsend, D. W., Berland, L. L., Parker, J. A., Hubner, K., Stabin, M. G., Zubal, G., Kachelriess, M., Cronin, V. & Holbrook, S. Procedure guideline for tumor imaging with [<sup>18</sup>F]FDG PET/CT 1.0. *J. Nucl. Med.* **47**, 885–895 (2006).
49. Gatenby, R. A. & Gillies, R. J. Why do cancers have high aerobic glycolysis? *Nat. Rev. Cancer* **4**, 891–899 (2004).
50. Wahl, R. L., Jacene, H., Kasamon, Y. & Lodge, M. A. From RECIST to PERCIST: Evolving Considerations for PET Response Criteria in Solid Tumours. *J. Nucl. Med.* **50**, 1–50 (2009).
51. Kostakoglu, L., Agress, H. & Goldsmith, S. J. Clinical role of FDG PET in evaluation of cancer patients. *Radiographics* **23**, 315–340 (2003).
52. Stroobants, S., Goeminne, J., Seegers, M., Dimitrijevic, S., Dupont, P., Nuyts, J., Martens, M., Van den Borne, B., Cole, P. & Sciot, R. <sup>18</sup>F-FDG-positron emission tomography for the early prediction of response in advanced soft tissue sarcoma treated with imatinib mesylate (Glivec®). *Eur. J. Cancer* **39**, 2012–2020 (2003).
53. Mayerhoefer, M. E., Raderer, M., Jaeger, U., Staber, P., Kiesewetter, B., Senn, D., Gallagher, F. A., Brindle, K., Porpaczy, E., Weber, M., Berzaczy, D., Simonitsch-Klupp, I., Sillaber, C., Skrabs, C. & Haug, A. Ultra-early response assessment in lymphoma treatment: [<sup>18</sup>F]FDG PET/MR captures changes in glucose metabolism and cell density within the first 72 hours of treatment. *Eur. J. Nucl. Med. Mol. Imaging* **45**, 931–940 (2018).

54. Langen, K. J., Hamacher, K., Weckesser, M., Floeth, F., Stoffels, G., Bauer, D., Coenen, H. H. & Pauleit, D. O-(2-[<sup>18</sup>F]fluoroethyl)-L-Tyrosine: uptake mechanisms and clinical applications. *Nucl. Med. Biol.* **33**, 287–294 (2006).
55. Pauleit, D., Stoffels, G., Bachofner, A., Floeth, F. W., Sabel, M., Herzog, H., Tellmann, L., Jansen, P., Reifenberger, G., Hamacher, K., Coenen, H. H. & Langen, K. J. Comparison of <sup>18</sup>F-FET and <sup>18</sup>F-FDG PET in brain tumors. *Nucl. Med. Biol.* **36**, 779–787 (2009).
56. Pöpperl, G., Kreth, F. W., Herms, J., Koch, W., Mehrkens, J. H., Gildehaus, F. J., Kretschmar, H. A., Tonn, J. C. & Tatsch, K. Analysis of <sup>18</sup>F-FET PET for grading of recurrent gliomas: Is evaluation of uptake kinetics superior to standard methods? *J. Nucl. Med.* **47**, 393–403 (2006).
57. Niu, G. & Chen, X. PET Imaging of Angiogenesis. *PET Clin.* **4**, 17–38 (2009).
58. Beer, A. J., Haubner, R., Wolf, I., Goebel, M., Luderschmidt, S., Niemeyer, M., Grosu, A. L., Martinez, M. J., Wester, H. J., Weber, W. A. & Schwaiger, M. PET-based human dosimetry of <sup>18</sup>F-Galacto-RGD, a new radiotracer for imaging  $\alpha_v\beta_3$  expression. *J. Nucl. Med.* **47**, 763–769 (2006).
59. Beer, A. J., Niemeyer, M., Carlsen, J., Sarbia, M., Nāhrig, J., Watzlowik, P., Wester, H. J., Harbeck, N. & Schwaiger, M. Patterns of  $\alpha_v\beta_3$  expression in primary and metastatic human breast cancer as shown by <sup>18</sup>F-Galacto-RGD PET. *J. Nucl. Med.* **49**, 255–259 (2008).
60. Ono, M., Oka, S., Okudaira, H., Nakanishi, T., Mizokami, A., Kobayashi, M., Schuster, D. M., Goodman, M. M., Shirakami, Y. & Kawai, K. [<sup>14</sup>C]Fluciclovine (alias anti-[<sup>14</sup>C]FACBC) uptake and ASCT2 expression in castration-resistant prostate cancer cells. *Nucl. Med. Biol.* **42**, 887–892 (2015).
61. Sakata, T., Ferdous, G., Tsuruta, T., Satoh, T., Baba, S., Muto, T., Ueno, A., Kanai, Y., Endou, H. & Okayasu, I. L-type amino-acid transporter 1 as a novel biomarker for high-grade malignancy in prostate cancer. *Pathol. Int.* **59**, 7–18 (2009).

62. Gusman, M., Aminsharifi, J. A., Peacock, J. G., Anderson, S. B., Clemenshaw, M. N. & Banks, K. P. Review of  $^{18}\text{F}$ -Fluciclovine PET for Detection of Recurrent Prostate Cancer. *Radiographics* **39**, 822–841 (2019).
63. Barthel, H., Cleij, M. C., Collingridge, D. R., Hutchinson, O. C., Osman, S., He, Q., Luthra, S. K., Brady, F., Price, P. M. & Aboagye, E. O. 3'-Deoxy-3'-[ $^{18}\text{F}$ ]fluorothymidine as a new marker for monitoring tumor response to antiproliferative therapy in vivo with positron emission tomography. *Cancer Res.* **63**, 3791–3798 (2003).
64. Grierson, J. R., Schwartz, J. L., Muzi, M., Jordan, R. & Krohn, K. A. Metabolism of 3'-deoxy-3'-[ $^{18}\text{F}$ ]fluorothymidine in proliferating A549 cells: Validations for positron emission tomography. *Nucl. Med. Biol.* **31**, 829–837 (2004).
65. Chen, W., Delaloye, S., Silverman, D. H. S., Geist, C., Czernin, J., Sayre, J., Satyamurthy, N., Pope, W., Lai, A., Phelps, M. E. & Cloughesy, T. Predicting treatment response of malignant gliomas to bevacizumab and irinotecan by imaging proliferation with [ $^{18}\text{F}$ ]fluorothymidine positron emission tomography: A pilot study. *J. Clin. Oncol.* **25**, 4714–4721 (2007).
66. Sharma, R., Mapelli, P., Hanna, G. B., Goldin, R., Power, D., Al-Nahhas, A., Merchant, S., Ramaswami, R., Challapalli, A., Barwick, T. & Aboagye, E. O. Evaluation of  $^{18}\text{F}$ -fluorothymidine positron emission tomography ([ $^{18}\text{F}$ ]FLT-PET/CT) methodology in assessing early response to chemotherapy in patients with gastro-oesophageal cancer. *EJNMMI Res.* **6(81)**, 1–9 (2016).
67. Peck, M., Pollack, H. A., Friesen, A., Muzi, M., Shoner, S. C., Shankland, E. G., Fink, J. R., Armstrong, J. O., Link, J. M. & Krohn, K. A. Applications of PET imaging with the proliferation marker  $^{18}\text{F}$ -FLT. *J Nucl Med Mol Imaging* **59**, 95–104 (2015).
68. Masaki, Y., Shimizu, Y., Yoshioka, T., Tanaka, Y., Nishijima, K. I., Zhao, S., Higashino, K., Sakamoto, S., Numata, Y., Yamaguchi, Y., Tamaki, N. & Kuge, Y. The accumulation mechanism of the hypoxia imaging probe 'FMISO' by imaging mass spectrometry: Possible involvement of low-molecular metabolites. *Sci. Rep.* **5**, 1–9 (2015).

69. Savi, A., Incerti, E., Fallanca, F., BettinarDi, V., Rossetti, F., Monterisi, C., Compierchio, A., Negri, G., Zannini, P., Gianolli, L. & Picchio, M. First evaluation of PET-based human bioDistribution and dosimetry of  $^{18}\text{F}$ -FAZA, a tracer for imaging tumor hypoxia. *J. Nucl. Med.* **58**, 1224–1229 (2017).
70. Eschmann, S., Paulsen, F., Reimold, M., Dittmann, H., Welz, S., Reischl, G., Machulla, H. & Bares, R. Prognostic Impact of Hypoxia Imaging with Before Radiotherapy. *Radiochemistry* **46**, 253–260 (2005).
71. Thorwarth, D., Eschmann, S. M., Holzner, F., Paulsen, F. & Alber, M. Combined uptake of [ $^{18}\text{F}$ ]FDG and [ $^{18}\text{F}$ ]FMISO correlates with radiation therapy outcome in head-and-neck cancer patients. *Radiother. Oncol.* **80**, 151–156 (2006).
72. Lee, S. T. & Scott, A. M. Hypoxia Positron Emission Tomography Imaging With [ $^{18}\text{F}$ ]Fluoromisonidazole. *Semin. Nucl. Med.* **37**, 451–461 (2007).
73. Halmos, G. B., De Bruin, L. B., Langendijk, J. A., Van Der Laan, B. F. A. M., Pruijm, J. & Steenbakkers, R. J. H. M. Head and neck tumor hypoxia imaging by [ $^{18}\text{F}$ ]fluoroazomycin-arabino-side  $^{18}\text{F}$ -FAZA-PET: A review. *Clin. Nucl. Med.* **39**, 44–48 (2014).
74. Jadvar, H., Desai, B. & Conti, P. S. Sodium  $^{18}\text{F}$ -Fluoride PET/CT of Bone, Joint and Other Disorders. *Semin. Nucl. Med.* **45**, 58–65 (2015).
75. Hara, T., Kosaka, N., Shinoura, N. & Kondo, T. PET Imaging of Brain Tumor with methyl- $^{11}\text{C}$ Choline. *J Nucl Med* **38**, 842–847 (1997).
76. Song, W. S., Nielson, B. R., Banks, K. P. & Bradley, Y. C. Normal organ standard uptake values in carbon-11 acetate PET imaging. *Nucl. Med. Commun.* **30**, 462–465 (2009).
77. Ito, K., Matsuda, H. & Kubota, K. Imaging spectrum and pitfalls of  $^{11}\text{C}$ -methionine positron emission tomography in a series of patients with intracranial lesions. *Korean J. Radiol.* **17**, 424–434 (2016).

78. Lindholm, P., Leskinen-kalilo, S., Minn, H., Bergman, J., Haaparanta, M. & Lehtikoinen, P. Comparison of Fluorine-18 and Carbon-11-Methionine in Head and Neck Cancer. *J Nucl Med* **34**, 1711–1716 (1993).
79. Leskinen-kallio, S., Ruotsalainen, U., Nää, K. & Terä, M. Uptake of Carbon-11 Methionine and Lymphoma: A PET Study. *J Nucl Med* **32**, 1211–1218 (1991).
80. Kaschten, B., Stevenaert, A., Sadzot, B., Deprez, M., Degueldre, C., Del Fiore, G., Luxen, A. & Reznik, M. Preoperative evaluation of 54 gliomas by PET with fluorine-18 fluorodeoxyglucose and/or carbon-11 methionine. *J. Nucl. Med.* **39**, 778–785 (1998).
81. Harris, S. M., Davis, J. C., Snyder, S. E., Butch, E. R., Vavere, A. L., Kocak, M. & Shulkin, B. L. Evaluation of the biodistribution of <sup>11</sup>C-methionine in children and young adults. *J. Nucl. Med.* **54**, 1902–1908 (2013).
82. Afshar-Oromieh, A., Malcher, A., Eder, M., Eisenhut, M., Linhart, H. G., Hadaschik, B. A., Holland-Letz, T., Giesel, F. L., Kratochwil, C., Haufe, S., Haberkorn, U. & Zechmann, C. M. PET imaging with a [<sup>68</sup>Ga]gallium-labelled PSMA ligand for the diagnosis of prostate cancer: biodistribution in humans and first evaluation of tumour lesions. *Eur. J. Nucl. Med. Mol. Imaging* **40**, 486–495 (2013).
83. Czarniecki, M., Mena, E., Lindenberg, L., Cacko, M., Harmon, S., Radtke, J. P., Giesel, F., Turkbey, B. & Choyke, P. L. Keeping up with the prostate-specific membrane antigens (PSMAs): An introduction to a new class of positron emission tomography (PET) imaging agents. *Transl. Androl. Urol.* **7**, 831–843 (2018).
84. Hofman, M. S., Hicks, R. J., Maurer, T. & Eiber, M. Prostate-specific membrane antigen PET: Clinical utility in prostate cancer, normal patterns, pearls, and pitfalls. *Radiographics* **38**, 200–217 (2018).
85. Kratochwil, C., Flechsig, P., Lindner, T., Abderrahim, L., Altmann, A., Mier, W., Adeberg, S., Rathke, H., Röhrich, M., Winter, H., Plinkert, P. K., Marme, F., Lang, M., Kauczor, H. U., Jäger, D., Debus, J., Haberkorn, U. & Giesel, F. L. <sup>68</sup>Ga-FAPI PET/CT: Tracer uptake in 28 different kinds of cancer. *J. Nucl. Med.* **60**, 801–805 (2019).

86. Varasteh, Z., Mohanta, S., Robu, S., Braeuer, M., Li, Y., Omidvari, N., Topping, G., Sun, T., Nekolla, S. G., Richter, A., Weber, C., Habenicht, A., Haberkorn, U. A. & Weber, W. A. Molecular imaging of fibroblast activity after myocardial infarction using a  $^{68}\text{Ga}$ -labeled fibroblast activation protein inhibitor, FAPI-04. *J. Nucl. Med.* **60**, 1743–1749 (2019).
87. Eder, M., Schäfer, M., Bauder-Wüst, U., Hull, W. E., Wängler, C., Mier, W., Haberkorn, U. & Eisenhut, M.  $^{68}\text{Ga}$ -complex lipophilicity and the targeting property of a urea-based PSMA inhibitor for PET imaging. *Bioconjug. Chem.* **23**, 688–697 (2012).
88. Eder, M., Wängler, B., Knackmuss, S., LeGall, F., Little, M., Haberkorn, U., Mier, W. & Eisenhut, M. Tetrafluorophenolate of HBED-CC: A versatile conjugation agent for  $^{68}\text{Ga}$ -labeled small recombinant antibodies. *Eur. J. Nucl. Med. Mol. Imaging* **35**, 1878–1886 (2008).
89. Lenzo, N., Meyrick, D. & Turner, J. Review of Gallium-68 PSMA PET/CT Imaging in the Management of Prostate Cancer. *Diagnostics* **8**, 16 (2018).
90. Hofman, M. S., Eu, P., Jackson, P., Hong, E., Binns, D., Irvani, A., Murphy, D., Mitchell, C., Siva, S., Hicks, R. J., Young, J. D., Blower, P. J. & Mullen, G. E. Cold Kit for Prostate-Specific Membrane Antigen (PSMA) PET Imaging: Phase 1 Study of  $^{68}\text{Ga}$ -Tris(Hydroxypyridinone)-PSMA PET/CT in Patients with Prostate Cancer. *J. Nucl. Med.* **59**, 625–631 (2018).
91. Banerjee, S. R. & Pomper, M. G. Clinical Applications of Gallium-68. *Appl. Radiat. Isot.* 2–13 (2013).
92. Makvandi, M., Dupis, E., Engle, J. W., Nortier, F. M., Fassbender, M. E., Simon, S., Birnbaum, E. R., Atcher, R. W., John, K. D., Rixe, O. & Norenberg, J. P. Alpha-Emitters and Targeted Alpha Therapy in Oncology: from Basic Science to Clinical Investigations. *Target. Oncol.* **13**, 189–203 (2018).
93. McBean, R., O’Kane, B., Parsons, R. & Wong, D. Lutetium-177-PSMA therapy for men with advanced prostate cancer: Initial 18 months experience at a single Australian tertiary institution. *J. Med. Imaging Radiat. Oncol.* 1–8 (2019).

94. Dowsett, M., Archer, C., Assersohn, L., Gregory, R. K., Ellis, P. A., Salter, J., Chang, J., Johnston, S. R. D., Powles, T. J. & Smith, I. E. Clinical studies of apoptosis and proliferation in breast cancer. *Endocr. Relat. Cancer* **6**, 25–28 (1999).
95. Wheeler, J. A., Stephens, L. C., Tornos, C., Eifel, P. J., Ang, K. K., Milas, L., Allen, P. K. & Meyn, R. E. Apoptosis as a Predictor of Tumour response to Radiation in Stage 1B Cervical Carcinoma. *Int J Radiat Oncol Biol Phys* **32**, 1487–1493 (1995).
96. Hannum, Y. A. Apoptosis and the Dilemma of Cancer Chemotherapy. *Blood* **89**, 1845–1853 (1997).
97. Ricci, M. S. Chemotherapeutic Approaches for Targeting Cell Death Pathways. *Oncologist* **11**, 342–357 (2006).
98. Ellis, P. A., Smith, I. E., McCarthy, K., Detre, S., Salter, J. & Dowsett, M. Preoperative chemotherapy induces apoptosis in early breast cancer. *Lancet* **349**, 849 (1997).
99. Alam, I. S., Neves, A. A., Witney, T. H., Boren, J. & Brindle, K. M. Comparison of the C2A Domain of Synaptotagmin-I and Annexin-V As Probes for Detecting Cell Death. *Bioconjug. Chem.* **21**, 884–891 (2010).
100. Neves, A. A. & Brindle, K. M. Imaging cell death. *J Nucl Med* **55**, 1–4 (2014).
101. Condliffe, S. B., Corradini, I., Pozzi, D., Verderio, C. & Matteoli, M. Endogenous SNAP-25 regulates native voltage-gated calcium channels in glutamatergic neurons. *J. Biol. Chem.* **285**, 24968–24976 (2010).
102. Lentz, B. R. Exposure of platelet membrane phosphatidylserine regulates blood coagulation. *Prog. Lipid Res.* **42**, 423–438 (2003).
103. Borisenko, G. G., Matura, T., Liu, S. X., Tyurin, V. A., Jianfei, J., Serinkan, F. B. & Kagan, V. E. Macrophage recognition of externalized phosphatidylserine and phagocytosis of apoptotic Jurkat cells - existence of a threshold. *Arch. Biochem. Biophys.* **413**, 41–52 (2003).

104. Leventis, P. a & Grinstein, S. The distribution and function of phosphatidylserine in cellular membranes. *Annu. Rev. Biophys.* **39**, 407–427 (2010).
105. Segawa, K. & Nagata, S. An Apoptotic ‘Eat Me’ Signal : Phosphatidylserine Exposure. *Trends Cell Biol.* **25**, 639–650 (2015).
106. Bretverhoven, B., Schlegel, R. A. & Williamson, P. Mechanisms of Phosphatidylserine Exposure, A Phagocyte Recognition Signal, on Apoptotic T Lymphocytes. *J. Exp. Med.* **182**, 1597–1601 (1995).
107. Wood, R. & Harlow, R. D. Structural analyses of rat liver phosphoglycerides. *Arch. Biochem. Biophys.* **135**, 272–281 (1969).
108. Authority, E. F. S. Scientific Opinion on the substantiation of health claims related to phosphatidyl serine (ID 552, 711, 734, 1632, 1927) pursuant to Article 13(1) of Regulation (EC) No 1924/2006. *EFSA J.* **8**, 1–15 (2010).
109. Gold, R., Schmied, M., Giegerich, G., Breitschopf, H., Hartung, H., Toyka, K. & Lassmann, H. Differentiation between cellular apoptosis and necrosis by the combined use of in situ tailing and nick translation techniques. *J. Tech. Methods Pathol.* **71**, 219–225 (1994).
110. Krysko, D. V., Vanden Berghe, T., D’Herde, K. & Vandenabeele, P. Apoptosis and necrosis: Detection, discrimination and phagocytosis. *Methods* **44**, 205–221 (2008).
111. Kerr, J. F. R., Wyllie, A. H. & Currie, A. R. Apoptosis: A basic biological phenomenon with wide-ranging implications in human disease. *Br. J. Cancer* **26**, 239–257 (1972).
112. Elmore, S. Apoptosis: A review of Programmed Cell Death. *Toxicol. Pathol.* **35**, 495–516 (2007).
113. Tait, S. W. G. & Green, D. R. Mitochondrial Regulation of Cell Death. *Cold Spring Harb Perspect Biol* **2013** **5**, 1–15 (2013).



114. Swers, J. S., Grinberg, L., Wang, L., Feng, H., Lekstrom, K., Carrasco, R., Xiao, Z., Inigo, I., Leow, C. C. & Wu, H. Multivalent Scaffold Proteins as Superagonists of TRAIL Receptor 2-Induced Apoptosis. *Mol. Cancer Ther.* **12**, 1235–1244 (2013).
115. Kroemer, G., Galluzzi, L., Vandenabeele, P., Abrams, J., Alnemri, E., Baehrecke, E., Blagosklonny, M., El-Deiry, W., Golstein, P., Green, D., Hengartner, M., Knight, R., Kumar, S., Lipton, S. a, Malorni, W., Nuñez, G., Peter, M., Tschopp, J., Yuan, J., Piacentini, M., Zhivotovsky, B. & Melino, G. Classification of Cell Death: *Cell Death Differ.* **16**, 3–11 (2009).
116. Clark, M. R. Flippin' lipids. *Nat. Immunol.* **12**, 373–375 (2011).
117. Denecker, G., Doms, H., Van Loo, G., Vercammen, D., Grooten, J., Fiers, W., Declercq, W. & Vandenabeele, P. Phosphatidyl serine exposure during apoptosis precedes release of cytochrome c and decrease in mitochondrial transmembrane potential. *FEBS Lett.* **465**, 47–52 (2000).
118. Sachet, M., Yu, Y. & Oehler, R. The immune response to secondary necrotic cells. *Apoptosis* **22**, 1189–1204 (2017).
119. Dean, E., Greystoke, A., Ranson, M. & Dive, C. Biomarkers of cell death applicable to early clinical trials. *Exp. Cell Res.* **318**, 1252–1259 (2012).
120. Dubash, S. R., Merchant, S., Heinzmann, K., Mauri, F., Lavdas, I., Inglese, M., Kozlowski, K., Rama, N., Masrou, N., Steel, J. F., Thornton, A., Lim, A. K., Lewanski, C., Cleator, S., Coombes, R. C., Kenny, L. & Aboagye, E. O. Clinical translation of [<sup>18</sup>F]ICMT-11 for measuring chemotherapy-induced caspase 3/7 activation in breast and lung cancer. *Eur. J. Nucl. Med. Mol. Imaging* **45**, 2285–2299 (2018).
121. Wuest, M., Perreault, A., Richter, S., Knight, J. C. & Wuest, F. Targeting phosphatidylserine for radionuclide-based molecular imaging of apoptosis. *Apoptosis* **24**, 221–244 (2019).
122. Mochizuki, T., Kuge, Y., Zhao, S., Tsukamoto, E., Hosokawa, M., Strauss, H. W., Blankenberg, F. G., Tait, J. F. & Tamaki, N. Detection of apoptotic tumor response

in vivo after a single dose of chemotherapy with  $^{99m}\text{Tc}$ -annexin V. *J. Nucl. Med.* **44**, 92–97 (2003).

123. AbCam. Abcam - Annexin V - FITC kit. [<https://www.abcam.com/annexin-v-fitc-apoptosis-staining--detection-kit-ab14085.html> accessed 14<sup>th</sup> July 2019].

124. Kirsch, T., Nah, H. D., Demuth, D. R., Harrison, G., Golub, E. E., Adams, S. L. & Pacifici, M. Annexin V-mediated calcium flux across membranes is dependent on the lipid composition: Implications for cartilage mineralization. *Biochemistry* **36**, 3359–3367 (1997).

125. Blankenberg, F. G., Katsikis, P. D., Tait, J. F., Davis, R. E., Naumovski, L., Ohtsuki, K., Kopiwoda, S., Abrams, M. J. & Strauss, H. W. Imaging of apoptosis (programmed cell death) with  $^{99m}\text{Tc}$  annexin V. *J. Nucl. Med.* **40**, 184–191 (1999).

126. Belhocine, T. Z. & Blankenberg, F. G.  $^{99m}\text{Tc}$ -Annexin A5 Uptake and Imaging to Monitor Chemosensitivity. *Methods Mol. Med.* **111**, 363–380 (2005).

127. Blankenberg, F. Monitoring of Treatment-Induced Apoptosis in Oncology with PET and SPECT. *Curr. Pharm. Des.* **14**, 2974–2982 (2008).

128. Boersma, H. H., Liem, I. H., Kemerink, G. J., Thimister, P. W. L., Hofstra, L., Stolk, L. M. L., Van Heerde, W. L., Pakbiers, M. T. W., Janssen, D., Beysens, A. J., Reutelingsperger, C. P. M. & Heidendal, G. A. K. Comparison between human pharmacokinetics and imaging properties of two conjugation methods for  $^{99m}\text{Tc}$ -Annexin A5. *Br. J. Radiol.* **76**, 553–560 (2003).

129. Boersma, H., Kietselaer, B., Stolk, L., Bennaghmouch, A., Hofstra, L., Narula, J., Heidendal, G. & Reutelingsperger, C. Past, Present, and Future of Annexin A5: From Protein Discovery to Clinical Applications. *J. Nucl. Med.* **46**, 2035–2050 (2005).

130. Kemerink, G. J., Boersma, H. H., Thimister, P. W., Hofstra, L., Liem, I., Pakbiers, M. T. W., Janssen, D., Reutelingsperger, C. P. & Heidendal, G. A.

Biodistribution and dosimetry of  $^{99m}\text{Tc}$ -BTAP-annexin-V in humans. *Eur. J. Nucl. Med.* **28**, 1373–1378 (2001).

131. Lahorte, C. M. M., Van de Wiele, C., Bacher, K., Van den Bossche, B., Thierens, H., Van Belle, S., Slegers, G. & Dierckx, R. A. Biodistribution and dosimetry study of  $^{123}\text{I}$ -rh-annexin V in mice and humans. *Nucl. Med. Commun.* **24**, 871–880 (2003).

132. Challapalli, A., Kenny, L. M., Hallett, W. A., Kozlowski, K., Tomasi, G., Gudi, M., Al-Nahhas, A., Coombes, R. C. & Aboagye, E. O. [ $^{18}\text{F}$ ]ICMT-11, a Caspase-3-Specific PET Tracer for Apoptosis: Biodistribution and Radiation Dosimetry. *J. Nucl. Med.* **54**, 1551–1556 (2013).

133. Reshef, A., Shirvan, A., Waterhouse, R. N., Grimberg, H., Levin, G., Cohen, A., Ulysse, L. G., Friedman, G., Antoni, G. & Ziv, I. Molecular Imaging of Neurovascular Cell Death in Experimental Cerebral Stroke by PET. *J. Nucl. Med.* **49**, 1520–1528 (2008).

134. Sun, L., Zhou, K., Wang, W., Zhang, X., Ju, Z., Qu, B., Zhang, Z., Wang, J., Ling, Z., Yu, X., Zhang, J. & Pan, L. ML-10 Imaging for Assessment of Apoptosis Response of Intracranial Tumor Early after Radiotherapy by PET/CT. *Contrast Media Mol. Imaging* 1–9 (2018).

135. Demirci, E., Ahmed, R., Ocak, M., Latoche, J., Radelet, A., DeBlasio, N., Mason, N. S., Anderson, C. J. & Mountz, J. M. Preclinical evaluation of  $^{18}\text{F}$ -ML-10 to determine timing of apoptotic response to chemotherapy in solid tumors. *Mol. Imaging* **16**, 1–8 (2017).

136. Shen, B., Jeon, J., Palner, M., Ye, D., Shuhendler, A., Chin, F. T. & Rao, J. Positron emission tomography imaging of drug-induced tumor apoptosis with a caspase-triggered nanoaggregation probe. *Angew. Chemie - Int. Ed.* **52**, 10511–10514 (2013).

137. Witney, T. H., Hoehne, A., Reeves, R. E., Ilovich, O., Namavari, M., Shen, B., Chin, F. T., Rao, J. & Gambhir, S. S. A systematic comparison of  $^{18}\text{F}$ -C-SNAT to established radiotracer imaging agents for the detection of tumor response to treatment. *Clin. Cancer Res.* **21**, 3896–3905 (2015).

138. Elvas, F., Vangestel, C., Pak, K., Vermeulen, P., Gray, B., Stroobants, S., Staelens, S. & Wyffels, L. Early Prediction of Tumor Response to Treatment: Preclinical Validation of  $^{99m}\text{Tc}$ -Duramycin. *J. Nucl. Med.* **57**, 805–811 (2016).
139. Lin, C. C., Seikowski, J., Pérez-Lara, A., Jahn, R., Höbartner, C. & Walla, P. J. Control of membrane gaps by synaptotagmin- $\text{Ca}^{2+}$  measured with a novel membrane distance ruler. *Nat. Commun.* **5**, 7 (2014).
140. Davletov, B. A. & Sudhof, T. C. a Single C2 Domain From Synaptotagmin-I Is Sufficient for High-Affinity Calcium/Phospholipid Binding. *J. Biol. Chem.* **268**, 26386–26390 (1993).
141. Shao, X., Fernandez, I., Südhof, T. C. & Rizo, J. Solution structures of the  $\text{Ca}^{2+}$ -free and  $\text{Ca}^{2+}$ -bound C2A domain of synaptotagmin I: Does  $\text{Ca}^{2+}$  induce a conformational change? *Biochemistry* **37**, 16106–16115 (1998).
142. Shao, X., Fernandez, I., Sudhof, T. C. & Rizo, J. Solution structures of the  $\text{Ca}^{2+}$ -free and  $\text{Ca}^{2+}$ -bound C2A domain of synaptotagmin I: does  $\text{Ca}^{2+}$  induce a conformational change? *Biochemistry* **37**, 16106–16115 (1998).
143. Krishnan, A., Neves, A. A., Brindle, K. M., de Backer, M. M., Hu, D.-E., Davletov, B. & Kettunen, M. I. Detection of Cell Death in Tumors by Using MR Imaging and a Gadolinium-based Targeted Contrast Agent. *Radiology* **246**, 854–862 (2008).
144. Jung, H., Kettunen, M. I., Davletov, B. & Brindle, K. M. Detection of Apoptosis Using the C2A Domain of Synaptotagmin I. 983–987 (2004).
145. Xie, B., Tomaszewski, M. R., Neves, A. A., Ros, S., Hu, D., Mullins, S. R., Tice, D., Sainson, R. C. A. & Bohndiek, S. E. Optoacoustic detection of early therapy-induced tumor cell death using a targeted imaging agent Statement of translational relevance : Tumors of the same type can show markedly different responses to the same. (2017).
146. Dirac, P. A. M. The Quantum Theory of the Electron. *Proc. R. Soc. London A* **117**, 610–624 (1928).

147. Lawrence, E. O. & Cooksey, D. On the apparatus for the multiple acceleration of light ions to high speeds. *Phys. Rev.* **50**, 1131–1140 (1936).
148. Reivich, M., Kuhl, D. E., Wolf, A., Greenberg, J., Phelps, M., Ido, T., Casella, V., Hoffman, E., Alavi, A. & Sokoloff, L. The [<sup>18</sup>F]Fluorodeoxyglucose method for the measurement of local cerebral glucose metabolism in man. *Circ. Res.* **44**, 127–137 (1979).
149. Zanzonico, P. Positron Emission Tomography: A Review of Basic Principles, Scanner Design and Performance, and Current Systems. *Semin. Nucl. Med.* **34**, 87–111 (2004).
150. Slomka, P. J., Pan, T. & Germano, G. Recent Advances and Future Progress in PET Instrumentation. *Semin. Nucl. Med.* **46**, 5–19 (2016).
151. Keereman, V., Mollet, P., Berker, Y., Schulz, V. & Vandenberghe, S. Challenges and current methods for attenuation correction in PET/MR. *Magn. Reson. Mater. Physics, Biol. Med.* **26**, 81–98 (2013).
152. Vandenberghe, S., Mikhaylova, E., D’Hoe, E., Mollet, P. & Karp, J. S. Recent developments in time-of-flight PET. *EJNMMI Phys.* **3**, (2016).
153. Surti, S., Kuhn, A., Werner, M. E., Perkins, A. E., Kolthammer, J. & Karp, J. S. Performance of Philips Gemini TF PET/CT scanner with special consideration for its time-of-flight imaging capabilities. *J. Nucl. Med.* **48**, 471–480 (2007).
154. Jung, J. H., Choi, Y. & Im, K. C. PET/MRI: Technical Challenges and Recent Advances. *Nucl. Med. Mol. Imaging (2010)*. **50**, 3–12 (2016).
155. Ehman, E. C., Johnson, G. B., Villanueva-meyer, J. E., Cha, S., Leynes, A. P., Eric, P., Larson, Z. & Hope, T. A. PET/MRI: Where Might It Replace PET/CT? *J Magn Reson. Imaging* **46**, 1247–1262 (2017).
156. Rahmim, A. & Zaidi, H. PET versus SPECT: strengths, limitations and challenges. *Nucl. Med. Commun.* **29**, 193–207 (2008).
157. Baker, M. The whole picture. *Nature* **463**, 977–980 (2010).

158. Mediso. AnyScan TRIO SCP installed at new NPL MEMPHYS centre – Bartec. [<https://www.bartectechnologies.com/news/2018/03/anyscan-trio-scp-installed-at-new-npl-memphys-centre> accessed 12<sup>th</sup> July 2019]
159. Businesswire. Eckert & Ziegler receives approval for gallium-68 generator for cost-effective diagnosis of cancer. at [<https://www.businesswire.com/news/home/20141204005402/en/Eckert-Ziegler-receives-approval-gallium-68-generator-cost-effective> accessed 12<sup>th</sup> July 2019]
160. Vincent, J. World’s most powerful MRI scanner will be strong enough to lift 60 metric tonnes. *The Independent* (2013) [<https://www.independent.co.uk/news/science/world-s-most-powerful-mri-scanner-will-be-strong-enough-to-lift-60-metric-tonnes-8902233.html> accessed 12<sup>th</sup> July 2019].
161. Heal, W. P. & Tate, E. W. Getting a chemical handle on protein post-translational modification. *Org. Biomol. Chem.* **8**, 731–738 (2010).
162. Lundbald, R. L. Chemical Reagents for Protein Modification. (CRC PRESS, 2005).
163. Mccarron, P. A., Olwill, S. A., Marouf, W. M. Y., Buick, R. J., Walker, B. & Scott, C. J. Antibody Conjugates And Therapeutic Strategies. *Mol. Interv.* **5**, 368–380 (2005).
164. Lewis Phillips, G. D., Li, G., Dugger, D. L., Crocker, L. M., Parsons, K. L., Mai, E., Blättler, W. A., Lambert, J. M., Chari, R. V. J., Lutz, R. J., Wong, W. L. T., Jacobson, F. S., Koeppen, H., Schwall, R. H., Kenkare-Mitra, S. R., Spencer, S. D. & Sliwkowski, M. X. Targeting HER2-positive breast cancer with trastuzumab-DM1, an antibody-cytotoxic drug conjugate. *Cancer Res.* **68**, 9280–9290 (2008).
165. Day, J. J., Marquez, B. V., Beck, H. E., Aweda, T. A., Gawande, P. D. & Meares, C. F. Chemically Modified Antibodies as Diagnostic Imaging Agents. *Curr Opin Chem Biol.* **14**, 803–809 (2010).

166. McFarlane, A. S. Labelling of plasma proteins with radioactive iodine. *Biochem. J.* **62**, 135–143 (1955).
167. Greenwood, F., Hunter, W. & Glover, J. The Preparation of <sup>131</sup>I-Labelled Human Growth Hormone of High Specific Radioactivity. *Biochem. J.* **89**, 114–123 (1963).
168. Saxon, E. & Bertozzi, C. R. Cell surface engineering by a modified Staudinger reaction. *Science* **287**, 2007–2010 (2000).
169. Bertozzi, C. R. Bioorthogonal Chemistry: Fishing for Selectivity in a Sea of Functionality. *Angew. Chem. Int. Ed. Engl.* **48**, 6974–6998 (2009).
170. Stairs, S., Neves, A. A., Stöckmann, H., Wainman, Y. A., Ireland-Zecchini, H., Brindle, K. M. & Leeper, F. J. Metabolic glycan imaging by isonitrile-tetrazine click chemistry. *Chembiochem* **14**, 1063–1070 (2013).
171. Stöckmann, H., Neves, A. a, Stairs, S., Ireland-Zecchini, H., Brindle, K. M. & Leeper, F. J. Development and evaluation of new cyclooctynes for cell surface glycan imaging in cancer cells. *Chem. Sci.* **2**, 932–936 (2011).
172. Wainman, Y. A., Neves, A. A., Stairs, S., Stöckmann, H., Ireland-Zecchini, H., Brindle, K. M. & Leeper, F. J. Dual-sugar imaging using isonitrile and azido-based click chemistries. *Org. Biomol. Chem.* **11**, 7297–7300 (2013).
173. Evans, H. L., Slade, R. L., Carroll, L., Smith, G., Nguyen, Q.-D., Iddon, L., Kamaly, N., Stöckmann, H., Leeper, F. J., Aboagye, E. O. & Spivey, A. C. Copper-free click--a promising tool for pre-targeted PET imaging. *Chem. Commun. (Camb)*. **48**, 991–3 (2012).
174. King, J. L. & Jukes, T. H. Non-Darwinian Evolution. *Science* **164**, 788–798 (1969).
175. Doolittle, R. F. Redundancies in Protein Sequences. Prediction of Protein Structure and the Principles of Protein Conformation (Springer, Boston, MA, 1989).

176. Wüst, F., Hultsch, C., Bergmann, R., Johannsen, B. & Henle, T. Radiolabelling of isopeptide N $\epsilon$ -( $\gamma$ -glutamyl)-L-lysine by conjugation with N-succinimidyl-4-[ $^{18}$ F]fluorobenzoate. *Appl. Radiat. Isot.* **59**, 43–48 (2003).
177. Vaidyanathan, G. & Zalutsky, M. R. Synthesis of N-succinimidyl 4-[ $^{18}$ F]fluorobenzoate, an agent for labeling proteins and peptides with  $^{18}$ F. *Nat. Protoc.* **1**, 1655–1661 (2006).
178. Chalker, J. M., Bernardes, G. J. L., Lin, Y. A. & Davis, B. G. Chemical modification of proteins at cysteine: Opportunities in chemistry and biology. *Chem. - An Asian J.* **4**, 630–640 (2009).
179. Younggyu, K., Ho, S. O., Gassman, N. R., Korlann, Y., Landorf, E. V. & Collart, F. R. Efficient Site-Specific Labeling of Proteins via Cysteines. *Bioconjug Chem* **19**, 786–791 (2008).
180. Takaoka, Y., Ojida, A. & Hamachi, I. Protein organic chemistry and applications for labeling and engineering in live-cell systems. *Angew. Chemie - Int. Ed.* **52**, 4088–4106 (2013).
181. Bednar, R. A. Reactivity and pH Dependence of Thiol Conjugation to N-Ethylmaleimide: Detection of a Conformational Change in Chalcone Isomerase. *Biochemistry* **29**, 3684–3690 (1990).
182. Markossian, K. A., Khanova, H. A., Kleimenov, S. Y., Levitsky, D. I., Chebotareva, N. A., Asryants, R. A., Muronetz, V. I., Saso, L., Yudin, I. K. & Kurganov, B. I. Mechanism of alkylation of rabbit muscle glyceraldehyde 3-phosphate dehydrogenase. *Biochemistry* **10**, 2456–2466 (1971).
183. Lindorff-Larsen, K. & Winther, J. R. Thiol alkylation below neutral pH. *Anal. Biochem.* **286**, 308–310 (2000).
184. Winther, J. R. & Thorpe, C. Quantification of Thiols and Disulfides. *Biochim Biophys Acta.* **1840**, 1–26 (2014).



185. Gorin, G., Martic, P. A. & Doughty, G. Kinetics of the reaction of *N*-ethylmaleimide with cysteine and some congeners. *Arch. Biochem. Biophys.* **115**, 593–597 (1966).
186. Koniev, O. & Wagner, A. Developments and recent advancements in the field of endogenous amino acid selective bond forming reactions for bioconjugation. *Chem. Soc. Rev.* **44**, 5495–5551 (2015).
187. Sharpless, N. E. & Flavin, M. The Reactions of Amines and Amino Acids with Maleimides. Structure of the Reaction Products Deduced from Infrared and Nuclear Magnetic Resonance Spectroscopy. *Biochemistry* **5**, 2963–2971 (1966).
188. Fontaine, S. D., Reid, R., Robinson, L., Ashley, G. W. & Santi, D. V. Long-term stabilization of maleimide-thiol conjugates. *Bioconjug. Chem.* **26**, 145–152 (2015).
189. Baldwin, A. D. & Kiick, K. L. Tunable degradation of maleimide-Thiol adducts in reducing environments. *Bioconjug. Chem.* **22**, 1946–1953 (2011).
190. Lyon, R. P., Setter, J. R., Bovee, T. D., Doronina, S. O., Hunter, J. H., Anderson, M. E., Balasubramanian, C. L., Duniho, S. M., Leiske, C. I., Li, F. & Senter, P. D. Self-hydrolyzing maleimides improve the stability and pharmacological properties of antibody-drug conjugates. *Nat. Biotechnol.* **32**, 1059–1062 (2014).
191. Ryan, C. P., Smith, M. E. B., Schumacher, F. F., Grohmann, D., Papaioannou, D., Waksman, G., Werner, F., Baker, J. R. & Caddick, S. Tunable reagents for multi-functional bioconjugation: Reversible or permanent chemical modification of proteins and peptides by control of maleimide hydrolysis. *Chem. Commun.* **47**, 5452–5454 (2011).
192. Shen, B. Q., Xu, K., Liu, L., Raab, H., Bhakta, S., Kenrick, M., Parsons-Reponte, K. L., Tien, J., Yu, S. F., Mai, E., Li, D., Tibbitts, J., Baudys, J., Saad, O. M., Scales, S. J., McDonald, P. J., Hass, P. E., Eigenbrot, C., Nguyen, T., Solis, W. A., Fuji, R. N., Flagella, K. M., Patel, D., Spencer, S. D., Khawli, L. A., Ebens, A., Wong, W. L., Vandlen, R., Kaur, S., Sliwkowski, M. X., Scheller, R. H., Polakis, P. & Junutula, J. R.

Conjugation site modulates the in vivo stability and therapeutic activity of antibody-drug conjugates. *Nat. Biotechnol.* **30**, 184–189 (2012).

193. Dawson, R. M. C. *Data for Biochemical Research* 3rd ed. (Oxford University Press, 1987).

194. Belhocine, T., Steinmetz, N., Hustinx, R., Bartsch, P., Jerusalem, G., Seidel, L., Rigo, P. & Green, A. Increased Uptake of the Apoptosis-imaging Agent  $^{99m}\text{Tc}$  Recombinant Human Annexin V in Human Tumors after One Course of Chemotherapy as a Predictor of Tumor Response and Patient Prognosis. *Clin. Cancer Res.* **8**, 2766–2774 (2002).

195. Tait, J. F., Smith, C. & Blankenberg, F. G. Structural Requirements for In Vivo Detection of Cell Death with  $^{99m}\text{Tc}$ -Annexin V. *J. Nucl. Med.* **46**, 807–816 (2005).

196. Murakami, Y., Takamatsu, H., Taki, J., Tatsumi, M., Noda, A. & Ichise, R.  $^{18}\text{F}$ -labelled annexin V: a PET tracer for apoptosis imaging. *Eur J Nucl Med Mol Imaging* **31**, 469–474 (2004).

197. Matos, M. J., Oliveira, B. L., Martínez-Sáez, N., Guerreiro, A., Cal, P. M. S. D., Bertoldo, J., Maneiro, M., Perkins, E., Howard, J., Deery, M. J., Chalker, J. M., Corzana, F., Jiménez-Osés, G. & Bernardes, G. J. L. Chemo- and Regioselective Lysine Modification on Native Proteins. *J. Am. Chem. Soc.* **140**, 4004–4017 (2018).

198. Vallabhajosula, S., Solnes, L. & Vallabhajosula, B. A broad overview of positron emission tomography radiopharmaceuticals and clinical applications: What is new? *Semin. Nucl. Med.* **41**, 246–264 (2011).

199. Jackson, I. M., Scott, P. J. H. & Thompson, S. Clinical Applications of Radiolabeled Peptides for PET. *Semin. Nucl. Med.* **47**, 493–523 (2017).

200. Tait, J. F. & Gibson, D. Phospholipid Binding of Annexin V : Effects of Calcium and Membrane Phosphatidylserine Content '. **298**, 187–191 (1992).

201. Appelt, U., Sheriff, A., Gaipf, U. S., Kalden, J. R., Voll, R. E. & Herrmann, M. Viable, apoptotic and necrotic monocytes expose phosphatidylserine : cooperative

binding of the ligand Annexin V to dying but not viable cells and implications for PS-dependent clearance. *Cell Death Differ.* 194–196 (2005).

202. Blankenberg, F. To scan or not to scan, it is a question of timing: Technetium-99m-annexin V radionuclide imaging assessment of treatment efficacy after one course of chemotherapy. *Clin. Cancer Res.* **8**, 2757–2758 (2002).

203. Fawcett, S. Detection of cell death using fluorescent and radiolabelled derivatives of the C2A domain of Synaptotagmin-I (PhD thesis) - University of Cambridge. (2012).

204. Sanchez-Crespo, A. Comparison of Gallium-68 and Fluorine-18 imaging characteristics in positron emission tomography. *Appl. Radiat. Isot.* **76**, 55–62 (2013).

205. Shiue, C. -Y., Wolf, A. P. & Hainfeld, J. F. Synthesis of <sup>18</sup>F-labelled *N*-(*p*-[<sup>18</sup>F]fluorophenyl)maleimide and its derivatives for labelling monoclonal antibody with <sup>18</sup>F. *Label. Compd. Radiopharm.* **26**, 287–289 (1989).

206. Toyokuni, T., Walsh, J. C., Dominguez, A., Phelps, M. E., Barrio, J. R., Gambhir, S. S. & Satyamurthy, N. Synthesis of a New Heterobifunctional Linker, *N*-[4-(Aminooxy)butyl]maleimide, for Facile Access to a Thiol-Reactive <sup>18</sup>F-Labeling Agent. *Bioconjug. Chem.* **14**, 1253–1259 (2003).

207. De Bruin, B., Kuhnast, B., Hinnen, F., Yaouancq, L., Amessou, M., Johannes, L., Samson, A., Boisgard, R., Tavitian, B. & Dollé, F. 1-[3-(2-[<sup>18</sup>F]fluoropyridin-3-yloxy)propyl]pyrrole-2,5-dione: Design, synthesis, and radiosynthesis of a new [<sup>18</sup>F]fluoropyridine- based maleimide reagent for the labeling of peptides and proteins. *Bioconjug. Chem.* **16**, 406–420 (2005).

208. Cai, W., Zhang, X., Wu, Y. & Chen, X. A thiol-reactive <sup>18</sup>F-labelling agent, *N*-[2-(4-[<sup>18</sup>F]fluorobenzamido)ethyl]maleimide, and synthesis of RGD peptide-based tracer for PET imaging of alpha v beta 3 integrin expression. *J. Nucl. Med.* **47**, 1172–80 (2006).

209. Yue, X., Kiesewetter, D. O., Guo, J., Sun, Z., Zhang, X., Zhu, L., Niu, G., Ma, Y., Lang, L. & Chen, X. Development of a new thiol site-specific prosthetic group

and its conjugation with [cys40]-exendin-4 for in vivo targeting of insulinomas. *Bioconjug Chem* **24**, 1191–1200 (2013).

210. Fujita, Y., Murakami, Y., Noda, A. & Miyoshi, S. Design and Synthesis of an Easily Obtainable Maleimide Reagent *N*-[2-(4-[<sup>18</sup>F]fluoro-*N*-methylbenzenesulfonamido)ethyl]maleimide ([<sup>18</sup>F]FBSEM) to Radiolabel Thiols in Proteins. *Bioconjug. Chem.* **28**, 642–648 (2017).

211. Gao, H., Niu, G., Yang, M., Quan, Q., Ma, Y., Murage, E. N., Ahn, J. M., Kiesewetter, D. O. & Chen, X. PET of insulinoma using <sup>18</sup>F-FBEM-EM3106B, a new GLP-1 analogue. *Mol. Pharm.* **8**, 1775–1782 (2011).

212. Lu, C., Jiang, Q., Hu, M., Tan, C., Yu, H. & Hua, Z. Preliminary biological evaluation of <sup>18</sup>F-FBEM-Cys-annexin V a novel apoptosis imaging agent. *Molecules* **20**, 4902–4914 (2015).

213. Lacroix, S., Egrise, D., Van Simaey, G., Doumont, G., Monclus, M., Sherer, F., Herbaux, T., Leroy, D. & Goldman, S. [<sup>18</sup>F]-FBEM, a tracer targeting cell-surface protein thiols for cell trafficking imaging. *Contrast Media Mol. Imaging* **8**, 409–416 (2013).

214. Ackermann, U., Plougastel, L., Goh, Y. W., Yeoh, S. D. & Scott, A. M. Improved synthesis of [<sup>18</sup>F]FLETT via a fully automated vacuum distillation method for [<sup>18</sup>F]2-fluoroethyl azide purification. *Appl. Radiat. Isot.* **94**, 72–76 (2014).

215. Kiesewetter, D. O., Jacobson, O., Lang, L. & Chen, X. Automated radiochemical synthesis of [<sup>18</sup>F]FBEM: A thiol reactive synthon for radiofluorination of peptides and proteins. *Appl. Radiat. Isot.* **69**, 410–414 (2011).

216. Tang, G., Zeng, W., Yu, M. & Kabalka, G. Facile synthesis of *N*-succinimidyl 4-[<sup>18</sup>F]fluorobenzoate ([<sup>18</sup>F]SFB) for protein labeling. *J. Label. Compd. Radiopharm.* **51**, 68–71 (2008).

217. Carroll, M., Yan, R., Aigbirhio, F., Soloviev, D. & Brichard, L. Single-step synthesis of *N*-succinimidyl-4-[<sup>18</sup>F]fluorobenzoate. *J. Nucl. Med.* **49**, 298P-298P (2008).
218. Olma, S. & Shen, C. K.-F. Simplified one-pot synthesis of [<sup>18</sup>F]SFB for radiolabelling. US2011263819A1 (2011).
219. Lee, B. C., Moon, B. S. & Kim, J. S. Method for Preparation of Fluorine-18-Labelled Flumazenil using Diaryliodonium Salt Precursor. **2**, (2014).
220. Hamamatsu Photonics Co. Ltd. 2013. JP2013216618 A. (2013).
221. Glaser, M. & Årstad, E. 'Click labeling' with 2-[<sup>18</sup>F]fluoroethylazide for positron emission tomography. *Bioconjug. Chem.* **18**, 989–993 (2007).
222. Neves, A. a, Stöckmann, H., Harmston, R. R., Pryor, H. J., Alam, I. S., Ireland-Zecchini, H., Lewis, D. Y., Lyons, S. K., Leeper, F. J. & Brindle, K. M. Imaging sialylated tumor cell glycans in vivo. *FASEB J.* **25**, 2528–37 (2011).
223. Wainman, Y. A. Developing Novel Chemical Probes for Molecular Imaging of Glycans in Cancer (PhD thesis) University of Cambridge. (2014).
224. Palmieri, A., Ley, S. V., Hammond, K., Polyzos, A. & Baxendale, I. R. A microfluidic flow chemistry platform for organic synthesis: the Hofmann rearrangement. *Tetrahedron Lett.* **50**, 3287–3289 (2009).
225. Guhlke, S., Coenen, H. H. & Stöcklin, G. Fluoroacylation agents based on small n.c.a. [<sup>18</sup>F]fluorocarboxylic acids. *Appl. Radiat. Isot.* **45**, 715–727 (1994).
226. Vaidyanathan, G. & Zalutsky, M. R. Labeling proteins with fluorine-18 using *N*-succinimidyl 4-[<sup>18</sup>F]fluorobenzoate. *Int. J. Radiat. Appl. Instrumentation.* **19**, 275–281 (1992).
227. Evans, H. L., Slade, R. L., Carroll, L., Smith, G., Nguyen, Q. De, Iddon, L., Kamaly, N., Stöckmann, H., Leeper, F. J., Aboagye, E. O. & Spivey, A. C. Copper-free click - A promising tool for pre-targeted PET imaging. *Chem. Commun.* **48**, 991–993 (2012).

228. Coleman, L. E., Bork, J. F. & Dunn, H. Reaction of Primary Aliphatic Amines with Maleic Anhydride. *J. Org. Chem.* **24**, 135–136 (1959).
229. Mantovani, G., Lecolley, F., Tao, L., Haddleton, D. M., Clerx, J., Cornelissen, J. J. L. M. & Velonia, K. Design and synthesis of *N*-maleimido-functionalized hydrophilic polymers via copper-mediated living radical polymerization: A suitable alternative to pegylation chemistry. *J. Am. Chem. Soc.* **127**, 2966–2973 (2005).
230. Kagiya, T., Izu, M., Kawai, S. & Fukui, K. Radiation-induced bulk polymerization of maleimide. *J. Polym. Sci. Part B Polym. Lett.* **4**, 387–392 (1966).
231. Lee, C. C. & Samuels, E. R. The Kinetics of Reaction Between L-Cysteine Hydrochloride and Some Maleimides. *Can. J. Chem.* **42**, 1961–1963 (1964).
232. Carroll, M. A., Nairne, J. & Woodcraft, J. L. Diaryliodonium salts: A solution to 3-<sup>[18F]</sup>fluoropyridine. *J. Label. Compd. Radiopharm.* **50**, 452–454 (2007).
233. Reed, C. D., Launay, G. G. & Carroll, M. A. Evaluation of tetraethylammonium bicarbonate as a phase-transfer agent in the formation of <sup>[18F]</sup>fluoroarenes. *J. Fluor. Chem.* **143**, 231–237 (2012).
234. Reed, C. D., Launay, G. G. & Carroll, M. A. Evaluation of tetraethylammonium bicarbonate as a phase-transfer agent in the formation of <sup>[18F]</sup>fluoroarenes. *J. Fluor. Chem.* **143**, 231–237 (2012).
235. Scott, P. J. H. & Shao, X. Fully automated, high yielding production of *N*-succinimidyl 4-<sup>[18F]</sup>fluorobenzoate (<sup>[18F]</sup>SFB), and its use in microwave-enhanced radiochemical coupling reactions. *J. Label. Compd. Radiopharm.* **53**, 586–591 (2010).
236. Smith, G., Perumal, M., Nguyen, Q. D., Aboagye, E. O., Glaser, M., Shan, B. & Årstad, E. Design, synthesis, and biological characterization of a caspase 3/7 selective isatin labeled with 2-<sup>[18F]</sup>fluoroethylazide. *J. Med. Chem.* **51**, 8057–8067 (2008).
237. Ackermann, U., O’Keefe, G., Lee, S. T., Rigopoulos, A., Cartwright, G., Sachinidis, J. I., Scott, A. M. & Tochon-Danguy, H. J. Synthesis of a

[<sup>18</sup>F]fluoroethyltriazolylthymidine radiotracer from 2-[<sup>18</sup>F]fluoroethyl azide and 5-ethynyl-2'-deoxyuridine. *J. Label. Compd. Radiopharm.* **54**, 260–266 (2011).

238. Dolle, F. Composes de maleimides marques, leur procede de preparation et leur utilisation pour le marquage de macromolecules. (Marketed maleimide compounds, method for preparing same and use thereof for marking molecules) WO2004/002984 A2. (2004)

239. Dong, W. K., Jeong, H. J., Seok, T. L., Sohn, M. H., Katzenellenbogen, J. A. & Dae, Y. C. Facile nucleophilic fluorination reactions using tert-alcohols as a reaction medium: Significantly enhanced reactivity of alkali metal fluorides and improved selectivity. *J. Org. Chem.* **73**, 957–962 (2008).

240. Zott, H. & Heusinger, H. Intermediates of radiation induced polymerisation of maleimides studied by ESR. *Eur. Polym. J.* **14**, 89–92 (1978).

241. O'Donnell, J. H. & Sothman, R. D. The radiation-induced solid-state polymerization of some *N*-alkyl maleimide. *J. Polym. Sci. Part B* **7**, 129–134 (1969).

242. Kagiya, T., Izu, M., Kawai, S. & Fukui, K. Radiation-induced bulk polymerization of maleimide. *J. Polym. Sci. Part A-1 Polym. Chem.* **5**, 1415–1423 (1967).

243. MacGregor, R. R., Schlyer, D. J., Fowler, J. S., Wolf, A. P. & Shiue, C. Y. Fluorine-18-*N*-methylspiroperidol: radiolytic decomposition as a consequence of high specific activity and high dose levels. *J. Nucl. Med.* **28**, 60–67 (1987).

244. Scott, P. J. H., Hockley, B. G., Kung, H. F., Manchanda, R., Zhang, W. & Kilbourn, M. R. Studies into Radiolytic Decomposition of Fluorine-18 Labeled Radiopharmaceuticals for Positron Emission Tomography. *Appl. Radiat. Isot.* **67**, 88–94 (2009).

245. Fawdry, R. M. Radiolysis of 2-[<sup>18</sup>F]fluoro-2-deoxy-d-glucose (FDG) and the role of reductant stabilisers. *Appl. Radiat. Isot.* **65**, 1193–1201 (2007).

246. Le Caër, S. Water Radiolysis: Influence of Oxide Surfaces on H<sub>2</sub> Production under Ionizing Radiation. *Water* **3**, 235–253 (2011).

247. Lousada, C. M., Soroka, I. L., Yagodzinsky, Y., Tarakina, N. V., Todoshchenko, O., Hänninen, H., Korzhavyi, P. A. & Jonsson, M. Gamma radiation induces hydrogen absorption by copper in water. *Sci. Rep.* **6**, (2016).
248. Schwarz, H. A. Free radicals generated by radiolysis of aqueous solutions. *J. Chem. Educ.* **58**, 101 (1981).
249. Petrik, N. G., Alexandrov, A. B. & Vall, A. I. Interracial energy transfer during gamma radiolysis of water on the surface of ZrO<sub>2</sub> and some other oxides. *J. Phys. Chem. B* **105**, 5935–5944 (2001).
250. Cal-Gonzalez, J., Herraiz, J. L., Espana, S., Corzo, P. M. G., Vaquero, J. J., Desco, M., Udias, J. M. & I. Positron range estimations with PeneloPET. *Phys. Med. Biol.* **58**, 5127–5152 (2013).
251. Robert, F. Method for promoting disulfide bond formation in recombinant proteins. US4572798A (1986).
252. Kachur, A. V., Koch, C. J., Biaglow, J. E., Kachur, A. V., Koch, C. J. & Mechanism, J. E. B. Mechanism of copper-catalyzed autoxidation of cysteine Mechanism of Copper-Catalyzed Autoxidation of Cysteine. *Free Radical Research* **31(1)**, 23–34 (1999).
253. Girault, P., The, P. & Metallomics, E. C. The role of copper in cysteine oxidation: study of intra- and inter-molecular reactions in mass spectrometry. *Metallomics* **1**, (2009).
254. Rigo, A., Corazza, A., Luisa, M., Rossetto, M., Ugolini, R. & Scarpa, M. Interaction of copper with cysteine : stability of cuprous complexes and catalytic role of cupric ions in anaerobic thiol oxidation. *J. Inorg. Biochem.* **98**, 1495–1501 (2004).
255. Mullen, G. E. D., Tavaré, R., De Rosales, R. T. M. & Blower, P. J. Efficient Site-Specific Radiolabeling of a Modified C2A Domain of Synaptotagmin I with [<sup>99m</sup>Tc(CO)<sub>3</sub>]<sup>+</sup>: A New Radiopharmaceutical for Imaging Cell Death. *Bioconjug. Chem.* **20**, 2071–2081 (2009).



256. Wolfson Brain Imaging Centre. GE PETtrace — Wolfson Brain Imaging Centre. [<https://www.wbic.cam.ac.uk/pettrace> accessed 12<sup>th</sup> December 2018]
257. Rad Pro Calculator: Free Online Radioactive Isotopes Decay Calculator. at [<http://www.radprocalculator.com/Decay.aspx> accessed 12<sup>th</sup> December 2018]
258. Xie, B., Tomaszewski, M. R., Neves, A. A., Ros, S., Hu, D. E., McGuire, S., Mullins, S. R., Tice, D., Sainson, R. C. A., Bohndiek, S. E., Wilkinson, R. W. & Brindle, K. M. Optoacoustic detection of early therapy-induced tumor cell death using a targeted imaging agent. *Clin. Cancer Res.* **23**, 6893–6903 (2017).
259. Diagnostics, C. Flow cytometry guide. (2019). [<https://www.creative-diagnostics.com/flow-cytometry-guide.htm> accessed 19<sup>th</sup> May 2019]
260. Ying, W., Alano, C. C., Garnier, P. & Swanson, R. A. NAD<sup>+</sup> as a metabolic link between DNA damage and cell death. *J. Neurosci. Res.* **79**, 216–223 (2005).
261. de Murcia, G., Schreiber, V., Molinete, M., Saulier, B., Poch, O., Masson, M., Niedergang, C. & de Murcia, J. M. Structure and function of poly(ADP-ribose) polymerase. *Mol. Cell. Biochem.* **138**, 15–24 (1994).
262. Virag, L. & Szabo, C. The Therapeutic Potential of Poly (ADP-Ribose). *Pharmacol. Rev.* **54**, 375–429 (2002).
263. Patrick, P. S., Hammersley, J., Loizou, L., Kettunen, M. I., Rodrigues, T. B., Hu, D. E., Tee, S. S., Hesketh, R., Lyons, S. K., Soloviev, D., Lewis, D. Y., Aime, S., Fulton, S. M. & Brindle, K. M. Dual-modality gene reporter for in vivo imaging. *Proc. Natl. Acad. Sci. U. S. A.* **111**, 415–420 (2014).
264. Marques, S. M. & Esteves Da Silva, J. C. G. Firefly bioluminescence: A mechanistic approach of luciferase catalyzed reactions. *IUBMB Life* **61**, 6–17 (2009).
265. Tuthill, M. H., Montinaro, A., Zinngrebe, J., Prieske, K., Draber, P., Prieske, S., Newsom-Davis, T., Von Karstedt, S., Graves, J. & Walczak, H. TRAILR2 specific antibodies and recombinant TRAIL can synergise to kill cancer cells. *Oncogene* **34**, 2138–2144 (2015).

266. Johnstone, R. W., Frew, A. J. & Smyth, M. J. The TRAIL apoptotic pathway in cancer onset, progression and therapy. *Nat. Rev. Cancer* **8**, 782 (2008).
267. Nikolettou, V., Markaki, M., Palikaras, K. & Tavernarakis, N. Crosstalk between apoptosis, necrosis and autophagy. *Biochim. Biophys. Acta - Mol. Cell Res.* **1833**, 3448–3459 (2013).
268. Los, M., Mozoluk, M., Ferrari, D., Stepczynska, A., Stroh, C., Renz, A., Herceg, Z., Wang, Z. Q. & Klaus, S.-O. Activation and Caspase-mediated Inhibition of PARP: A Molecular Switch between Fibroblast Necrosis and Apoptosis in Death Receptor Signaling. *Mol. Biol. Cell* **13**, 1338–1351 (2002).
269. Strober, W. Trypan Blue Exclusion Test of Cell Viability. *Curr. Protoc. Immunol.* **21**, 1–3 (1997).
270. Nexcelom Bioscience. Comparison of trypan blue and fluorescence-based viability detection methods via morphological observation. (2015). [<http://www.nexcelom.com/Applications/measure-cell-viability-using-trypan-blue-or-AOPI.php> accessed 12<sup>th</sup> May 2019]
271. Takebe, T., Sekine, K., Enomura, M., Koike, H., Kimura, M., Ogaeri, T., Zhang, R. R., Ueno, Y., Zheng, Y. W., Koike, N., Aoyama, S., Adachi, Y. & Taniguchi, H. Vascularized and functional human liver from an iPSC-derived organ bud transplant. *Nature* **499**, 481–484 (2013).
272. Lancaster, M. A., Renner, M., Martin, C. A., Wenzel, D., Bicknell, L. S., Hurles, M. E., Homfray, T., Penninger, J. M., Jackson, A. P. & Knoblich, J. A. Cerebral organoids model human brain development and microcephaly. *Nature* **501**, 373–379 (2013).
273. ‘Stop Vivisection’ initiative. [<http://www.stopvivisection.eu/> accessed 25<sup>th</sup> May 2019].

274. Menache, A. European Citizens' Initiative - Stop Vivisection. at [<https://ec.europa.eu/citizens-initiative/public/initiatives/successful/details/2012/0000> accessed 25<sup>th</sup> May 2019].
275. Mak, I. W. Y., Evaniew, N. & Ghert, M. Lost in translation: Animal models and clinical trials in cancer treatment. *Am. J. Transl. Res.* **6**, 114–118 (2014).
276. Junod, S. FDA and Clinical Drug Trials: A Short History. *FDA*, 25–55 (2008). [<https://www.fda.gov/media/110437/download> accessed 21<sup>st</sup> March 2019].
277. Wu, G. S., Burns, T. F., Zhan, Y., Alnemri, E. S. & El-Deiry, W. S. Molecular cloning and functional analysis of the mouse homologue of the KILLER/DR5 tumor necrosis factor-related apoptosis-inducing ligand (TRAIL) death receptor. *Cancer Res.* **59**, 2770–2775 (1999).
278. Greer, Y., Gilbert, S., Tice, D. & Lipkowitz, S. MEDI3039, a novel highly potent tumor necrosis factor (TNF)-related apoptosis-inducing ligand (TRAIL) receptor agonist, induces apoptotic cell death in breast cancer cells. *Breast Cancer Res.* **21(1)**, 1–27 (2016).
279. Delgado, M. E., Grabinger, T. & Brunner, T. Cell death at the intestinal epithelial front line. *FEBS J.* **283**, 2701–2719 (2016).
280. Pertea, M., Shumate, A., Pertea, G., Varabyou, A., Chang, Y. C., Madugundu, A. K., Pandey, A. & Salzberg, S. Thousands of large-scale RNA sequencing experiments yield a comprehensive new human gene list and reveal extensive transcriptional noise. *bioRxiv* 332825 (2018).
281. Hillier, L. W., Coulson, A., Murray, J. I., Bao, Z., Sulston, J. E. & Waterston, R. H. Genomics in *C. elegans*: So many genes, such a little worm. *Genome Res.* **15**, 1651–1660 (2005).
282. Apweiler, R., Hermjakob, H. & Sharon, N. On the frequency of protein glycosylation, as deduced from analysis of the SWISS-PROT database. *Biochim. Biophys. Acta* **1473**, 4–8 (1999).

283. Craig Venter, J., Adams, M. D., Myers, E. W., Li, P. W., Mural, R. J., Sutton, G. G., Smith, H. O., Zhu, X. *et al.* The sequence of the human genome. *Science* **291**, 1304–1351 (2001).
284. Berg, J. M., Tymoczko, J. L. & Stryer, L. *Biochemistry*, 7th ed. (W.H. Freeman and Company, 2012).
285. Varki, A., Cummings, R. D., Esko, J. D., Freeze, H. H., Stanley, P., Bertozzi, C. R., Hart, G. W. & Etzler, M. E. *Essentials of Glycobiology*. (Cold Spring Harbor Laboratory Press, 2009).
286. Varki, A. Loss of *N*-Glycolylneuraminic Acid in Humans. *Yearb. Phys. Anthropol.* **69**, 54–69 (2001).
287. Vasudevan, D. & Haltiwanger, R. S. Novel roles for O-linked glycans in protein folding. *Glycoconj. J.* **31**, 417–426 (2014).
288. de Beer, T., Vliegthart, J. F. G., Löffler, A. & Hofsteenge, J. The Hexopyranosyl Residue That Is C-Glycosidically Linked to the Side Chain of Tryptophan-7 in Human RNase Us Is  $\alpha$ -Mannopyranose. *Biochemistry* **34**, 11785–11789 (1995).
289. Doucey, M. A., Hess, D., Blommers, M. J. J. & Hofsteenge, J. Recombinant human interleukin-12 is the second example of a C-mannosylated protein. *Glycobiology* **9**, 435–441 (1999).
290. Stepper, J., Shastri, S., Loo, T. S., Preston, J. C., Novak, P., Man, P., Moore, C. H., Havlíček, V., Patchett, M. L. & Norris, G. E. Cysteine S-glycosylation, a new post-translational modification found in glycopeptide bacteriocins. *FEBS Lett.* **585**, 645–650 (2011).
291. Pinho, S. S. & Reis, C. A. Glycosylation in cancer: Mechanisms and clinical implications. *Nat. Rev. Cancer* **15**, 540–555 (2015).

292. Bennett, E. P., Mandel, U., Clausen, H., Gerken, T. A., Fritz, T. A. & Tabak, L. A. Control of mucin-type O-glycosylation: A classification of the polypeptide GalNAc-transferase gene family. *Glycobiology* **22**, 736–756 (2012).
293. Moremen, K. W., Tiemeyer, M. & Nairn, A. V. Vertebrate protein glycosylation: diversity, synthesis and function. *Nat. Rev. Mol. Cell Biol.* **13**, 448–462 (2012).
294. Holst, S., Wuhrer, M. & Rombouts, Y. Glycosylation characteristics of colorectal cancer. *Advances in Cancer Research* **126**, 203–256 (Elsevier Inc., 2015).
295. Holst, S., Deuss, A. J. M., Van Pelt, G. W., Van Vliet, S. J., Garcia-Vallejo, J. J., Koeleman, C. A. M., Deelder, A. M., Mesker, W. E., Tollenaar, R. A., Rombouts, Y. & Wuhrer, M. *N*-glycosylation profiling of colorectal cancer cell lines reveals association of fucosylation with differentiation and caudal type homeobox 1 (CDX1)/Villin mRNA expression. *Mol. Cell. Proteomics* **15**, 124–140 (2016).
296. Bird-Lieberman, E. L., Neves, A. A., Lao-Sirieix, P., O'Donovan, M., Novelli, M., Lovat, L. B., Eng, W. S., Mahal, L. K., Brindle, K. M. & Fitzgerald, R. C. Molecular imaging using fluorescent lectins permits rapid endoscopic identification of dysplasia in Barrett's esophagus. *Nat. Med.* **18**, 315–321 (2012).
297. Kuo, J. C. H., Ibrahim, A. E. K., Dawson, S., Parashar, D., Howat, W. J., Guttula, K., Miller, R., Fearnhead, N. S., Winton, D. J., Neves, A. A. & Brindle, K. M. Detection of colorectal dysplasia using fluorescently labelled lectins. *Sci. Rep.* **6**, 2–10 (2016).
298. Davis, A. P. & Wareham, R. S. Carbohydrate Recognition through Noncovalent Interactions: A Challenge for Biomimetic and Supramolecular Chemistry. *Angew. Chemie* **38**, 2978–2996 (1999).
299. Baeten, J., Suresh, A., Johnson, A., Patel, K., Kuriakose, M., Flynn, A. & Kademani, D. Molecular imaging of oral premalignant and malignant lesions using fluorescently labeled lectins. *Transl. Oncol.* **7**, 213–220 (2014).

300. Neves, A. A., Stöckmann, H., Wainman, Y. A., Kuo, J. C., Fawcett, S., Leeper, F. J. & Brindle, K. M. Imaging cell surface glycosylation in vivo using 'double click' chemistry. *Bioconjug. Chem.* **24**, 934–941 (2013).
301. Neves, A. A., Wainman, Y. A., Wright, A., Kettunen, M. I., Rodrigues, T. B., McGuire, S., Hu, D. E., Bulat, F., Geninatti Crich, S., Stöckmann, H., Leeper, F. J. & Brindle, K. M. Imaging Glycosylation in Vivo by Metabolic Labeling and Magnetic Resonance Imaging. *Angew. Chemie - Int. Ed.* **55**, 1286–1290 (2016).
302. Moons, S. J., Adema, G. J., Derks, M. T. G. M., Boltje, T. J. & Büll, C. Sialic acid glycoengineering using *N*-acetylmannosamine and sialic acid analogs. *Glycobiology* **29**, 433–445 (2019).
303. Oliveira, B. L., Guo, Z. & Bernardes, G. J. L. Inverse electron demand Diels-Alder reactions in chemical biology. *Chem. Soc. Rev.* **46**, 4895–4950 (2017).
304. Späte, A.-K., Bußkamp, H., Niederwieser, A., Schart, V. F., Marx, A. & Wittmann, V. Rapid Labeling of Metabolically Engineered Cell-Surface Glycoconjugates with a Carbamate-Linked Cyclopropene Reporter. *Bioconjug Chem*, **25(1)**, 147–154 (2014).
305. Hang, H. C., Yu, C., Kato, D. L. & Bertozzi, C. R. A metabolic labeling approach toward proteomic analysis of mucin-type O-linked glycosylation. *Proc. Natl. Acad. Sci.* **100**, 14846–14851 (2003).
306. Laughlin, S. T. & Bertozzi, C. R. Metabolic labeling of glycans with azido sugars and subsequent glycan-profiling and visualization via staudinger ligation. *Nat. Protoc.* **2**, 2930–2944 (2007).
307. Kolb, H. C., Finn, M. G. & Sharpless, K. B. Click Chemistry: Diverse Chemical Function from a Few Good Reactions. *Angew. Chemie* **40**, 2004–2021 (2001).
308. Wittig, G. & Krebs, A. Zur Existenz niedergliederiger Cycloalkine. *Chem. Ber.* 3260–3275 (1961).

309. Huisgen, R., Ooms, P. H. J. & Mingin, M. Exceptional Reactivity of the Bicyclo[2.2.1]heptene Double Bond. *J. Am. Chem. Soc.* **102**, 3951–3953 (1980).
310. Hamlin, T. A., Levandowski, B. J., Narsaria, A. K., Houk, K. N. & Bickelhaupt, F. M. Structural Distortion of Cycloalkynes Influences Cycloaddition Rates both by Strain and Interaction Energies. *Chem. Eur. J.* **25**, 6342–6348 (2019).
311. Harris, T. & Alabugin, I. V. Strain and stereoelectronics in cycloalkyne click chemistry. *Mendeleev Commun.* **29**, 237–248 (2019).
312. Agard, N. J., Prescher, J. A. & Bertozzi, C. R. A Strain-Promoted [3 + 2] Azide - Alkyne Cycloaddition for Covalent Modification of Biomolecules in Living Systems. *J. Am. Chem. Soc.* **126**, 15046–15047 (2004).
313. Stöckmann, H., Neves, A. A., Day, H. A., Stairs, S., Brindle, K. M. & Leeper, F. J. (*E,E*)-1,5-Cyclooctadiene: a small and fast click-chemistry multitalent. *Chem. Commun. (Camb)*. **47**, 7203–7205 (2011).
314. Neves, A. A., Stoeckmann, H., Wainman, Y. A., Kuo, J. C., Fawcett, S., Leeper, F. J. & Brindle, K. M. Imaging Cell Surface Glycosylation in Vivo Using “Double Click” Chemistry. *Bioconjug Chem* **24**, 934–941 (2013).
315. Laughlin, S. T., Baskin, J. M., Amacher, S. L. & Bertozzi, C. R. In Vivo Imaging of Membrane-Associated Glycans in Developing Zebrafish. *Science* **320**, 664–667 (2008).
316. Laughlin, S. T. & Bertozzi, C. R. Imaging the glycome. *Proc. Natl. Acad. Sci. U. S. A.* **106**, 12–17 (2009).
317. Yang, J., Liang, Y., Šečkutèa, J., Houkb, K. N. & Devaraj, N. K. Synthesis and Reactivity Comparisons of 1-Methyl-3-Substituted Cyclopropene Mini-tags for Tetrazine Bioorthogonal Reactions. *Chemistry (Easton)*. **20**, 3365–3375 (2014).
318. Patterson, D. M., Nazarova, L. A., Xie, B., Kamber, D. N. & Prescher, J. A. Functionalized cyclopropenes as bioorthogonal chemical reporters. *J. Am. Chem. Soc.* **134**, 18638–18643 (2012).

319. Cole, C. M., Yang, J., Jolita, S. & Devaraj, N. K. Fluorescent Live-Cell Imaging of Metabolically Incorporated Unnatural Cyclopropene-Mannosamine Derivatives. *ChemBioChem* **14**, 205–208 (2013).
320. Yang, J., Šečkute, J., Cole, C. M. & Devaraj, N. K. Live-cell imaging of cyclopropene tags with fluorogenic tetrazine cycloadditions. *Angew. Chemie - Int. Ed.* **51**, 7476–7479 (2012).
321. Patterson, D. M., Jones, K. A. & Prescher, J. A. Improved cyclopropene reporters for probing protein glycosylation. *Mol. Biosyst.* **10**, 1693–1697 (2014).
322. Darko, A., Wallace, S., Dmitrenko, O., Machovina, M. M., Mehl, R. A., Chin, J. W. & Fox, J. M. Conformationally strained trans-cyclooctene with improved stability and excellent reactivity in tetrazine ligation. *Chem. Sci.* **5**, 3770–3776 (2014).
323. Taylor, M. T., Blackman, M. L., Dmitrenko, O. & Fox, J. M. Design and synthesis of highly reactive dienophiles for the tetrazine-trans-cyclooctene ligation. *J. Am. Chem. Soc.* **133**, 9646–9649 (2011).
324. Elliott, T. S., Townsley, F. M., Bianco, A., Ernst, R. J., Sachdeva, A., Elsässer, S. J., Davis, L., Lang, K., Pisa, R., Greiss, S., Lilley, K. S. & Chin, J. W. Proteome labeling and protein identification in specific tissues and at specific developmental stages in an animal. *Nat. Biotechnol.* **32**, 465–472 (2014).
325. Weber, P. C., Ohlendorf, D. H., Wendoloski, J. J. & Salemme, F. R. Structural Origins of High-Affinity Biotin Binding to Streptavidin. *Science* **243**, 85–88 (1989).
326. Kalofonos, H. P., Rusckowski, M., Siebecker, D. A., Sivolapenko, G. B., Snook, D., Lavender, J. P., Epenetos, A. A. & Hnatowich, D. J. Imaging of Tumor in Patients with Indium-111 Labeled Biotin and Streptavidin Conjugated Antibodies: Preliminary Communication. *J. Nucl. Med.* **31**, 1791–1797 (1990).
327. Paganelli, G., Belloni, C., Magnani, P., Zito, F., Pasini, A., Sassi, I., Meroni, M., Mariani, M., Vignali, M., Siccardi, A. G. & Fazio, F. Two-step tumour



targetting in ovarian cancer patients using biotinylated monoclonal antibodies and radioactive streptavidin. *Eur. J. Nucl. Med.* **19**, 322–329 (1992).

328. Vervaet, C., Baert, L. & Remon, J. P. Enhancement of *in vitro* drug release by using polyethylene glycol 400 and PEG-40 hydrogenated castor oil in pellets made by extrusion / spheronisation. *Int. J. Pharm.* **108**, 207–212 (1994).

329. Vossen, A. C. Van Der, Velde, I. Van Der, Smeets, O. S. N. M., Postma, D. J., Eckhardt, M., Vermes, A., Koch, B. C. P., Vulto, A. G. & Hanff, L. M. Formulating a poorly water soluble drug into an oral solution suitable for paediatric patients; lorazepam as a model drug. *Eur. J. Pharm. Sci.* **100**, 205–210 (2017).

330. Fahr, A. & Liu, X. Drug delivery strategies for poorly water-soluble drugs. *Expert Opin. Drug Deliv* **4**, 403–416 (2007).

331. Muller, B. W. & Brauns, U. Pharmaceutical compositions containing drugs which are instable or sparingly soluble in water and methods for their preparation. US6407079B1 (1985).

332. Hirabayashi, J. *Experimental Glycoscience - Glycochemistry - Glycan Profiling*. (Springer, 2008).

## 8 APPENDICES

### 8.1 GE TRACERlab FX<sub>FN</sub> programming sequence for 2-<sup>18</sup>F]fluoroethyl azide

0 Set Temp. Setpoint Reactor = 40

0 Set Vacuum Pump = On

0.1 Set Process Control = Status Text (taken from comment)

0.1 Wait TFeomr p. Regulator Status Reactor = Temp. OK

t1+0.2 Set V24 = Open

t1+0.2 Set HPLC UV Detector Lamp = Off

t1+0.2 Set Process Control = Status Text (taken from comment)

t1+0.4 Set V19 = Open

t1+0.5 Set V25 = b (down)

t1+0.5 Set V03 Vial3 = Open

t1+5 Set Stirrer = On

t1+10 Set V24 = Close

t1+10 Set V19 = Close

t1+10 Set Temp. Setpoint Reactor = 88

t1+10 Set V03 Vial3 = Close

t1+11 Set Stirrer = Off

t1+2'0 Set Stirrer = On

t1+2'3 Set Stirrer = Off

t1+3'40 Set Stirrer = On

t1+3'43 Set Stirrer = Off

t1+5'20 Set Stirrer = On

t1+5'23 Set Stirrer = Off

t1+8'0 Set Stirrer = On

t1+10'4 Set Stirrer = Off

t1+10'4 Set Temp. Setpoint Reactor = 40

## 8.2 GE TRACERlab FX<sub>FN</sub> programming sequence for *N*-(5-[<sup>18</sup>F]fluoropentyl)maleimide preparation

### Drying <sup>18</sup>F automated procedure sequence

Show message with abort 0 Set Process Control = button and wait

t1+0.1 Set Process Control = Show message with abort button and wait

t2+0 Set Stirrer = On

t2+0 Set V20 = Open

t2+0 Set Vacuum Pump = On

t2+0.1 Set Process Control = Start Region

t2+10 Set V25 = b (down)

t2+10 Set V20 = Close

t2+10 Set V24 = Open

t2+10 Set Process Control = End Region

t2+12 Set V10 = b (left)

t2+12 Set V11 = b (left)

t2+12 Set V23 = Open

t2+12 Set V24 = Close

t2+12 Set V25 = a (up)

t2+50 Set V10 = a (right)

t2+50 Set V23 = Close

t2+50 Set V11 = a (right)

t2+50 Set V13 = Open

t2+50 Set V01 Vial1 = Open

t2+50 Set V24 = Open

t2+1'10 Set Temp. Setpoint Reactor = 95

t2+1'20 Set V20 = Open

t2+1'20 Set V13 = Close

t2+1'20 Set V01 Vial1 = Close

t2+1'22 Wait TFeomr p. Regulator Status Reactor = Temp. OK

t3+1'2 Set V02 Vial2 = Open

t3+1'2 Set V02 Vial2 = Close

t3+2'8 Set V02 Vial2 = Open

t3+2'8 Set V02 Vial2 = Close

t3+3'16 Set V02 Vial2 = Open

t3+3'18 Set V02 Vial2 = Close

t3+8'0 Set V25 = b (down)

t3+8'0 Set V20 = Close

Time List:

Time Device Value Dur. Comment

Check gases pressures

(He: 130kPa, CA: 360kPa)

Confirm transfer of activity has been completed

**Precursor labelling with fluorine-18 and furan deprotection to form *N*-(5-[<sup>18</sup>F]fluoropentyl) maleimide**

0 Set Vacuum Pump = On

0 Set V19 = Open

0 Set Temp. Setpoint Reactor = 50

0.1 Wait TFeomr p. Regulator Status Reactor = Temp. OK

t1+0 Set Temp. Setpoint Reactor = 92

t1+0.1 Set Process Control = Status Text (taken from comment)

t1+0.2 Set Process Control = Status Text (taken from comment)

t1+0.2 Set HPLC UV Detector Lamp = On

t1+0.2 Set V24 = Open

t1+0.4 Set V19 = Open

t1+0.5 Set V25 = b (down)

t1+0.5 Set V03 Vial3 = Open

t1+5 Set V19 = Close

t1+5 Set V24 = Close

t1+5 Set V03 Vial3 = Close

t1+5 Set Stirrer = On

t1+12'0 Set V04 Vial4 = Open

t1+12'1 Set V24 = Open

t1+12'2 Set V19 = Close

t1+12'2 Set V04 Vial4 = Close

t1+12'2 Set V24 = Close

t1+12'3 Set Temp. Setpoint Reactor = 160

t1+12'3 Wait TFeomr p. Regulator Status Reactor = Temp. OK

t2+5'30 Set Temp. Setpoint Reactor = 22

t2+5'31 Wait TFeomr p. Regulator Status Reactor = Temp. OK  
t3+6'1 Set Needle Reactor 1 = Down  
t3+6'1 Set V12 = OFF (to HPLC vial)  
t3+6'1 Set V14 = Open  
t3+6'1 Set V20 = Open  
t3+6'6 Set Needle Reactor 1 = Up  
t3+6'21 Set V20 = Close

### ***N*-(5-[<sup>18</sup>F]fluoropentyl)maleimide purification using HPLC**

0 Set Vacuum Pump = Off  
0.2 Set HPLC Pump Flow Set Point = 0.5  
1 Set HPLC UV Detector Lamp = On  
2.3 Set V12 = OFF (to HPLC vial)  
5 Set HPLC Pump Flow Set Point = 1  
8 Set V20 = Close  
8.1 Set V14 = Close  
9 Set HPLC Pump Flow Set Point = 2  
11 Set HPLC Pump Flow Set Point = 3  
12 Set V26 = b (left)  
13 Set V12 = ON (to waste)  
13.1 Wait Fluoride Detector = On  
t1+0.1 Wait Fluoride Detector = Off  
t2+0.1 Set Load/Inject Valve = Inject  
t2+0.1 Set V26 = a (right)  
t2+10 Wait Chromatography Peak Detector = Start of Peak  
t3+30 Wait Chromatography Peak Detector = End of Peak

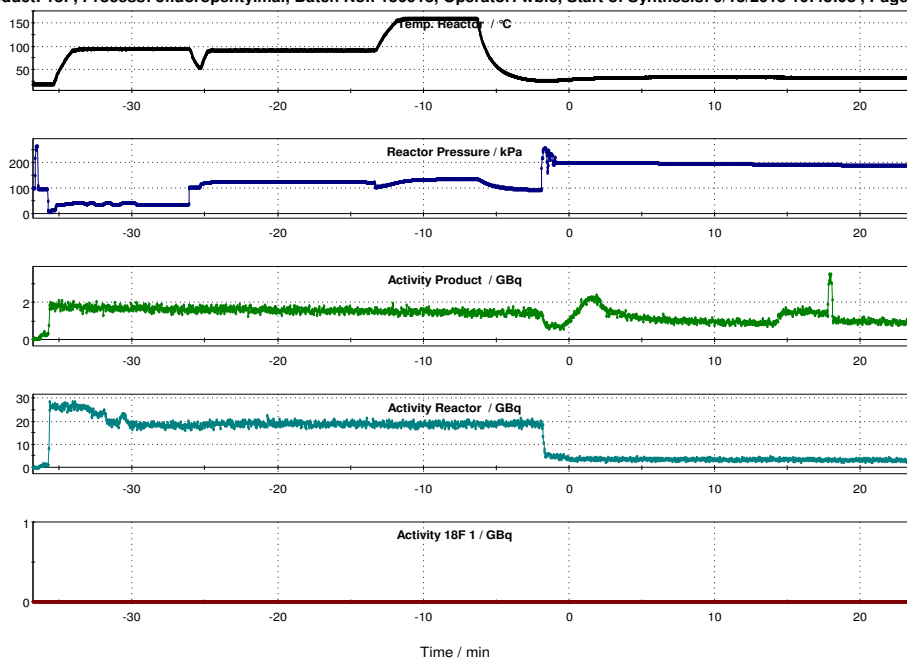
### ***N*-(5-[<sup>18</sup>F]fluoropentyl)maleimide trap and release on Sep-Pak C18(formulation)**

t1+0 Set V18 (HPLC Fraction) = a (left)  
t1+0.1 Set V21 = b (down)  
t1+0.2 Set V17 = a (left)  
t1+0.3 Set V15 = a (left)  
t1+40 Set V21 = a (up)  
t1+40.1 Set V17 = b (right)

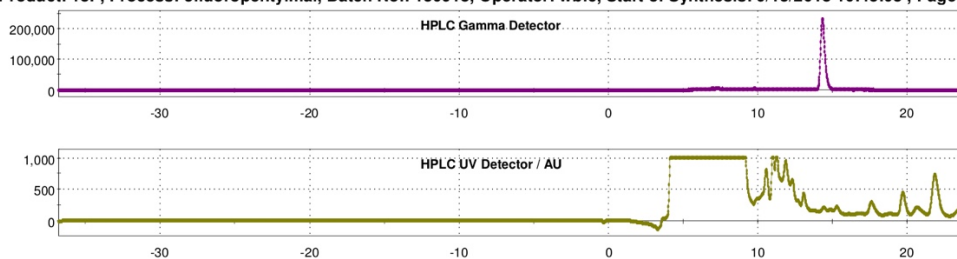
- t1+40.2 Set V15 = b (right)
- t1+40.3 Set V19 = Open
- t1+40.4 Set V08 Vial8 = b (up)
- t1+41 Set V09 Vial9 = b (up)
- t1+41.5 Set V22 = a (right)
- t1+1'6 Set V19 = Close
- t1+1'6 Set Process Control = Stop Synthesis
- t1+1'6 Set Process Control = Show message and wait

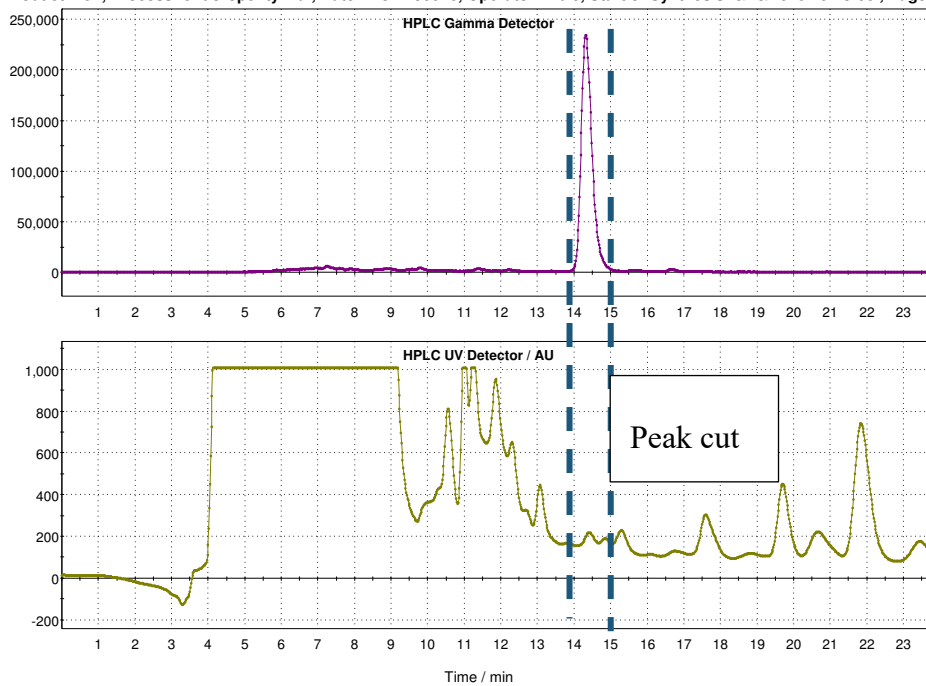
### 8.3 GE TRACERlab FX<sub>FN</sub> activity report for *N*-(5-[<sup>18</sup>F]fluoropentyl)maleimide radiosynthesis and semi-prep purification chromatogram

Product: 18F, Process: 5fluoropentylmal, Batch No.: 130918, Operator: wbic, Start of Synthesis: 9/13/2018 10:43:08 , Page 1/2



Product: 18F, Process: 5fluoropentylmal, Batch No.: 130918, Operator: wbic, Start of Synthesis: 9/13/2018 10:43:08 , Page 2/2





8.4 Advion Nanotek activity balance sheet for [<sup>18</sup>F]SFB radiosynthesis

<i>ACTIVITY BALANCE</i>			Radionuclide:	18F
			Half-life, min:	109.77
EOB:		10:30:00		
Start of Synthesis (SOS)		10:47		
#1 25 1' uA 0.2uAh	activity A(t)	time (hh:mm)	activity at SOS	% decay corrected
<sup>18</sup> F-fluoride EOB	1752.0	10:47	1752.0	---
Conc.vial	33.0	13:13	180.0	10.3%
QMA trap	7.0	12:27	13.2	0.8%
<sup>18</sup> O-water	408.0	11:52	615.1	35.1%
Product vial 1	0.0	12:27	0.0	0.0%
Product vial 2	3.0	12:33	5.9	0.3%
Product vial 3	0.2	12:33	0.4	0.0%
Product vial 4	33.0	13:06	79.4	4.5%
Waste	23.0	13:10	56.7	3.2%
Total activity recovered			950.6	54.3%
QC: % Fluoride	0			
% Product	0			
% Others				
Missing Activity, MBq:			801.4	45.7%



## 8.5 Protocol for culturing Colo205D cancer cells

These are semi-suspension cells thus they grow in suspension and attached to the flask.

1. Transfer growth media (~ 20 mL for T75 flask) and floating cells in a sterile 50 mL Falcon centrifuge tube.

2. Rinse flask containing the attached cell layer with 1 x PBS (5 mL) and transfer PBS to Falcon tube.

3. Add Gibco 0.25% Trypsin- 1 mM EDTA (1.5 mL) to the T75 flask and return to incubator at 37°C to facilitate dissociation from vessel for 3 minutes.

Do not agitate the cells to avoid clumping of cells.

4. Wash flask with RPMI-1640 (4.5 mL) (with added 10% heat inactivated FBS) growth media and aspirate cells by gently pipetting.

5. Transfer the detached cells into the 50 mL centrifuge tube containing the old medium and centrifuge at 1,200 rpm for 3min.

6. Remove the supernatant and resuspend the cell pellet in 10 mL of fresh and pre-warmed growth media.

7. Add an appropriate aliquot of the cell suspension to a new culture T75 flask containing fresh RPMI-1640 medium (20 mL) and incubate cells at 37 °C.

Growth media: Gibco RPMI-1640, REF 21875-034 supplemented with 10% heat inactivated FBS

Subculture: Passage cells every 2 to 3 days. A subcultivation ratio of 1:4 to 1:8 is recommended.

## 8.6 Protocol for culturing MDA-MB-231-D cancer cells

These are adherent cells thus they grow attached to the culture flask.

1. Aspirate old growth media (~ 20mL for T75 flask).
2. Rinse flask containing the attached cell layer with 1 x PBS (5 mL) and aspirate the PBS.
3. Add Gibco 0.25% Trypsin - 1 mM EDTA (1.5 mL) to the T75 flask and return to incubator at 37 °C to facilitate dissociation from vessel for 3 minutes.
4. Wash flask with Gibco with 10% heat inactivated FBS (4.5 mL) growth media and aspirate cells by gently pipetting.
5. Transfer the detached cells into the 50 mL centrifuge tube containing the old medium and centrifuge at 1,200 rpm for 3min.
6. Remove the supernatant and resuspend the cell pellet in 10 mL of fresh and pre-warmed growth media.
7. Add an appropriate aliquot of the cell suspension to a new culture T75 flask containing 20 mL fresh medium and incubate cells at 37°C.

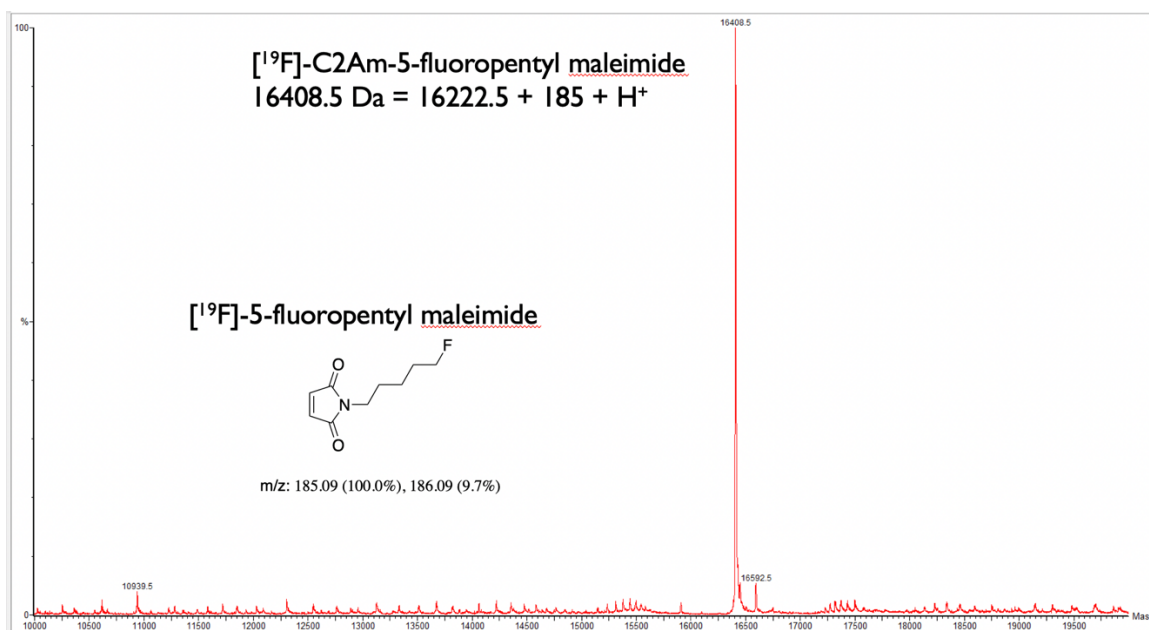
Growth media: Gibco DMEM 1X (Dulbecco's Modified Eagle's Medium, REF 41966-029) supplemented with 10% heat inactivated FBS

Subculture: Passage cells every 2 to 3 days.

## 8.7 Liquid Chromatography Mass Spectrometry spectrum of reduced C2Am (Deconvoluted)



## 8.8 Liquid chromatography mass spectrometry spectrum of *N*-(5-fluoropentyl)maleimide-C2Am (deconvoluted)



## 8.9 HPLC chromatograms of FPenM-C2Am standard and [<sup>18</sup>F]FPenM-C2Am

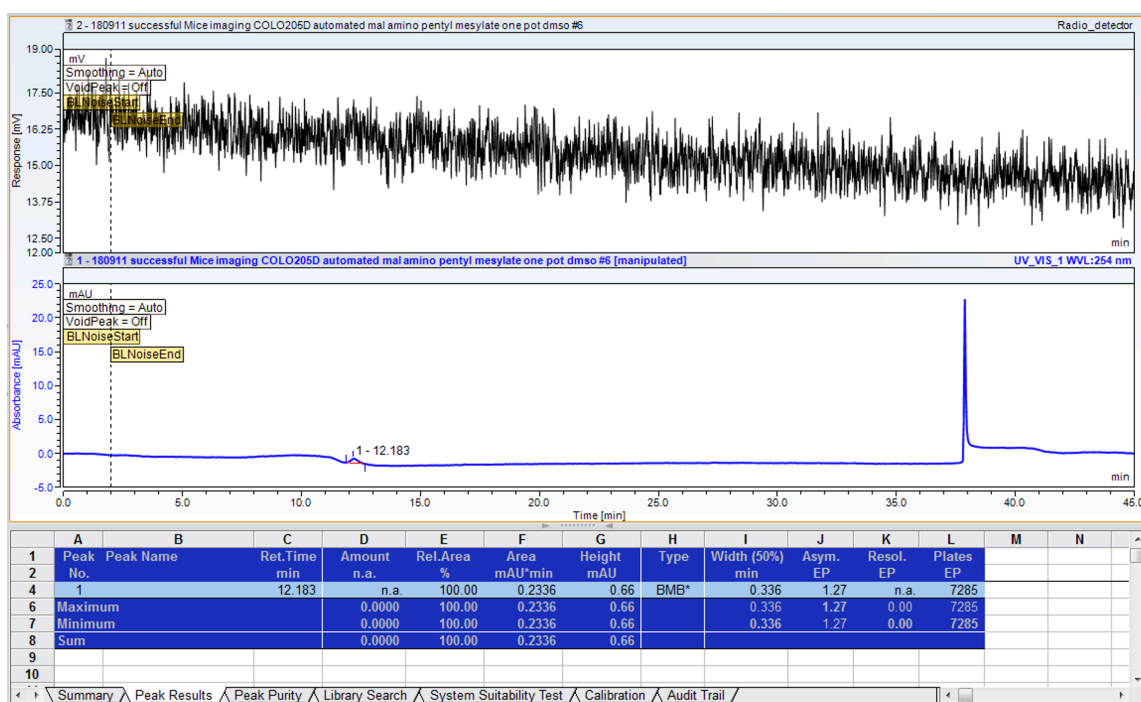


Figure 93. FPenM-C2Am HPLC standard- HPLC chromatogram - radio detector top, 254 nm UV trace bottom (peak at 12.183 min). C2Am (5 ug, 20 uL) protein was injected on the column.

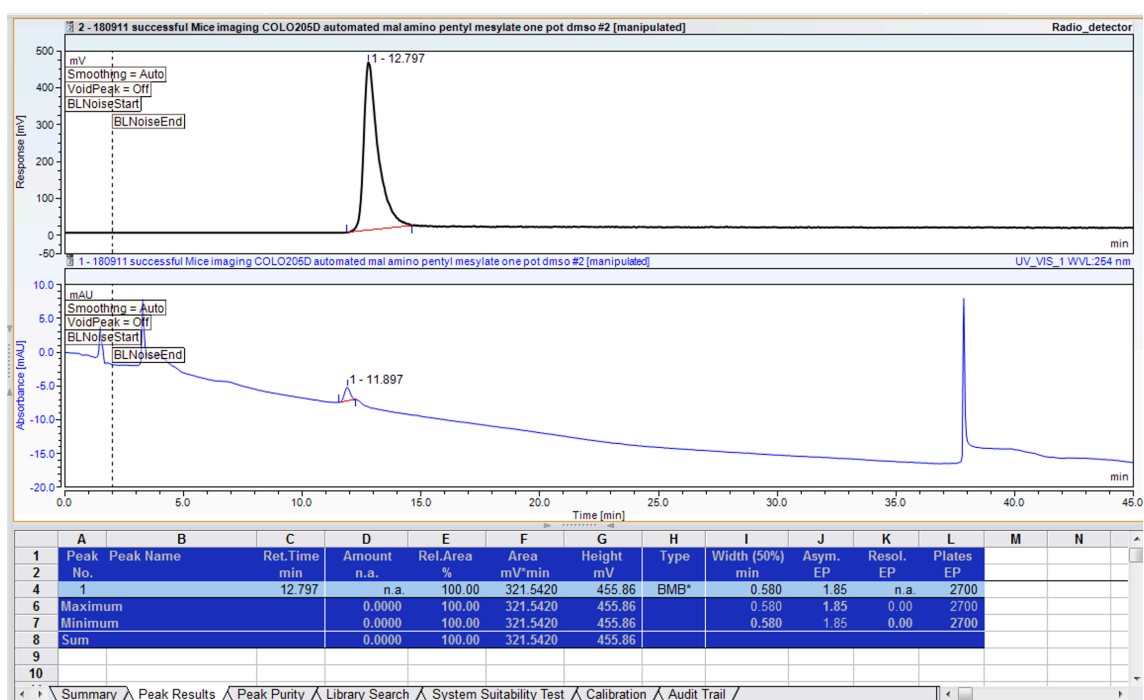
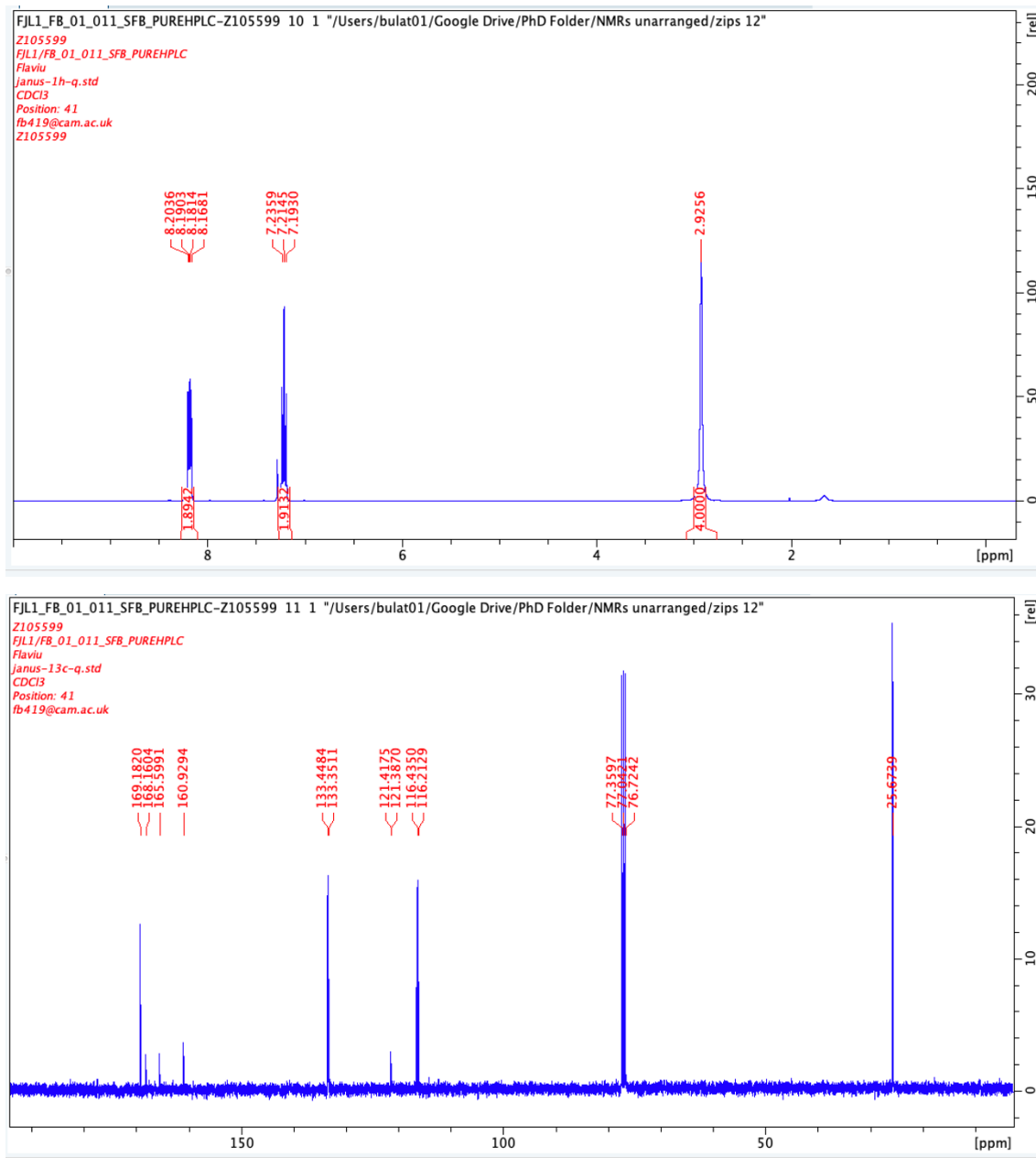
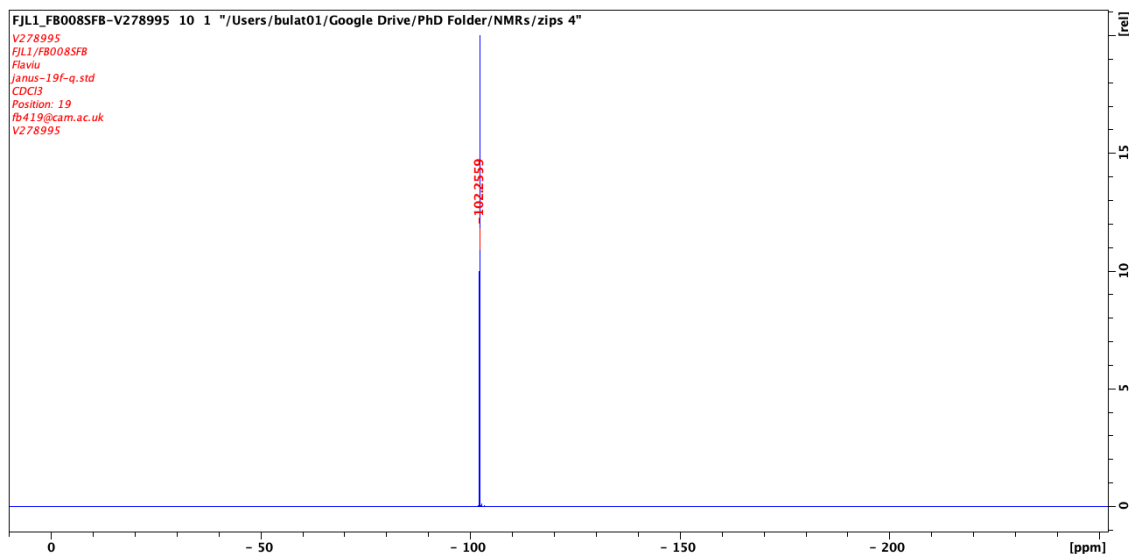


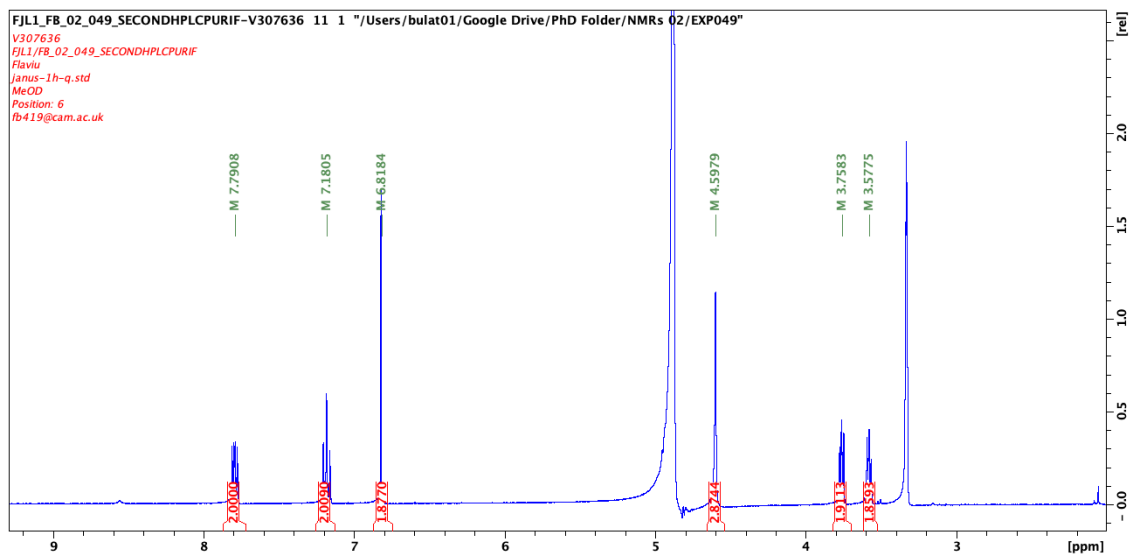
Figure 94. 2. [ $^{18}\text{F}$ ]FPenM-C2Am HPLC chromatogram - radio detector top (peak at 12.797), 254 nm UV tracer bottom (peak at 11.897 min). 20uL of [ $^{18}\text{F}$ ]FPenM-C2Am (1.85 ug, 4 MBq) was injected on the column.

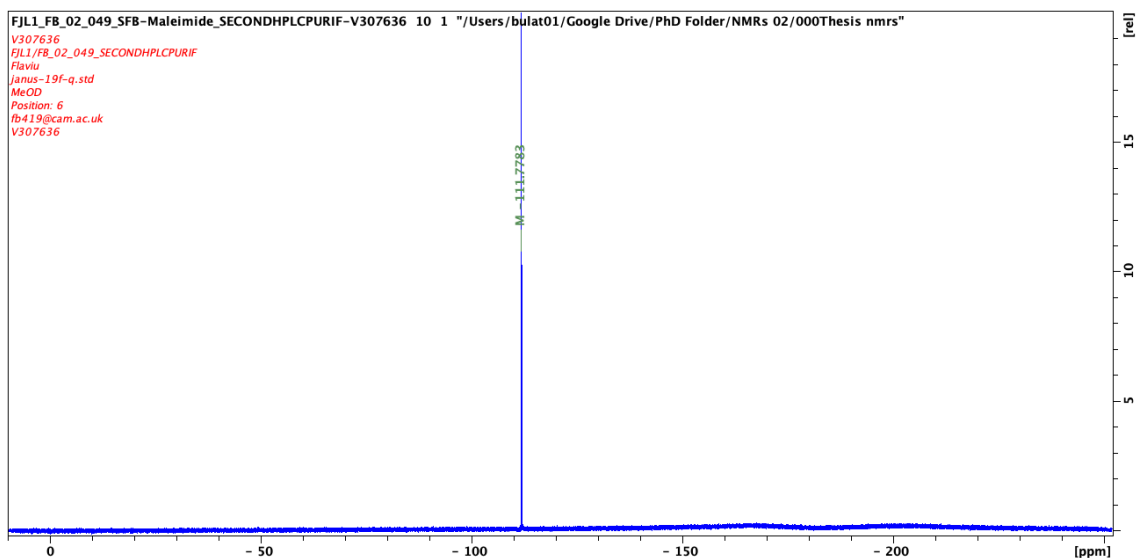
## 8.10 $^1\text{H}$ , $^{13}\text{C}$ and $^{19}\text{F}$ NMR spectra for *N*-succinimidyl-4-fluorobenzoate standard



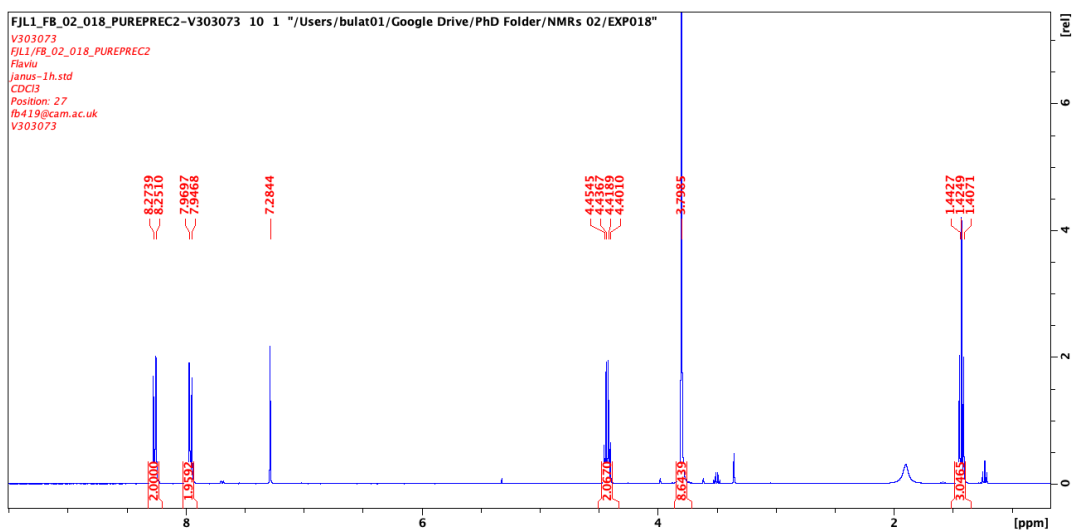


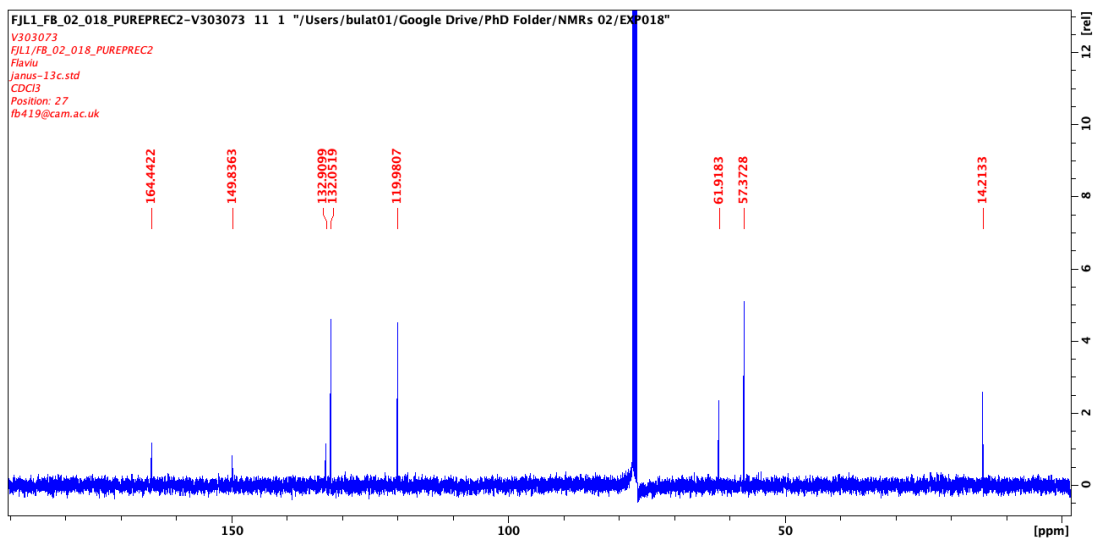
### 8.11 $^1\text{H}$ and $^{19}\text{F}$ NMR spectra for *N*-(2-(2,5-dioxo-2,5-dihydro-1H-pyrrol-1-yl)ethyl)-4-fluorobenzamide



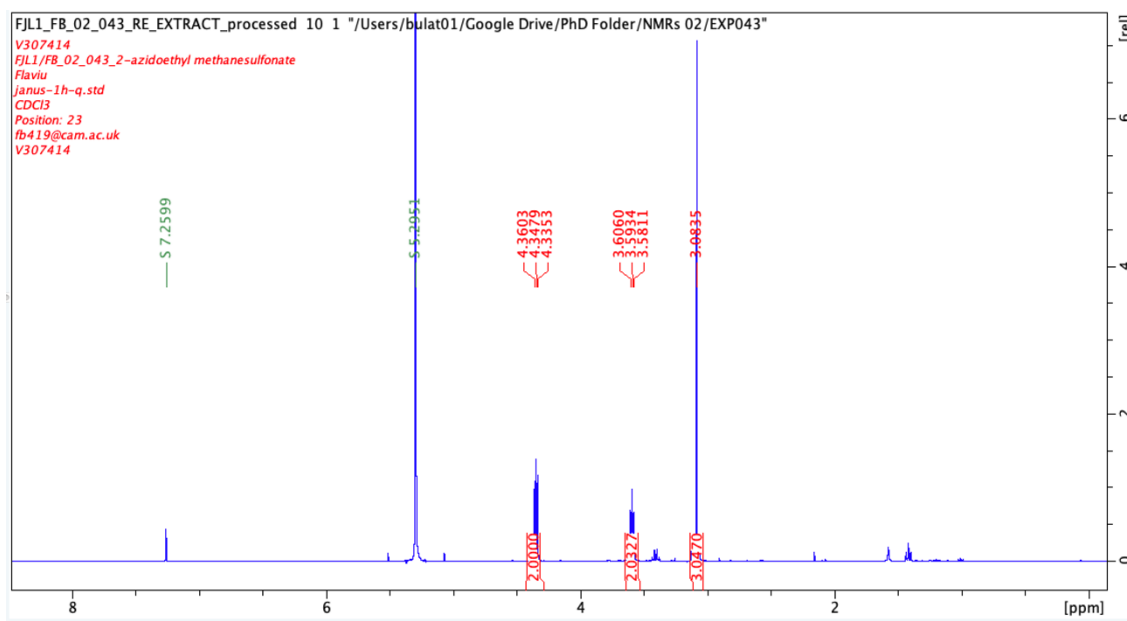


## 8.12 $^1\text{H}$ and $^{13}\text{C}$ NMR spectra for Ethyl 4-(trimethylammonium triflate) benzoate precursor

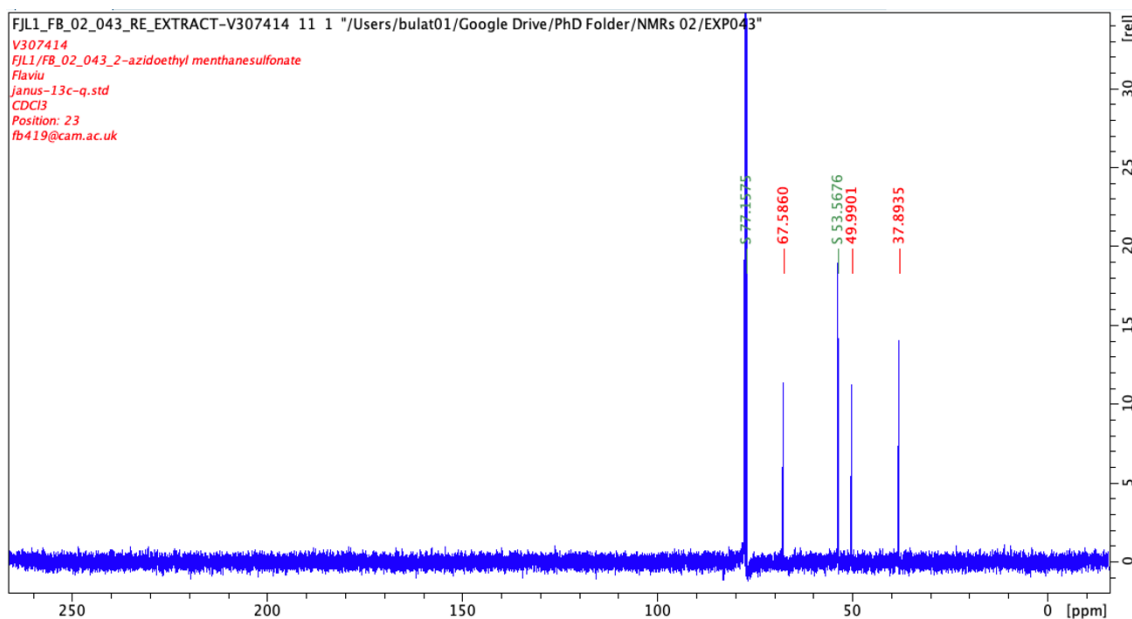




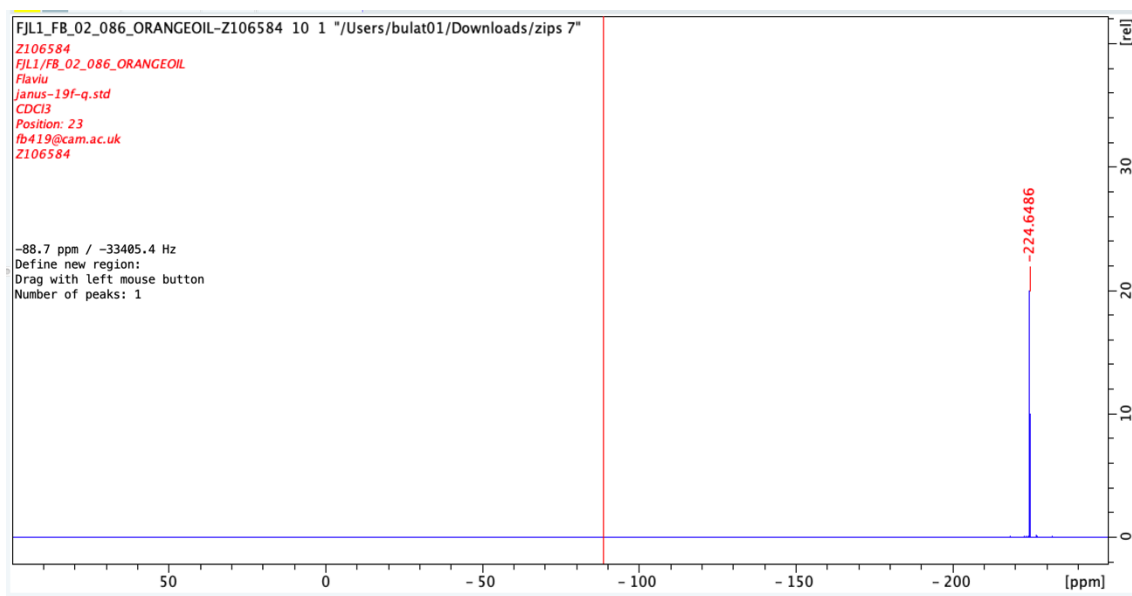
### 8.13 <sup>1</sup>H and <sup>13</sup>C NMR spectra for 2-azidoethyl methylsulfonate precursor



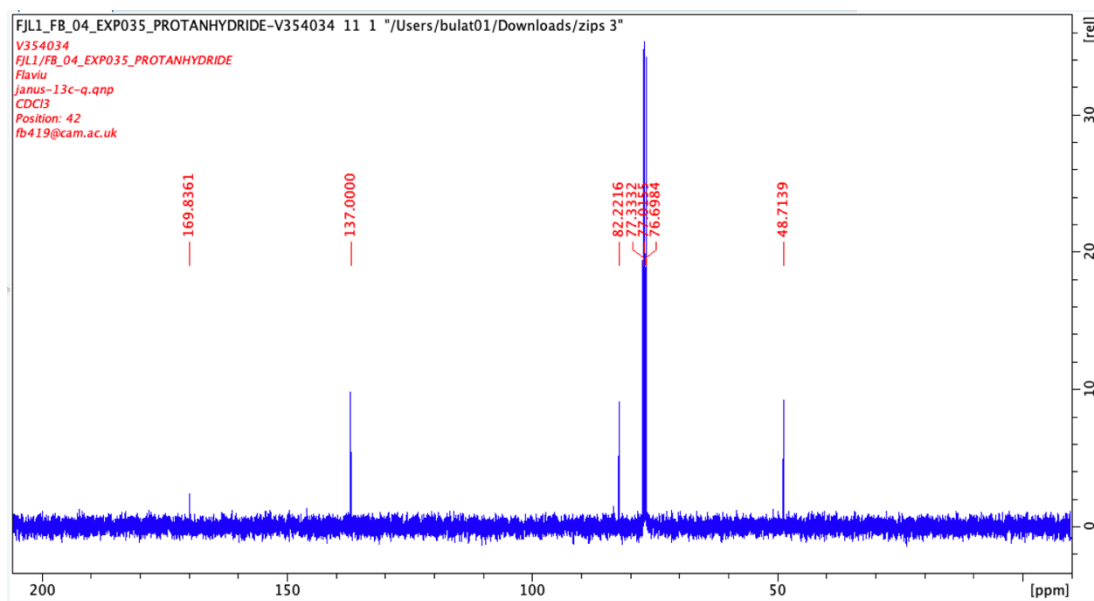
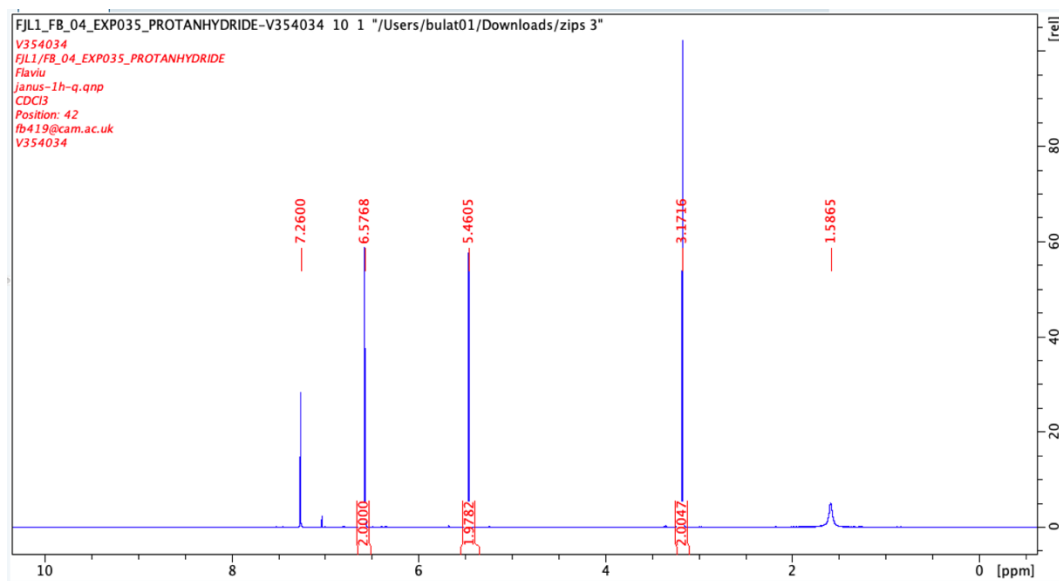




## 8.14 $^{19}\text{F}$ NMR spectrum for 2-fluoroethylazide (HPLC standard)



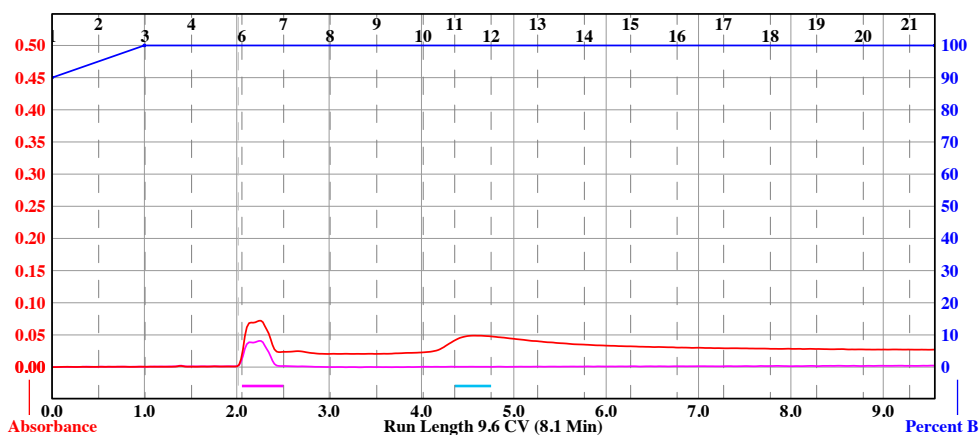
## 8.15 7-Oxanorborn-5-ene-2,3-dicarboxylic anhydride



# 8.16 2-(5-Hydroxypentyl)-3a,4,7,7a-tetrahydro-1H-4,7-epoxyisoindole-1,3(2H)-dione

Sample: 190317@21-46-1      CombiFlash NEXTGEN : NextGen Demo      Sunday 17 March 2019 09:46PM  
 Column: Silica 24g Gold      Peak Tube Volume: Max.  
 SN: E00401509BDA20B1 Lot: 282229603W Non-Peak Tube Volume: Max.  
 Flow Rate: 40 ml/min      Loading Type: Solid  
 Equilibration Volume: 5.0 CV      Wavelength 1 (red): 254nm  
 Initial Waste: 0.0 CV      Peak Width: 1 min  
 Air Purge: 1.0 min      Threshold: 0.20 AU  
 Solvent A: Pet Ether 40-60      Wavelength 2 (purple): 280nm  
 Solvent B: Ethyl Acetate

Run Notes:



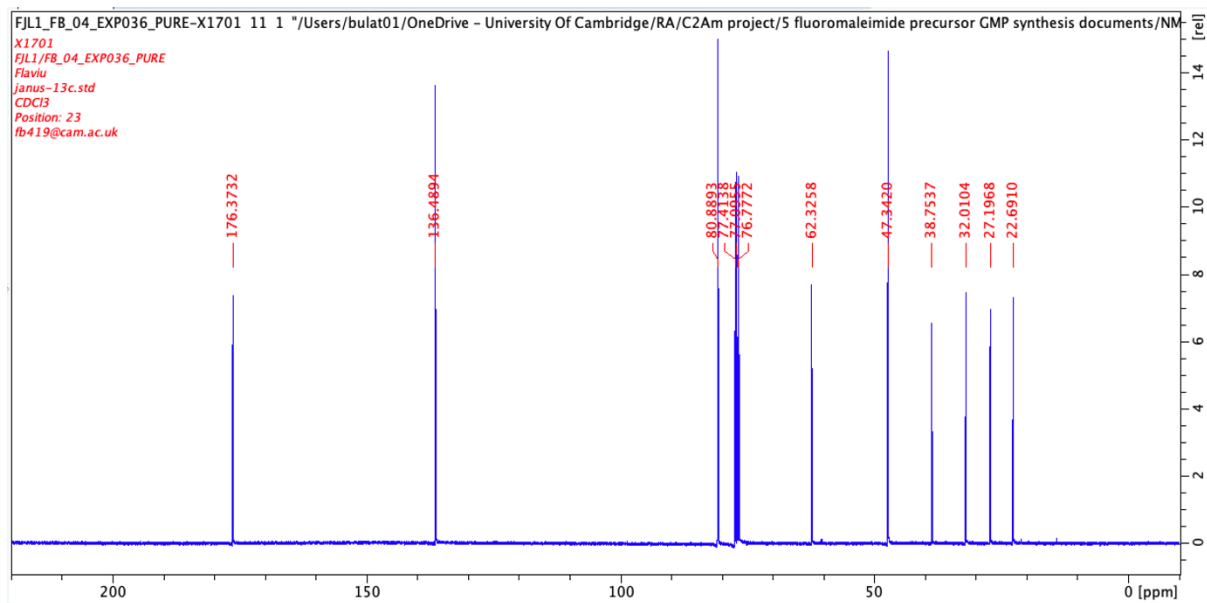
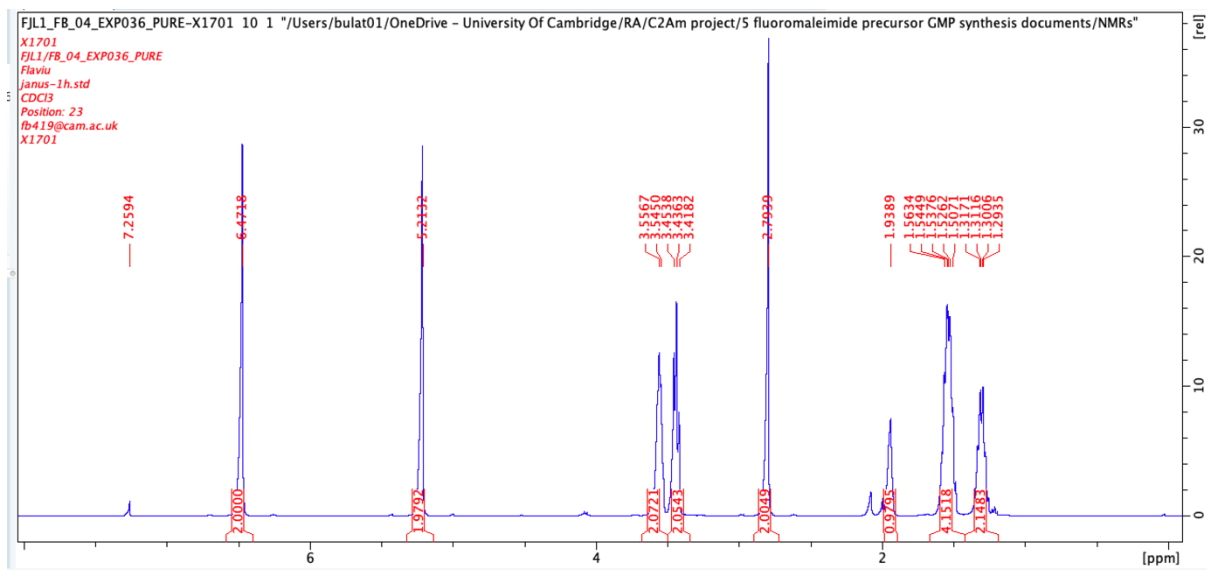
Rack A					Peak #	Start Tube	End Tube
71	72	73	74	75	1	A:6	A:6
70	69	68	67	66	2	A:11	A:11
61	62	63	64	65			
60	59	58	57	56			
51	52	53	54	55			
50	49	48	47	46			
41	42	43	44	45			
40	39	38	37	36			
31	32	33	34	35			
30	29	28	27	26			
21	22	23	24	25			
20	19	18	17	16			
11	12	13	14	15			
10	9	8	7	6			
1	2	3	4	5			

Duration	%B	Solvent A	Solvent B
0.0	90.0	Pet Ether 40-60	Ethyl Acetate
1.0	100.0	Pet Ether 40-60	Ethyl Acetate
8.6	100.0	Pet Ether 40-60	Ethyl Acetate

16 mm x 150 mm Tubes

# Targeted Imaging Agents for Detecting Tumour Cell Death following Therapy



# 8.17 5-(1,3-Dioxo-1,3,3a,4,7,7a-hexahydro-2H-4,7-epoxyisoindol-2-yl)pentyl methanesulfonate

Sample: 190325@12-44-1

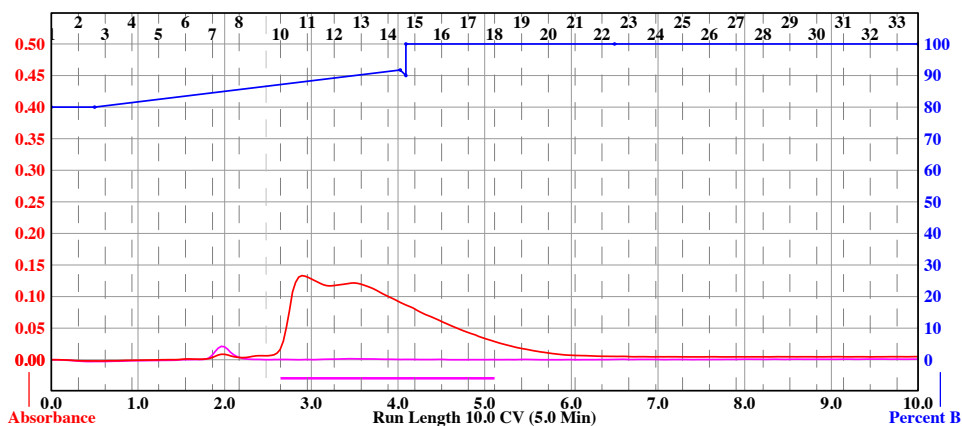
CombiFlash NEXTGEN : NextGen Demo

Monday 25 March 2019 12:44PM

Column: Silica 40g Gold  
 SN: E00401509C461798 Lot: 291117603W  
 Flow Rate: 110 ml/min  
 Equilibration Volume: 0.0 CV  
 Initial Waste: 0.0 CV  
 Air Purge: 1.0 min  
 Solvent A: Pet Ether 40-60  
 Solvent B: Ethyl Acetate

Peak Tube Volume: Max.  
 Non-Peak Tube Volume: Max.  
 Loading Type: Solid  
 Wavelength 1 (red): 254nm  
 Peak Width: 30 sec  
 Threshold: 0.25 AU  
 Wavelength 2 (purple): 280nm

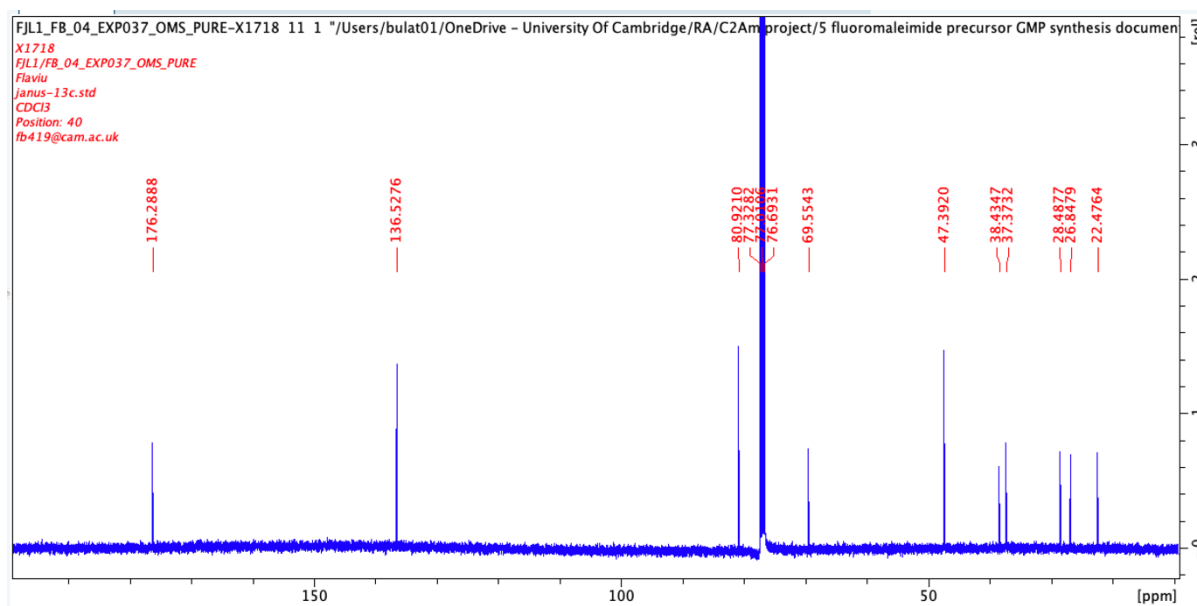
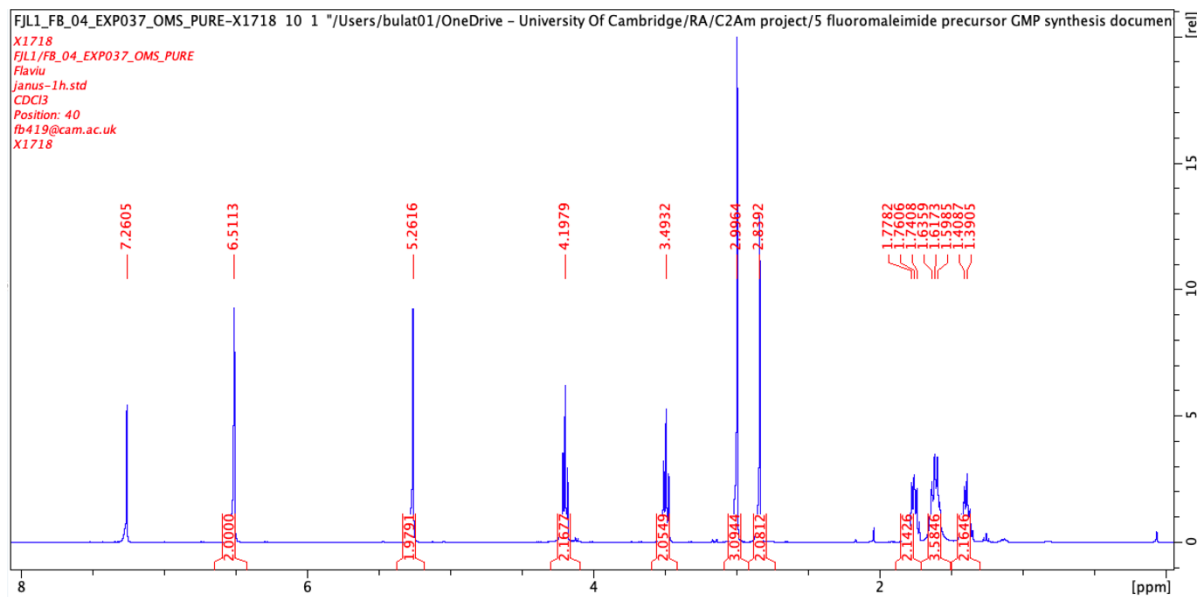
Run Notes:



Rack B					Peak #	Start Tube	End Tube	
					1	B:10	B:17	
71	72	73	74	75				
70	69	68	67	66				
61	62	63	64	65				
60	59	58	57	56				
51	52	53	54	55				
50	49	48	47	46				
41	42	43	44	45				
40	39	38	37	36				
31	32	33	34	35				
30	29	28	27	26				
21	22	23	24	25				
20	19	18	17	16				
11	12	13	14	15				
10	9	8	7	6				
1	2	3	4	5				
16 mm x 150 mm Tubes					Duration	%B	Solvent A	Solvent B
					0.0	80.0	Pet Ether 40-60	Ethyl Acetate
					0.5	80.0	Pet Ether 40-60	Ethyl Acetate
					3.5	91.8	Pet Ether 40-60	Ethyl Acetate
					0.1	90.0	Pet Ether 40-60	Ethyl Acetate
					0.0	100.0	Pet Ether 40-60	Ethyl Acetate
					2.4	100.0	Pet Ether 40-60	Ethyl Acetate
					3.5	100.0	Pet Ether 40-60	Ethyl Acetate

Page 1 of 1

# Targeted Imaging Agents for Detecting Tumour Cell Death following Therapy



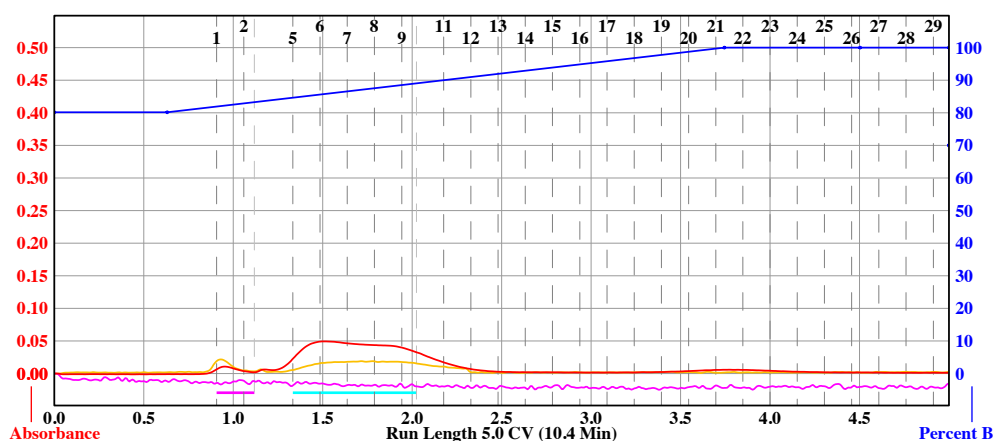
# 8.18 2-(5-Fluoropentyl)-3a,4,7,7a-tetrahydro-1H-4,7-epoxyisoindole-1,3(2H)-dione

Preparative purification of 2-(5-fluoropentyl)-3a,4,7,7a-tetrahydro-1H-4,7-epoxyisoindole-1,3(2H)-dione using the Teledyne Isco NextGen CombiFlash Rf+

Sample: 5-fluoropentyl\_furanmaleimide      Rf+ : Lisa      Sunday 16 June 2019 04:17PM

RediSep Column: Silica 80g      Peak Tube Volume: Max.      All Wavelength (orange): 200-300nm  
 SN: E0410A4DEEA6B Lot: 272131604X      Non-Peak Tube Volume: Max.      Peak Width: 2 min  
 Flow Rate: 60 ml/min      Loading Type: Solid (Pause)      Threshold: 0.20 AU  
 Equilibration Volume: 2.0 CV      Wavelength 1 (red): 254nm  
 Initial Waste: 0.0 CV      Peak Width: 2 min  
 Air Purge: 0.0 min      Threshold: 0.20 AU  
 Solvent A: Pet Ether      Wavelength 2 (purple): 210nm  
 Solvent B: Ethyl Acetate

Run Notes:



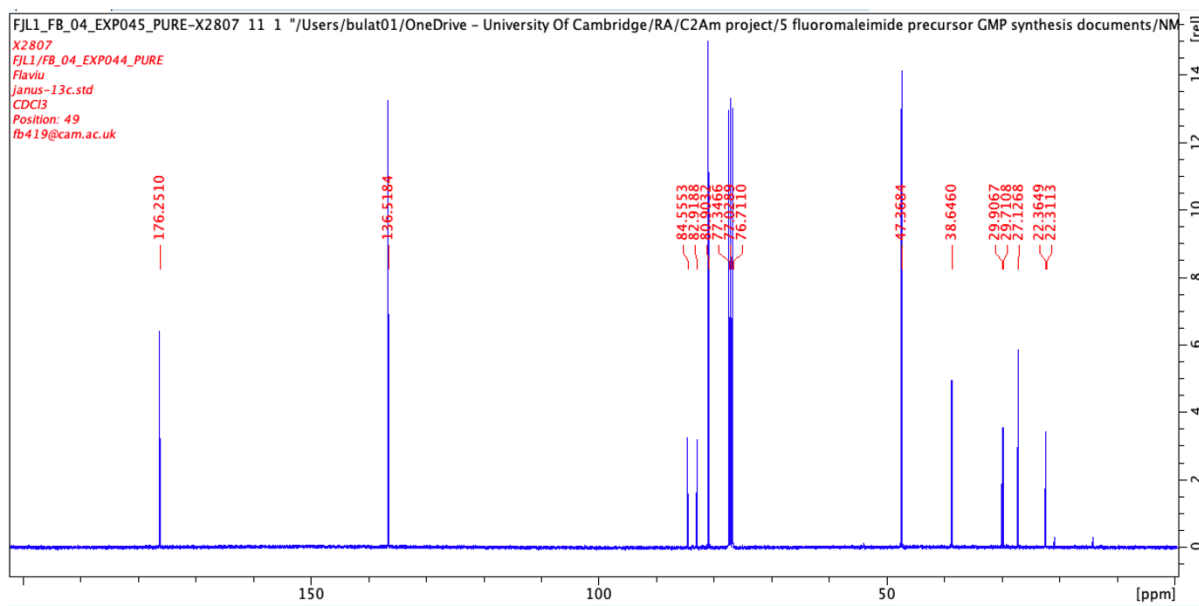
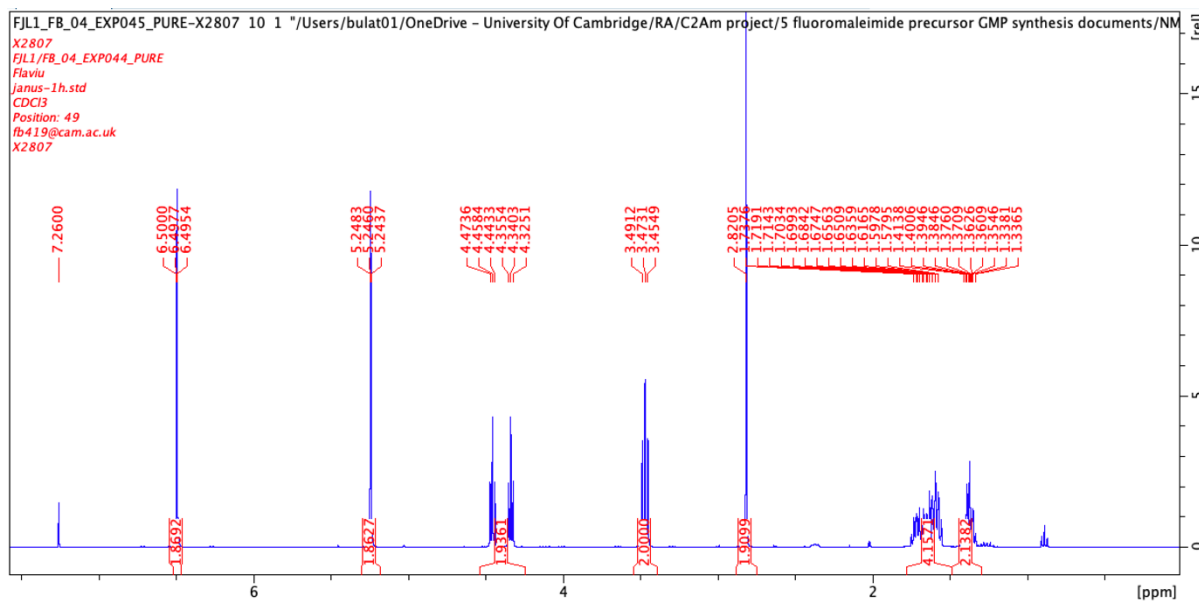
Rack A					Peak #	Start Tube	End Tube
71	72	73	74	75	1	A:1	A:2
70	69	68	67	66	2	A:5	A:9
61	62	63	64	65			
60	59	58	57	56			
51	52	53	54	55			
50	49	48	47	46			
41	42	43	44	45			
40	39	38	37	36			
31	32	33	34	35			
30	29	28	27	26			
21	22	23	24	25			
20	19	18	17	16			
11	12	13	14	15			
10	9	8	7	6			
1	2	3	4	5			

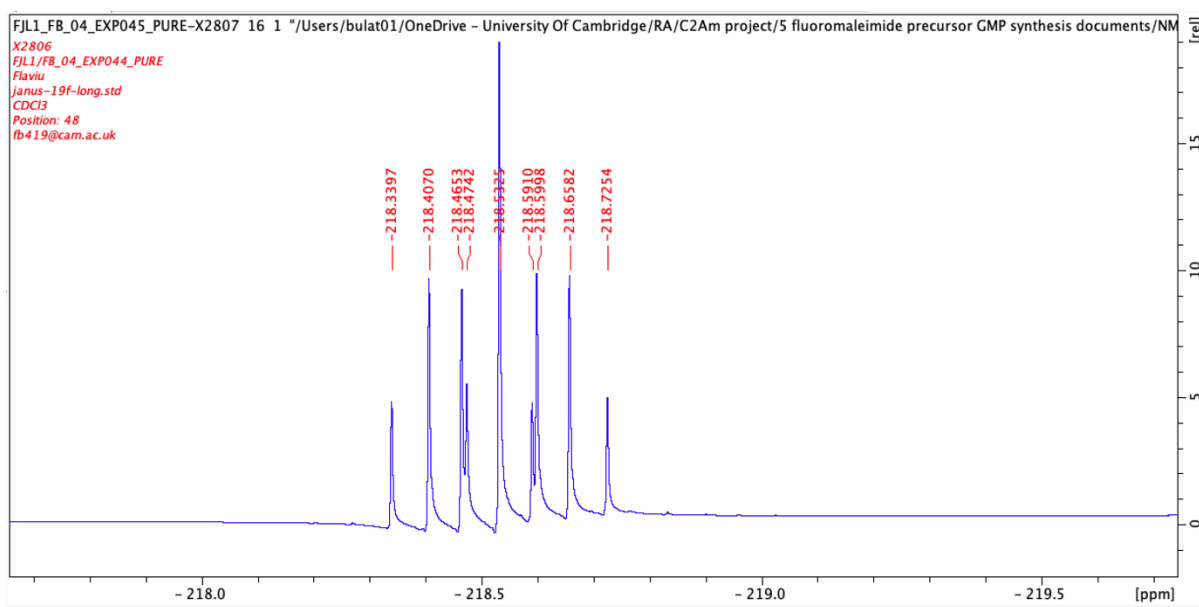
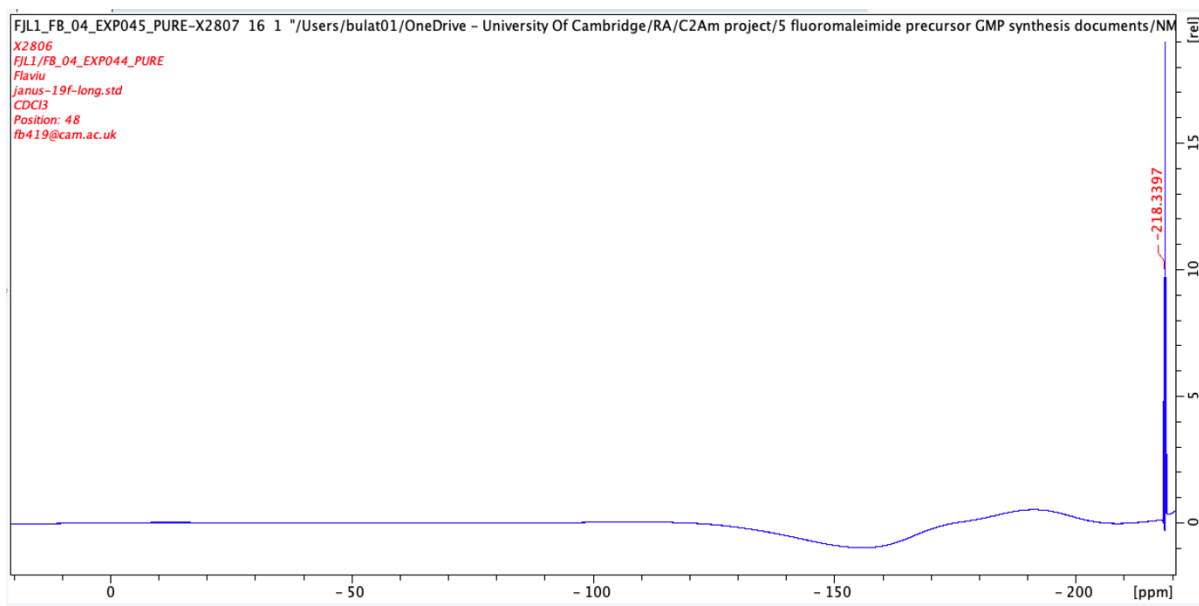
Duration	%B	Solvent A	Solvent B
0.0	80.2	Pet Ether	Ethyl Acetate
0.6	80.2	Pet Ether	Ethyl Acetate
3.1	100.0	Pet Ether	Ethyl Acetate
0.8	100.0	Pet Ether	Ethyl Acetate
0.5	100.0	Pet Ether	Ethyl Acetate
0.0	70.0	Pet Ether	Ethyl Acetate
0.0	70.0	Pet Ether	Ethyl Acetate

16 mm x 150 mm Tubes

$^1\text{H}$ ,  $^{13}\text{C}$  and  $^{19}\text{F}$  NMR spectra of spectra of 2-(5-fluoropentyl)-3a,4,7,7a-tetrahydro-1H-4,7-epoxyisoindole-1,3(2H)-dione







## 8.19 1-(5-Fluoropentyl)-1H-pyrrole-2,5-dione

Preparative purification of *N*-(5-fluoropentyl)maleimide standard

# Targeted Imaging Agents for Detecting Tumour Cell Death following Therapy

Sample: 5-fluoropentylmaleimide

Rf+ : Lisa

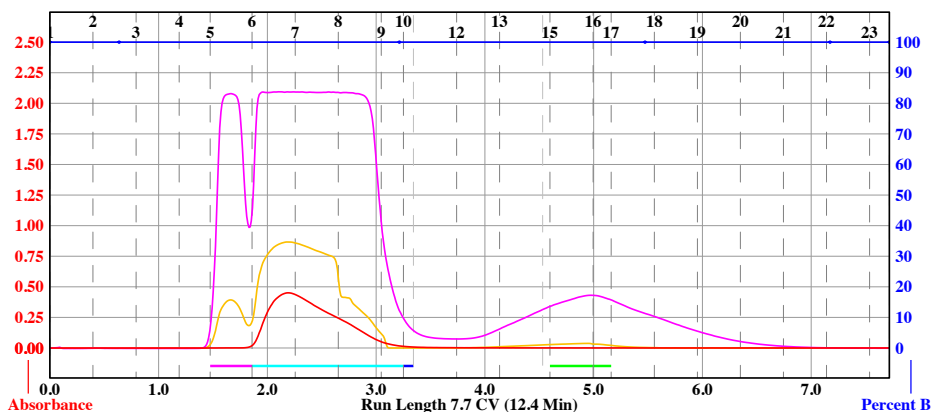
Sunday 16 June 2019 07:56PM

RediSep Column: Silica 40g  
 SN: E04150644E21F8 Lot: 262217001Y  
 Flow Rate: 30 ml/min  
 Equilibration Volume: 4.0 CV  
 Initial Waste: 0.0 CV  
 Air Purge: 2.0 min  
 Solvent A: Pet Ether  
 Solvent B: Diethyl Ether

Peak Tube Volume: Max.  
 Non-Peak Tube Volume: Max.  
 Loading Type: Solid (Pause)  
 Wavelength 1 (red): 300nm  
 Peak Width: 2 min  
 Threshold: 0.20 AU  
 Wavelength 2 (purple): 210nm

All Wavelength (orange): 200-300nm  
 Peak Width: 2 min  
 Threshold: 0.20 AU

**Run Notes:**



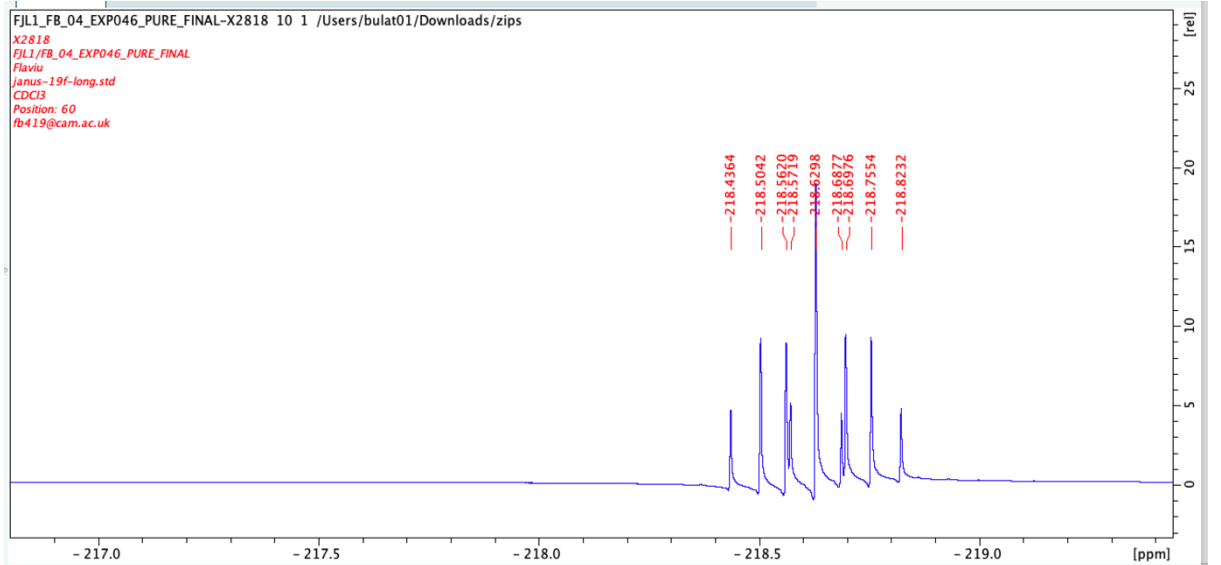
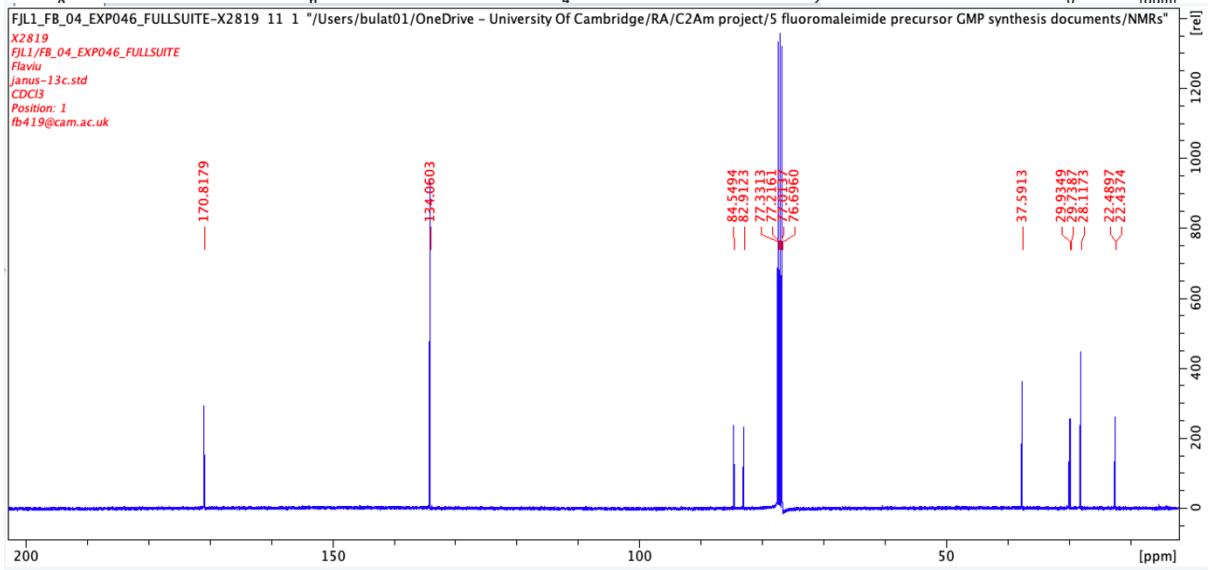
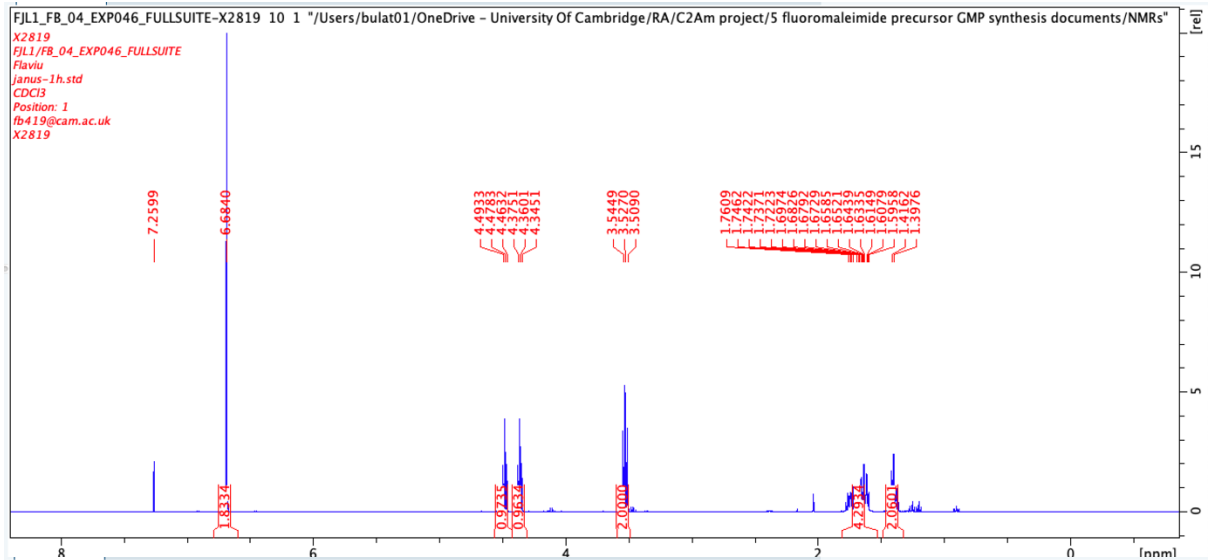
Rack A					Peak #	Start Tube	End Tube
71	72	73	74	75	1	A:5	A:5
70	69	68	67	66	2	A:6	A:9
61	62	63	64	65	3	A:10	A:10
60	59	58	57	56	4	A:15	A:16
51	52	53	54	55			
50	49	48	47	46			
41	42	43	44	45			
40	39	38	37	36			
31	32	33	34	35			
30	29	28	27	26			
21	22	23	24	25			
20	19	18	17	16			
11	12	13	14	15			
10	9	8	7	6			
1	2	3	4	5			

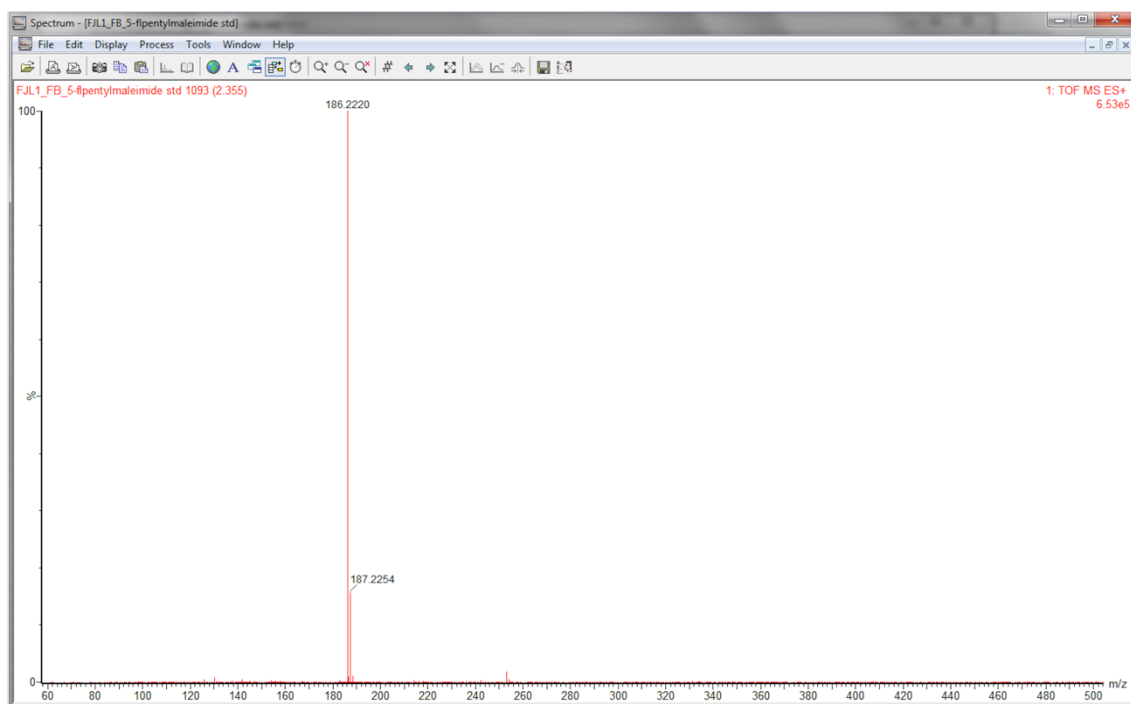
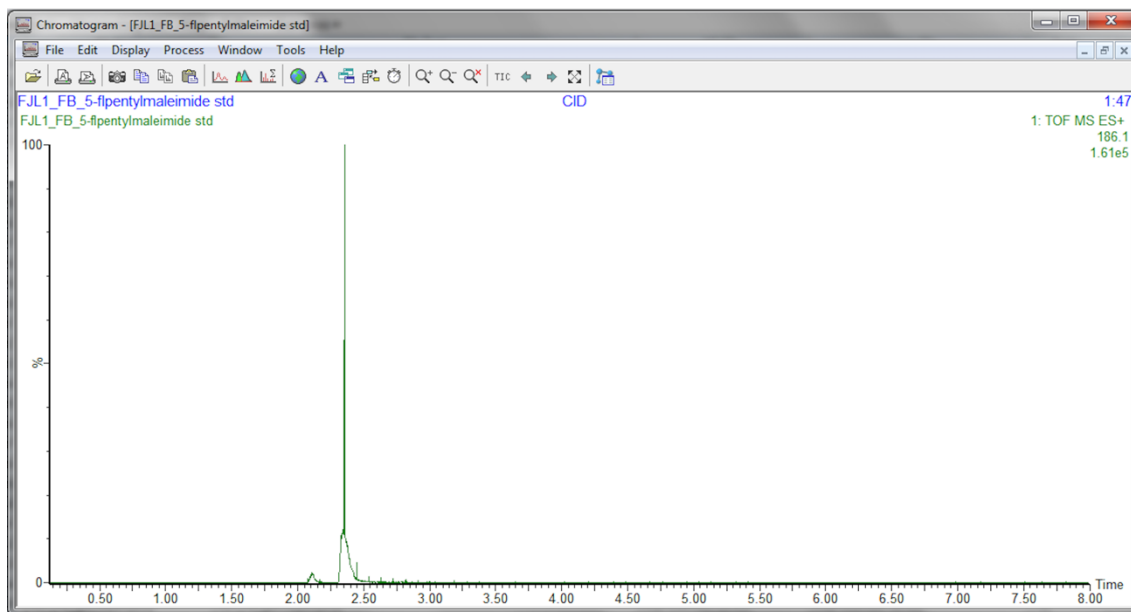
Duration	%B	Solvent A	Solvent B
0.0	100.0	Pet Ether	Diethyl Ether
0.6	100.0	Pet Ether	Diethyl Ether
2.6	100.0	Pet Ether	Diethyl Ether
2.3	100.0	Pet Ether	Diethyl Ether
1.7	100.0	Pet Ether	Diethyl Ether
0.5	100.0	Pet Ether	Diethyl Ether

16 mm x 150 mm Tubes

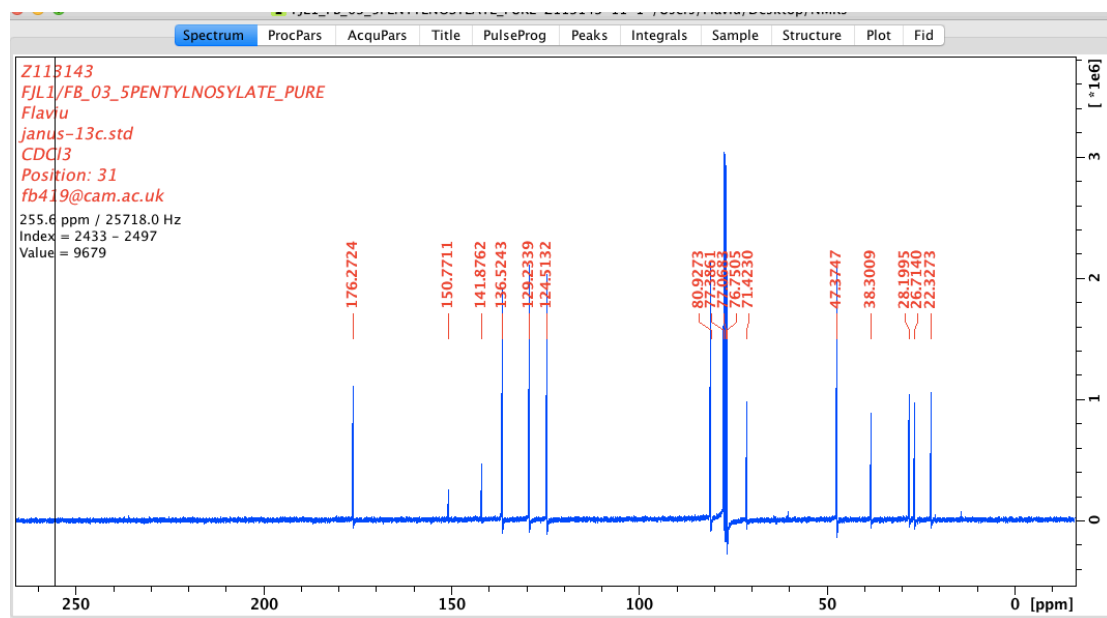
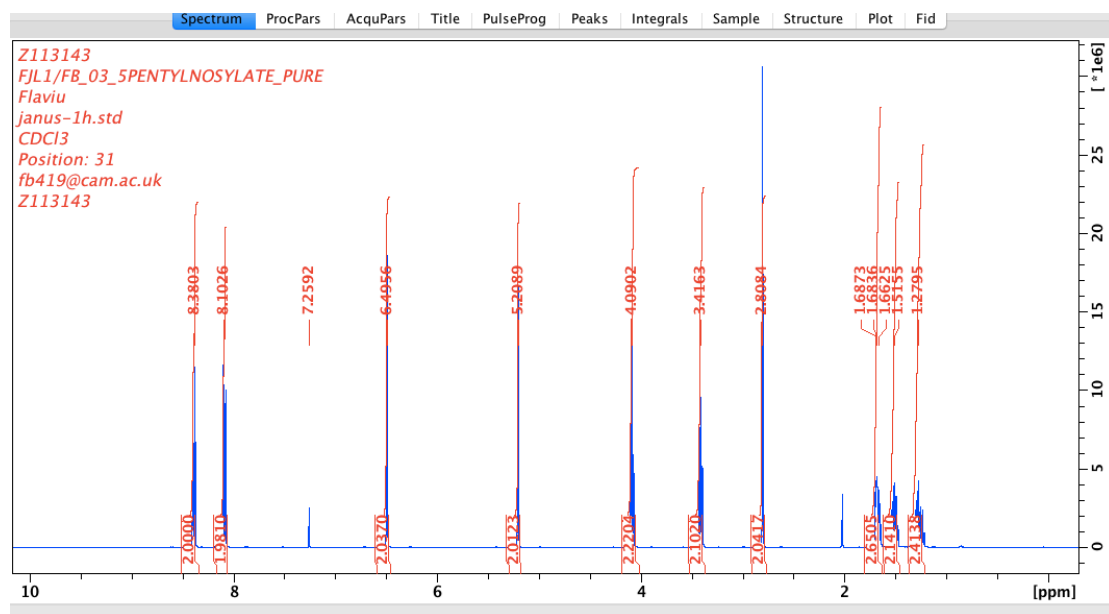
<sup>1</sup>H, <sup>13</sup>C and <sup>19</sup>F NMR spectra of 1-(5-fluoropentyl)-1H-pyrrole-2,5-dione



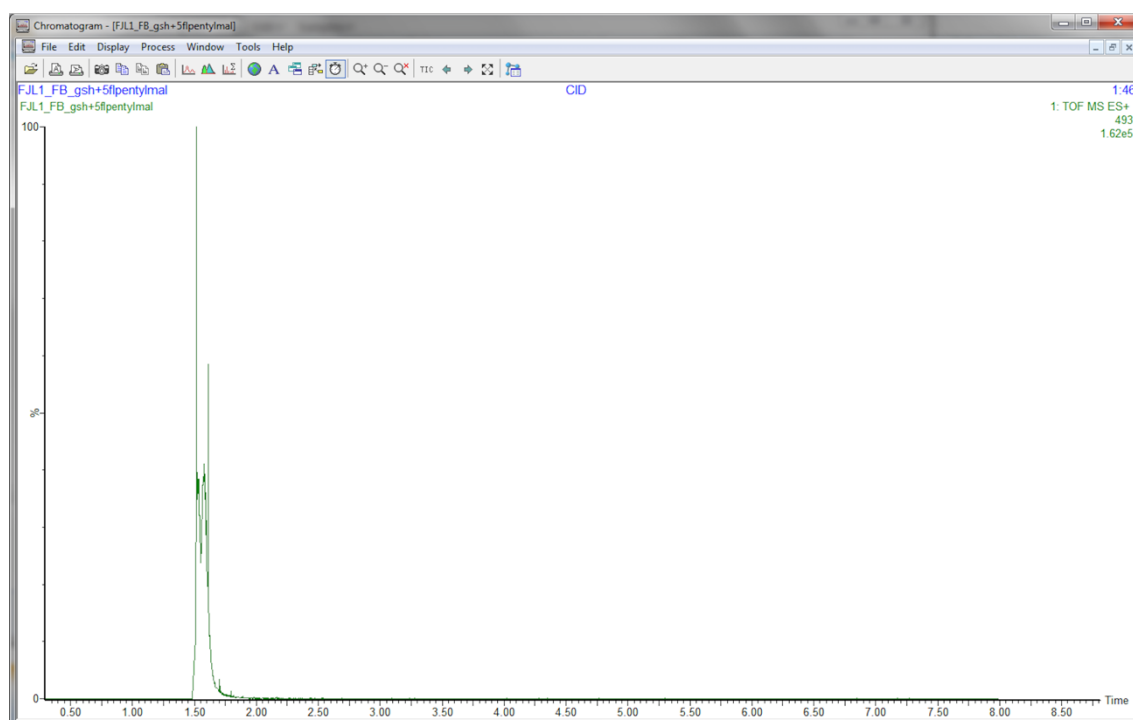
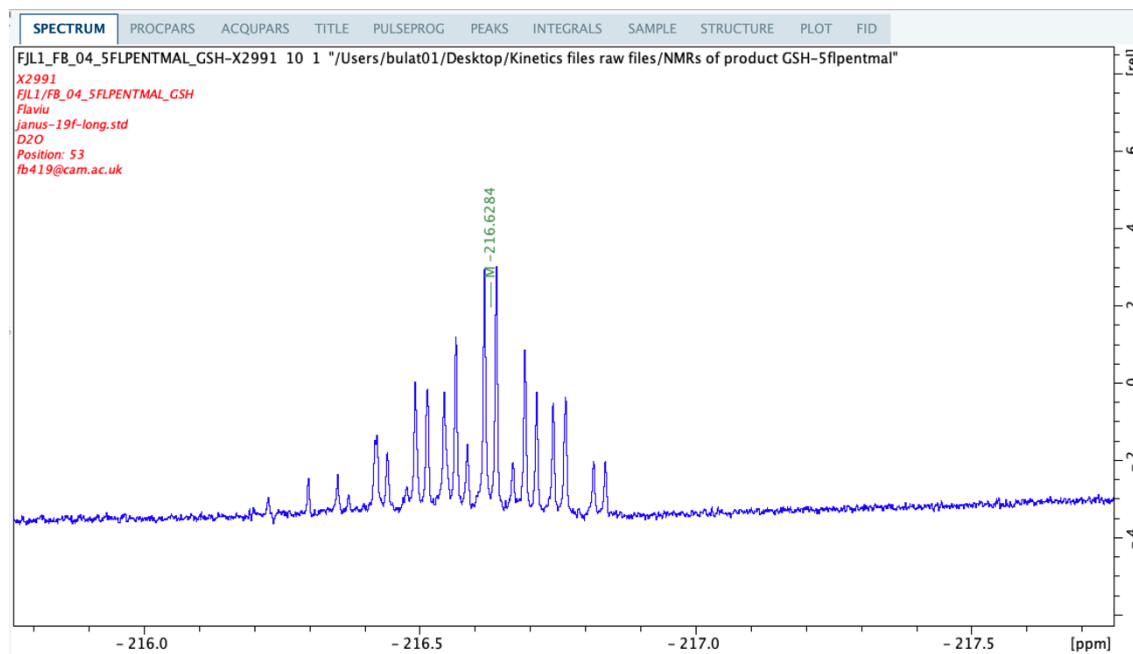
Accurate mass spectra of 1-(5-fluoropentyl)-1H-pyrrole-2,5-dione

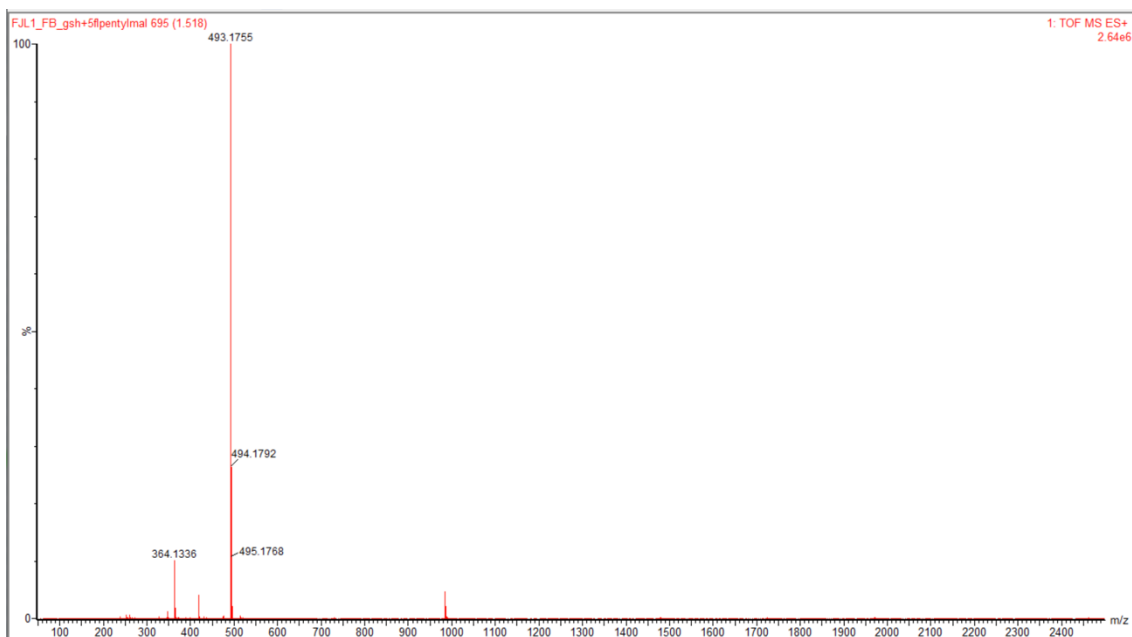


## 8.20 $^1\text{H}$ and $^{13}\text{C}$ NMR spectra of 5-(1,3-Dioxo-1,3,3a,4,7,7a-hexahydro-2H-4,7-epoxyisoindol-2-yl) pentyl 4-nitrobenzenesulfonate

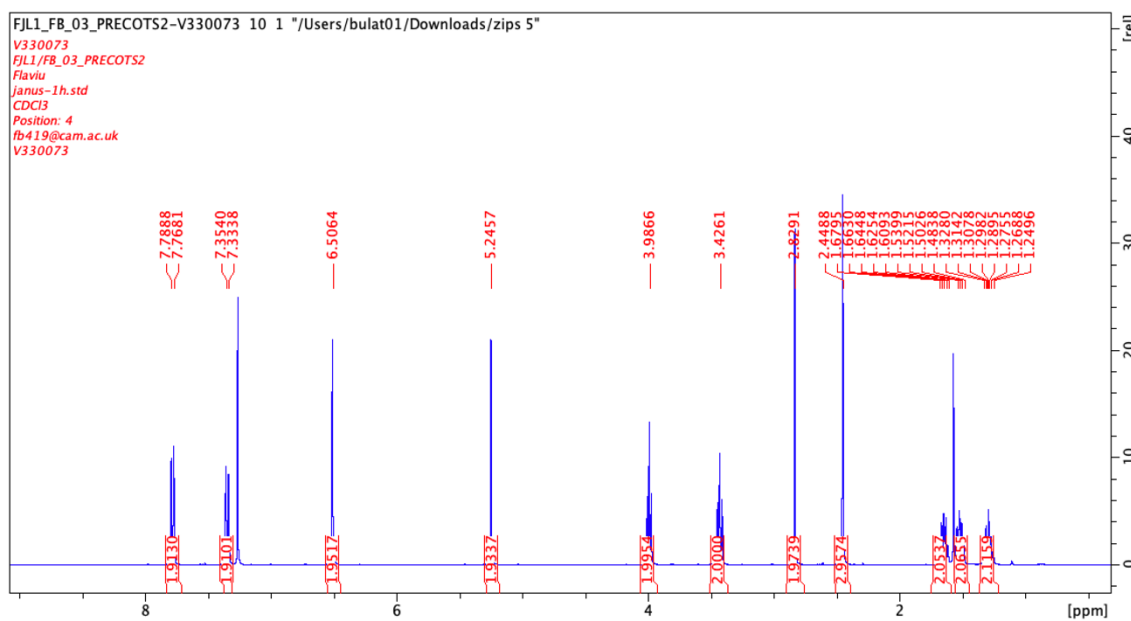


## 8.21 $^{19}\text{F}$ NMR and accurate mass spectra of $N^5$ -(1-((Carboxymethyl)amino)-3-((1-(5-fluoropentyl)-2,5-dioxopyrrolidin-3-yl)thio)-1-oxopropan-2-yl)glutamine



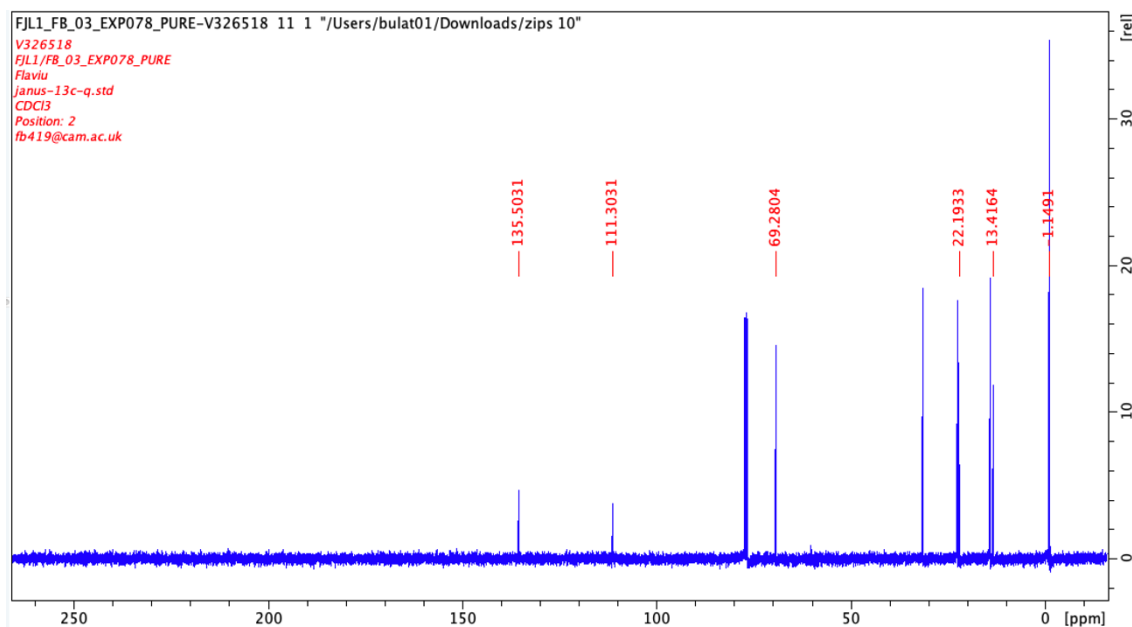
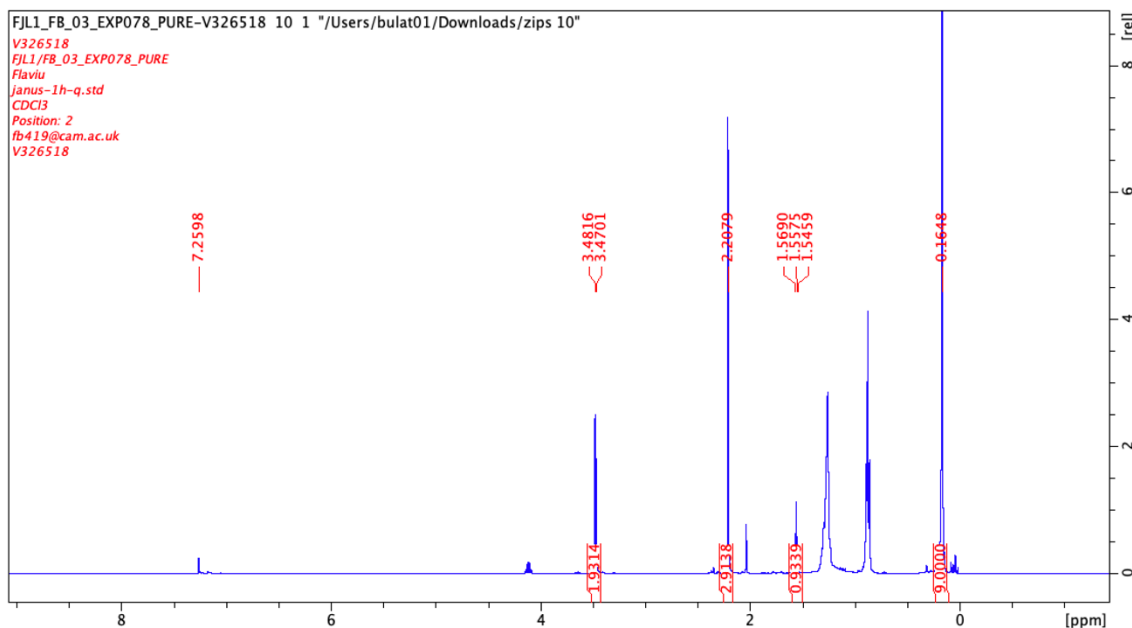


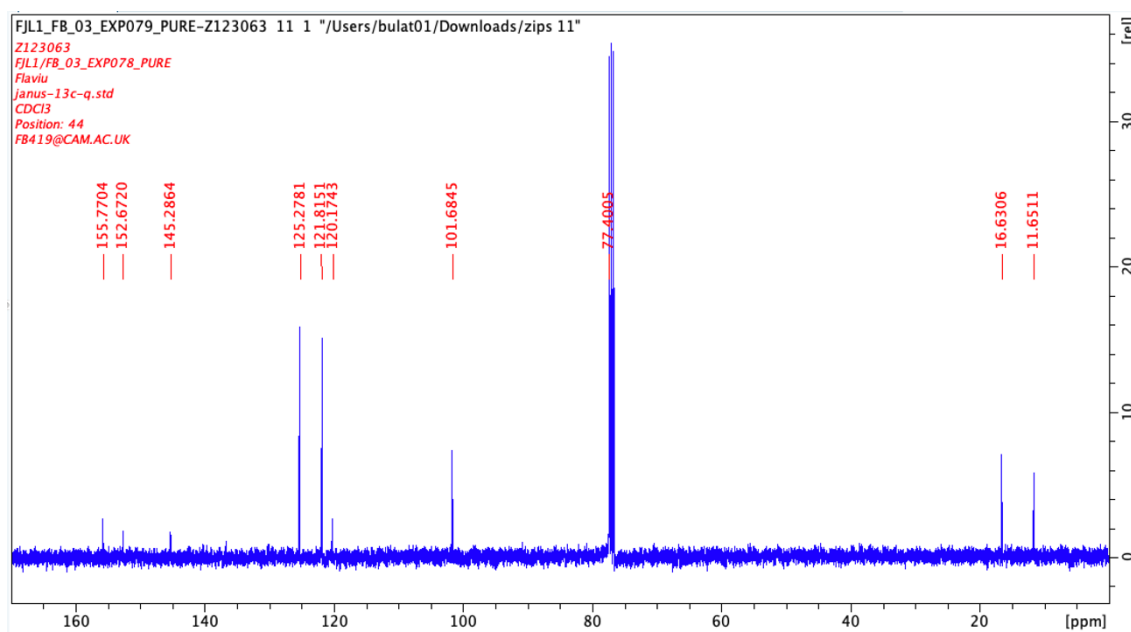
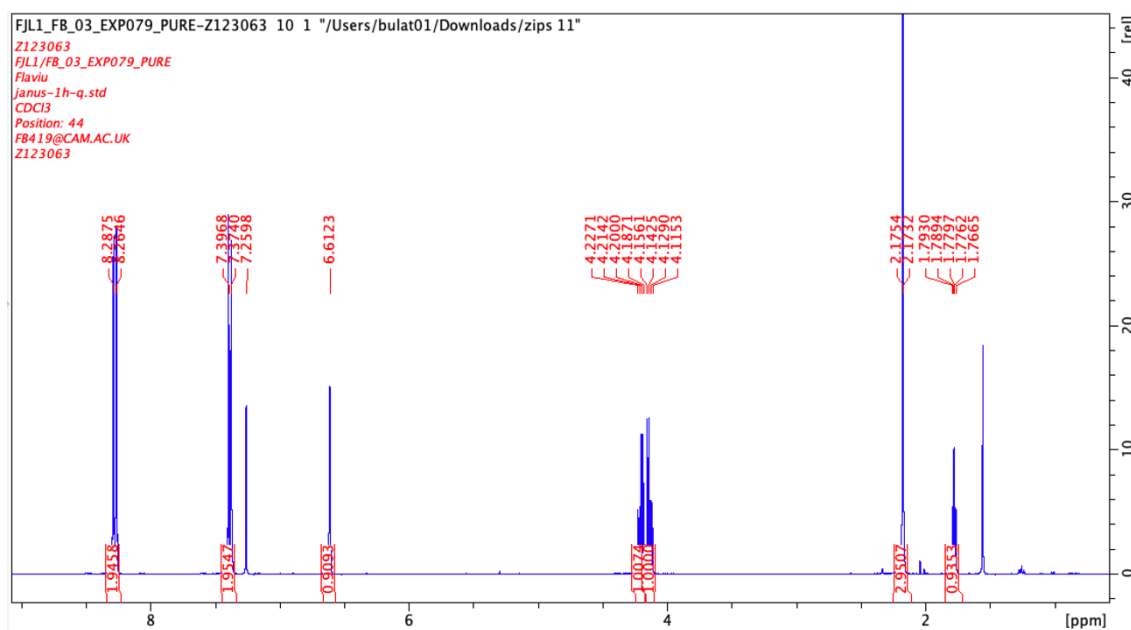
## 8.22 <sup>1</sup>H NMR spectra of 5-(1,3-Dioxo-1,3,3a,4,7,7a-hexahydro-2H-4,7-epoxyisoindol-2-yl) pentyl 4-methyl-benzenesulfonate





## 8.23 $^1\text{H}$ and $^{13}\text{C}$ NMR spectra of (2-Methyl-3-(trimethylsilyl)cycloprop-2-en-1-yl)methanol (**31**)



8.24  $^1\text{H}$  and  $^{13}\text{C}$  NMR spectra of 2-(Methylcycloprop-2-en-1-yl)methyl (4-nitrophenyl) carbonate (**33**)

## 8.25 $^1\text{H}$ NMR spectra of *N*-(((2-Methylcycloprop-2-en-1-yl)methoxy)carbonyl)mannosamine tetraacetate (36) Ac<sub>4</sub>ManCCp

